

**NANOTECHNOLOGY-BASED APPROACHES FOR  
REGENERATIVE MEDICINE AND BIOSENSING**

**BY ANIRUDDH P. SOLANKI**

A dissertation submitted to the  
Graduate School—New Brunswick  
Rutgers, The State University of New Jersey  
in partial fulfillment of the requirements  
for the degree of  
Doctor of Philosophy  
Graduate Program in Chemistry and Chemical Biology

Written under the direction of  
Professor Ki-Bum Lee  
and approved by

---

---

---

---

New Brunswick, New Jersey

May, 2013

## **ABSTRACT OF THE DISSERTATION**

# **Nanotechnology-based Approaches for Regenerative Medicine and Biosensing**

**by Aniruddh P. Solanki**

**Dissertation Director: Professor Ki-Bum Lee**

The recent emergence of nanotechnology has set high expectations in many fields of science, especially in biology and medicine. Nanotechnology-based approaches are expected to solve key questions in the emerging field of regenerative medicine. Regenerative medicine essentially deals with regeneration of cells, ultimately leading to the formation of tissues and organs. For this purpose, stem cells (embryonic stem cells or adult stem cells) are thought to be ideal resources. However, controlling the differentiation of stem cells into cells of a specific lineage is extremely vital and challenging. Addressing this challenge, in this work, novel nanotechnology-based approaches for controlling the differentiation of neural stem cells (NSCs) into neurons has been presented. Regeneration of damaged neurons, due to traumatic injuries or degenerative diseases, is extremely challenging. For this purpose, NSCs can be used as resources that can differentiate into neurons, thus having great potential in solving needs of many patients suffering from such conditions.

The initial part of this work presents the use of nanomaterials for efficiently delivering soluble cues such as small molecules and small interfering RNA (siRNA) into NSCs for controlling their differentiation into neurons. However, for regenerative purposes, it is preferred that least amounts of the delivery vehicle be used. Thus, the following

part of the thesis presents the development and applications of nanotechnology-based approaches for enhancing the differentiation of NSCs into neurons using insoluble cues. The cellular microenvironment, consisting for the extracellular matrix (ECM) was modified by the use of nanostructures, to deliver siRNA into NSCs to enhance neuronal differentiation. NSC differentiation was also controlled by the use of protein micropatterns, wherein the pattern geometry and size defined the fate of the NSCs. Lastly, graphene, in combination with nanoparticles was used as component of the ECM to not only enhance the differentiation of NSCs into neurons, but also align the axons of the differentiated NSCs, having significant implications for its use in regenerating injured spinal cords.

The final portion of the thesis focusses on developing highly sensitive and selective biosensors, for detecting biomarkers implicated in various diseases such as cancer and acute pancreatitis.

## Acknowledgements

First and foremost I would like to thank my Guru and spiritual master Guruhari Hariprasad Swamiji, because of whom I have been able to come to the United States and finish my graduate studies. There was a time when coming to study in the United States would have only been left as a dream if it were not for His constant inspiration to become the best at whatever you do, and the fact that God is taking care of me at each and every moment, hence whatever happens, happens only for the good. He has taught me how to use my eyes, ears and mouth correctly and that is something even my parents did not teach me. He has been with me at each and every step of my adult life and in fact it was Him who suggested I should move to New Jersey (when I was in New York) to pursue my graduate studies. His words, such as *work while you work, play while you play; mind your own; man is defined by the company he keeps; you have no right to judge anybody even for a fraction of a second; genius is ever genius*, have played a big role in shaping my life today. Whatever I have been able to achieve today, is only because of His blessings.

Next, I would like to thank Prof. KiBum Lee, who has been an exceptional mentor, guide, advisor and whatever other words there may be. But most importantly he has been a great friend. Being his first student he will always have a special place in my heart. I still remember the days when we did not have our own space and were complaining about dripping water and old buildings. It was at those times that his inspirational talks really helped me get motivated and focused. He always maintained that our competition was not within the Rutgers departments but with the top schools in the world, and that labs in many big schools were worse than ours, but produced great science. So, there was no excuse for mediocre work. He has always shared his experiences with me, trying to remind me not to make the same mistakes he made. I believe it takes a lot of humility and courage to be able to share mistakes with your

students and I really appreciate that. Being his student, and his first student, has prepared me well for a position in academia, and I could not have asked for anything more. In terms of research, Prof. Lee is the best mentor anyone could ask for. He had given me full academic freedom to pursue any idea I had, provided it is backed by a good hypothesis. It is precisely why I have not been bored doing research at all in the past 5 years. I really thank him from the bottom of my heart and I thank God for giving me such a brilliant, yet humble, advisor.

I would also like to thank my friends in the KBLee group. It has been a great pleasure to see the group grow and grow, people come and people go for over 5 years. I would especially like to thank Prasad and Birju, who were there from the beginning, for helping me with everything, bearing with my sloppiness, and most importantly, doing my lab duties for me. I hope we always remain friends and I also apologize for anything I may have done or said in the time we have been together in the lab. A special thanks to Shreyas Shah, who has been one of my best friends in lab and outside and has been with me in the lab from the start, first as an undergrad and then as a graduate student. His dedication, focus and attention to detail in many ways, has set a bar in the lab. I believe there is nothing Shrey cannot do, and that is awesome in so many ways. I would also take this moment to thank Sahishnu Patel, who is not only my friend in the lab but also my roommate. I would like to thank him for bearing with my laziness and helping me with whatever it is I need at whatever time. I am truly fortunate to have his company. Finally I would like to thank Dean (Sy-Tsong) Chueng, who is the IT person in our lab and a true genius. I would like to thank him for all the troubleshooting he has done for me and helping me with LaTeX in writing this thesis. Evenings at the gym with him will definitely be one of the memorable moments spent at Rutgers. I would also like to thank Perry for never saying no for anything I required, and Raj Kappera for helping with the characterization and synthesis of graphene and MoS<sub>2</sub>. I also appreciate the fact that Raj has not given up on our idea of making a MoS<sub>2</sub>-based biosensor.

I believe this is a good time to thank Prof. Kathryn Uhrich, who has agreed to be a part of my thesis committee. It is because of her that I am at Rutgers and I will

never forget the help she provided. In addition to being a brilliant scientist, she is an exceptional teacher, the best I have had so far at Rutgers. I was fortunate to have taken the polymer class when she taught it. That was the most fun class I have taken. Her open-mindedness, straight-forwardness and clarity of thought is something I aspire to achieve some day. I would also like to thank Prof. Eric Garfunkel and Prof. Manish Chhowalla for being a part of my thesis committee and providing valuable guidance throughout the years.

I would also like to thank Kishanji, the youth leader at my temple, who has been an exceptional friend and someone I look up to. He has always been there for all the problems I have had in my life, personal and professional. His presence and words have helped me get back on track without wasting my time. I would also take this moment to thank all my brothers in *Sarvam* and *Shabri*. I am not sure what I would do without their help.

Finally, I come to family and I have two families to thank. I lived with one during my studies at Rutgers and I grew up with the other (in Bombay) before I came to the United States. First, I would like to thank the one I stayed with in the United States. Dinesh Uncle, Hina Aunty, Prerakbhai and Bhaktiben. I would not have been able to finish my studies in time if it were not for them. They have not given me a chance to wash dishes, do laundry, or even make my bed. Their sole purpose had been to take care of me so I could study. I have no words to describe what they have done for me and how fortunate I am. Next, my parents back in India, who have always asked me to study hard and that if I do not study right now I would regret it later in life. They have always made sure that my brother and I get everything we need so we can have the best education. Despite all the trying times we have had, they have not given me a chance to complain. I thank them for their blessings, love and care for all these years. Finally, I would like to thank my younger brother Mihir, who has always believed in me and asked me to stay away from jobs in industry as he believes academia offers the most creative freedom. I thank him for his advice and all the help he has given me whenever I have asked for it. He has always had my back.

## Dedication

I would like to dedicate this work to Lord Swaminarayan and my spiritual master Guruhari Hairprasad Swamiji. I would also like to dedicate this work to Pujya Prabodh Swamiji, Ashok Uncle, Kishanji and to my friends who were highly qualified individuals in the United States, but left all their aspirations behind to become teachers at Atmiya Vidya Mandir in India. Finally, this work is also dedicated to my parents Prakash Solanki and Sheela Solanki who have worked all their life for making sure I can achieve all my dreams.

## Table of Contents

<b>Abstract</b> . . . . .	ii
<b>Acknowledgements</b> . . . . .	iv
<b>Dedication</b> . . . . .	vii
<b>List of Tables</b> . . . . .	xiv
<b>List of Figures</b> . . . . .	xv
<b>1. Introduction</b> . . . . .	1
1.1. Nanoparticles for Drug Delivery and Molecular Imaging in Stem Cells . . . . .	4
1.1.1. Magnetic Nanoparticles . . . . .	5
1.1.2. Quantum Dots . . . . .	11
1.1.3. Gold Nanoparticles . . . . .	18
1.1.4. Dendrimers . . . . .	19
1.2. Nanotopography for Controlling Stem Cell Behaviors . . . . .	23
1.2.1. Patterning of Topographical Cues . . . . .	24
1.2.2. Nanomaterials for Generating Topographical Cues . . . . .	27
1.3. Nanomaterials for Developing Biosensors . . . . .	32
1.3.1. Carbon Nanotubes . . . . .	32
1.3.2. Graphene . . . . .	34
1.3.3. Silicon Nanowires . . . . .	35
1.4. Conclusion . . . . .	37
1.5. Overview of Dissertation . . . . .	38
<b>2. Nanomaterials for siRNA Delivery into Neural Stem Cells</b> . . . . .	41

2.1. Selective Inhibition of Human Brain Tumor Cells through Multifunctional Quantum-Dot-Based siRNA Delivery . . . . .	42
2.1.1. Introduction . . . . .	42
2.1.2. Results and Discussion . . . . .	43
Multifunctional quantum-dots for delivery and tracking of siRNA	44
EGFP knockdown and target-specific intracellular delivery of siRNA-QDs . . . . .	45
Knockdown of EGFRvIII as a chemotherapeutic target by siRNA-QDs . . . . .	51
2.1.3. Conclusions . . . . .	54
2.1.4. Materials and Methods . . . . .	54
Synthesis of the Core-Shell QDs . . . . .	55
Synthesis of QD conjugates with siRNA . . . . .	55
Cell Culture of U87-EGFP and U87-EGFRVIII . . . . .	56
Targeted delivery of siRNA-QDs . . . . .	56
Transmission electron microscopy and fluorescence microscopy .	57
Cell viability assay . . . . .	57
Western blot analysis . . . . .	57
2.2. Simultaneous Delivery of siRNA and Small Molecule Using Polyamine-Cyclodextrins to Enhance Neuronal Differentiation of Neural Stem Cells	58
2.2.1. Introduction . . . . .	58
2.2.2. Results and Discussion . . . . .	60
DexAM: Structure and Synthesis . . . . .	61
GFP knockdown efficiency of DexAM . . . . .	63
DexAM is non-cytotoxic and biocompatible . . . . .	65
Enhanced neuronal differentiation of NSCs using DexAM . . . . .	66
2.2.3. Conclusions . . . . .	69
2.2.4. Materials and Methods . . . . .	69
Detailed synthesis of DexAM . . . . .	70

Inclusion of retinoic acid (RA) into DexAM . . . . .	75
Formation of polyplexes between siRNA and DexAM . . . . .	76
Neural stem cell culture and differentiation . . . . .	77
Cell viability assay . . . . .	77
Immunocytochemistry . . . . .	77
<b>3. Manipulating Surface Chemistry to Enhance Neuronal Differentiation of Neural Stem Cells . . . . .</b>	<b>79</b>
3.1. Nanotopography-mediated Reverse Uptake of siRNA for Enhancing Neu- ronal Differentiation of Neural Stem Cells . . . . .	80
3.1.1. Introduction . . . . .	80
3.1.2. Results and Discussion . . . . .	84
Nanotopographical features determine siRNA-based gene knock- down in NSCs . . . . .	84
NanoRU delivers only siRNA into NSCs and not SiNPs . . . . .	86
Controlling neuronal differentiation of NSCs using NanoRU . . . . .	88
NanoRU for delivering siRNA into other mammalian cells and miRNA into NSCs . . . . .	90
NanoRU does not damage cell membranes and is non-toxic . . . . .	92
3.1.3. Conclusions . . . . .	93
3.1.4. Materials and Methods . . . . .	94
NanoRU preparation . . . . .	94
Coating NanoRU with laminin and siRNA . . . . .	95
Rat neural stem cell (NSC) culture and differentiation . . . . .	95
Culturing U87-EGFRvIII, SUM159, and Astrocytes . . . . .	96
Cell viability assays . . . . .	96
Immunocytochemistry . . . . .	97
PCR analysis . . . . .	97

3.2. Controlling Differentiation of Neural Stem Cells Using Extracellular Matrix Protein Patterns . . . . .	99
3.2.1. Introduction . . . . .	99
3.2.2. Results and Discussion . . . . .	101
Differentiating neural stem cells on ECM protein patterns . . . . .	102
Neuronal differentiation is dependent on the geometry of ECM micropatterns . . . . .	103
Neuronal differentiation is influenced by the size of ECM micropatterns . . . . .	107
3.2.3. Conclusions . . . . .	110
3.2.4. Materials and Methods . . . . .	111
Synthesis and Characterization of $EG_4-(CH_2)_{11}-SH$ . . . . .	111
Generating ECM protein patterns . . . . .	112
Rat neural stem cell (NSC) culture and differentiation . . . . .	113
Immunocytochemistry . . . . .	113
3.3. Nanoparticle Arrays Decorated with Graphene Align Axons and Enhance Neuronal Differentiation of Human Neural Stem Cells . . . . .	115
3.3.1. Introduction . . . . .	115
3.3.2. Results and Discussion . . . . .	117
Human NSCs align on GO and SiNP-GO substrates . . . . .	117
GO and SiNP-GO substrates enhance cell survival . . . . .	121
Neuronal differentiation of hNSCs . . . . .	122
Axonal alignment on pristine graphene . . . . .	123
Human NSC alignment on flexible polymeric substrates . . . . .	125
3.3.3. Conclusions . . . . .	127
3.3.4. Materials and Methods . . . . .	127
Synthesis of chemically derived graphene, pristine graphene and $MoS_2$ nanoflakes . . . . .	127
Preparation of different substrates . . . . .	128

Human neural stem cell (hNSC) culture and differentiation . . .	130
Image analysis . . . . .	131
Cell viability assay . . . . .	131
Immunocytochemistry . . . . .	132
PCR analysis . . . . .	132

**4. Developing Biosensors for Highly Sensitive and Selective Detection of Biomarkers . . . . . 134**

4.1. Graphene-Encapsulated Nanoparticle-based Biosensor for the Selective Detection of Cancer Biomarkers . . . . .	135
4.1.1. Introduction . . . . .	135
4.1.2. Results and Discussion . . . . .	136
Fabrication of arrays of graphene-encapsulated nanoparticles . .	136
Gating effect of rGO-NP device . . . . .	139
Sensitivity and selectivity of rGO-NP biosensor for detecting HER2140	
Sensitivity and selectivity of rGO-NP biosensor for detecting EGFR142	
4.1.3. Conclusions . . . . .	143
4.1.4. Materials and Methods . . . . .	144
Preparation of reduced graphene oxide and SiO <sub>2</sub> NPs . . . . .	144
Synthesis of 4-(pyren-1-yl)butanal . . . . .	144
Surface molecular patterning . . . . .	144
Metal deposition and measurement of graphene devices . . . . .	145
Functionalization the rGO-NPs with monoclonal antibodies . . .	145
4.2. Label-free Polypeptide-based Enzyme Detection Using a Graphene-nanoparticle Hybrid Sensor . . . . .	146
4.2.1. Introduction . . . . .	146
4.2.2. Results and Discussion . . . . .	148
4.2.3. Conclusions . . . . .	158
4.2.4. Materials and Methods . . . . .	159

Metal deposition and measurement of graphene devices . . . . .	159
Synthesis of 1-butyl-3-methylimidazolium hexafluorophosphate (BMIM- PF <sub>6</sub> ) . . . . .	159
Synthesis of 4-(pyren-1-yl)butanal . . . . .	160
Synthesis of the amino acid N-carboxy anhydrides (2, NCAs) . .	160
Deposition and Patterning of Graphene . . . . .	160
Synthesis of 3-armed polypeptides (5) . . . . .	161
4.3. Zinc Oxide Thin Film Transistor Immunosensor with High Sensitivity and Selectivity . . . . .	163
4.3.1. Introduction . . . . .	163
4.3.2. Results and Discussion . . . . .	164
Sensitivity of the ZnO-bioTFT immunosensor . . . . .	165
Selectivity of the ZnO-bioTFT immunosensor . . . . .	165
4.3.3. Conclusions . . . . .	167
4.3.4. Materials and Methods . . . . .	168
Device fabrication . . . . .	168
Bio-functionalization of device with antibodies . . . . .	171
<b>5. Conclusions and Perspectives . . . . .</b>	<b>172</b>
<b>References . . . . .</b>	<b>176</b>

## List of Tables

3.1. Primers for PCR analysis . . . . .	98
3.2. Primers for PCR analysis . . . . .	133

## List of Figures

1.1. Range of scale of biomolecular interactions. . . . .	2
1.2. Nanotechnology-based approaches for regulating stem cell fate [1]. . . . .	3
1.3. Neural stem cells labeled with magnetic nanoparticles . . . . .	6
1.4. Magnetic resonance images of SPION-labeled stem cells . . . . .	9
1.5. Transplanted oligodendrocyte precursor cells (OPCs) into organotypic slice cultures . . . . .	11
1.6. Excitation and emission spectra of quantum dots . . . . .	12
1.7. Emission properties of ZAIS quantum dots . . . . .	14
1.8. Mesenchymal stem cells labeled with quantum dots . . . . .	15
1.9. Multiplex imaging of embryonic stem cells labeled with quantum dots . . . . .	16
1.10. <i>In utero</i> electroporation for labelling neural stem and progenitor cells . . . . .	17
1.11. Dendrimer-based gene delivery into mesenchymal stem cells . . . . .	21
1.12. Tracking neural stem cells labeled with magnetodendrimers . . . . .	22
1.13. Nanoscale features for controlling stem cell behaviors . . . . .	23
1.14. Cells cultured on different patterned features . . . . .	24
1.15. Mesenchymal stem cells differentiated on ECM protein patterns . . . . .	26
1.16. Human neural stem cell growth and polarization on CNT patterns coated with laminin . . . . .	27
1.17. Polarization-controlled neuronal differentiation of individual hNSCs us- ing CNT patterns . . . . .	28
1.18. Human neural stem cells cultured on graphene . . . . .	30
1.19. Nanofibers for differentiation of rat neural stem cells . . . . .	31
1.20. Schematic diagram for functionalization of carbon nanotubes . . . . .	33
1.21. Detection of biomolecules using silicon nanowire biosensor . . . . .	35

2.1. siRNA-QDs for delivery and tracking . . . . .	44
2.2. Toxicity of QDs using MTS assay . . . . .	46
2.4. Targeted delivery of multifunctional siRNA-QDs . . . . .	47
2.3. Knockdown of EGFP in U87 cells using siRNA-QD . . . . .	48
2.5. Knockdown efficiency of EGFP using multifunctional siRNA-QDs . . . . .	50
2.6. EGFP knockdown using siRNA (without QDs) and siRNA-QDs . . . . .	51
2.7. Knockdown of EGFRvIII in U87 EGFRvIII using multifunctional siRNA-QDs . . . . .	53
2.8. Schematic diagram showing the application of DexAM for stem cells . . . . .	60
2.9. General Scheme for the Synthesis of DexAM . . . . .	62
2.10. siRNA complexation efficiency of DexAM . . . . .	63
2.11. Delivery of DexAM-siRNA for GFP Knockdown in neural stem cells . . . . .	64
2.12. DexAM cytotoxicity in neural stem cells . . . . .	65
2.13. Neural stem cell differentiation using DexAM . . . . .	68
2.14. First Round of Michael Addition and Amidation for synthesizing DexAM . . . . .	70
2.15. Second Round of Micheal Addition and Amidation for synthesizing DexAM . . . . .	72
2.16. Synthesis of mono-tosylated cyclodextrin . . . . .	73
2.17. Conjugation of $\beta$ -CD to the Polyamine Backbone . . . . .	74
2.18. Inclusion of RA into DexAM . . . . .	76
2.19. Polyplex formation of DexAM and siRNA . . . . .	76
3.1. Schematic diagram depicting the application of NanoRUs . . . . .	82
3.2. Characterizing cellular uptake of siRNA from NanoRU . . . . .	85
3.3. TEM images to confirm uptake of SiNPs . . . . .	87
3.4. Effect of endocytosis inhibitors on GFP knockdown . . . . .	88
3.5. NSC differentiation on NanoRU coated with SOX9 siRNA (siSOX9) . . . . .	89
3.6. Colocalization of neuronal markers . . . . .	90
3.7. Cellular uptake of siRNA and cellular viability in different cell types . . . . .	91
3.8. siRNA uptake within Astrocytes . . . . .	91
3.9. NanoRU for miRNA uptake . . . . .	92

3.10. Time-dependent siRNA Uptake . . . . .	93
3.11. A schematic diagram of ECM protein patterns for NSC differentiation .	101
3.12. Immunostaining with anti-laminin IgG . . . . .	102
3.13. Growth and differentiation of NSCs on the laminin patterns . . . . .	105
3.14. Quantitative analysis of NSC differentiation . . . . .	107
3.15. NSC alignment and differentiation on combinatorial ECM patterns . . .	108
3.16. Actin and nestin staining for NSCs on squares and stripes of laminin . .	109
3.17. Colocalization of TuJ1 and synapsin within cells on grid patterns . . . .	110
3.18. Schematic diagram depicting the influence of nanoparticle monolayers coated graphene oxide . . . . .	117
3.19. Aligned growth and extension of axons . . . . .	118
3.20. Scanning electron microscopy and MTS assay of hNSCs . . . . .	120
3.21. Axonal alignment and cell density . . . . .	121
3.22. Enhanced neuronal differentiation of hNSCs on SiNP-GO . . . . .	123
3.23. Axonal alignment on pristine graphene . . . . .	124
3.24. Axonal alignment on pristine graphene . . . . .	125
3.25. Axonal Alignment on flexible polymeric substrates . . . . .	126
3.26. Raman Spectroscopy and SEM imaging . . . . .	130
4.1. Fabrication process of biomolecular sensor based on graphene-coated NPs	136
4.2. AFM analysis of graphene oxide . . . . .	137
4.3. Reduced GO-NP patterns and the electrical property of the rGO-NP device	139
4.4. Real-time detection of cancer marker, HER2 . . . . .	141
4.5. Real-time detection of cancer marker, EGFR . . . . .	143
4.6. Schematic of the enzyme biosensor . . . . .	149
4.7. Characterization data of the biosensor using AFM and SEM . . . . .	152
4.8. Measurement of the hysteresis change due to enzyme exposure . . . . .	155
4.9. Enzyme detection using the graphene-nanoparticle hybrid sensor . . . . .	157
4.10. Synthetic scheme of polypeptide linkers . . . . .	162
4.11. Sensitivity of the ZnO-bioTFT immunosensor . . . . .	165

4.12. Selectivity of the ZnO-bioTFT immunosensor . . . . .	167
4.13. Transconductance curve of the ZnO-bioTFT and characteristic curves .	169
4.14. Schematic diagram of ZnO-bioTFT immunosensor . . . . .	170

# Chapter 1

## Introduction

It was in 1959, that the Nobel Prize winner Richard Feynmann put forth the ground breaking idea of developing molecular machines. Ever since, the scientific community has dug deeper and deeper into the role that - what we call today as nanotechnology - has played in the various facets of society. The underlying principle of any approach or methodology based on nanotechnology is the ability to control the properties of materials by assembling them at the nanoscale. We have witnessed tremendous progress of nanotechnology over the past few decades. The recent emergence of nanotechnology, however, has set very high expectations in biological and medical sciences. This is not surprising at all, given that the sizes of functional elements in biology such as proteins and polynucleic acids are in the nanometer scale range [2]. In addition, nanomaterials have novel electronic, optical, magnetic, and structural properties that cannot be obtained from either individual molecules or bulk materials. These unique features can be precisely tuned to explore biological phenomena through numerous innovative techniques. In fact, we believe the current nanotechnology-based approaches can resolve key questions concerning biological systems by giving us the ability to investigate, probe and manipulate these systems at the nanoscale. However, in order to apply nanotechnology to investigating and solving the key questions in biology and medicine, several conditions must be considered: i) the nanomaterials used must be designed to interact with proteins and cells without interfering with their biological activities, ii) nanomaterials must maintain their physical properties after surface modification, and iii) nanomaterials must be non-toxic.

One of the important technological aspects of nanotechnology-based applications lies in the ability to tune materials in a way that their spatial and temporal scales

are compatible with biomolecules. That said, materials and devices fabricated at the nanometer scale can investigate and control the interactions between biomolecules and their counterparts at almost the single molecule level. This, in turn, indicates that nanomaterials and nanodevices can be fabricated to show high sensitivity, selectivity, and control properties, which usually cannot be achieved in bulk materials. The wide range of the scale of biointeractions is described in Figure 1.1.

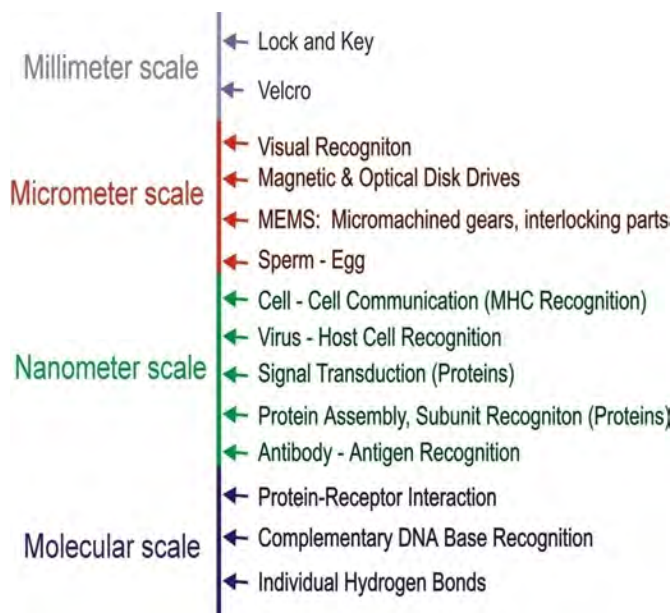


Figure 1.1: Range of scale of biomolecular interactions.

Most of the nanotechnology-based approaches developed thus far, including nanomaterials for drug and gene delivery, molecular imaging, and biosensing, have had their applications mainly in cancer biology. However, recent advancements in stem cell biology and the potential of stem cells in regenerative medicine have led to a significant boost in the applications of nanotechnology in regenerative medicine. This might be due to a number of factors including (1) developing safer and smarter nanomaterials for biomedical applications, (2) a growth in the awareness amongst materials scientists and tissues engineers about the potential impact and usefulness of stem cells, (3) a tremendous success in the application of nanotechnologies in medicine, and (4) isolation and development of novel sources of stem cells [3]. Therefore, it is not surprising that the last decade has seen a significantly large proportion of chemists, materials scientists

and biomedical engineers working hand-in-hand with medical experts to develop novel approaches for using stem cells to address the current limitations in medical science. Figure 1.2 [1] summarizes some of the important nanotechnology-based approaches for stem cell research. This chapter will broadly cover the applications of nanotechnology in regenerative medicine with a focus on (i) nanostructures for drug delivery and molecular imaging in stem cells (ii) nanotopography for controlling stem cell behaviors (iii) nanomaterials for developing biodetection.

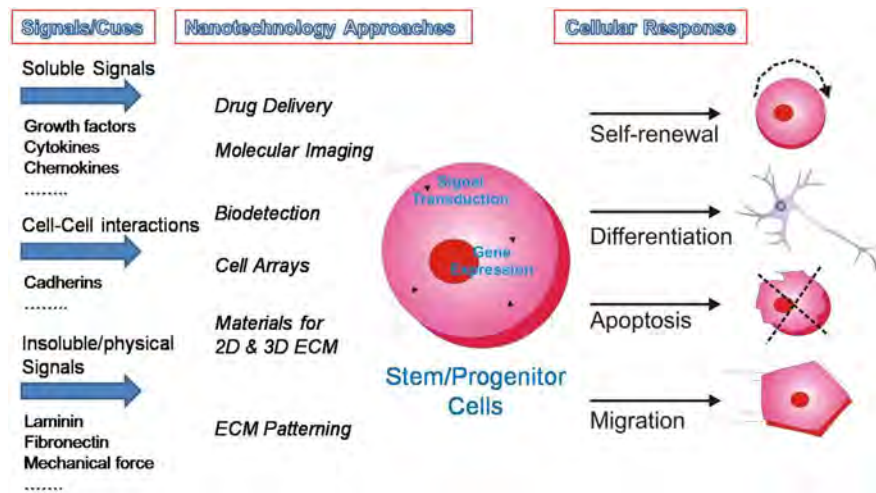


Figure 1.2: Nanotechnology-based approaches for regulating stem cell fate [1].

## 1.1 Nanoparticles for Drug Delivery and Molecular Imaging in Stem Cells

Nanoparticles (NPs) are attractive due to several unique properties owing to their size, which is between that of bulk materials and individual atoms or small molecules. Due to their small size, they exhibit unique pharmacokinetics, requiring minimal renal filtration. Nanoparticles also have enormous surface-to-volume ratios which afford modification with various ligands and functional groups that can help target, internalize or stabilize the NPs. They can be synthesized or generated from a wide variety of materials, thus exhibiting unique optical, magnetic and electrical properties. While many of such properties may be described as intermediate between bulk materials and small molecules, other properties such as superparamagnetism and quantum confinement are unique to the nanoscale.

Nanoparticles have a number of properties which are quite useful for investigating and controlling stem cell behaviors. These NPs are typically inorganic, dendritic or polymeric and their small size allows them to be easily taken up by the cell. Furthermore, the particles can interact with individual biomolecules at the molecular level. Size is known to have a profound effect on the properties of nanoparticles and by controlling the conditions of nanoparticle synthesis, the size and shape can be controlled within a very tight distribution [1]. By making use of inorganic, organic, and surface chemistry, biomolecules such as antibodies [4] or peptides [5] can be added to nanoparticles to include functionality (for targeting) or to improve cellular uptake. Nanoparticles are used for delivery of the desired cargo into stem cells and also for tracking the stem cells once they are transplanted *in vivo*. Important types of NPs used for probing stem cell behaviors, with an overall goal of bringing significant improvements to regenerative medicine, will be discussed.

### 1.1.1 Magnetic Nanoparticles

Transplanting various stem cells for tissue regeneration is an extremely promising therapeutic strategy. One of the key factors in this approach is the availability of techniques which would allow for long term, non-invasive detection of transplanted stem cells and at the same time allow for monitoring their differentiation, survival and proliferation within the desired organs. Several techniques such as magnetic resonance imaging (MRI), bioluminescence, positron emission tomography, and multiple photon microscopy are now available for *in vivo* cellular imaging. Of these, MRI offers several advantages such as high resolution, speed, easy accessibility and three dimensional capabilities [6, 7]. In addition to providing information about the transplanted stem cells, a significant advantage of MRI is that it provides information about the surrounding tissues (e.g. edema, lesion, or inflammation), which may have an effect on the fate of grafted stem cells or may hinder the recovery of damaged tissues [8]. Magnetic nanoparticles (MNPs), whose sizes can be precisely tuned, offer great potential for MRI applications. The magnetic nanocrystals tend to behave as a single magnetic domain in which all nuclear spins couple to create a single large magnetic domain. At certain temperatures and crystal sizes, these moments wander randomly (superparamagnetic), or become locked in one direction, making the material ferromagnetic [9]. Magnetic nanocrystals of differing compositions and sizes can be synthesized to generate ultra-sensitive molecular images as shown in Figure 1.3 [10].

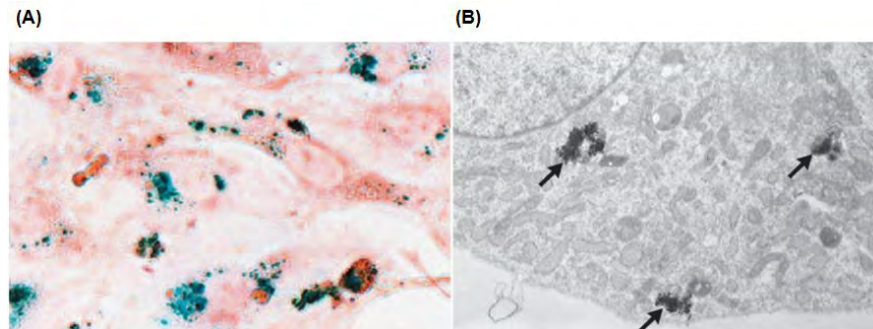


Figure 1.3: Neural stem cells labeled with magnetic nanoparticles. (A) Photomicrograph showing iron oxide nanoparticles (blue) in neural stem cells stained with Prussian blue and counterstained with neutral red.(B) Transmission electron photomicrograph of neural stem cells showing iron oxide nanoparticles in the nuclear and cell membranes [10].

Magnetic nanoparticles can either bind to the external cell membrane or be internalized into the cytoplasm. Particles that are bound externally do not affect cell viability and can be used for remotely actuating the MNPs which causes the activation of signaling pathways within the cells or causes the release of drugs from the MNPs [11]. However, the externally bound MNPs may interfere with cell-surface interactions or simply detach from the cell membrane [12]. On the other hand, the surfaces of MNPs can be modified to ensure that they are internalized within cells in a highly efficient manner, with minimum deleterious effects on the cells [13]. For example, dextran or other similar polymers have been used to coat the surfaces of superparamagnetic iron oxide nanoparticles (SPIONs) to enhance the stability and solubility of SPIONs [14] and also prevents aggregation [15]. The coated SPIONs are useful for tracking and studying stem cells with magnetic resonance imaging (MRI). In this regard, magnetic iron oxide nanoparticles and their composites are emerging as novel contrast agents for MRI and are much more sensitive than conventional gadolinium-based contrast agents [7]. The use of SPIONs as *in vivo* cellular imaging agents is rapidly increasing. Since their unique properties allow precise control of size and composition, MNPs offer great potential for highly specific MRI to track stem cells. The major transfer mechanism of nanoparticles through the cell membrane, in order to label stem cells, is endocytosis or more specifically pinocytosis [16–18].

Dextran coated SPIONs are commonly used to label stem cells. However, they may be unfavorable to endocytosis, thus reducing their labeling efficiency. Therefore, higher concentrations of nanoparticles and additional transfection agents would be required to label stem cells. Furthermore, several studies have found that iron oxide nanoparticles, which tend to dissolve within the cells, may increase the formation of free hydroxyl radicals and reactive oxygen species. These may have toxic effects, such as an increase in the rate of apoptosis or cell death and alterations in cellular metabolism [19], potentially due to the dissolved  $\text{Fe}^{2+}$  ions from the dissolved iron oxide nanoparticles. This is highly undesirable for labeling stem cells as they need to survive for longer periods. In order to protect stem cells from the toxic effects of SPIONs and to successfully track the behavior of stem cells *in vivo*, a very attractive alternative is to coat the SPIONs with gold. A gold coating provides an inert shell around the nanoparticles and protects them from rapid dissolution within the cytoplasmic endosomes [20]. In addition, the gold coated shell significantly enhances MRI contrast. More importantly, gold has very well defined surface chemistry with thiol (-SH) or amine (-NH<sub>2</sub>) moieties. This offers an attractive and convenient route for further functionalization of the SPIONs with biomolecules via thiol or amine coupling chemistry [21]. For instance, magnetic iron oxide nanoparticles (MIONs) were coated with gold to form a typical core-shell structure [20]. These Au-MIONs, of 20 nm hydrodynamic size, were used to label NSCs obtained from the rat spinal cord. When the labeled NSCs were transplanted within the spinal cord, the Au-MION system offered a strong and durable signal such that, as little as 20 cells could be detected with relative ease under optimal conditions using MRI. In addition, the Au-MION labeling helped distinguish the labeled NSCs from the haemoglobin breakdown products *in vivo*. False positives obtained due to Prussian Blue staining of haemoglobin products in histology could be avoided by using a selective stain for gold. In another study, Zhu and coworkers [10] labeled human neural stem cells with SPIONs using a non-liposomal lipid-based transfecting agent. The labeled cells were then implanted in the region of brain damage in a patient suffering from brain trauma. The migration of neural stem cells from the site of injection to the border of the injured tissue of the brain was successfully detected (Figure 1.3) [10]. One of

the challenges of using SPIONs is the potential transfer of the contrast agent from the labeled stem cells to other cell types such as macrophages, which metabolize iron after engulfing the stem cells. However, through detailed studies and experimentation, Zhu and coworkers excluded the possibility that magnetic signals could have been generated by macrophages engulfing the neural stem cells, and thus concluded that the signals were indeed generated by the migrating stem cells and not by the engulfed stem cells.

Stem cells can be labeled with SPIONs by modifying their surfaces with internalizing ligands such as the HIV-Tat peptide, dendrimers, and polycationic (PC) transfection agents. In addition to internalizing ligands, the SPIONs can be multifunctionalized using fluorescent and isotope labels. These multifunctional nanoparticles can be used to combine methods such as optical and nuclear imaging with MRI in order to validate the cellular behavior *in vivo*. This was aptly demonstrated by Lewin et al [5]. The magnetic nanoparticles used by the group consisted of small (5 nm) monocrystalline superparamagnetic iron oxide cores which were stabilized by coating with crosslinked (CL) aminated dextran. The overall size of the nanoparticles further increased to 45 nm. In order to modify the nanoparticles with a fluorescent label, the internalizing ligands, FITC-derivatized HIV-TAT peptides, were attached to the coat of the aminated dextran. In addition, the SPIONs were further modified for concomitant nuclear imaging by reacting the dextran coating with a chelator, diethylenetriamine pentaacetic acid (DTAP), so as to label the nanoparticles (NPs) with  $^{111}\text{In}$  isotope. The modified SPIONs, with a triple label (magnetic, fluorescent, and isotope), efficiently internalized into hematopoietic stem and neural progenitor cells. The group further demonstrated that the labeled neural progenitor cells retained their capability for differentiation and the iron incorporation did not have any effect on viability and proliferation of hematopoietic (CD34+) cells. In another study, dextran-coated magnetic iron oxide nanoparticles with a core diameter of  $4.6 \pm 1.2$  nm and an overall size, after coating with dextran, of 8-20 nm were covalently attached to OX-26, an anti-transferrin receptor monoclonal antibody [22]. The antibody-functionalized nanoparticles were used to label oligodendrocyte progenitor cells by targeting the transferrin receptors (Tfr) on the cells. The

progenitor cells were made highly magnetic by incubating them with iron oxide nanoparticles. Since the oligodendrocyte progenitor cells have previously shown to myelinate significantly large areas in the central nervous system [23] they were transplanted into the spinal cord of myelin-deficient rats. After neurotransplantation, these cells could be easily tracked using MRI and the extent of myelination could be determined (Figure 1.4A). The progenitor cells were found to fully retain their capacity for myelination and migration *in vivo* [22]. Similarly, MSCs labeled with magnetic nanoparticles, when transplanted within a rat experimental model of stroke, migrated from the site of injection into the lesion. The MSCs could be tracked for three weeks after transplantation. MRI showed a decrease in the concentration of magnetic nanoparticles at the injection site and an increase within the lesion after the second and third weeks following injection (Figure 1.4B) [8].

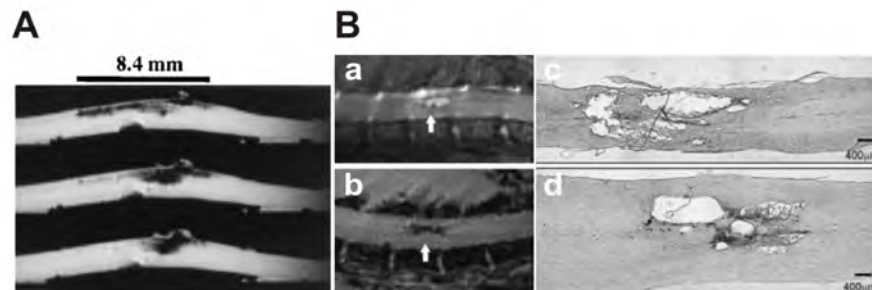


Figure 1.4: Magnetic resonance (MR) images of SPION-labeled stem cells. (A) MR images of the spinal cord (three consecutive slices) show the cellular migration of the SPION labeled oligodendrocyte progenitor cells, over a distance of 8.4 mm, 10 days after transplantation [22] (B) SPION-labeled MSCs intravenously injected into a rat spinal cord. (a) The lesion in the spinal cord appears as a hyperintensive area (bright spot, arrow), (b) SPION-labeled MSCs are visible as a hypointensive spot (dark spot), (c) Prussian Blue staining of a lesion in the spinal cord of a control animal (without MSCs), (d) Prussian Blue staining of a lesion in the spinal cord of a rat injected with SPION-labeled MSCs. The lesion is populated with Prussian Blue-positive MSCs [8].

Tracking of stem cell migration is not limited to neural stem cells. It is also possible to study the migration of stem cells labeled with SPIONs in other systems such as the cardiovascular system. Regenerative medicine for cardiac diseases will have enormous therapeutic potential in the future for situations involving ischemic cardiac injury, which involves irreversible cardiac damage. Bulte and coworkers [24] demonstrated the

potential of MRI in tracking magnetically labeled mesenchymal stem cells (MSCs) in a swine model of myocardial infarction. The mesenchymal stem cells were labeled with dextran-coated SPIONs (Feridex<sup>®</sup>) in order to noninvasively track the quantity and location of the MSCs after myocardial infarction. It was concluded that the MRI tracking of the MSCs labeled with Feridex<sup>®</sup> was feasible and represented a preferred method for studying engraftment of MSCs in myocardial infarction.

Magnetic nanoparticles are not only used as imaging agents, but can be used for delivering genetic materials into stem cells using an external magnetic field. This process is referred to as magnetofection. In addition to being a very efficient method for delivering cargo into stem cells, it has the added advantage of being able to label the stem cells, and thus track them using MRI when transplanted *in vivo*. Pickard et al. used magnetofection to transfect plasmid DNA having the gene expressing green fluorescent proteins (GFP) into NPCs [25]. They demonstrated that using magnetofection the NPCs could be transfected multiple times (multifection) leading to enhanced transfection efficiency with negligible toxicity. The NPCs that were multifected survived and differentiated in 3D neural tissue post-transplantation. Furthermore, the multifection process had no adverse effects on NPC proliferation or differentiation. In another study by the same group, it was demonstrated that oligodendrocyte precursor cells (OPCs) can be transfected with reporter and therapeutics genes using magnetofection [26].

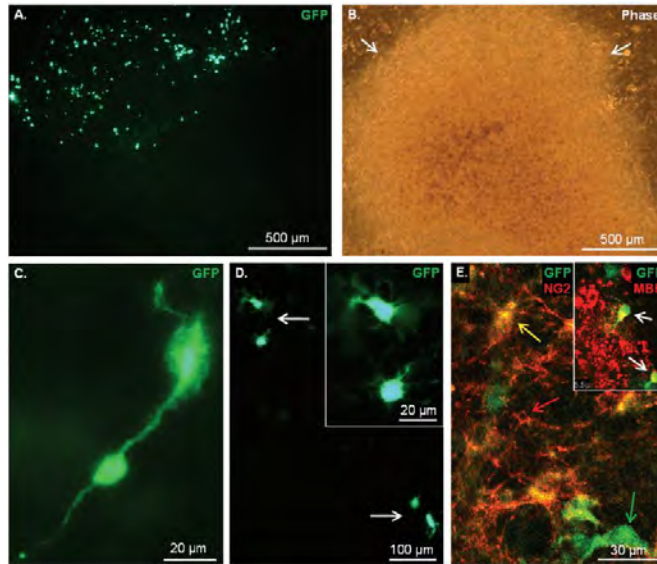


Figure 1.5: Transplanted oligodendrocyte precursor cells into organotypic slice cultures where the transplanted OPCs survive, migrate, proliferate and differentiate following transplantation. (A) Fluorescence microscopy image of GFP-labeled OPCs immediately post-transplantation. (B) Corresponding phase image. (C) GFP-labeled cells were observed having bipolar morphologies typical of migrating OPCs at 24 h. (D) Proliferation of OPCs at 48 h and multipolar morphologies indicating normal differentiation (D, inset). (E) Confocal microscopy image of NG2-positive (OPC marker) transplanted OPCs (yellow arrow) against a background of red NG2-positive host OPCs (red arrow). Inset shows MBP-positive (oliodendrocyte marker) cells at 48 h post-transplantation indicating differentiation of OPCs [26].

The transfection efficiency was significantly enhanced by applied static or oscillating magnetic fields. The researchers showed that the transfection and the subsequent expression of the genes was highly competitive or better than the widely used current methods such as nonviral transfection using cationic lipids and electroporation. They found that when the magnetofected OPCs were transplanted into brain slices (host tissue), the cells could migrate, divide, give rise to daughter cells, and integrate within the host tissue (Figure 1.5). Magnetofection is thus a simple and effective alternative to current methods for gene transfection into stem cells.

### 1.1.2 Quantum Dots

Quantum dots (QDs) are robust fluorescent semiconducting nanocrystals with broad absorption spectra and narrow emission spectra (Figure 1.6) [27]. Apart from MNPs,

QDs are being extensively used for applications in cell biology such as cell labeling, cell tracking, and *in vivo* imaging due to their potential in imaging and detection applications. Quantum dots overcome limitations of conventional imaging methods such as fluorescence microscopy and differential interference contrast microscopy. Conventional methods are limited by a lack of quantitative data, high background noise from labeled biomolecules, and a requirement for long observation times due to photobleaching, which gradually leads to a loss of signals [28]. Quantum dots, on the other hand, exhibit extreme brightness and resistance to photobleaching, which allows the use of lasers having low intensities over long periods of time, thus making them extremely useful for live cell imaging. Additionally, QDs offer many advantages such as high fluorescent intensity from high quantum yields and high molar extinction coefficients, resistance to chemical degradation, and long fluorescence lifetimes ( $>10$  ns).

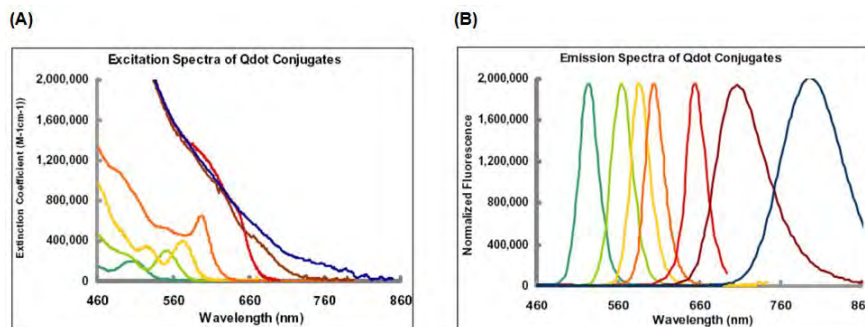


Figure 1.6: Excitation and emission spectra of quantum dots (QDs). (A) Broad excitation spectra of QDs. (B) Narrow emission spectra of QDs [27].

Multiple QDs with different emission wavelengths can be used in parallel for multiplex imaging [29–32]. The interesting optical properties of QDs originate from the interactions between electrons, holes, and their local environments, which can be precisely controlled to generate desired emission and absorption spectra. Since absorption and emission spectra exhibit sensitive changes depending on particle size, a wide range of emission spectra from ultraviolet (UV) to infrared (IR) can be obtained. Therefore, unique emission spectra by synthesizing particles with different diameters have been acquired [33–35]. Quantum dots generally have a core composed of heavy metals, such as Cadmium-Selenide (CdSe), Cadmium-Telluride (CdTe), with a surrounding ZnS shell.

The thickness of the shell can be tuned depending on the reaction time. Typically, the core/shell QDs with sizes ranging from 2-8 nm in diameter are synthesized by changing reaction conditions such as temperature, duration, and ligands. The unique photophysical properties of QDs stems from their nanometer scale size. By changing sizes and compositions, their optical properties can be precisely controlled for many applications. For example, QDs can be used effectively in multiplexing experiments where multiple biological units can be labeled simultaneously. Moreover, due to the resistance to photobleaching, QDs have enabled scientists to study live cells and complex mechanisms of biological processes in a real-time manner [36, 37]. A new generation of QDs have recently become popular as their emission properties depend on the materials from which are synthesized and not on their sizes. For instance, Subramaniam et al. synthesized a library of non-toxic QDs from a combination of zinc (Zn), silver (Ag), Indium (In) and sulfide (S) [38]. These QDs are known as ZAIS QDs and were synthesized using ultrasonication. A library of ZAIS QDs was synthesized by changing the ratios of each of the four elements, thus giving unique emission profiles for the same size (Figure 1.7). Considering the toxicity of the heavy metals such as cadmium and selenide, the non-toxic ZAIS QDs seem to be an attractive choice for cellular delivery and molecular imaging.

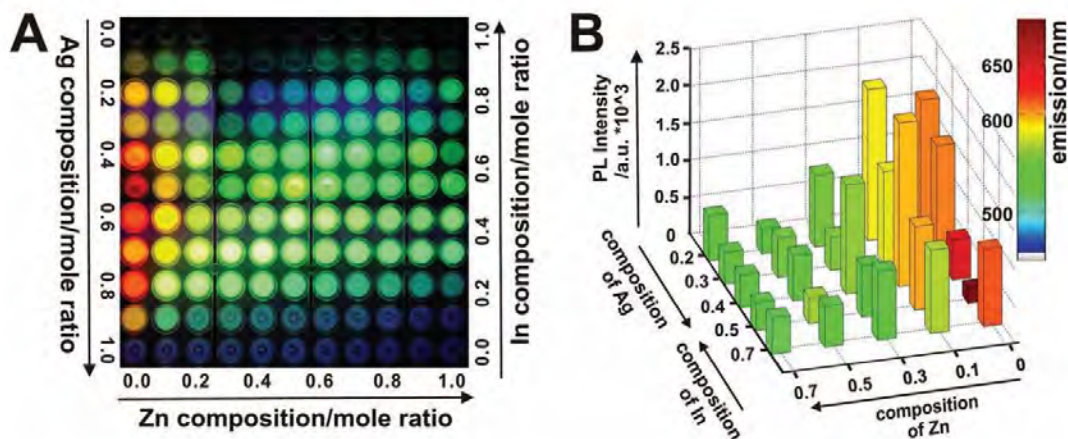


Figure 1.7: Emission properties of ZAIS QDs. (A) Entire library of ZAIS QDs synthesized using sonochemistry by varying the compositions of Zn, Ag, In, and S. (B) Heat map showing the photoluminescence (z axis) vs Zn (x axis) and Ag/In (y axis) concentrations for selected compositions of the ZAIS QD library. The color in each column indicates the maximum emission wavelength [38].

The distinctive photophysical properties of QDs, coupled with their diverse biological applications make them very attractive probes for investigating stem cell behavior (Figure 1.8). In fact, QDs have opened doors to a range of diverse applications in biological sciences such as real-time monitoring of physiological events taking place in cells by labeling specific cellular structures or proteins with QDs having different colors, monitoring cell migration, tracing cell lineage, and *in vivo* cell tracking [39–42]. Further, QDs are beneficial for studying dynamic changes occurring in membranes of stem cells. Functionalized QDs selectively bind to individual molecules on the cell surface and help in tracking the motion of those individual molecules. In a study by Chen et al. [43], functionalized QDs were used to demonstrate changes in the integrin dynamics during osteogenic differentiation of human bone marrow derived progenitor cells. In this study, quantum dots conjugated with integrin antibodies enabled precise optical identification of integrin molecules, which led to a detailed examination of the molecular dynamics of integrin molecules involved in osteogenic differentiation of the progenitor cells [43]. In stem cell-based therapy, it is extremely important to monitor the survival and location of stem cells after they are transplanted to the desired location. Transplanted stem cells, which may be either embryonic or adult stem cells, are

expected to remodel and differentiate in response to surrounding microenvironments, resulting in tissue regeneration and repair [10]. Mesenchymal stem cells labeled with bright, photostable QDs were shown to couple functionally with cardiomyocytes in co-culture, thus demonstrating the usefulness of QDs as labeling agents in culture (Figure 1.8) [44]. Human mesenchymal stem cells were labeled with QDs bioconjugated with RGD (arginine-glycine-aspartic acid) peptide during self-replication and multilineage differentiations into chondrogenic, androgenic, and adipogenic cells in a long term labeling study. Human MSCs labeled with QDs remained viable as the unlabeled hMSCs from the same subpopulation, thus suggesting the use of QDs are useful probes from long term labeling of stem cells [45].

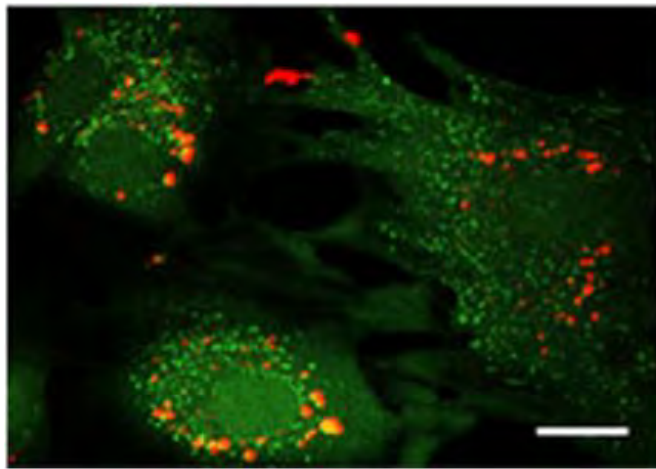


Figure 1.8: Mesenchymal stem cells (MSCs) labeled with QDs and co-labeled with calcein (green). The QDs were seen distributed within the perinuclear region within the MSCs. The QDs remained bright and were easy to detect even as the MSCs proliferated [44].

Quantum dots have also been shown to elucidate the mechanisms involved in mechanical integration of stem cells to the surrounding tissues and their differentiation into specific cell lineages *in vivo* [40]. In addition, multiplex imaging (i.e. tracking different cell populations labeled with QDs which exhibit different emission wavelengths at the same time) is one of the biggest advantages of using quantum dots for tracking stem cells *in vivo*. Wu and coworkers [27] successfully demonstrated *in vivo* multiplex imaging of mouse ESCs labeled with QDs. They subcutaneously injected ESCs labeled with six different QDs, having diverse emission wavelengths 525, 565, 605, 655, 705,

and 800, into various locations on the back of athymic nude mice and detected the labeled cells *in vivo* using a single excitation wavelength (425 nm) as shown in Figure 1.9 . They also concluded that within the sensitivities of the screening assays, the QDs did not affect the viability, proliferation, and differentiation capacity of the ESCs [27].

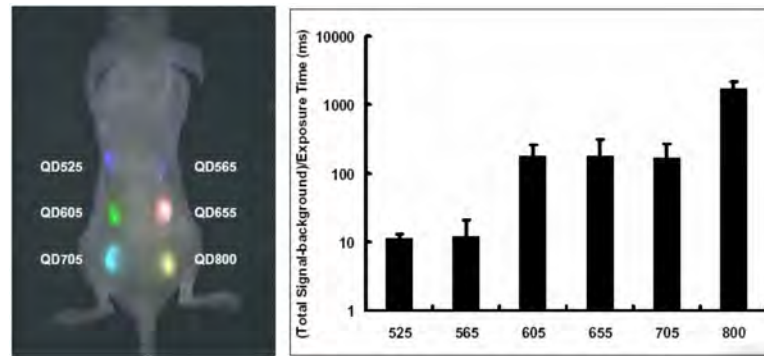


Figure 1.9: Multiplex imaging of embryonic stem cells (ESCs) labeled with QDs. (A) ESCs labeled with QD 525, 565, 605, 655, 705, and 800 were injected subcutaneously in back of athymic nude mice right after labeling, and imaged right after injection using a single excitation wavelength. (B) Quantified fluorescent signal intensity of QDs [27].

In another recent study by Rak-Raszewska et al, mouse ESCs and kidney stem cells (KSCs) labeled with QDs were used to investigate how they affect stem cell behavior and if they have any adverse effects on cell-cell fusion [46]. The researchers showed that the QDs had no effect on cell viability, proliferation or differentiation for the ESCs and KSCs. The QDs did not affect the degree of cell-cell fusion and the extent of QDs transferred to neighboring cells was found to be minimal (less than 4%). Furthermore, the authors suggested that as cell labeling probes, QDs were only suitable for short-term stem cell tracking as most of the QDs were rapidly depleted from both the stem cell populations. Quantum dots can be efficiently used to label neural stem and progenitor cells (NSPCs) *in vivo* and can be used to study the migration and differentiation of NSPCs during mammalian development. However, direct QD-labeling of NSPCs is a considerable challenge and not many techniques to directly and efficiently label QDs exist. Haydar and coworkers [41], developed novel *in utero* electroporation and ultrasound-guided delivery techniques to directly label the NSPCs *in vivo*. NSPCs labeled with QDs using the above techniques were found to differentiate into three principle cell types: oligodendrocyte progenitors, astrocytes and neurons. Quantum

dots were found in all the three types of cells after differentiation. The cells were also found to migrate away from the site of injection, suggesting that neither the QDs nor the *in vivo* labeling techniques had any effect on migration and differentiation of the NSPCs (Figure 1.10). Furthermore, their method demonstrated lack of toxicity and good tolerance of NSPCs for QDs, especially during the early embryonic mammalian development [41].

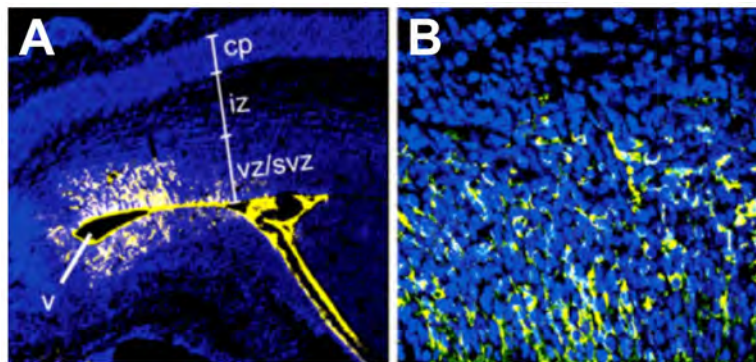


Figure 1.10: *In utero* electroporation for labelling NSPCs and ultrasound-guided delivery of NSPCs labeled with QDs *in vivo*. (A) NSPCs labeled with QDs in the ventricular zone and subventricular zone of the E16.5 mouse embryo. (B) Highly magnified confocal optical image showing efficiency of QD (bright) labeling of NSPCs surrounding the lateral ventricle [41].

Despite having unique optical properties and a host of advantages over the conventional tracking agents, toxicity is a primary concern for the application of QDs in biology. Stem cells tend to be extremely sensitive, and thus toxicity is a primary determinant in deciding whether QDs would be feasible for stem cell tracking, especially *in vivo*. Some literature studies do suggest that QDs are nontoxic; nevertheless, recent data shows that cytotoxicity is dependent upon the physicochemical properties, dose and exposure concentrations [47]. Although the mechanism of cytotoxicity is not yet clearly known and is under thorough investigation, concerns about toxicity of QDs have been raised as they are used for cell tracking studies in live animals. Quantum dots contain heavy metals such as cadmium and selenium, and the cytotoxicity is observed due to the presence of  $\text{Cd}^{2+}$  and  $\text{Se}^{2-}$  ions [48, 49]. Toxicity can be considerably reduced by coating the core made of CdSe with a shell of a material such as ZnS, which significantly reduces toxicity by blocking the oxidation of CdSe by air [50]. Although

the toxicity may not be critical at the low concentrations optimized for labeling, it could be detrimental for the embryo development at higher concentrations. Nevertheless, the problem could be solved by coating the QDs and making them biologically inert [50]. Larger molecules such as proteins (e.g. Streptavidin, bovine serum albumin) further slow down the photooxidation of the core [51]. Bioconjugation of QDs with biomolecules such as RGD did not show any toxic effect on hMSCs as compared to unlabeled hMSCs [45]. In a dose-dependent study involving the labeling of MSCs with QDs, it was observed that if the exposure of QDs to MSCs was optimized and limited to low concentrations then the QDs were not significantly toxic [44]. Addressing the cytotoxicity issues concerning the application of QDs synthesized from heavy metals, Subramaniam et al. used ZAIS QDs to deliver siRNA into MSCs and GFP-labeled brain tumor cells [38]. The ZAIS QDs were found to be non-toxic towards both the cells and provided excellent imaging capabilities.

### 1.1.3 Gold Nanoparticles

Gold nanoparticles (AuNPs) have been attractive candidates for delivery of payloads into cells. These payloads include small molecules, proteins, DNA or siRNA. They have been widely used in a variety of cells. They have very unique physical and chemical properties, which enables precise and accurate delivery of biomolecules across the cells membranes. The gold core is inert and non-toxic and monodisperse AuNPs can be synthesized with relative ease in large quantities, with the sizes ranging from 1 nm -150 nm [52]. Furthermore, their surfaces can be readily functionalized, typically through thiol linkages [53]. They also have extensive applications in biosensing and diagnostics.

Gold nanoparticles were recently used in bone tissue engineering, for stimulating osteogenic differentiation of mesenchymal stem cells (MSCs). Yi et al investigated the effect that the AuNPs had on the differentiation of MSCs and the related molecular mechanisms [54]. The MSCs were treated with different concentrations of AuNPs and cultured in the presence of osteogenic supplements. The osteogenic differentiation was measured by measuring the activity of alkaline phosphatase (ALP), a specific marker for bone formation. As the MSCs can also undergo adipogenic differentiation (fat cells),

the adipogenic differentiation was measured using oil red. The researchers found that the ALP activity was increased when a higher concentration of AuNPs was used. The ALP activity was measured at 7, 10 and 14 days. They also observed that on day 14, the ALP activity was significantly higher for all concentrations of AuNPs, as compared to the activity on day 7 and 10. Their results, therefore confirmed that the osteogenic differentiation of MSCs could be controlled in a dose- and time-dependent manner using AuNPs. Their study also showed that while the AuNPs promoted osteogenic differentiation, they inhibited adipogenic differentiation. On further investigating the signaling pathways affected by AuNPs, they found that the AuNPs interact with proteins within the cytoplasm, thus interfering with certain signaling pathways. The AuNPs also interact with the extracellular matrix (ECM), leading to the up-regulation of integrins. Both these events cause stress on MSCs, which leads to the activation of the p38 MAPK signaling pathway, which in turn causes the up-regulation of osteogenic genes and down-regulation of adipogenic genes. This study clearly demonstrates the impact of AuNPs on cellular events which ultimately determines the fate of the MSCs.

#### **1.1.4 Dendrimers**

Dendrimers are synthetic polymers that are built from a series of branches around an inner core. They are tree-like or star-shaped polymers that adopt generally a quasi-spherical shape [55]. They have unique molecular weights and their dimensions are extremely small, having diameters (depending on the generation) in the range of 2-10 nm. Dendrimers have been finding increasing use in the field of drug and gene delivery because they are synthetic, highly branched, mono-disperse polymers in the nanometer size range which offer the control that modern drug delivery and targeting demands, namely: control of chemical nature of carrier, control of molecular weight, control of surface and internal structure and character, vital in targeting and control of dimensions. The genetic material can be attached to the surfaces of dendrimers with relative ease due to the high concentration of positively charged functional groups. These functional groups can also be modified to attach targeting moieties like folic acid, transferrin and antibodies [56]. Amongst these, the earliest synthesized and commercialized dendrimers

are polyamidoamine (PAMAM) dendrimers.

Gebhart et al. compared the performance of several dendrimeric systems and found that the transfection efficiency depends not only on the vector molecule but also the type of cells to be transfected [57]. Therefore, several investigations on developing more efficient and less toxic dendrimers are currently ongoing to control the cellular behavior. To this end, Santos et al. showed that PAMAM dendrimers, without any surface functionalization, were able to transfect the bone morphogenetic protein-2 (BMP-2) to MSCs, although at a low efficiency. The group also showed *in vitro* osteogenic differentiation of the MSCs by checking the expression levels of various osteogenic markers [55]. However, MSCs are very promising and clinically relevant due to their properties. Thus, increasing the transfection efficiency of the PAMAM dendrimers was vital. The same group then functionalized the PAMAM dendrimers with arginine-glycine-aspartic acid (Arg-Gly-Asp, RGD) peptide sequence, which provided a major recognition system for the integrin receptors expressed on the MSCs. RGD tripeptide sequence play a key role in cell adhesion and has been used in numerous studies as a cell-targeting agents in antitumor therapies, imaging and drug/gene delivery [58]. In this study, Pandita et al. increased the density of the surface charges on the PAMAM dendrimers and conjugated them to RGD peptides, thus forming nanoclusters of RGD on the dendrimers. These nanoclusters complexed with pDNA were able to enter the MSCs with high efficiency through a mechanism which resulted from a balance between electrostatic interactions between the positively charged complexes and the negatively charged cell surface and the specific interactions between the RGD peptides and the integrin receptors expressed on the surface of MSCs. They showed that the RGD motifs played a big role in improving the transfection efficiency, with the sixth generation of the PAMAM dendrimer (G6) having 8 arms of RGD being the most efficient (Figure 1.11). EGFP, luciferase and BMP-2 pDNA were delivered and the proteins were successfully expressed by the MSCs [58].

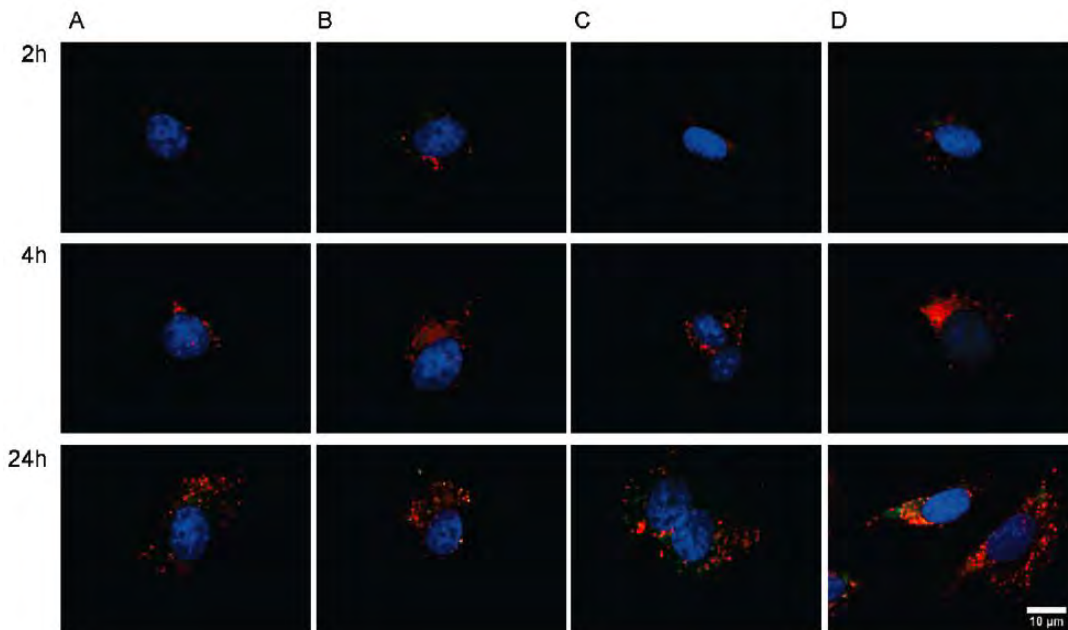


Figure 1.11: Dendrimer-based gene delivery into mesenchymal stem cells. Cellular distribution of dye-labeled pDNA (red) in MSCs at 2,4, and 24 h post-transfection. (A), (B), (C), and (D) represent confocal fluorescent images showing MSCs transfected with PAMAM G5, RGD8-G5, G6, and RGD8-G6 respectively. The cell nuclei were stained with DAPI (blue), and the acidic endosomes and lysosomes were stained with LysoSensor Green DND-189 (green) [58].

Besides naked dendrimers and surface-functionalized dendrimers, dendrimer composites of iron oxide nanoparticles, also known as magnetodendrimers, represent a versatile new class of contrast agents for MRI. They were developed by Bulte et al. and were shown to efficiently label mammalian cells, including neural stem cells and mesenchymal stem cells [6]. They were shown to have an oligocrystalline structure of 7-8 nm. It was observed that labeling NSCs and MSCs with magnetodendrimers did not affect their growth rate and they exhibited a growth rate which was similar to that of unlabeled stem cells. The cellular uptake of these composites is through a non-specific adsorption process, thus offering a great opportunity to label a variety of stem cells without regard to their origin or animal species (Figure 1.12).

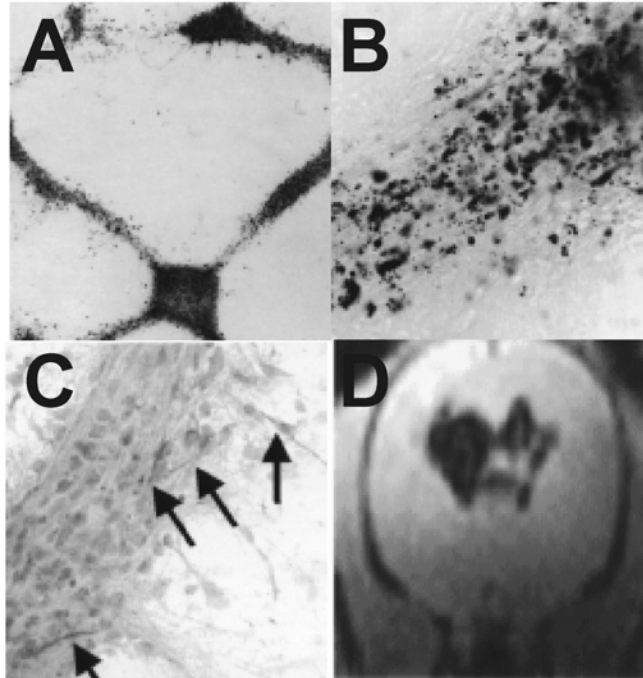


Figure 1.12: Tracking neural stem cells (NSCs) labeled with magnetodendrimers (MD-100). (A) NSCs labeled with MD-100 stained with Prussian Blue images after 24 h. (B) MD-100-labeled NSCs at higher magnification. (C) MD-100-labeled NSCs immunostained with anti-MAP2 (neuronal marker) confirming that labeling NSCs with MD-100 does not affect the neuronal differentiation of NSCs. (D) *In vivo* MR image of MD-100-labeled NSCs 42 days after intraventricular transplantation [6].

## 1.2 Nanotopography for Controlling Stem Cell Behaviors

In stem cell biology, specific environments called niches are formed consisting of cells and extracellular matrix (ECM) molecules such as collagen, fibronectin, elastin, laminin etc. These ECM molecules are typically secreted by the cell surrounding the stem cells. The ECM molecules act as physical cues for the stem cells, providing them with specific surface chemistry and topographical features at the nanoscale [59]. The ECM molecules provide for adhesion sites via integrins and transmembrane proteins. The physical cues provided by the ECM molecules generate an instructive microenvironment which guides stem cell behavior (Figure 1.13). The receptors on the stem cells bind to the fibers of the ECM and activate signaling pathways which affect adhesion, migration, proliferation and differentiation [60]. Having the ability to manipulate surfaces by creating the complexities of the ECM, which includes nanotopographies has gone a long way in improving our understanding of how stem cells respond to nanotopographical features.

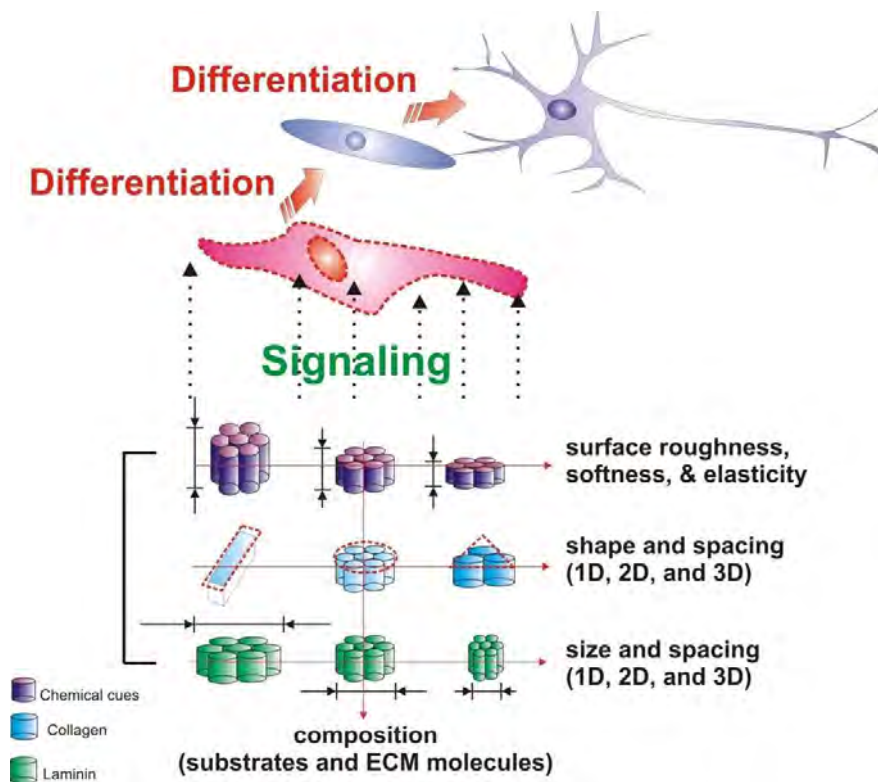


Figure 1.13: Nanoscale features for controlling stem cell behaviors.

### 1.2.1 Patterning of Topographical Cues

Stem cells are sensitive to physical cues and surface features in the micrometer to nanometer range. By probing the extracellular microenvironment with fingerlike membrane projections known as filopodia, feedback mechanisms are generated depending on the specific types of physical cues which then result in the expression of certain genes. This process of converting the detection of certain physical cues into biochemical responses is known as mechanotransduction [61]. Although complicated, researchers are now modifying surface features for investigating and controlling stem cell behaviors.

Micro- and nanopatterned surfaces are generally fabricated using soft lithographic techniques such as e.g microcontact printing [62, 63] and micronscale plasma-initiated patterning [64, 65], and hard lithography such as photolithography [66]. Various shapes - the most common ones being circles, squares, triangles, stripes, grids and stars - can be generated using the two methods. The background, which is the area surrounding the patterned features, is generally passivated using polyethylene glycol molecules to prevent nonspecific attachment of proteins and cells. The stem cells are then cultured, grown and differentiated on these surface features to investigate and control their fate (Figure 1.14).

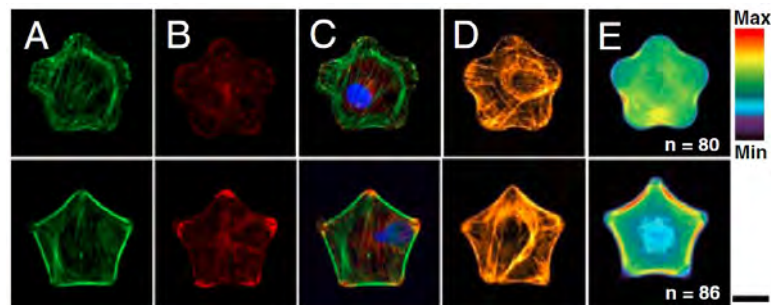


Figure 1.14: Cells cultured on different patterned features. (A)-(C) Cells immunostained for F-actin (green), vinculin (red) and nuclei (blue). (D) Cell immunostained for myosin IIa. (E) Fluorescent heat maps of cells stained for myosin IIa as a quantitative measure of contractility. (Scale bar: 20  $\mu\text{m}$ ) [67].

The patterned surface features have been used to differentiate adult stem cells into lineage specific terminal cells such as osteoblasts, neurons, cardiac cells etc. For instance, Solanki et al. investigated the differentiation of neural stem cells (NSCs) on

micropatterns of laminin, which is an essential ECM protein required for the adhesion and growth of NSCs [68]. They grew and differentiated the NSCs on square, stripe and grid patterns of laminin to investigate the role and effect of pattern geometry, shape and cell-cell interactions on differentiation of NSCs. They found that that the differentiation of NSCs was determined by the pattern shape and geometry which ultimately also controlled cell-cell interactions. The NSCs differentiated on the grid patterns showed the highest cell-cell interactions and a higher percentage of NSCs differentiated into neurons as compared to the NSCs differentiated on the other patterns.

In a similar study, Kilian et al. investigated the role of fibronectin patterns on the adipogenic and osteogenic differentiation of human MSCs [67]. They determined the effect of adhesive areas and curvatures of micropatterned regions on the differentiation of MSCs. For this reason they generated islands of fibronectin in a variety of shapes such as rectangle, star and flower, having different aspect ratios and curvatures. The aspect ratio was defined as the ratio of the length to the width. The MSCs were cultured on these patterns and differentiated in mixed differentiation medium for adipocytes and osteoblasts (Figure 1.15). They reported that when the MSCs differentiated on small islands of fibronectin ( $1000 \mu\text{m}^2$ ) they differentiated into chondrocytes and when they were differentiated on large islands ( $5000 \mu\text{m}^2$ ), they differentiated into osteoblasts. When the size of the islands was between these two sizes ( $2500 \mu\text{m}^2$ ), they obtained mixed populations of adipocytes and osteoblasts.

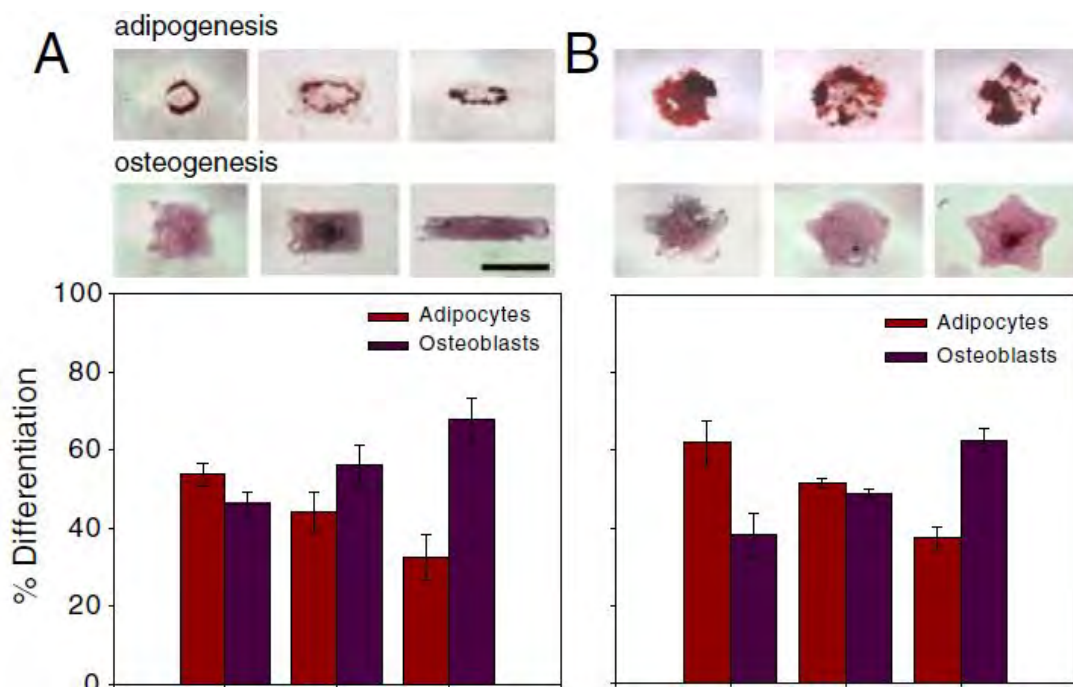


Figure 1.15: Mesenchymal cells differentiated on protein patterns having different shapes. (A) Percentage of MSCs differentiated into adipocytes or osteoblasts on islands having different aspect ratios. (B) Percentage of MSCs differentiated on islands of fibronectin having fivefold symmetric shapes. (Scale bar: 50  $\mu\text{m}$ ) [67].

To investigate the chondrogenic and myogenic differentiation of MSCs, Gao et al. cultured and differentiated human MSCs on square patterns of fibronectin of varying sizes on polydimethylsiloxane (PDMS) substrates using microcontact printing [69]. They observed that the MSCs that were well-spread on large micropatterned islands (10000  $\mu\text{m}^2$ ) resulted in higher myogenic differentiation, whereas the MSCs differentiated on smaller islands were not allowed to spread and flatten showed higher chondrogenic differentiation. MSCs showing myogenic differentiation showed higher Rac1 activity and no change in RhoA as compared to the cells undergoing chondrogenic differentiation. Thus it was concluded that Rac1 activity is crucial for myogenic differentiation and inhibition of chondrogenic differentiation. It was also demonstrated that Rac1 signaling upregulated N-cadherin which is required for myogenic differentiation. Therefore, MSC fate depended on cell shape, Rac1 and N-cadherin.

### 1.2.2 Nanomaterials for Generating Topographical Cues

Nanoscale features can also be created using a variety of nanomaterials such as nanofibers, nanoparticles, and nanotubes. Nanomaterial-ECM protein composites have been investigated and are known to control stem cell differentiation [70, 71].

Park et al. demonstrated polarization-controlled differentiation of human neural stem cells (hNSCs) using synergistic cues of ECM protein and carbon nanotube (CNT) patterns [71]. Laminin was selectively adsorbed on CNT patterns to provide the optimal nanotopography, which resulted in selective adhesion and growth of hNSCs. Laminin coated CNTs were extremely biocompatible and provided a good handle for controlling the nanotopographical features (Figure 1.16).

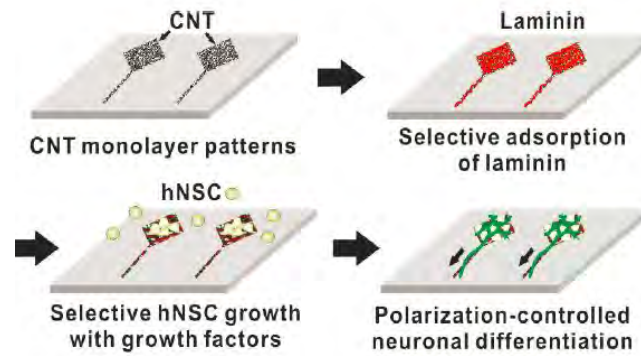


Figure 1.16: Human neural stem cell growth and polarization on CNT patterns coated with laminin. The schematic shows polarization-controlled neuronal differentiation using CNT patterns. CNT monolayer patterns were generated on a glass substrate using microcontact printing and laminin was selectively adsorbed on the CNT patterns. The hNSCs attached to the CNT-laminin patterns which resulted in polarization-controlled neuronal differentiation [71].

Overall, the results clearly showed that CNT patterns played a critical role in controlling the hNSC outgrowths during the growth and differentiation process, due to cell-cell interactions and cytoskeletal tensions. They observed that the hNSCs differentiated to form neural networks along the inside of the line patterns. Notably, the structural-polarization-controlled differentiation of individual hNSCs was achieved using CNT patterns having one square and a single line protruding from the square. After seeding the cells, the hNSCs selectively adhered to the squares and grew along the line protruding from the squares (Figure 1.17). The differentiated hNSCs grew their axons

along the protruding line. While the hNSCs differentiated with controlled structural polarity on the CNT patterns, they maintained their capabilities of differentiating into the main phenotypes found in the nervous system, namely neurons and astrocytes.

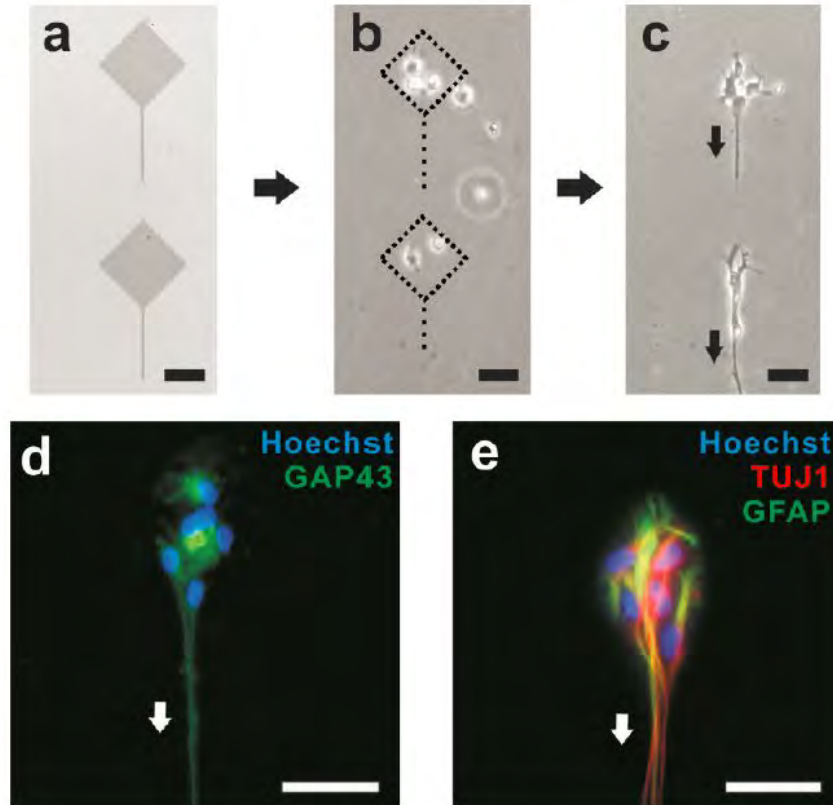


Figure 1.17: Polarization-controlled neuronal differentiation of individual hNSCs using CNT patterns. (a) SEM image showing the CNT patterns have a single protruding narrow strips. (b) Phase contrast image showing the attachment of hNSCs on the CNT patterns. The dotted lines represent the CNT patterned area. (c) Phase contrast image showing the growth on hNSCs, where the hNSCs were seen to extend along the narrow strip during differentiation. (d) Image showing differentiated hNSCs immunostained for axonal marker, growth-associated protein 43 (GAP43, green) and Hoechst (blue) for nucleus. (e) Image showing differentiated hNSCs immunostained for neural markers GFAP(astrocyte, green) and TuJ1(neurons, red). (Scale bar: 50  $\mu\text{m}$ ) [71].

Similarly, Baik et al. [70] used patterns of carbon nanotubes as cues for osteogenesis of human MSCs in an effort to enhance osteogenesis. In this study, they demonstrated that osteogenic differentiation of hMSCs was induced by single walled CNTs (swCNTs) as ECM cues, without any chemical treatments. Interestingly, it was also observed

that the surface treatment of swCNTs using oxygen plasma (O-swCNTs) showed enhanced differentiation as well as adhesion of hMSCs. Their results showed enhanced cell spreading on swCNTs as compared to the glass substrates. The authors believe that this might have been due to the nanoscale surface roughness of the swCNTs. Furthermore, the O-swCNTs layers showed greater cell spreading than the swCNTs. This was presumably due to the chemical changes of the O-swCNTs, such as increased hydrophilicity and surface oxygen content, which also helped enhancing the proliferation and adhesion of hMSCs on them. The osteogenic induction capacity of the swCNTs was checked by immunostaining for the osteogenic marker proteins such as osteocalcin and alkaline phosphatase. In addition to these markers, the expression of core binding factor alpha1 (CBFA1) was checked. CBFA1 is the main transcription factor for committing hMSCs to an osteogenic lineage. They showed that osteogenic differentiation of hMSCs was promoted on swCNT layers without the use of osteogenic induction media. In addition, they found that simple oxygen plasma treatment amplified the adhesion, proliferation and osteogenic differentiation of the hMSCs by adding chemical effects to the main topographical features.

Graphene, as a nanomaterial, is an excellent biocompatible material which provides nanotopographical features and does not hinder the proliferation of stem cells. In fact, it was observed that the presence of graphene leads to accelerated differentiation of human MSCs into osteoblasts [72]. Park et al. [73] cultured and differentiated human NSCs on graphene and observed that the NSCs cultured on graphene showed enhanced adhesion, and after three weeks on differentiation a higher number of NSCs were still attached on graphene as compared to tissue culture plates (Figure 1.18). They also observed enhanced neuronal differentiation of NSCs on graphene with a significant difference in morphology, with the NSCs differentiated on graphene showing higher number of neurite outgrowths. They thus concluded that graphene created an ideal microenvironment for the neuronal differentiation of NSCs [73] .

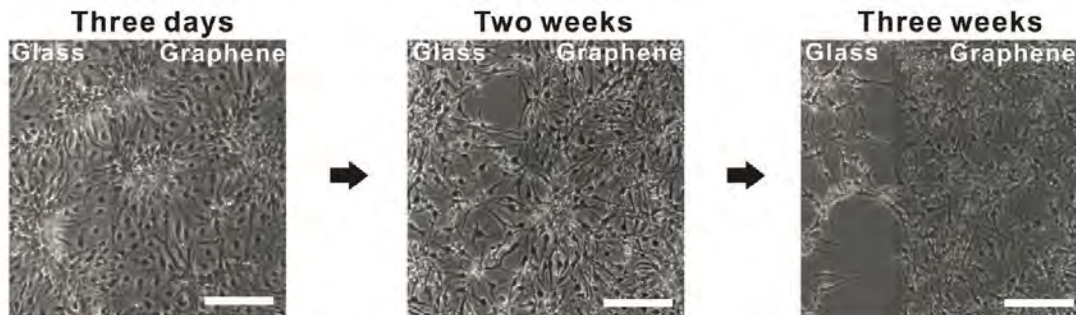


Figure 1.18: Human neural stem cells (hNSCs) cultured on graphene. Bright-field images representing the growth and differentiation of hNSCs for three days (left), two weeks (middle), and three weeks (right). The hNSCs differentiated on graphene remain attached even after three weeks, but those on glass gradually get detached. (Scale bar: 200  $\mu\text{m}$ ) [73].

Nanofibers have been increasingly used to create nanotopographical features, in an effort to mimic the microenvironment found in tissues. Shih et al. showed that human MSCs cultured and grown on 500-1000 nm were well-spread and showed higher viability and lower mobility as compared to the MSCs grown on tissue culture plates [74]. In another study, Christopherson et al. differentiated rat NSCs on nanofibers having different diameters to investigate how the diameters affect the differentiation of NSCs [75]. They found that NSCs cultured on nanofibers having smaller diameters (283 nm) differentiated preferentially into oligodendrocyte precursors, whereas the NSCs cultured on nanofibers having larger diameters (749 nm) differentiated preferentially into neurons. Alignment of nanofibers has also been shown to play a significant role in determining the fate of stem cells (Figure 1.19).

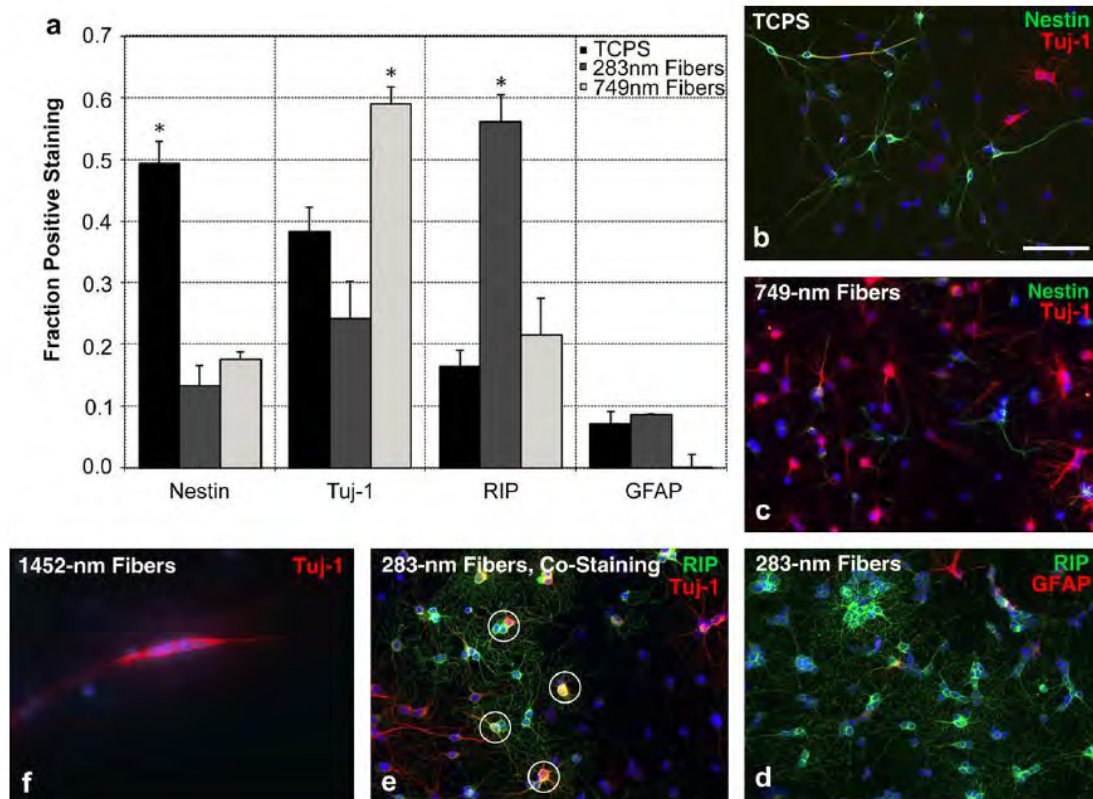


Figure 1.19: Nanofibers for differentiation of rat neural stem cells (NSCs). The NSCs were cultured on different substrates having different sizes of nanofibers in the presence of 1  $\mu\text{M}$  retinoic acid and 1% fetal bovine serum for 5 days. (a) Quantification of immunostaining results for different neural markers and nestin which is a marker for NSCs. Images showing NSCs stained for (b) nestin and Tuj1 (neurons) on tissue culture polystyrene (TCPS), (c) nestin and Tuj1 on 749 nm nanofibers, (d) RIP (oligodendrocytes) and GFAP (astrocytes) on 283 nm nanofibers, (e) RIP and Tuj1 (circles represent NSCs double-positive for RIP and Tuj1). (Scale bar: 100  $\mu\text{m}$ ) [75].

In one such study, Lim et al. reported that a higher percentage of NSCs cultured on aligned poly-caprolactone (PCL) nanofibers coated with poly-ornithine (PLO) and laminin differentiated into neurons as compared to the NSCs cultured on random nanofibers and unpatterned surfaces coated with PLO and laminin [76]. They further reported that aligned PCL nanofibers having a diameter of 480 nm showed the highest percentage of neuronal differentiation as compared to nanofibers having diameters of 260 nm and 930 nm.

### 1.3 Nanomaterials for Developing Biosensors

Significant advances in nanotechnology have paved the way for development of better devices for biodetection. The unique physical, chemical and electrical properties of nanomaterials have resulted in the rapid development of devices having improved sensitivity and selectivity, fabricated either through the bottom-up or top-down approaches. A variety of nanomaterials having different sizes, shapes and properties have been used to fabricate devices [77]. In the past decade, nanomaterial-based biosensors have offered significant advantages over conventional methods for detecting biomolecules as the interactions with these biomolecules and nanomaterials involves electrostatic interactions and charge transfers, which can be detected by the electrical devices with relative ease. From all the different methods that can be used for biodetection, we will review some of the advances in the development of nanomaterial-based electrical devices for biodetection.

For the development of electrical devices as biosensors various nanomaterials, such as carbon nanotubes (CNTs), graphene, and silicon nanowire (SiNW) have been used owing to their unique physical, chemical and electrical properties which confers remarkably enhanced sensitivity and selectivity for detecting the target biomolecules [78].

#### 1.3.1 Carbon Nanotubes

Carbon nanotubes are allotropes of carbon consisting of graphene sheets wrapped into hollow cylinders having ends which are capped or open. Single-walled CNTs (swCNTs) are single graphene sheets rolled into cylinders, whereas multiwalled CNTs (mwCNTs) consist of concentric cylinders having a space of 0.34 nm in between each cylinder. Due to their excellent electrical (mwCNTs) and semiconducting (swCNTs) properties, CNTs in general are an excellent choice of nanomaterials for incorporating into an electrical device. Pacios et al. developed a novel CNT-based field effect transistor (FET), modified with aptamers for specifically detecting thrombin protein in real time [79]. The CNTs on the device were functionalized with the aptamers by first conjugating the CNTs with pyrene carboxylic acid (1-2 pyrenebutyric acid) followed by EDC-NHS

coupling form an amide bond. The authors reported that the device was highly sensitive with the detection limit being 20 pM of thrombin. Furthermore, the device was capable of specifically detecting thrombin in the presence of other protein, thus demonstrating remarkable selectivity [79].

In another recent study, Lerner et al. used a CNT-FET to detect osteopontin, a new prostate cancer biomarker. The CNTs were functionalized with genetically engineered single chain variable fragment (scFv) protein having a high binding affinity for OPN [80]. The scFv was covalently linked to the CNTs using diazonium salts (Figure 1.20).

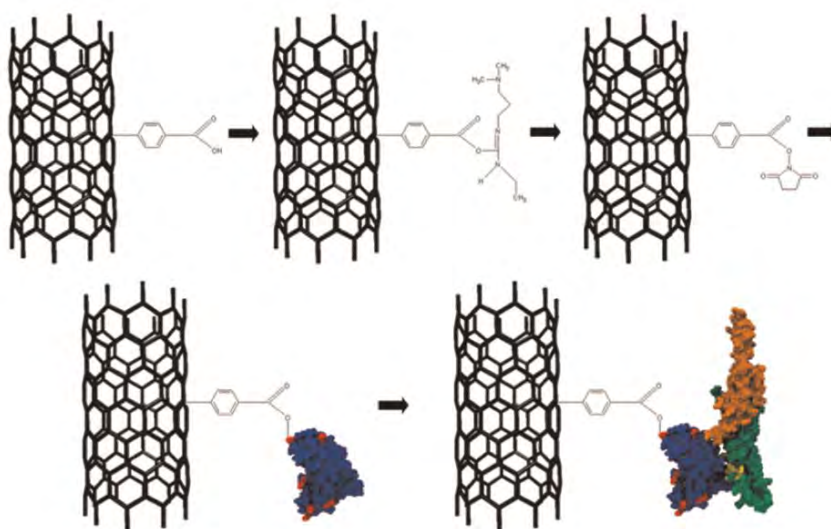


Figure 1.20: Schematic diagram for functionalization of CNTs with scFv antibody against OPN. The  $sp^3$ -hybridized sites are created on the CNTs by incubating them in a solution of diazonium salt. The carboxylic acid group is then activated using EDC and NHS. The scFv fragment forms a stable amide bond by displacing NHS (amine groups from lysine are in red). The OPN binds preferentially to the scFv on the CNTs (OPN shown in yellow) [80].

Based on the electron transport measurements on the binding of OPN to scFv, it was concluded that the CNT-FET is a good choice for detecting small concentrations of OPN. A concentration-dependent increase in source-drain current was observed with a detection limit of 30 fM. In addition to the excellent sensitivity, the device also demonstrated excellent selectivity by responding only to OPN in a background of concentrated bovine serum albumin, without loss of signal. The authors attributed the detection mechanism to the changes in scattering at the scFv protein-occupied defect

sites on the CNT side walls [80]. Although the CNT-FET was used to detect OPN, the chemical functionalization could be adopted to make a similar device to detect any specific antigen using the corresponding protein.

### 1.3.2 Graphene

Graphene is a planar sheet of  $sp^2$ -bonded carbon atoms arranged in a honeycomb lattice. This novel nanomaterial has found exciting application across a range of disciplines. Graphene is two-dimensional in structure having remarkable physicochemical and structural properties and has been anticipated to provide for newer opportunities for developing electrical devices, especially for biodetection [81]. In the last decade many devices using graphene have been developed for detecting biological and chemical molecules [82]. For instance, a pristine graphene-based device was developed by Ohno et al. to detect bovine serum albumin (BSA) with a lower detection limit of 0.3 nM. However, this sensor lacked specificity of detection. The presence of BSA was detected by the nonspecific adsorption of protein on graphene, which led to an increase in conductance of graphene biased at the p-type region [83]. Improving upon this technology, Mao et al. used reduced graphene oxide (rGO) for making a sensor specific for immunoglobulin G (IgG) [84]. The authors reported a very low detection limit of 13 pM. In this work, gold nanoparticles (AuNPs) were conjugated to anti-IgG antibodies and assembled on rGO sheets by electrospraying and using electrostatic force directed assembly. Additionally, the unfunctionalized regions on the rGO were passivated using Tween 20 to prevent non-specific binding of proteins.

In an interesting work reported by Myung et al. rGO-based biosensor was developed for selectively detecting breast cancer biomarkers HER2 and EGFR [85]. In this work, positively charged silica nanoparticles (SiNPs, 100 nm) were encapsulated by GO sheets and then reduced to form rGO. The 3D nanostructures significantly increased the surface area available for functionalization of the antibodies against HER2 and EGFR. The functionalization was carried out using pyrene aldehyde which assembles on the rGO. This was followed by reductive amination in the presence of sodium cyanoborohydride to form an amide bond between the antibodies and the pyrene aldehyde. The authors

reported that they could selectively detect HER2 having a detection limit of 100 pM and EGFR with a detection limit of 10 nM. When the positively charged HER2 and EGFR biomolecules were bound to the antibodies on rGO surfaces it led to a positive gating effect, which in turn reduced the hole density in the p-type rGO [85].

### 1.3.3 Silicon Nanowires

The use of silicon nanowires (SiNWs) as components of electrical devices to detect biomolecules at extremely low concentrations has been one of the hot topics in the field of biosensing. SiNWs can be prepared as single crystals and can have diameters as small as 2-3 nm [77]. They happen to be one of the most explored and characterized semi-conducting nanowires. Extensive investigations about their physicochemical properties, synthesis and applications have been carried out. The reason SiNWs are popular as components of FET-based biosensors is because of their sensitivity. This sensitivity stems from the high carrier mobility and high surface-to-volume ratio which ensures that the mass carriers can be controlled with relative ease by simple applying a weak electric field on the gate [86]. Like we saw with the use of CNTs and graphene, the use of SiNWs has two major advantages: high sensitivity and fast responses without tedious labeling steps. The unique advantages of these nanomaterials come from their one-dimensional morphological structures, and many researchers are trying to utilize them as a highly sensitive and selective signal transduction medium. The scheme (Figure 1.21) [87] illustrates a basic structure of electrical detection of biomolecules with silicon nanowire biosensor.

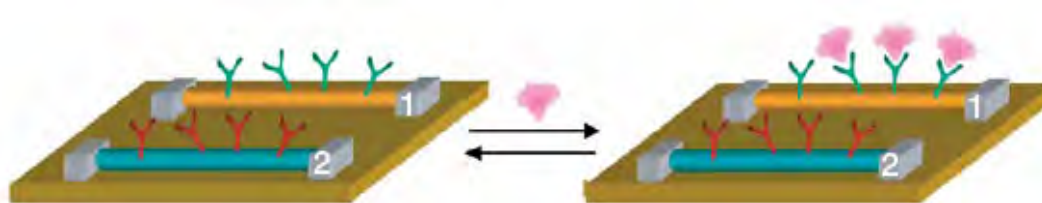


Figure 1.21: Schematic diagram showing the detection of biomolecules using silicon nanowire biosensor. The schematic showing two nanowire devices, 1 and 2, within an array, where nanowires were modified with different (1, green; 2, red) antibody receptors [87].

Lieber and coworkers [87] synthesized SiNWs with peptide nucleic acid (PNA) functionalization, and demonstrated how the synthetic material could detect DNA without labeling. A subsequent study modified SiNWs with biotin to detect picomolar concentrations of streptavidin and demonstrated high sensitivity to change in conductivity of the nanowires upon the biotin-streptavidin binding. Similar studies have also been carried out by Chen et al. [88], where they focused on the application of carbon nanotubes as a material for the sensitive detection.

## 1.4 Conclusion

Nanotechnology-based platforms have highly attractive applications in regenerative medicine, where they not only aid in controlling stem cell behaviors but also help in labeling cells which can then be easily tracked when transplanted *in vivo*. Magnetic nanoparticles have been excellent for delivering payloads and tracking stem cells using MRI. However, there is a gradual loss of MRI signal due to cell division. Such limitations need to be addressed in the future. Although quantum dots seem to be a good alternative for long term labeling of stem cells, in addition to being good delivery systems, the limitation to the accessibility of whole animal imaging restricts its use for *in vivo* tracking. Quantum dots, however, are excellent probes for *ex vivo* assays due to their high fluorescent intensities and resistance to photobleaching.

For harnessing the true potential of stem cells, smart biomaterials in the form of scaffolds are required. Although rapid advancements in developing biomaterials for regenerative medicine have taken place in the past decade, novel biodegradable materials that can provide a three-dimensional ECM to regulate tissue formation need to be developed. These scaffolds can incorporate nanomaterials to deliver biomolecules in a controlled manner depending upon an external stimulus, such as a magnetic field or light. We have seen that nanotopography plays an extremely important role in controlling stem cell differentiation. In fact, some of the influences of nanotopography may even preclude the use of small molecules in the future. However, there is a clear need to include such textures within scaffolds such that they can guide the differentiation of stem cells into the desired final lineage.

Overall, nanomaterials have played a significant role in advancing the fields of regenerative medicine and biosensing. Moreover, the advancement in nanotechnology-based approaches allows scientists in cell biology and physiology to investigate targeted bio-interactions at the fundamental molecular level. What is now required is an interdisciplinary approach from a high level of expertise in each field of science.

## 1.5 Overview of Dissertation

All the above nanotechnology-based approaches provide remarkable inspiration for anyone aspiring to do develop newer approaches to investigate cellular behaviors and develop more efficient biosensing methods. I took great inspiration from such techniques and started working on developing drug and siRNA delivery systems using novel nanomaterials. My aim was to develop new approaches for regulating stem cell differentiation. The approaches I developed over the course of my doctoral work could be applied to any adult stem cell line, but I chose to specifically work with neural stem cells (NSCs) as a resource for obtaining neurons. The regenerative capability of the damaged neurons in the central nervous system, which includes the brain and the spinal cord, is extremely slow and scarce. Utilizing NSCs as a resource is an excellent opportunity to further advance the field of regenerative medicine. However, to make this process of differentiation of NSCs into neurons more efficient, I developed novel nanotechnology-based approaches.

We started with using quantum dots (QDs) to deliver siRNA into human brain tumor cells, with the hopes of optimizing a siRNA deliver system into a mammalian brain tumor cell line. We were quite successful at developing a delivery system which not only enabled us to deliver the siRNA into the brain tumor cells, but also allowed us to track the delivery. We were able to inhibit the proliferation of the brain tumor cells using a specifically designed siRNA against a mutant gene. Overall the project provided inspiration to further develop such a system for controlling the differentiation of stem cells. For the next project, we developed a siRNA delivery system called DexAM, which is a dendritic polyamine conjugated to a cyclodextrin molecule. The cyclodextrin (CD) molecule was used to encapsulate hydrophobic small molecules which are typically delivered using toxic solvents such as DMSO and DMF. The polyamine backbone was used to complex with siRNA. We used DexAM to deliver siRNA against SOX9, the inhibition of which led to enhanced neuronal differentiation. We further enhanced the neuronal differentiation by co-delivering retinoic acid encapsulated within the CD. Retinoic acid is a well-known small molecule used for differentiating NSCs into

neurons.

Although DexAM provided good results for enhancing the differentiation of NSCs into neurons, we wanted to develop a system wherein the delivery vehicle itself does not enter the stem cells. We then developed NanoRU, which is a Nanotopography-mediated Reverse Uptake platform for delivering siRNA into NSCs. NanoRU was developed by making positively charged nanoparticle films on a glass substrate and coating the films with ECM protein (laminin) and siRNA. The NSCs took up only the siRNA and not the nanoparticles, which was remarkable. We optimized NanoRU using siRNA against GFP and then used siRNA against SOX9 to enhance neuronal differentiation. NanoRU was found to be extremely biocompatible allowing long term cell growth and differentiation on the platform without having the need to remove the cells from NanoRU. Furthermore, it was also used to deliver siRNA into normal cell lines such as astrocytes, and breast and brain cancer cell lines.

In another project, I worked on developing a strategy for regulating NSC differentiation into neurons without using any soluble cues such as small molecules and siRNA. We wanted to differentiate the NSC using only the physical cues present within the microenvironment of the stem cells. For this reason, we generated ECM protein patterns having different geometries and sizes. We then identified a specific geometry which gave us the highest neuronal differentiation of NSCs into neurons. Grid patterns of laminin provided the highest differentiation of NSCs into neurons. The NSCs differentiated in the absence of soluble cues, by purely sensing the physical signals provided by the protein patterns.

Lastly, we developed a strategy to include a novel nanomaterial into the ECM and investigate its impact on neuronal differentiation. We used chemically-derived graphene or graphene oxide (GO) as it offers a number of advantages due to its unique chemical and physical structure. Its high surface area was extremely useful for adsorbing ECM proteins for culturing stem cells. We observed that GO-coated glass substrates led to significant alignment of axons from differentiating human NSCs (hNSCs). However, when the hNSCs were differentiated on SiNP films, it led to an increase in the length of the axons. We thus coated the SiNP films with GO (SiNP-GO) and that condition led to

increased alignment, increased lengths of axons and increased neuronal differentiation of the hNSCs. We believe using graphene-based hybrid nanomaterials is significantly advantageous as the material was also found to be very biocompatible, supporting the growth and differentiation of hNSCs for over 3 weeks. We believe our work wherein the differentiating hNSCs align and express higher neuronal markers will be significant for spinal cord injuries where the main emphasis is on guiding the axonal growth to connect the distal and proximal ends of damaged neurons.

We also developed new biosensors, using graphene and graphene oxide. These biosensors were fabricated using traditional photolithography and had very good selectivity and sensitivity for detecting breast cancer biomarkers such as HER2 and EGFR. We also developed a sensor for detecting the enzyme carboxypeptidaseB, which is a biomarker for acute pancreatitis. Our biosensors, developed using a combination of graphene and nanoparticles, have contributed immensely to the new area of graphene-based biosensing.

This dissertation provides the details of my work on all projects related to regenerative medicine and biosensing.

## Chapter 2

### Nanomaterials for siRNA Delivery into Neural Stem Cells

RNA interference (RNAi) technology, wherein the gene of interest is inhibited using either small interfering RNA (siRNA), microRNA (miRNA) or small hairpin RNA (shRNA). We have seen the use of siRNA for inhibiting the expression of specific genes for inducing cell death of cancer cells. While this is very important, the use of siRNA in stem cells for inhibiting specific genes in order to control their differentiation is also important. However, the most challenging part is delivering the siRNA into the cancer/stem cells. Many nanomaterials have been used, which is evidenced by the abundant literature available. In an effort to optimize siRNA delivery and track their location within cells, we used quantum dots (QDs), which are highly fluorescent nanoparticles, to deliver siRNA into brain tumor cells. In this chapter we will see how the QDs successfully delivered the therapeutic siRNA into the brain tumor cells leading to their apoptosis.

We then synthesized a cyclodextrin-polyamine construct (DexAM) having a highly positively charged dendritic polyamine and a cyclodextrin molecule conjugated to it. The dendritic structure and its synthesis gave us a very good handle on controlling its positive charge and the subsequent conjugations. The challenge to balance between the cytotoxicity and efficiency of such delivery vehicles was achieved by conjugating a cyclodextrin molecule. In this chapter we will see DexAM was used to simultaneously deliver small molecules and siRNA into neural stem cells to enhance their neuronal differentiation.

## 2.1 Selective Inhibition of Human Brain Tumor Cells through Multifunctional Quantum-Dot-Based siRNA Delivery

### 2.1.1 Introduction

One of the most promising new chemotherapeutic strategies is the RNA interference (RNAi)-based approach, wherein small double-stranded RNA molecules can sequence-specifically inhibit the expression of targeted oncogenes [89, 90]. In principle, this method has high specificity and broad applicability for chemotherapy. For example, the small interfering RNA (siRNA) strategy enables manipulation of key oncogenes that modulate signaling pathways and thereby regulate the behavior of malignant tumor cells. To harness the full potential of this approach, the prime requirements are to deliver the siRNA molecules with high selectivity and efficiency into tumor cells and to monitor both siRNA delivery and the resulting knock-down effects at the single cell level. Although several approaches such as polymer- and nanomaterial-based methods have been attempted [91–94], limited success has been achieved for delivering siRNA into the target tumor cells. Moreover, these types of approaches mainly focus on the enhancement of transfection efficiency, knock-down of non-oncogenes (e.g. green fluorescent protein (GFP)), and the use of different nanomaterials such as quantum dots (QDs), iron oxide nanoparticles, and gold nanoparticles [95–100]. Therefore, to narrow the gap between current nanomaterial-based siRNA delivery and chemotherapies, there is a clear need to develop methods for target-oriented delivery of siRNA [101, 102], for further monitoring the effects of siRNA-mediated target gene silencing via molecular imaging probes [96], and for investigating the corresponding up/down regulation of signaling cascades [103]. Perhaps most importantly, to begin the development of the necessary treatment modalities, the nanomaterial-based siRNA delivery strategies must be demonstrated on oncogenes involved in cancer pathogenesis.

Herein, we describe the synthesis and target-specific delivery of multifunctional siRNA-QD constructs for selectively inhibiting the expression of epidermal growth factor receptor variant III (EGFRvIII) in target human U87 glioblastoma cells, and

subsequently monitoring the resulting down-regulated signaling pathway with high efficiency [104].

### **2.1.2 Results and Discussion**

Glioblastoma multiforme (GBM) is the most malignant, invasive, and difficult-to-treat primary brain tumor. Successful treatment of GBM is rare with a mean survival of only 10-12 months [105, 106]. EGFRvIII, the key growth factor receptor triggering cancer cell proliferation in many cancer diseases such as brain tumors and breast cancer, is a constitutively active mutant of EGFR which is expressed in only human GBM and several other malignant cancers, but not in normal healthy cells (Figure 2.1) [107, 108]. We targeted EGFRvIII, since it has been known that knock-down of this gene is one of the most effective ways to down-regulate the PI3K/Akt signaling pathway, a key signal cascade for cancer cell proliferation and apoptosis [103, 109, 110]. Hence by targeting EGFRvIII, our multi-functional nanoparticle-based siRNA delivery strategy could potentially minimize the side effects caused by conventional chemotherapies, specifically immune suppression, while significantly improving the efficacy of chemotherapy against GBM.

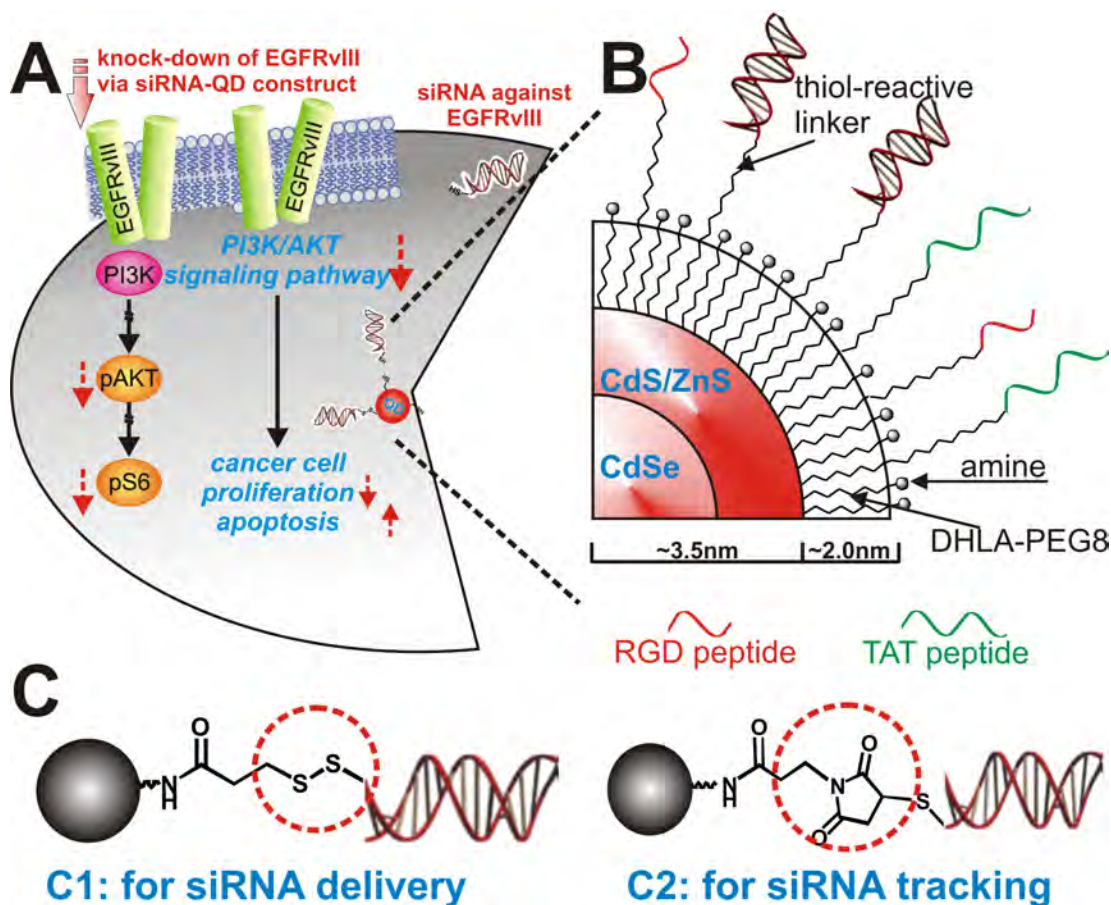


Figure 2.1: siRNA-QDs for delivery and tracking. Quantum dots as a multi-functional nanoplatform to deliver siRNA and to elucidate of EGFRvIII - knockdown effect of PI3K signaling pathway in U87-EGFRvIII (A) Detailed structural information of multifunctional siRNA-QDs. (C) Two different strategies for the siRNA-QD conjugate. (C1) Linker for attaching siRNA to QDs through a disulfide linkage which was easily reduced within the cells to release the siRNA. (C2) Linker for covalently conjugating siRNA to QDs which enabled tracking of siRNA-QDs within the cells [111].

### Multifunctional quantum-dots for delivery and tracking of siRNA

We prepared two types of siRNA-QD conjugates, one for siRNA delivery and the other for siRNA tracking (Figure 2.1A and Figure 2.1B). Core-shell CdSe/CdS/ZnS QDs with a 7 nm diameter were synthesized [112, 113]. The QDs were coated with trioctyl-phosphine oxide (TOPO) or hexadecylamine (HDA). In order to make the QD constructs water-soluble and suitable for conjugating with siRNA, we displaced these hydrophobic ligands with a dihydrolipoic acid (DHLA) derivatized with an amine terminated poly [ethylene glycol] (PEG) spacer. The expectation was that the dithiol

moiety would provide strong coordination to the QD surface and increase stability in aqueous media, the PEG spacer would increase water solubility and reduce non-specific binding, and the amine group would enable conjugation to the siRNA element [114,115]. Two bifunctional linkers were synthesized and evaluated for siRNA conjugation. Linker C1, PTPPf [3-(2-pyridyl)-dithiopropionic acid pentafluorophenyl ester], was designed to release siRNA upon cellular entry through cleavage of the disulfide linkage, through enzymatic reduction or ligand-exchange (e.g. glutathione) [116–118]. Linker C2, MPPF (3-maleimidopropionic acid pentafluorophenyl ester), was designed to be more robust, thereby enabling evaluation of cellular uptake and localization of the siRNA construct within the cellular compartments [119].

The final design component was to functionalize the construct for tumor cell-selective transfection. For this purpose two functional peptides, thiol-modified RGD peptide and thiol-modified HIV-Tat derived peptide, were attached to the siRNA-QDs via the conjugation methods described above. Brain tumor cells (U87 and U87-EGFRvIII) over-express the integrin receptor protein  $\alpha\beta3$ , which strongly binds to the RGD binding domain [120]. RGD functionalized siRNA-QDs selectively accumulate in brain tumor cells *in vitro*, and can be tracked by fluorescence microscopy [121]. In addition, the HIV-Tat peptide enables efficient transfection of siRNA-QDs in cells when directly attached to the QD surface [122,123]. The density of siRNA on the QDs and the ratio between siRNA strands and peptides were optimized for gene knockdown. It was found that the density of 10 siRNAs/per nanoparticle and the ratio of 1:10 (siRNA: each peptide) was in close agreement with literature values [8], and was optimal for knocking down the target genes (EGFP and EGFRvIII) overexpressed in our U87 cell lines.

### **EGFP knockdown and target-specific intracellular delivery of siRNA-QDs**

To optimize gene silencing with our siRNA-QD constructs and to assess the transfection efficiency and RNA interference (RNAi) activity, we examined the suppression of EGFP expressed in U87 cell lines that were genetically modified to express EGFP. Cytotoxicity of the constructs was tested by serial dilution studies. The range of concentration causing minimal/negligible cytotoxicity was identified and the subsequent experiments

employed the concentrations within this range Figure 2.2 [49,124].

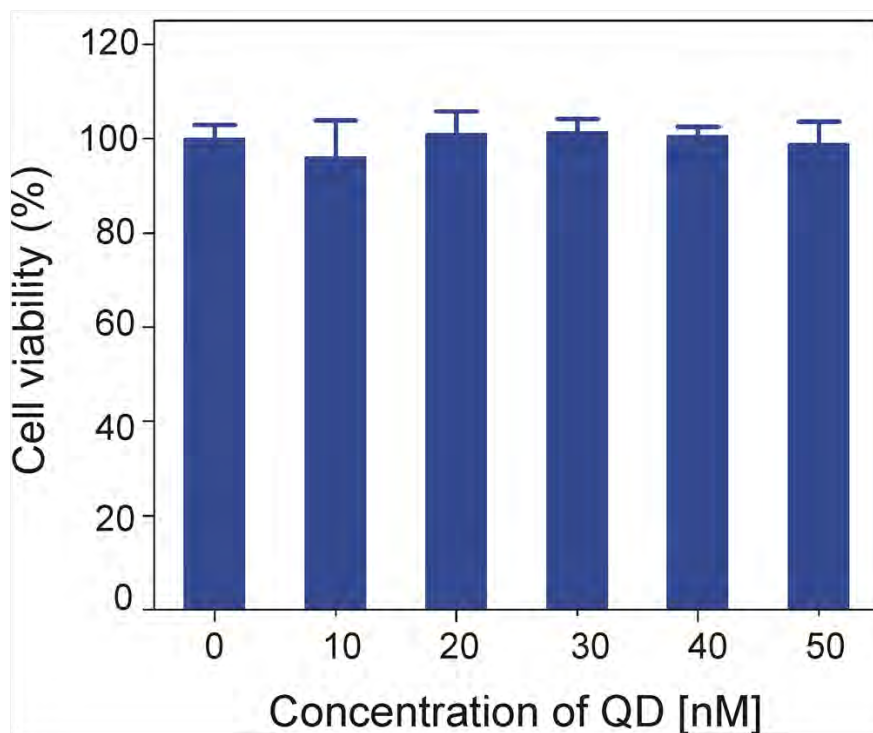


Figure 2.2: Toxicity of QDs using MTS assay. Most of U87 cells were found to be viable across the concentration range of QDs. The QDs tested within the above range were found to be non-cytotoxic and all knockdown experiments were conducted within the 50 nM range. [111]

Importantly, the EGFP cell line has been widely used to investigate siRNA-based silencing of EGFP, since the suppression of EGFP expression does not compromise cell viability. The transfection efficiency of three different kinds of constructs were evaluated; constructs modified with the RGD peptide only, those modified with the HIV-Tat peptide only, and those with both HIV-Tat and RGD peptide. Although the siRNA-QDs modified with only RGD showed considerable selective internalization within U87-EGFP cells, siRNA-QDs modified with a combination of RGD and HIV-Tat peptides (the ratio of siRNA: RGD: HIV-Tat being 1:10:10 per QD) showed maximum internalization within U87-EGFP cells, in close agreement with previous studies [8]. This optimal condition was used for subsequent siRNA-QD experiments.

The U87-EGFP cell line was then treated with siRNA-QDs (siRNA:QDs = 0.12  $\mu$ M:0.11  $\mu$ M), modified with HIV-Tat [ 1.2  $\mu$ M] and RGD [ 1.2  $\mu$ M], and simultaneously

imaged using fluorescence microscopy (Figure 2.3). Cationic lipids (X-tremeGENE, Roche) were used to further enhance cellular uptake and prevent degradation of the siRNA within the endosomal compartment of the cells. The siRNA-QDs showed significant internalization into the cells. Knockdown of the EGFP signal was observed after 48-72 hrs (Figure 2.3B). Fluorescence intensity was influenced by other factors such as exposure time, media condition, and cell shrinkage. To minimize the influence from these external factors, the control U87-EGFP cells (without siRNA) were trypsinized and co-cultured with U87-EGFP cells transfected with siRNA-QDs in the same well. The U87 cells containing siRNA-QDs were easily distinguishable from the control cells due to the bright fluorescent property of the QDs (Figure 2.3C2). Cells with internalized siRNA-QDs showed considerable knockdown of the EGFP protein when compared with the surrounding control U87-EGFP cells (Figure 2.3C).

To further demonstrate the target-specific delivery of the siRNA-QDs, we incubated the siRNA-QDs modified with Tat and RGD against EGFP in co-cultures of the U87-EGFP cell line with other less-tumorigenic cell lines, such as PC-12 and SK-N-BE(2)C (Figure 2.4), having a considerably small number of integrin receptors [125–127]

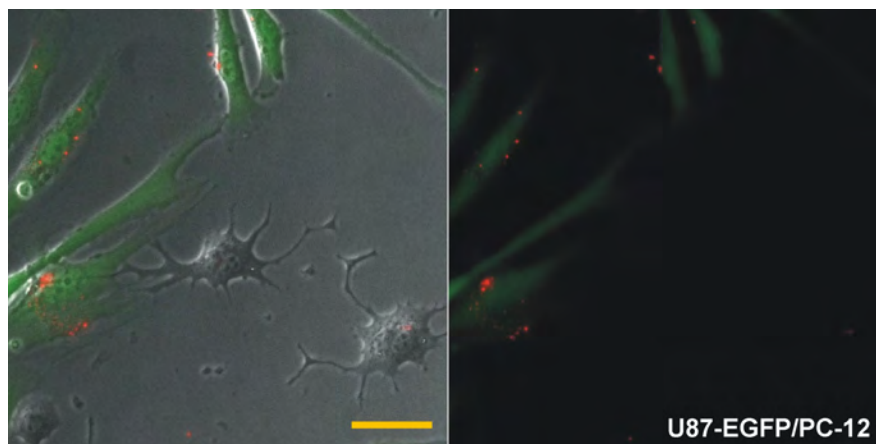


Figure 2.4: Targeted delivery of multifunctional siRNA-QDs. The multifunctional siRNA-QDs (red), when incubated in a co-culture of malignant tumor cells (U87-EGFP) and less tumorigenic cells (SK-N-BE(2)C, PC-12), selectively transfected the U87 cells. Very few siRNA-QDs internalized within the less tumorigenic cells [111]. (Scale bar: 50  $\mu\text{m}$ )

The presence of RGD tripeptide molecules on the surface of the siRNA-QDs led

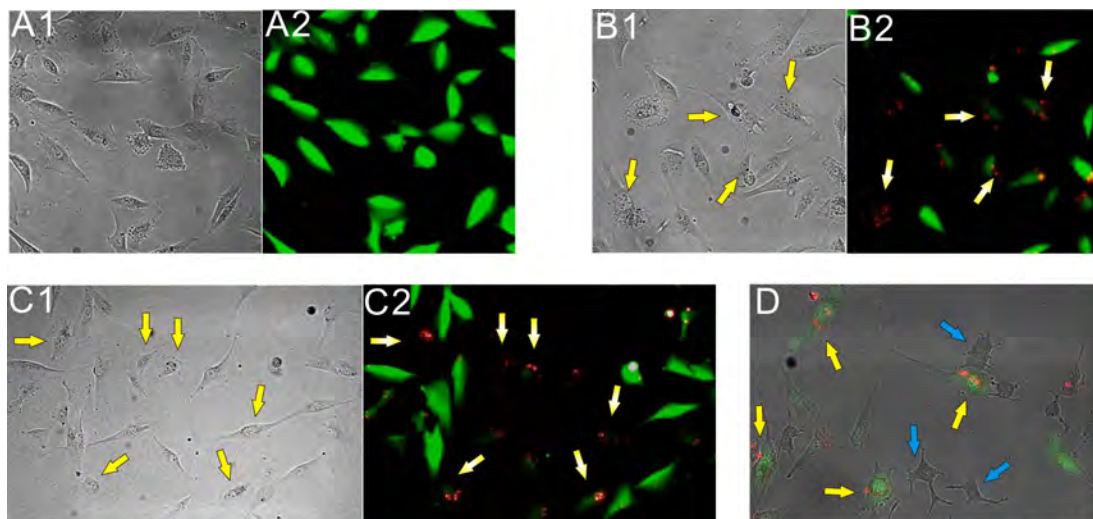


Figure 2.3: Knockdown of EGFP in U87 cells using siRNA-QD modified with RGD and HIV-Tat peptides (note that yellow arrows represent U87-EGFP cells transfected with the siRNA-QDs and the blue arrows indicate PC-12 cells). (A) Control U87-EGFP cells without siRNA-QDs; (A1) represents the phase contrast image and (A2) is the corresponding fluorescence image. (B) EGFP knockdown using multi-functional siRNA-QDs; (B1) Phase contrast image showing that the morphology of U87-EGFP cells has not changed as compared to the control cells in (A). (B2) Fluorescence image clearly shows the knockdown of EGFP in cells (marked by yellow arrows) which have internalized the siRNA-QDs (red) after 48 hrs. (C) Co-cultures of U87-EGFP control cells (without siRNA-QDs) and U87-EGFP cells transfected with siRNA-QDs so as to investigate them under the same conditions; (C1) Phase contrast image clearly shows no difference in the morphology of the U87-EGFP control cells and the siRNA-QDs transfected cells. (C2) Fluorescence image clearly shows the decrease in the EGFP signal in the U87-EGFP cells transfected with siRNA-QD as compared to the surrounding U87-EGFP control cells. (D) Phase contrast image showing the target-oriented delivery of siRNA-QDs in co-cultures of the malignant U87-EGFP cells, overexpressing the  $\alpha_3$  integrin receptors, and the less tumorigenic PC-12 cells (blue arrows) incubated with the siRNA-QDs. It can be clearly seen that most of the siRNA-QDs, due to the presence of RGD and HIV-tat peptides, were taken up by the U87-EGFP cells and not by the PC-12 cells [111]. (Scale bar: 100  $\mu\text{m}$ ).

to specific binding with integrin receptors overexpressed in the U87 cells, resulting in higher cellular uptake by the malignant U87 cells as compared to the less tumorigenic PC-12 cells as seen by the selective accumulation of the QDs within the U87-EGFP cells (Figure 2.4D). These results confirmed our hypothesis that the target-specific delivery of the siRNA-QDs into brain cancer cells can be significantly enhanced by functionalizing the QDs with targeting moieties like RGD tripeptide.

The intracellular delivery of the siRNA-QDs within the U87-EGFP cells was also confirmed by transmission electron microscopy (TEM), which clearly shows the presence of QDs in the cytoplasm of the cells (Figure 2.5A).

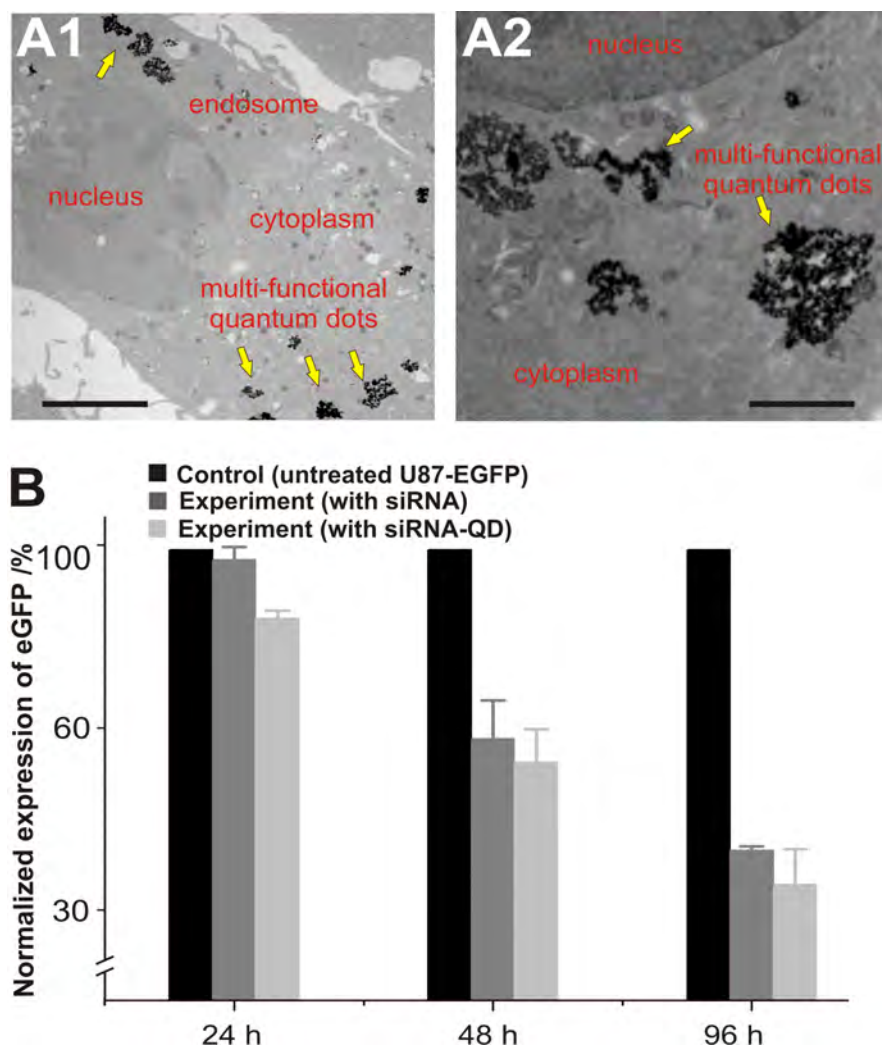


Figure 2.5: Knockdown efficiency of EGFP within U87-EGFP cells and internalization of multifunctional siRNA-QDs. (A) TEM analysis of the internalization of the multifunctional siRNA-QDs into the U87-EGFP cells; (A1) Presence of multi-functional siRNA-QDs (yellow arrows) within the cytoplasm and the endosome (Scale bar: 5 μm). (A2) Zoomed-in image showing individual siRNA-QDs within the cytoplasm (Scale bar: 2.5 μm). (B) The bar graph represents the knockdown of EGFP over 24h, 48h, and 96h in U87-EGFP cells treated with siRNA only (dark grey), and siRNA-QD (light grey). The EGFP knockdown data was normalized with the expression levels of EGFP in the control U87-EGFP cells (black) [111].

The knockdown efficiency of the siRNA-QDs was similar to or slightly better than that of the positive control consisting of U87-EGFP cells transfected with only siRNA using X-tremeGENE (Figure 2.6).

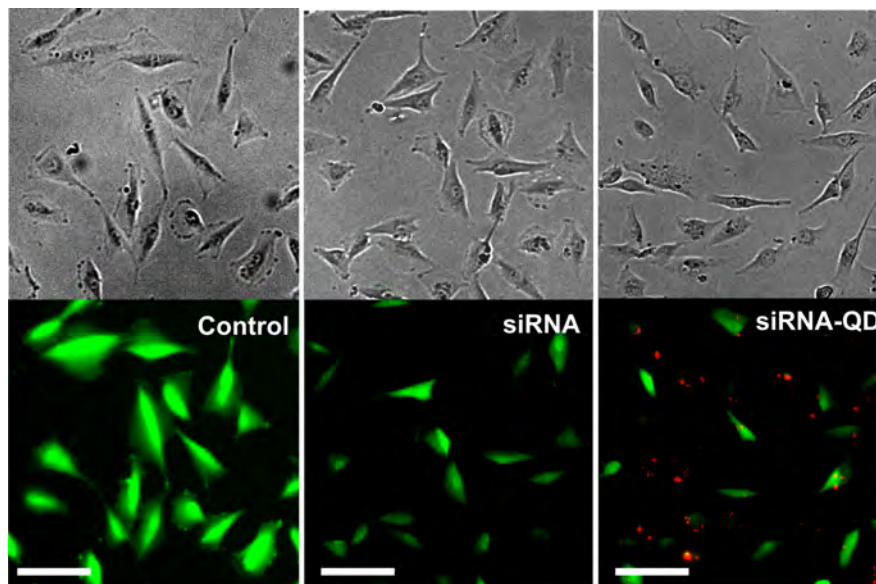


Figure 2.6: EGFP knockdown using siRNA (without QDs) and siRNA-QDs. The knockdown efficiency of siRNA-QD (red) against EGFP was slightly better or comparable to the knockdown efficiency of naked siRNA [111] (Scale bar = 100  $\mu\text{m}$ ).

This high transfection efficiency appears to be due to synergistic effects of the two transfection peptides. Decrease in fluorescence intensities (EGFP signal, green fluorescence) within cells treated with the above mentioned systems were then compared with the intensity of U87-EGFP without siRNA. As shown in Figure 2.5B, the decrease in fluorescence intensity of U87-EGFP incubated with siRNA-QDs and siRNA alone was comparable, but drastically lower than that observed for the control without siRNA. Cells with internalized siRNA-QDs show decreased green fluorescence (EGFP signal) when compared with the control. This data strongly suggests that siRNA-QDs can be simultaneously used as delivery and imaging probes.

### **Knockdown of EGFRvIII as a chemotherapeutic target by siRNA-QDs**

Having demonstrated the selective manipulation of the U87-EGFP cell line, we then focused on the knockdown of EGFRvIII with our siRNA-QD constructs. U87-EGFRvIII cells were genetically modified to overexpress EGFRvIII, a mutant-type epidermal growth factor receptor (EGFR) only expressed within cancer cells [128]. This cell type was incubated with our siRNA-QDs modified with Tat and RGD peptides and

armed with EGFRvIII-targeting siRNA. The cells were simultaneously imaged for the internalization of siRNA-QDs using fluorescence microscopy.

Significant cell death was observed in the wells loaded with siRNA-QDs against EGFRvIII after 48h (Figure 2.7A). Quantitative analysis revealed that the number of viable U87-EGFRvIII cells, as observed via fluorescence microscopy, decreased with increased incubation time. When compared with the control (U87-EGFRvIII without siRNA-QDs), there was a significant decrease in the number of viable cells, thus demonstrating the effectiveness of our nanoparticle-based siRNA delivery to knock-down the oncogene. The result was confirmed using the MTT assay which showed a decrease in the number of viable cells in the well incubated with siRNA-QDs against EGFRvIII (Figure 2.7B). This assay further confirmed that the QDs themselves were noncytotoxic when used alone as they did not result in any appreciable cell death (Figure 2.2). The knockdown of EGFRvIII and the inhibition of the downstream proteins in the PI3K signaling pathway were confirmed using Western Immunoblotting. The results (Figure 2.7C) confirm a considerable decrease in the expression of EGFRvIII, and down-regulation of phospho-Akt and phospho-S6 as compared to the control. Thus, these results demonstrate the specificity of the siRNA against EGFRvIII, the inherent noncytotoxicity of the QDs, and the facile evaluation and manipulation of cancer cell proliferation with multifunctional-QD constructs.

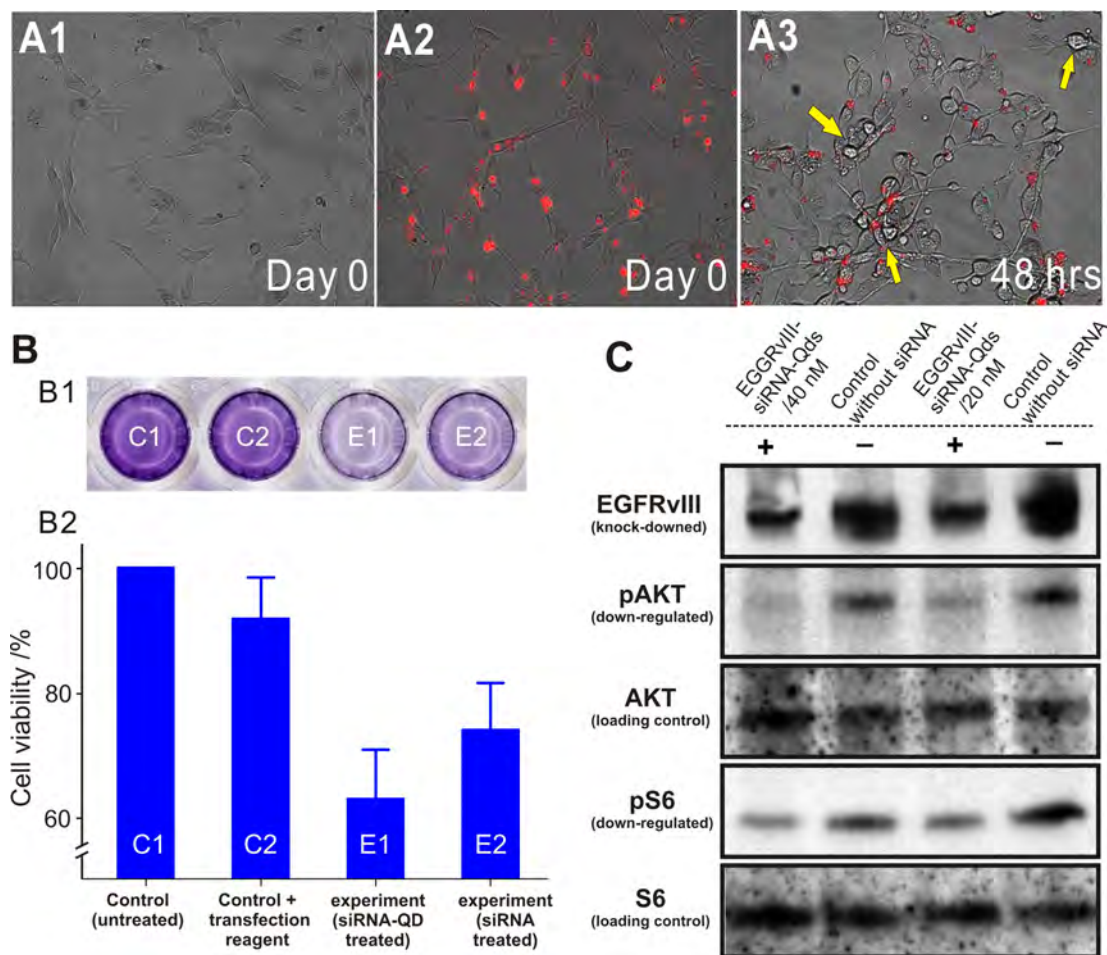


Figure 2.7: Knockdown of EGFRvIII in U87 EGFRvIII using multifunctional siRNA-QDs (A) Phase contrast images showing the internalization of siRNA-QDs into the U87-EGFRvIII cells. (A1) Morphology of U87-EGFRvIII cells before incubation with siRNA-QDs on Day 0. (A2) U87-EGFRvIII cells after incubation with siRNA-QDs (red) on Day 0. (A3) Morphology of U87-EGFRvIII 48hrs after incubation with siRNA-QDs. Note that effect of the EGFRvIII knockdown by the siRNA-QDs can be clearly seen as they have clearly shrunk (yellow arrows) and look collapsed as compared to Day 0, marking the onset of apoptosis (Scale bar = 100  $\mu$ m). (B) Cell viability assay using MTT assay. (B1) Optical image of cell viability (MTT) assay in a well plate. Dark blue color represents high number of viable cells and pale blue indicates low viable cell population. (B2) MTT assayed wells were quantified with UV absorbance and converted to cell viability. Untreated control C1 and C2 represent control cell population and viable cell population in presence of a cationic lipid based transfection reagent respectively. siRNA-QD transfected cells in experiment E1 and siRNA treated cells in E2 show low numbers of the viable cells due to knockdown of EGFRvIII gene. (C) Western Immunoblotting to show silencing effect of EGFRvIII gene. Protein expression level of EGFRvIII is dramatically decreased, and phosphorylation levels of key proteins in PI3K signaling pathway are reduced significantly. The upstream protein (AKT) and the downstream protein (S6), which play an important role in cell proliferation are selected to investigate the gene-knockdown effect on the PI3K signaling pathway [111].

### 2.1.3 Conclusions

In summary, this work is a demonstration of the multi-functional siRNA-QD strategy focusing on targeted delivery, high transfection efficiency, and multi-modal imaging/tracking. Our siRNA-QDs could be used for the development of novel chemotherapies and diagnostics relevant to brain cancer research. These novel methods and applications complement recent advances in nanomaterial-based siRNA delivery, nanomaterial-based molecular imaging, as well as siRNA-based chemotherapeutic strategies reported recently. While the ability to functionalize as well as control the surface of quantum dots with specific linkers and multi-functional molecules (siRNA and peptides) is critical for nanoparticle-based drug delivery, this method could also provide highly useful information regarding bio-surface chemistry of nanomaterials. In addition, the application of multi-functional siRNA-QDs to modulate the key cancer signaling pathways is important not only for selective chemotherapeutic strategy but also for dissecting signaling cascades triggered by inhibiting specific proteins. Collectively, our multi-functional QD-based siRNA delivery strategy has significant potential for simultaneous prognosis, diagnosis, and therapy.

### 2.1.4 Materials and Methods

Starting materials, reagents, and solvents were purchased from commercial suppliers (Aldrich, Acros, Lancaster, and Fisher) and used as received unless otherwise noted. All reactions were conducted in flame-dried glassware with magnetic stirring under an atmosphere of dry nitrogen. Reaction progress was monitored by analytical thin layer chromatography (TLC), using 250  $\mu\text{m}$  silica gel plates (Dynamic Absorbents F-254). Visualization was accomplished with UV light and potassium permanganate stain, followed by heating. Proton nuclear magnetic resonance ( $^1\text{H}$  NMR) spectra were recorded on either a Varian-300 instrument (300 MHz), Varian-400 instrument (400 MHz), or a Varian-500 instrument (500 MHz). Chemical shifts of new compounds are reported in ppm relative to tetramethylsilane (TMS) as the internal standard. Data are reported as follows: chemical shift, integration, multiplicity (s=singlet, d=doublet, t=triplet,

q=quartet, br=broad, m=multiplet), and coupling constants (Hz). Carbon nuclear magnetic resonance ( $^{13}\text{C}$  NMR) spectra were recorded on either a Varian-300 instrument (75 MHz), Varian-400 instrument (100 MHz), or a Varian-500 instrument (125 MHz). Chemical shifts of new compounds are reported in ppm relative to tetramethylsilane (TMS) as the internal standard. Mass spectra were recorded on a Finnigan LCQ-DUO mass spectrometer.

### **Synthesis of the Core-Shell QDs**

CdSe/CdS/ZnS core-shell QDs (7nm) were synthesized using well established protocols from the literature [112,113]. The QDs were then characterized for size and distribution using a transmission electron microscope (TEM). The spectroscopic properties of the QDs were characterized using a fluorometer (FluoroMax-3, HORIBA Scientific).

### **Synthesis of QD conjugates with siRNA**

The siRNA molecules for EGFP and EGFRvIII containing 5-thiol group were purchased from Dharmacon and Invitrogen respectively. The siRNA for EGFP was designed as follows; Sense sequence was 5-thiol-GGCUACGUCCAGGAGCGCACC and antisense sequence was 5-phosphate-UGCGCUCCUGGACGUAGCCUU. For the knockdown of EGFRvIII, 5-thiol-GAAAGGUAAUUAUGUGGUGdTdT (sense) and 5-phosphate-CA-CCACAUAUUACC UUUCdTdT (antisense) were used. QDs in PBS were mixed with 1000 fold excess of the cross linker, MPPf (3-maleimidopropionic acid pentafluorophenyl ester) and PTPPf [3-(2-pyridyl)-dithiopropionic acid pentafluorophenyl ester], for one hour. After removing the unreacted linkers by ultracentrifugation, siRNA molecules were coupled to QDs by mixing together for one hour. After the conjugation, free siRNA was removed using ultracentrifugation. For the quantification of ratio of QD and siRNA, the siRNA linked to QDs via PTPPf (disulfide bond) were treated with DTT for one hour. After centrifugation, the supernatant was analyzed under UV at 260 nm quantifying the siRNA detached from QDs. By determining the concentration of QDs in the same volume at the first absorption peak, the siRNA molecules per QD were estimated. For the conjugation of HIV-Tat(CYGRKKRRQRRR) and RGD(RGDC) to

siRNA-QDs, the same method as that used to conjugate siRNA to QD was used with the ratio of 1:10:10 (siRNA:RGD:HIV-Tat).

### **Cell Culture of U87-EGFP and U87-EGFRVIII**

Cells were cultured in the following growth media: DMEM (Dulbeccos modified Eagles medium) with high glucose (Invitrogen), 10 % Fetal Bovine Serum (FBS), 1 % streptomycin-penicillin, 1% glutamax (Invitrogen), and selection markers, G418 (100  $\mu\text{g}/\text{ml}$ ) and hygromycin B (30  $\mu\text{g}/\text{ml}$ ) for U87-EGFP and U87-EGFRvIII respectively. For the knockdown experiment, passaged cells were prepared to 40-60 % confluency in 96-well plates. For the knockdown experiment and cell viability assay, media was exchanged with serum-free basal media (150  $\mu\text{l}$ ) and siRNA-QDs solution (30  $\mu\text{l}$ ) with the cationic lipid based transfection reagent, X-tremeGENE (0.4  $\mu\text{l}$ , Roche), was added after 20-30 minutes. After incubation for 12 hours, media was exchanged with normal media. Fluorescence measurement and cellular assays were performed after 48-96 hours from the starting point. Once intensity of EGFP was decreased, it was trypsinized and co-cultured with control U87-EGFP (1:1 ratio) in 48-well plates for direct comparison of knockdown level. Cells were washed with DPBS and fixed with 2-4 % paraformaldehyde solution for long term storage at 4°C.

### **Targeted delivery of siRNA-QDs**

U87-EGFP cells were co-cultured with control cells (or control neuroblastomas or neuroendocrine tumor), which are PC12 and SK-N-BE(2)C. Each control cell was passaged in 96 well plates, and 6 - 8 hours later U87-EGFP cells were co-cultured. Cell culture media for PC12 and U87 well plate was a mixture of DMEM, 10% horse serum, 5%FBS, and 1% streptomycin-penicillin. For U87 cells, DMEM, 10% FBS, and 1% streptomycin-penicillin was used as a culture media. F12 and MEM mixture (1:1), 10% FBS, and 1% streptomycin-penicillin were used to prepare the media for SK-N-BE(2)C. For the delivery of HIV-tat and RGD peptide conjugated siRNA-QDs, media was exchanged with serum free DMEM or Opti-MEM media. After adding the QD solution, the cells were incubated for 6 - 8 hrs. The media was removed and washed with serum free

media. Fluorescence images were taken after replacing the media with regular media.

### **Transmission electron microscopy and fluorescence microscopy**

U87-EGFP transfected with siRNA-QDs samples were prepared using the Spurrs kit (EMS, Hatfield, PA). The images were obtained using the TEM (JEOL 100CX TEM).

Cells in well plates were washed with DMEM and refilled with normal media. For the fluorescence, DIC, and phase contrast images were obtained using the Zeiss Axio observer inverted epifluorescence microscope. Each image was captured with different channels and focus. Images were processed and overlapped using Image-Pro (Media-Cybernetics) and ImageJ (NIH).

### **Cell viability assay**

Cell viability assays were performed using MTT and MTS by following the standard protocols provided by company (Molecular Probes, Invitrogen).

### **Western blot analysis**

Cells were lysed with RIPA buffer (Thermo scientific, Rockford, IL) with protease inhibitor cocktail (Sigma-Aldrich) and phosphates inhibitor cocktail I, II (Sigma-Aldrich). After centrifugation, cell lysates were assayed for protein concentration using the Bio-Rad protein assay kit (Bio-Rad, Hercules, CA). Proteins (20  $\mu$ g) were separated in 10% SDS polyacrylamide gels by electrophoresis, then transferred to a nitrocellulose membrane and subjected to immunoblotting. The following primary antibodies were used; polyclonal rabbit anti-human EGFRvIII (Spring Bioscience, Pleasanton, CA), polyclonal mouse anti-human EGFR (Santa Cruz Biotechnology, Santa Cruz, CA), monoclonal mouse anti-human S6 (Santa Cruz Biotechnology) and monoclonal mouse anti-human phospho-S6 (Ser235/236) (Santa Cruz Biotechnology). Horse radish peroxidase (HRP)-conjugated polyclonal anti-mouse IgG and anti-rabbit IgG were used as the secondary antibodies. Immunoreactive bands were detected with the enhanced chemiluminescence (ECL) kit (GE Healthcare, Piscataway, NJ).

## 2.2 Simultaneous Delivery of siRNA and Small Molecule Using Polyamine-Cyclodextrins to Enhance Neuronal Differentiation of Neural Stem Cells

### 2.2.1 Introduction

Stem cells are becoming increasingly attractive as treatment options for regenerative medicine due their ability to differentiate into specialized cells of interest. However, achieving a controlled and reproducible means to direct stem cell differentiation is the single most critical concern scientists have been trying to address ever since the discovery of stem cells. In this regard, a chemical approach has been widely applied wherein small molecules are used to modulate specific signaling cascades and in turn gene expression within the cell. For instance, novel small molecules have been screened and identified that can control a variety of stem cell fates and functions including stem cell maintenance, differentiation and reprogramming [9, 129–132]. Examples of small molecules that have been used to modulate stem cell phenotypes include retinoic acid, cytidine analogues, histone-deacetylase inhibitors and protein kinase inhibitors [129]. To this end, the use of small molecules to alter stem cell behavior is particularly advantageous since they provide a high degree of temporal control over protein function by either rapid inhibition or activation of single or multiple targets within a protein family [130]. Nevertheless, a majority of the small molecules used for such studies tend to be very hydrophobic and lack solubility in physiological solutions, which can greatly impair its delivery and efficacy [133]. As a result, organic solvents such as dimethyl sulfoxide (DMSO) are often used to dissolve such compounds [134]. However, these solvents tend to be cytotoxic and require careful dilution to avoid stem cell death and undesired side-effects [135].

In contrast to the chemical approach, a more delicate control of gene expression has been demonstrated using RNA interference (RNAi) [90]. RNAi is a post-transcriptional process that involves using short double-stranded RNA molecules (small interfering RNA [siRNA], small hairpin RNA [shRNA] or miRNA) to selectively silence a gene of interest by destroying the target mRNA [136]. Similar to the use of small molecule

drugs in chemotherapies, RNAi has been widely used for treating genetic diseases and cancers [111,137]. However, many studies in the last decade have demonstrated this strategy to be equally important for directing stem cell differentiation [138–140]. For example, the application of siRNA to promote differentiation was first established by inducing myogenesis of pluripotent P19 teratocarcinoma cells [141]. Thereafter, another group went on to demonstrate that the knockdown of p53 in ESCs under retinoic acid induction promoted their differentiation into muscle cells [142]. While RNAi shows great potential for directing stem cell differentiation, a major challenge for achieving efficient gene knockdown is the robust and reliable intracellular delivery of siRNA molecules into stem cells [143–145]. The negatively charged backbone of siRNA molecules makes it difficult to penetrate the cellular membrane, often requiring a biocompatible exogenous vehicle to facilitate the delivery [146]. Moreover, the stem cells are sensitive to exogenous treatments and must typically maintain high cellular viability over an extended time period after transfections to ensure the differentiated cellular sub-types can be effectively used for further studies (e.g. *in vivo* transplantation, animal studies, etc) [147,148].

Both chemical (via small molecules) and genetic (via RNAi) treatments offer unique advantages in their own regard, with varying mechanisms of action targeting different proteins and biomolecules within the stem cell. Therefore, we believe that the simultaneous delivery of these two molecules (siRNA and small molecules) can provide an enhanced stem cell differentiation outcome compared to either treatment alone. Yet, the common challenge in applying both approaches for controlling stem cell differentiation is the efficient, non-toxic and reliable delivery to the target stem cell. Based on these concerns, there is a need for single delivery platform which provides: i) minimal cytotoxicity, ii) high transfection efficiency and iii) the ability to simultaneously deliver nucleic acids and small organic molecules to achieve a synergistic enhancement in stem cell differentiation. Herein, we demonstrate the synthesis and application of a multifunctional vehicle for the simultaneous delivery of siRNA molecules and small organic molecules to direct the differentiation of a multipotent adult stem cell line (Figure 2.8).

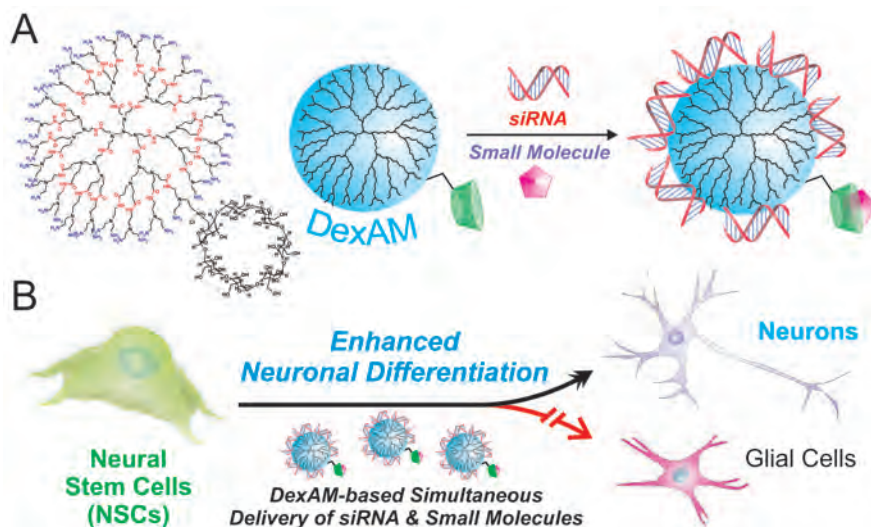


Figure 2.8: Schematic diagram showing the application of DexAM for stem cells. (A) DexAM molecule is complexed with siRNA via electrostatic interactions with the polyamine backbone and the small molecule via encapsulation within the  $\beta$ -cyclodextrin. (B) DexAM constructs are delivered to neural stem cells (NSCs) to enhance their differentiation into neurons.

### 2.2.2 Results and Discussion

In order to achieve the dual delivery of these molecules, the delivery platform (termed DexAM) consists of a dendritic polyamine linked with  $\beta$ -cyclodextrins ( $\beta$ -CD). In this way, the positively-charged polyamine backbone was used to complex the negatively-charged siRNA molecules, while the  $\beta$ -CD increased the solubility of the hydrophobic small molecule by encapsulation in the inner cavity. As a proof-of-concept, we first assessed the efficiency of RNAi by examining the suppression of green fluorescent protein (GFP) in NSCs that were genetically modified to express GFP. Based on the GFP knockdown studies, we then used the optimized conditions to simultaneously deliver a specific siRNA and small molecule to enhance the differentiation of NSC to a neuronal cell fate. In particular, the siRNA selected to silence the expression of the neural switch gene was SOX9, and the small molecule used was the well-known neurogenesis-promoting vitamin A derivative, retinoic acid (RA). The simultaneous delivery of SOX9 siRNA and RA was found to greatly enhance neuronal differentiation, compared to differentiation incurred by either molecule individually. By maintaining minimal cytotoxicity with high delivery efficiency of multiple molecules of interest, our study provides

a reliable methodology to ensure long-term stem cell survival and differentiation for applications in regenerative medicine and tissue engineering.

### **DexAM: Structure and Synthesis**

Our cyclodextrin-modified dendritic polyamine construct (DexAM) combines the unique properties of two distinct chemical moieties in a single delivery vehicle. First, the  $\beta$ -CD component, a widely used structure in pharmaceutical applications, serves to improve the solubility of hydrophobic compounds [149, 150]. Cyclodextrins are cyclical sugar molecules containing a hydrophilic exterior and hydrophobic interior cavity, wherein the inclusion of hydrophobic moieties within the inner cavity serves to enhance the solubility, stability and bioavailability of hydrophobic small molecules [149, 151]. Given that most small molecules and drugs have poor water solubility and necessitate the use of cytotoxic organic solvents, such as DMSO, the presence of  $\beta$ -CD in our delivery vehicle enhances water solubility of drugs/small molecules and allows for optimal cellular uptake and drug efficacy while avoiding the use of cytotoxic solvents. Second, the dendritic polyamine backbone provides a high density of positive surface charge, which can be used to condense negatively charged nucleic acids into cationic complexes. This would allow for effective intracellular delivery and endosomal escape within the stem cell [152]. While maintaining a high degree of positive charge is crucial for proper complexation with siRNA molecules, the primary amines have been reported to interact with cellular components and impart undesired side-effects and cytotoxicity [153]. Therefore, it is critical to achieve a balance between the cytotoxicity and complexation capacity of our DexAM construct.

In our previous study, we developed a synthetic methodology to generate a series of highly water soluble dendritic polyamine compounds conjugated to  $\beta$ -cyclodextrin ( $\beta$ -CD) molecules [154]. By precisely controlling the number of primary amine head groups on the dendritic polyamine backbone from 4 to 48, we assessed the complexation ability and cytotoxicity of four different generations of DexAMs (D1-D4). Based on these results, we identified D4 (47 primary amines + 1 $\beta$ -CD) to show optimal siRNA complexation with minimal cytotoxicity in brain cancer cells [154]. Based on these

observations, we utilized D4 in the current study (herein referred to as DexAM) to facilitate the dual delivery of siRNA and small molecules for directing the differentiation of neural stem cells (NSCs) into neurons.

The DexAM molecule was synthesized by using a multistep solution-phase and solid-phase synthesis (see Materials and Methods in the above subsection). Briefly, the dendritic polyamine backbone was synthesized by the Michael addition of tris(2-aminoethyl)amine and methyl acrylate, followed by amidation of the amino esters generated after Michael addition (Figure 2.9). Thereafter, this synthetic route (Michael addition followed by amidation) was repeated to yield a polyamine backbone consisting of 48 primary amines. The conjugation of  $\beta$ -CD to the polyamine backbone was performed by the tosylation of  $\beta$ -CD, followed by nucleophilic addition to the amine group. This yielded our final DexAM molecule, which we used for the simultaneous delivery of siRNA and small molecules to NSCs.

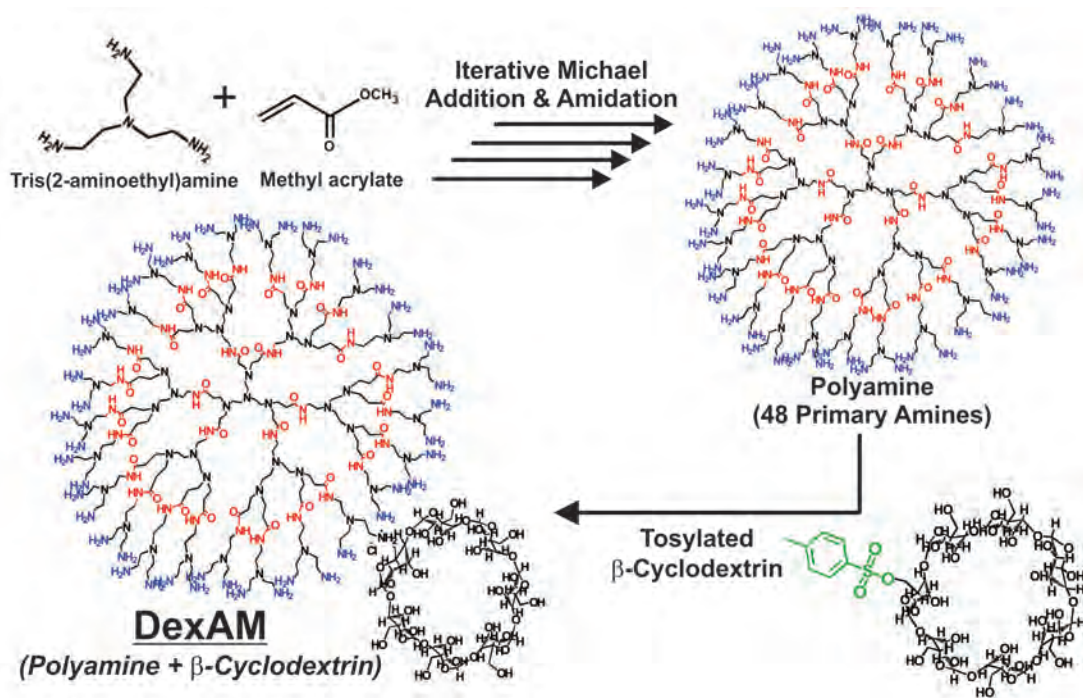


Figure 2.9: General Scheme for the Synthesis of DexAM. The polyamine backbone is initially synthesized by the iterative Michael addition of tris(2-aminoethyl)amine and methyl acrylate, followed by amidation. Tosylated  $\beta$ -cyclodextrin is then used to form the final DexAM molecule.

### GFP knockdown efficiency of DexAM

The optimization of gene silencing with our DexAM construct and assessment of knock-down efficiency was first performed by measuring the suppression of green fluorescent protein (GFP) in NSCs, which were genetically modified to constitutively express GFP. Prior to transfection, we assessed the capability of DexAM to spontaneously form complexes with the negatively charged siRNA. Using a well-established dye exclusion assay (Picogreen Assay), we identified a range of DexAM concentrations which showed about 75% of the siRNA binding to the DexAM molecule (Figure 2.10).

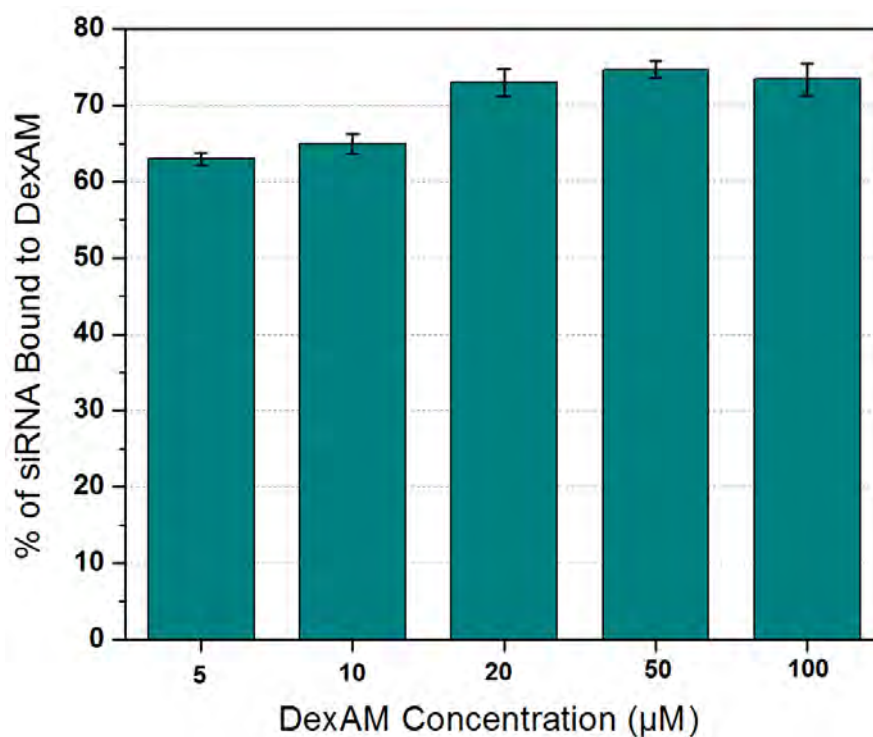


Figure 2.10: siRNA complexation efficiency of DexAM measured by Picogreen dye exclusion assay (Absorption = 480 nm, Emission = 520 nm).

Thereafter, varying concentrations of the DexAM molecule was mixed with a given amount of GFP siRNA (100 pmol) to form the DexAM-siRNA complexes. The zeta potential of the resulting complexes were found to be in the range of 10-12 mV at pH 7.4, while exhibiting hydrodynamic diameters of 300 to 350 nm [154]. In order to visualize the efficiency of delivery, the DexAM molecule was conjugated with a fluorescent dye (AlexaFluor<sup>®</sup> 594) prior to complexation with the GFP siRNA. The decrease in green

fluorescence intensity was monitored using fluorescence microscopy over a time period of 48-96 h (Figure 2.11A). Successful transfection of the DexAM-siRNA constructs was evident as visualized by the presence of the dye fluorescence expression (conjugated to DexAM) in the NSCs (Figure 2.11C). We observed a dose-dependent knockdown of GFP expression, wherein the NSCs treated with 75  $\mu\text{M}$  DexAM (complexed with GFP siRNA) showed a significant 80% knockdown in GFP intensity after 96 hours of siRNA treatment compared to the untreated control cells (Figure 2.11B).

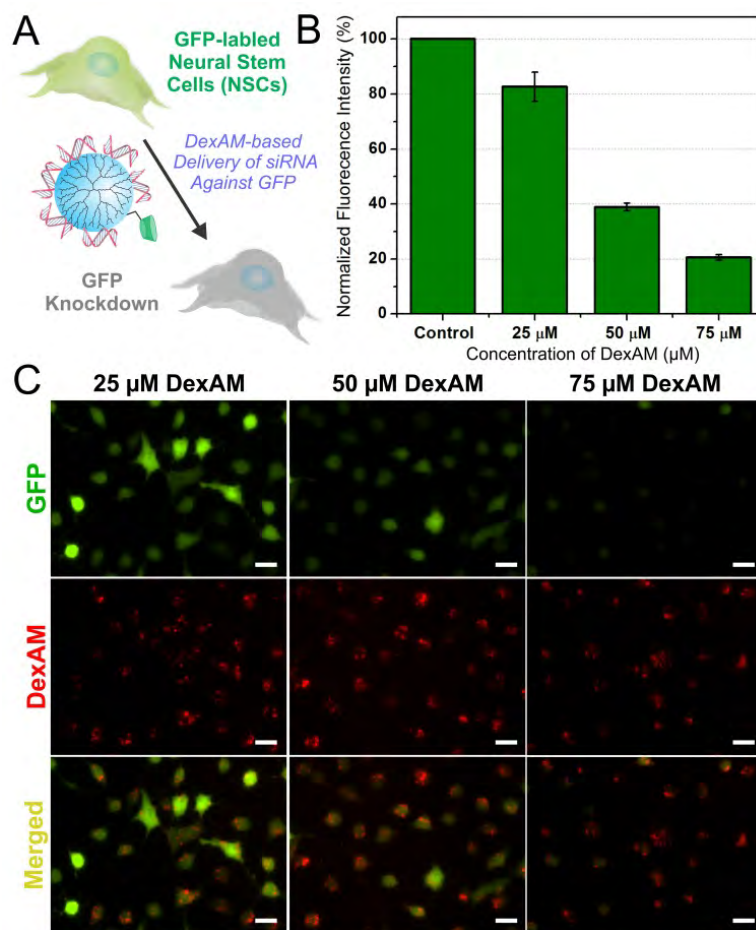


Figure 2.11: Delivery of DexAM-siRNA for GFP Knockdown in NSCs. (A) Scheme depicting the delivery of DexAM complexed with siRNA targeting GFP to NSCs. (B) Quantitative comparison of the percentage of GFP knockdown in NSCs with varying concentrations of DexAM at 4 d. (C) Fluorescence images of cell with varying concentrations of DexAM showing GFP expression (green) and dye-labeled DexAM (red) at 4 d. Scale bars: 20  $\mu\text{m}$ .

### DexAM is non-cytotoxic and biocompatible

While we achieved a remarkable knockdown efficiency with the DexAM-siRNA constructs, maintaining high cellular viability was equally important. Evaluating the cytotoxicity of the DexAM molecules is especially critical for applications in stem cell biology, which generally require both longer time periods of culture (at least one week) and differentiated sub-type specific cells that are functionally active for subsequent *in vitro* and *in vivo* studies. We assessed the cytotoxicity of the DexAM molecules using MTS assay, which confirmed that our delivery vehicle shows negligible toxicity (Figure 2.12). While cationic polyamine-based polymers have been observed to show dose-dependent cytotoxicity in mammalian cells, we believe the biocompatibility of our DexAM constructs is due to the presence of CD, which can potentially reduce the non-specific binding of the DexAM with cellular proteins and components [153, 155–157].

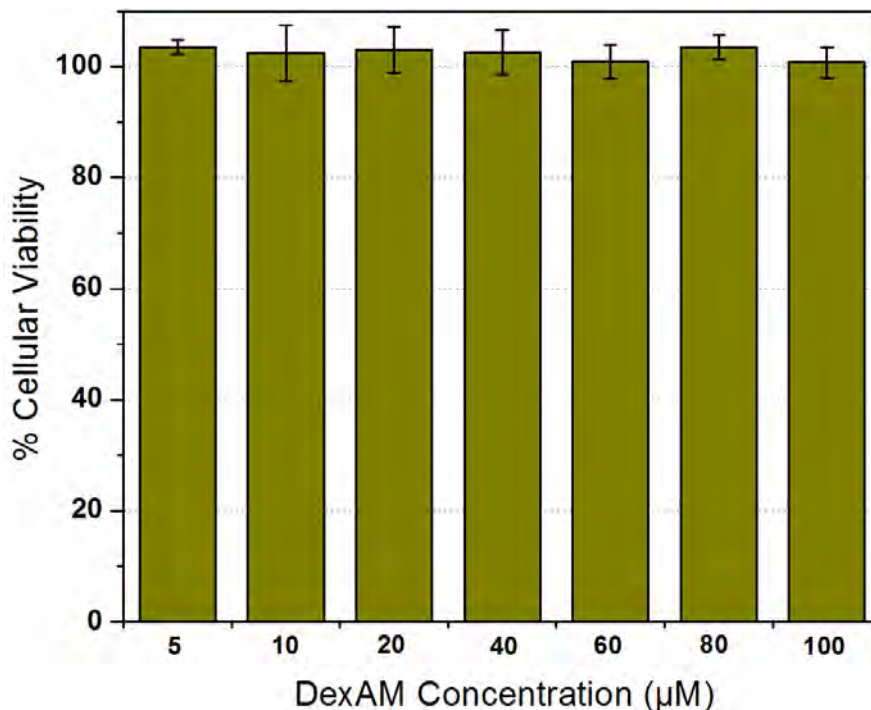


Figure 2.12: DexAM cytotoxicity in NSCs. The percentage of viable cells was estimated using MTS assay following incubation of cells with the DexAM for 96 h. The data was obtained as absorbance of water-soluble formazan at 490 nm, following incubation with only DexAMs for 96 h. The fluorescence for treated samples was normalized to that of untreated controls.

## Enhanced neuronal differentiation of NSCs using DexAM

The key advantage of our delivery platform is its versatility in delivering both negatively charged nucleic acids (via complexation with the cationic polyamine backbone) and hydrophobic small molecules (via complexation within the  $\beta$ -CD cavity). Having demonstrated the efficient gene silencing capability of DexAM by delivering siRNA against GFP, we focused on using our delivery vehicle for codelivering siRNA and small molecules to enhance the neuronal differentiation of NSCs. For the siRNA molecule, we designed a sequence to knockdown a well-established transcription factor known as SOX9, which acts as a switch between neuronal and glial differentiation [158]. When the SOX9 gene is turned on, a higher percentage of NSCs differentiate into astrocytes (glial cells), and when turned off, a higher percentage of NSCs differentiate into neurons [145, 158, 159]. For the small molecule, we selected the well-established vitamin A derivative all-trans retinoic acid (RA), which is known to play a crucial role in central nervous system development [160]. RA functions by binding to RA receptors (RARs) in the cellular nucleus to form a ligand-receptor complex, which in turn binds to RA response elements to activate gene expression [161]. However, this activation first requires the efficient intracellular delivery of RA into the cytoplasm, whereby the binding of RA to cytoplasmic proteins facilitates the abovementioned downstream effects in the nucleus. Previous studies have reported that the treatment of RA tends to upregulate the expression of a variety of neuronal genes in cultured stem cells [158, 162, 163]. Interestingly, exogenous expression of a SOX9 gene prior to the RA treatment was found to actually counteract the neuronal-promoting effect caused by RA, by suppressing neuronal gene expression [158]. SOX9 is thus known to actively induce glial traits while simultaneously repressing neuronal traits [158, 164]. The knockdown of SOX9 and exposure to RA in NSCs has each individually been demonstrated to induce NSC differentiation into neurons. However, given the two factors (RA and SOX9) have varying mechanisms of action and target different signaling pathways in NSCs, we hypothesized that the simultaneous suppression of SOX9 expression and treatment with RA could greatly enhance the neuronal differentiation of NSCs.

To this end, we utilized our DexAM construct to facilitate the co-delivery of RA and siRNA against SOX9 (termed siSOX9). RA has been used in previous studies for inducing neuronal differentiation, but given that it is extremely hydrophobic, it requires the use of toxic organic solvents like DMSO for delivery. For our studies, RA was loaded within the  $\beta$ -CD cavity of DexAM under reflux conditions to obtain highly water soluble complexes, thus evading the use toxic organic solvents. The RA-loaded DexAM ( $2 \mu\text{M}$ ) was complexed with the negatively charged siRNA (100 pmol; as described earlier) to form the DexAM constructs containing the siSOX9 and RA in a single delivery vehicle (Figure 2.13A). The NSCs were plated into culture plates at 0 d, followed by transfection with the DexAM-SOX9-RA constructs at 1 d. To confirm our hypothesis that the simultaneous delivery of siSOX9 and RA would enhance neuronal differentiation, we also transfected NSCs with: 1) DexAM complexed with only siSOX9 (without RA), 2) DexAM complexed with RA (and Silencer<sup>®</sup> negative control siRNA to maintain the charge ratio), and 3) control (untreated) cells. At 7 d, we quantified the extent of differentiation by immunostaining for neuronal (TuJ1) and glial (GFAP) marker (Figure 2.13B-C)

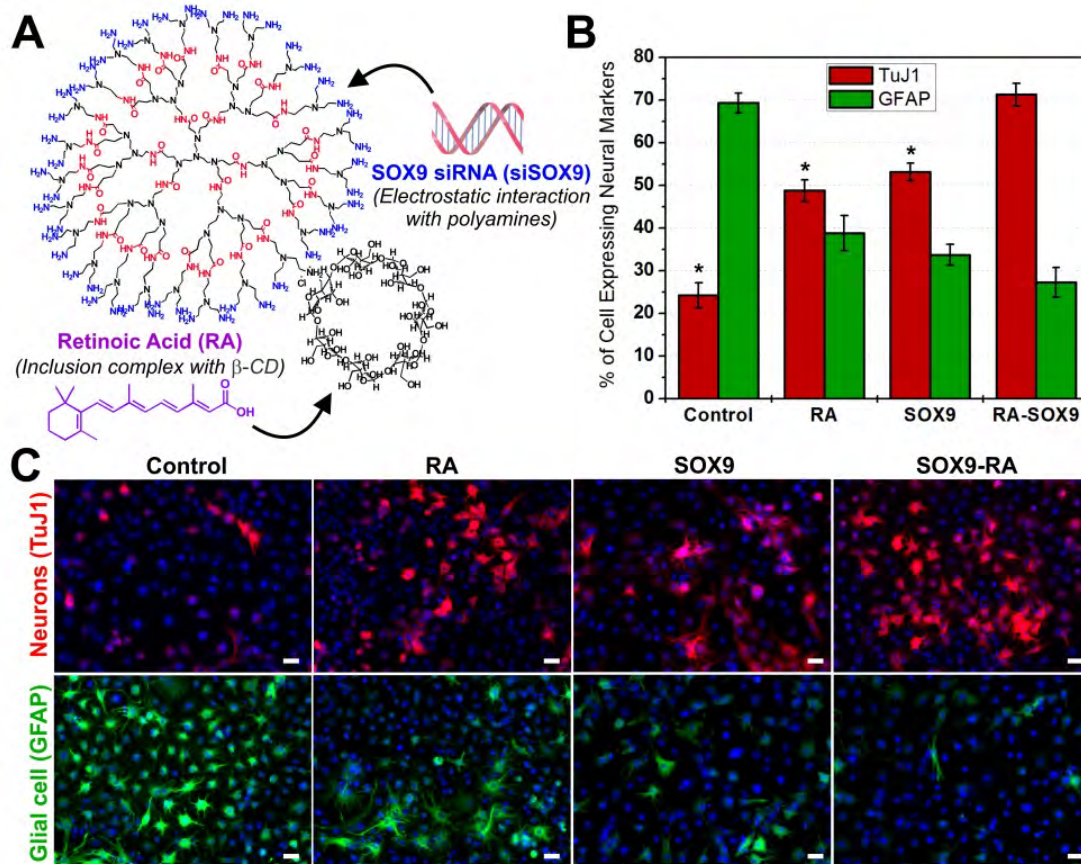


Figure 2.13: NSC differentiation using DexAM constructs complexed with SOX9 siRNA and Retinoic Acid. (A) Scheme depicting the complexation to DexAM. (B) Quantitative comparison of the percentage of cells expressing TuJ1 and GFAP at 6 d. Student's unpaired t-test was used for evaluating the statistical significance for cells stained for TuJ1, compared to the RA-SOX9 treatment (\* =  $P < 0.001$ ). (C) Fluorescence images of cells stained for the nucleus (blue), the neuronal marker TuJ1 (red, top row) and the astrocyte marker GFAP (green, bottom row) at 6 d. Scale bars: 20  $\mu$ m.

The control (untreated) cells showed the majority of the NSCs differentiated into glial cells (70%) versus neuronal cells (25%), which is an expected differentiation pattern as observed previously [68]. Conditions containing only RA and only siSOX9 resulted in about a two-fold increase in neuronal differentiation compared to the control, showing about 49% and 53% of the cells expressing the neuronal marker TuJ1, respectively (Figure 2.13B). Compared to each of the conditions described above, the simultaneous delivery of RA and siSOX9 to the NSCs using our DexAM molecule resulted in a remarkable increase in neuronal differentiation, wherein in about 71% of the cells were expressing TuJ1 (Figure 2.13B). The enhanced neuronal differentiation using

the combined DexAM-RA-siSOX9 construct was found to be statistically significant, confirming the synergistic effect of combining RA and siSOX9 for a single treatment to control NSC behavior.

### 2.2.3 Conclusions

Overall, introduction of exogenous nucleic acids combined with small molecules into stem cells represents a powerful approach for manipulating stem cell differentiation. We have demonstrated a novel delivery platform capable of efficient and simultaneous delivery of siRNAs and hydrophobic small molecules into neural stem cells. Our synthetic methodology allows for facile manipulation of the core chemical structure to attain remarkable transfection efficiency while maintaining negligible cytotoxicity. Moreover, our multimodal delivery vehicle enables a methodology by which we can target multiple signaling pathways and mechanisms to successfully enhance the neuronal differentiation of neural stem cells. While our study provides a specific application for directing neural stem cell behavior using retinoic acid and SOX9 siRNA, our delivery system are amendable to any combination of cell line, small molecules and siRNA sequences. With the increasing interest in achieving precise control over stem cell differentiation, our DexAM delivery system serves as a step towards bridging the gap between basic science and clinically-relevant treatment strategies.

### 2.2.4 Materials and Methods

$\beta$ -cyclodextrin, tosylimidazole, tris(aminoethyl)amine, methyl acrylate, amberlite IRA 900 were obtained from Sigma-Aldrich and used as received unless otherwise noted. Other chemicals and solvents were of analytical reagent grade. All reactions were conducted in flame-dried glassware with magnetic stirring under an atmosphere of dry nitrogen. Reaction progress was monitored by analytical thin layer chromatography (TLC) using 250 m silica gel plates (Dynamic Absorbents F-254). Visualization was accomplished with UV light and potassium permanganate stain, followed by heating. Proton nuclear magnetic resonance ( $^1\text{H}$  NMR) spectra were recorded on either a Varian-300 instrument (300 MHz), Varian-400 instrument (400 MHz) or a Varian-500

instrument (500 MHz). Chemical shifts of the compounds are reported in ppm relative to tetramethylsilane (TMS) as the internal standard. Data are reported as follows: chemical shift, integration, multiplicity (s=singlet, d=doublet, t=triplet, q=quartet, br=broad, m=multiplet), and coupling constants (Hz).

### Detailed synthesis of DexAM

*Synthesis of hexamethyl-3,3',3'',3''',3''',3''''-(2,2',2''-nitriлотris(ethane-2,1-diyl)tris(azanetriyl))hexapropanoate (1) (Figure 2.14)*

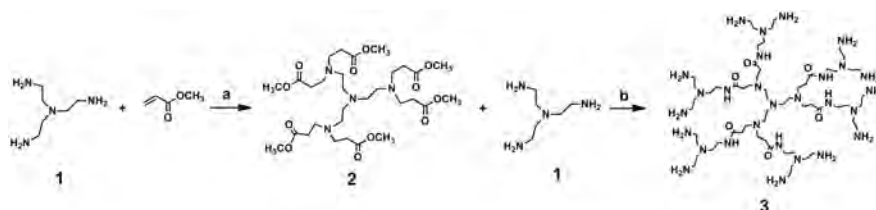


Figure 2.14: First Round of Michael Addition and Amidation, a) MeOH, 0°C, 1h/ RT, 48h, b) MeOH, 0°C, 1 h, RT, 7 days.

A solution of tris(aminoethyl)amine (1, 4.3872g, 30 mmol) in methanol (25 mL) was added dropwise to a stirred solution of methyl acrylate (19.37 g, 225 mmol) in methanol (25 mL) for 1 h in an ice-water bath. The resulting solution was stirred for 1 h in an ice-water bath and then allowed to warm to room temperature and stirred for further 48 h. The solvent and excess acrylate were removed under reduced pressure using a rotary evaporator. The residue was purified by column chromatography to afford the product (2) as a colorless oil. Yield: 16.88 g, 85%.; NMR (300 MHz, CDCl<sub>3</sub>):  $\delta$  2.44 (t, J=6.9 Hz, 12H), 2.49 (s, J=6 Hz, 12H), 2.74 (t, J=6.9 Hz, 12H), 3.67 (s, 18H). MS (m/z): calculated, 662.37 for C<sub>30</sub>H<sub>54</sub>N<sub>4</sub>O<sub>12</sub>; found, 685.76 for [M + Na]<sup>+</sup>.

*3,3',3'',3''',3''',3''''-(2,2',2''-nitriлотris(ethane-2,1-diyl)tris(azanetriyl))hexakis(N-(2-bis(2-aminoethyl)amino)ethyl)propanamide (3)*

A solution of 2 (2.17 g, 3.3 mmol) in methanol (20 mL) was added dropwise to solution of tris(aminoethyl)amine (1, 5.8 g, 39.6 mol) in methanol (20 mL) and stirred over a period of 1 h in an ice bath. The resulting solution was allowed to warm to room temperature and stirred for 7 days at room temperature at which time no methyl ester

was detectable by NMR spectroscopy. The solvent was removed under reduced pressure using a rotary evaporator and then the excess tris(aminoethyl)amine was removed using an azeotropic mixture of toluene and methanol (90:10 v/v). The remaining toluene was removed by azeotropic distillation using methanol. Finally, the remaining methanol was removed under vacuum. The residue was purified by dialysis and centrifugal filtration to afford the desired product. Finally the product was kept under vacuum to obtain the amino-terminated product (**3**, 4.4 g, 99%) as colorless oil. NMR (300 MHz, CDCl<sub>3</sub>):  $\delta$  1.25 (s, J=6.0 Hz, 24H), 2.44 (t, J=6.9 Hz, 12H), 2.48 (m, J=8 Hz, 72H), 2.74 (t, J=6.9 Hz, 12H), 3.25 (t, 12H), 8.0 (s, 6H). MS (m/z): calculated, 1347.14 for C<sub>60</sub>H<sub>138</sub>N<sub>28</sub>O<sub>6</sub>; found, 1370.0391 for [M + Na]<sup>+</sup>.

*Synthesis of methyl ester of 3 (4)*

A solution of **3** (1.48g, 1.1 mmol) in methanol (5 mL) was added dropwise to a stirred solution of methyl acrylate (2.84 g, 33.0 mmol) in methanol (5 mL) for 1 h in an ice bath. The resulting solution was stirred for 30 min in an ice bath and then for 60 h at room temperature. The volatiles were removed under reduced pressure. The residue was purified by column chromatography using DCM:MeOH (10:1 v/v) to afford the desired product (**4**) as a yellow oil. Yield: (3.41 g, 91%); NMR (300 MHz, CDCl<sub>3</sub>):  $\delta$  2.44 (t, J=6.9 Hz, 12H), 2.49 (s, J=6 Hz, 12H), 2.74 (t, J=6.9 Hz, 12H), 3.67 (s, 18H). MS (m/z): calculated, 3410.03 for C<sub>158</sub>H<sub>284</sub>N<sub>26</sub>O<sub>54</sub>; found, 3435.08 for [M + Na]<sup>+</sup>.

*Synthesis of the polyamine backbone of DexAM (5) (Figure 2.15)*

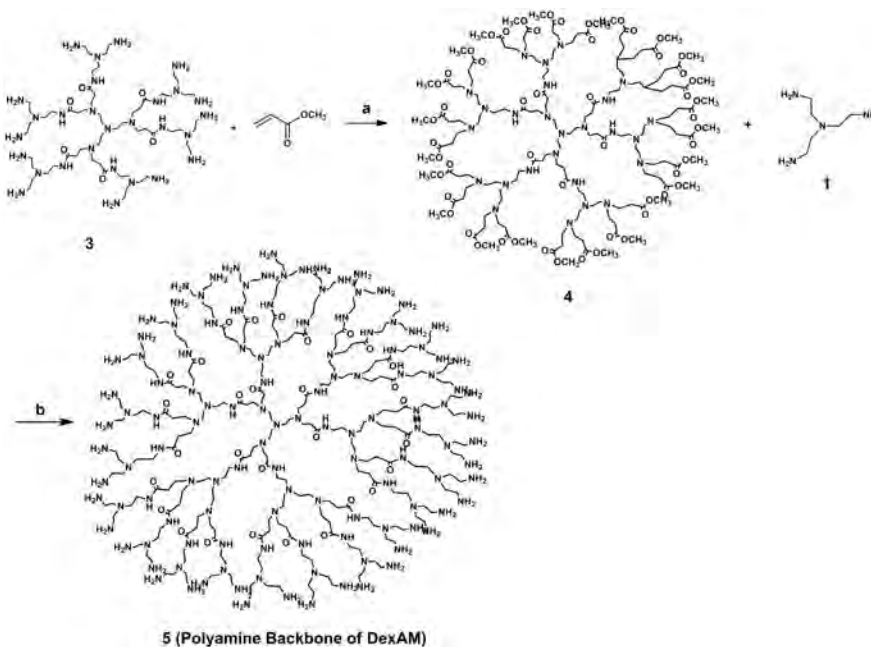


Figure 2.15: Second Round of Micheal Addition and Amidation, a) MeOH, 0°C, 1 h, RT, 60 h, b) MeOH, 0°C, 1 h, RT, 7 days.

A solution of ester 4 (3.41g, 1 mmol) in methanol (20 mL) was added dropwise to a stirred solution of tris(aminoethyl)amine (1, 7.02 g, 48 mmol) in methanol (20 mL) over a period of 1 h in an ice bath. The resulting solution was allowed to warm to room temperature and stirred for 7 days at room temperature at which time no methyl ester was detectable by NMR spectroscopy. The solvent was removed under reduced pressure the excess tris(aminoethyl)amine was removed using an azeotropic mixture of toluene:MeOH (90:10 v/v). The product was further purified by washing with anhydrous ether twice, yielding a highly viscous liquid. Finally the product was kept under vacuum to provide the amino-terminated final product (5) as a light yellow liquid. Yield (6.1 g, 99%); NMR (300 MHz, CDCl<sub>3</sub>):  $\delta$  1.25 (s, J=6.0 Hz, 24H), 2.44 (t, J=6.9 Hz, 12H), 2.48 (m, J=8 Hz, 72H), 2.74 (t, J=6.9 Hz, 12H), 3.25 (t, 12H), 8.0 (s, 6H). MS (m/z): calculated, 6151.06 for C<sub>276</sub>H<sub>618</sub>N<sub>124</sub>O<sub>30</sub>; found, 6177.66 for [M + Na]<sup>+</sup>.

*Synthesis of mono-tosylated cyclodextrin (7) (Figure 2.16)*

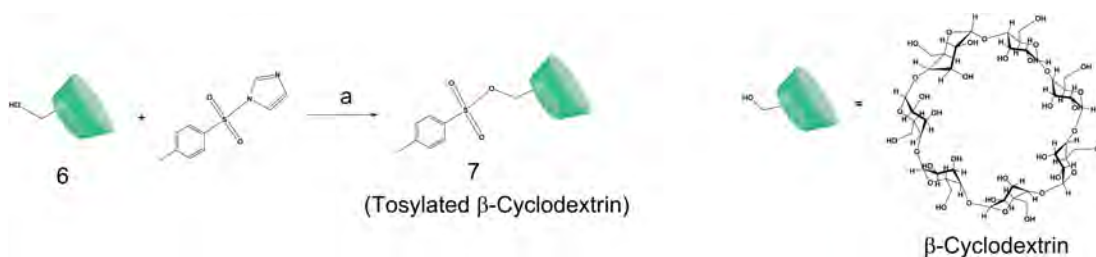


Figure 2.16: Synthesis of mono-tosylated cyclodextrin.

$\beta$ -cyclodextrin (6, 8.75 g, 7.71 mmol) and tosylimidazole (2.22g, 10.0 mmol) was dissolved in 88 ml deionized water. The solution was vigorously stirred for 4 h at room temperature. Aqueous NaOH solution (1% (w/v), 10.0 ml) was gradually added to the solution and stirred for an additional 10 min. The insoluble solid was filtered off and the filtrate was collected. The filtrate was neutralized to pH 7 using NH<sub>4</sub>Cl to induce precipitation. The precipitate was then collected by filtration, washed with cold water (25 ml 3) and with acetone (25 ml 4). The solid was dried in a drying oven at 60°C under vacuum (10 mm Hg) overnight to yield 7 as a white solid (4.5 g, 51% yield). <sup>1</sup>H NMR (300 MHz, DMSO-d<sub>6</sub>),  $\delta$  7.72 (d, J=8.4 Hz, 2H), 7.41 (d, J = 8.4 Hz, 2H), 5.605.89 (m, 14H), 4.754.81 (m, 7H), 4.154.62 (m, 6H), 3.453.72 (m, 28H), 3.153.47 (m, 24H), 2.41 (s, 3H). MS (m/z): calculated, 1,288.4 for C<sub>49</sub>H<sub>76</sub>O<sub>37</sub>S; found, 1,311.5 for [M + Na]<sup>+</sup>.

Synthesis of water-soluble CD-Polyamine tosylate (8) (Figure 2.17)

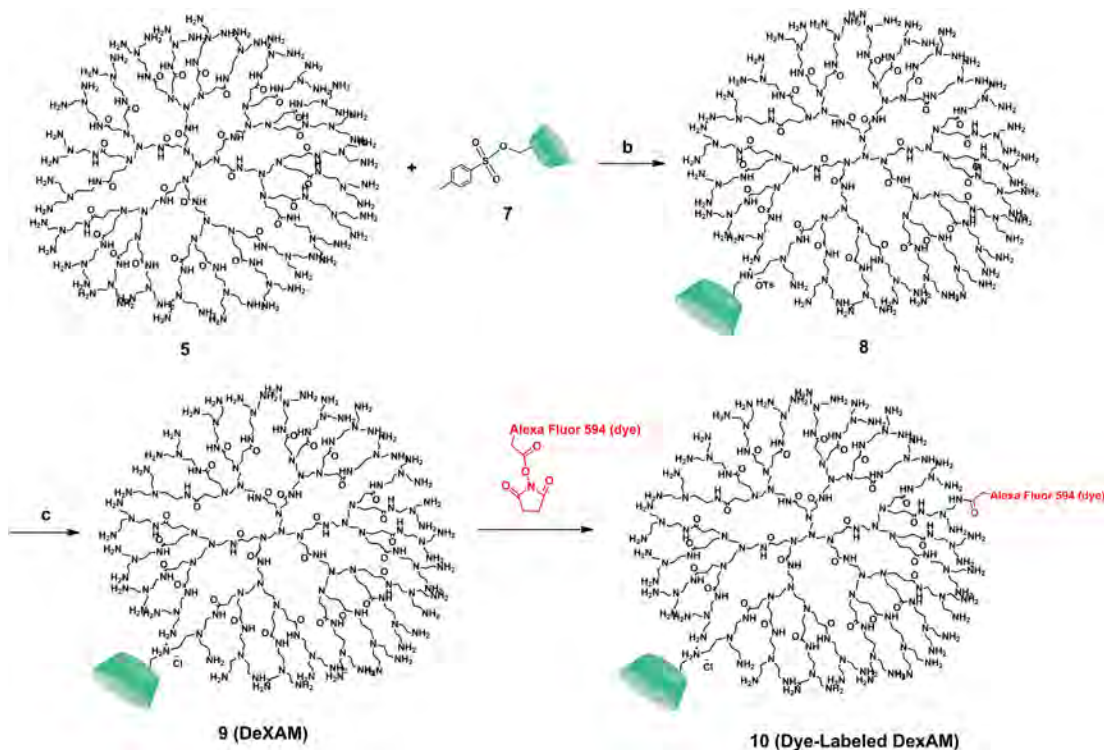


Figure 2.17: Conjugation of  $\beta$ -CD to the Polyamine Backbone, a) ddH<sub>2</sub>O, RT, 4h / 1 % NaOH, 10min/NH<sub>4</sub>Cl, b) DMF, 90°C, 48h, c) Amberlite IRA900.

Tosylated  $\beta$ -CD (7, 1.29g, 1mmol) and polyamine of DexAM 4 (5, 6.1g, 1 mmol) were dissolved in DMF (10 mL) in a 25 mL one-necked round-bottomed flask equipped with Liebig's condenser and a stir bar. The flask was degassed and purged with nitrogen. The mixture was stirred and refluxed at 90 °C for 48 h. The reaction mixture was cooled down to room temperature and product precipitated out by the addition of acetone (20 mL). The precipitate was collected by filtration, washed with acetone and dried overnight at 60°C in a vacuum oven (10 mm Hg) to yield 8 as a brown solid. Yield: (6.6g, 89%); <sup>1</sup>H NMR (300 MHz, DMSO-d<sub>6</sub>),  $\delta$  1.25 (s, J=6.0 Hz, 24H), 2.41 (s, 3H), 2.44 (t, J=6.9 Hz, 12H), 2.48 (m, J=8 Hz, 72H), 2.74 (t, J=6.9 Hz, 12H), 3.153.47 (m, 24H), 3.25 (t, 12H), 3.453.72 (m, 28H), 4.154.62 (m, 6H), 4.754.81 (m, 7H), 5.605.89 (m, 14H), 7.21 (d, J = 8.4 Hz, 2H), 7.52 (d, J=8.4 Hz, 2H), 8.0 (s, 6H). MH+7444.84 or 8733.01

*Anion exchange reaction for obtaining DexAM (9)*

CD-polyamine tosylate (8, 3.72g, 0.5 mmol) was dissolved in 40 mL deionized water. A 50 mL solid-phase synthesis vessel was packed with Amberlite IRA-900 ion-exchange resin to about half the vessel volume. The solution was transferred into the solid phase vessel. After 1 h, the eluent was collected and the water was distilled off under reduced pressure using a vacuum pump. The solid residue was dried overnight at 60°C in a vacuum oven (10 mm Hg) to yield 9 as a brown solid. Yield: (3.47g, 95%); <sup>1</sup>H NMR (300 MHz, DMSO-d<sub>6</sub>),  $\delta$  1.25 (s, J=6.0 Hz, 24H), 2.41 (s, 3H), 2.44 (t, J=6.9 Hz, 12H), 2.48 (m, J=8 Hz, 72H), 2.74 (t, J=6.9 Hz, 12H), 3.153.47 (m, 24H), 3.25 (t, 12H), 3.453.72 (m, 28H), 4.154.62 (m, 6H), 4.754.81 (m, 7H), 5.605.89 (m, 14H), 8.0 (s, 6H). MH+7309.10 or 8462.53.

*Conjugation of Alexa-Fluor 594 dye to DexAM 4 (10)*

Alexa-Fluor<sup>®</sup>594 dye (100 nM, Molecular Probes) and DeXAM 4 (9, 100 nM) were dissolved in PBS buffer solution (0.5 mL). The reaction mixture was allowed to vortex for 5 minutes. After being vortexed, the mixture was shaken at room temperature for 3 h.

**Inclusion of retinoic acid (RA) into DexAM**

Retinoic acid (RA) was solubilized in 2 molar equivalents of DexAMs in distilled water. Briefly, 7.3 mg of RA was added to a solution of 370 mg of DexAM in 3 mL of water, heated until fully dissolved, stirred for 8 h, and then rapidly cooled on ice to room temperature. This solution was filtered and freeze-dried. Thereafter, 200  $\mu$ L PBS was added to DexAM complex (10  $\mu$ mol) and allowed to stand at room temperature to dissolve for a few minutes. Finally, the complex was purified through by centrifugal filtration using an appropriate MWCO membrane. DexAM-RA solutions of various concentrations were prepared by maintaining the molar ratio between RA and DexAMs (Figure 2.18).

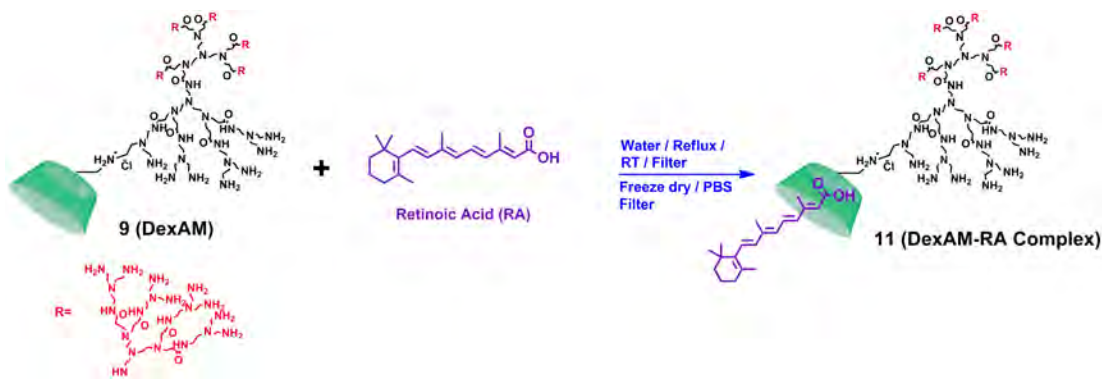


Figure 2.18: Inclusion of RA into DexAM.

### Formation of polyplexes between siRNA and DexAM

siRNA complexation: DexAM/siRNA complexes were prepared by adding equal volumes of DexAM solution (DexAM dissolved in dH<sub>2</sub>O) and siRNA (dissolved in water) at varying different concentrations. The resultant solution was then incubated for 30 min at room temperature before transfection (Figure 2.19). The GFP siRNA sequence was: Antisense 5-CCAACGACAUCAGCGACUAUU-, Sense 3-UUGGUUGCUGUAGUC-GCUGAU-5. The SOX9 siRNA sequence was Antisense 5-AACGAGAGCGAGAAGA-GACCC-3, Sense 3-TTGCUCUCGCUCUUCUCUGGG-5.

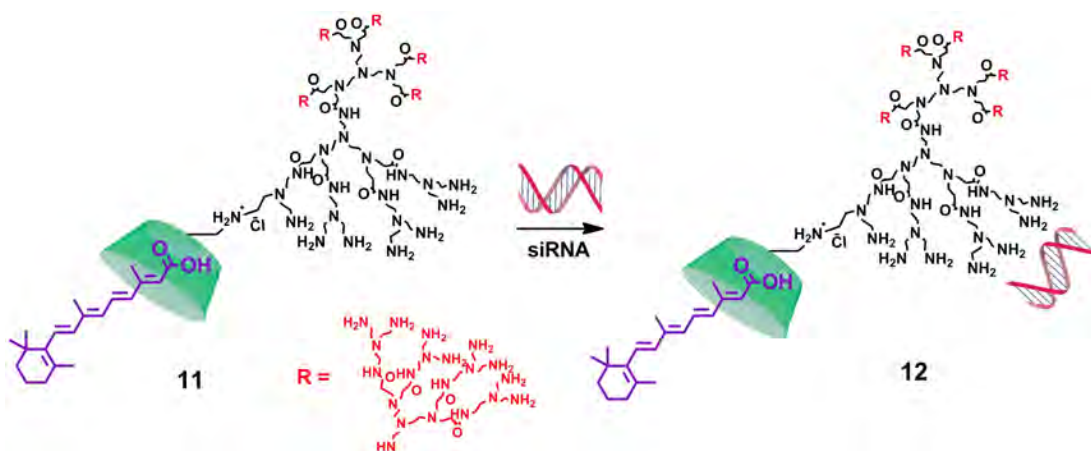


Figure 2.19: Polyplex formation of DexAM and siRNA.

### **Neural stem cell culture and differentiation**

Rat neural stem cell line (Millipore) were purchased and routinely expanded according to the manufactures protocol. The NSCs were maintained in laminin (Sigma, 20  $\mu\text{g}/\text{ml}$ ) coated culture dishes precoated with poly-L-lysine (10  $\mu\text{g}/\text{ml}$ ) in Millitrace media (Millipore) supplemented with the antibiotics, penicillin and streptomycin (Life Technologies), in the presence of basic fibroblast growth factor (bFGF-2, 20 ng/ml, Millipore). All of the cells were maintained at 37°C in a humidified atmosphere of 5% CO<sub>2</sub>. For consistency, the experiments were carried out on cells between passages 2 and 5. Neural differentiation was initiated by changing the medium to basal medium (without bFGF-2). The cells were allowed to differentiate for 6 days with the basal medium in each being exchanged every other day.

### **Cell viability assay**

The percentage of viable cells was determined by MTS assay following standard protocols described by the manufacturer. All experiments were conducted in triplicate and averaged. The quantification of cytotoxicity was done using MTS assay after incubating cells in the presence of the DexAM complexes.

### **Immunocytochemistry**

To investigate the extent of neuronal differentiation, at Day 6, the basal medium was removed and the cells fixed for 15 minutes in Formalin solution (Sigma) followed by two PBS washes. Cells were permeabilized with 0.1% Triton X-100 in PBS for 10 minutes and non-specific binding was blocked with 5% normal goat serum (NGS, Life Technologies) in PBS for 1 hour at room temperature. To study the extent of neuronal differentiation the primary mouse antibody against TuJ1 (1:500, Covance) and primary rabbit antibody against MAP2 (1:100, Cell Signaling) was used and for glial differentiation the primary rabbit antibody against GFAP (1:300, Dako) was used. The fixed samples were incubated overnight at 4°C in solutions of primary antibodies in PBS containing 10% NGS. After washing three times with PBS, the samples were incubated

for 1 h at room temperature in solution of anti-mouse secondary antibody labeled with Alexa-Fluor<sup>®</sup>647 and anti-rabbit secondary antibody labeled with Alexa-Fluor<sup>®</sup>546 (1:200, Life Technologies), Hoechst 33342 (1:500, Life Technologies) in PBS containing 10% NGS to observe neuronal and glial differentiation. After washing the samples thrice with PBS, the substrates were mounted on glass slides using ProLong<sup>®</sup>Gold antifade (Life Technologies). The mounted samples were imaged using Nikon TE2000 Fluorescence Microscope. ImageJ (NIH) was used for comparative analysis and quantifying the cells expression TuJ1 and GFAP.

## Chapter 3

### Manipulating Surface Chemistry to Enhance Neuronal Differentiation of Neural Stem Cells

In previous chapter, we used nanomaterials to deliver siRNA and small molecules (soluble cues) into brain tumor cells and NSCs. Solution-based transfections were used in both cases. In this chapter we will see the application of nanotechnology and surface modification for enhancing neuronal differentiation of NSCs using insoluble cues. We will see that the nanomaterials used form a part of the extracellular matrix (ECM) and thus impact the behavior of NSCs. We will see the impact of nanotopography on the delivery of siRNA into NSCs. We will then see how micropatterns of the ECM proteins affect stem cell differentiation and how they can be utilized to control differentiation. Finally, we will see the emerging impact of novel nanomaterials in stem cell biology and how they can affect the behaviors of stem cells.

### 3.1 Nanotopography-mediated Reverse Uptake of siRNA for Enhancing Neuronal Differentiation of Neural Stem Cells

#### 3.1.1 Introduction

One of the critical barriers to harnessing the full therapeutic potential of stem cells is the development of an easy, effective, and non-toxic methodology to control differentiation into specific cell lineages. Stem cell differentiation can be controlled by modulating key gene expression levels or signaling pathways within the cell, which has been achieved by several conventional gene delivery methods [3, 165–168]. For example, RNA interference (RNAi) for controlling gene expression levels using siRNA or miRNA is emerging as an important tool in stem cell biology [139, 140, 169]. For the successful genetic manipulation of stem cells, the cells must typically maintain their viability for an extended period of time after single or multiple siRNA transfections, without affecting the intrinsic cellular functions. However, many of the conventional methods used to deliver siRNA into stem cells, including lipid-based transfections, cationic polyplexes, viral vectors and electroporation techniques, result in significant cytotoxicity and undesirable side-effects [146, 170–172]. This presents a considerable challenge for achieving robust and reliable siRNA delivery into stem cells to control their differentiation into the desired cell lineages.

One of the most common methods to deliver siRNA into stem cells is solution-mediated delivery (or forward transfection), wherein the siRNA is added directly to the culture media above the seeded cells. In this approach, exogenous chemical materials are generally used to enhance cellular internalization of the siRNA. The most widely used exogenous materials include non-viral cationic lipids (such as Lipofectamine2000) [173, 174] and cationic polymers (such as PEI) [146, 167, 168, 175], which tend to condense the negatively charged siRNA to form complexes that can be readily taken up by the cell. While this approach has been found to facilitate siRNA delivery into a variety of cell types including stem cells, these exogenous materials tend to be cytotoxic and thereby need to be removed after a certain incubation period. Moreover, global gene expression studies using cDNA microarray technologies have even revealed inadvertent,

nonspecific changes in gene expression within the target cells after treatment with cationic lipid and polymer-based gene delivery systems [176,177]. Such undesired side-effects can greatly exacerbate, attenuate or even mask the desired genetic change, while also compromising the ability of stem cells to proliferate, migrate and differentiate [1,148,178,179]. Therefore, there are several limitations associated with the solution-mediated delivery methods for manipulating gene expression within stem cells [180].

While most studies have aimed to improve the efficiency of siRNA delivery by trying to improve the delivery vehicle, modulating the cellular microenvironment is an attractive means to achieve superior transfection efficiency. In turn, increasing attention has been given to substrate-mediated delivery (or reverse transfection), wherein the cells directly uptake the gene vector from the underlying substrate [181–184]. This approach has been found to result in greater internalization and functional expression of the gene vectors (i.e. DNA plasmids) compared to forward transfection [182]. However, up to now, these approaches have relied on using cationic lipids or polymers to complex the gene vector prior to immobilizing on the substrate, in turn suffering from issues with cytotoxicity and nonspecific changes in gene expression. Substrate-mediated methods which do not utilize cationic materials have also been successful at delivering biomolecules into cells [185–188]. However, the cell survival on such substrates for extended periods, which is especially important for advancing stem cell therapies, is critically important and less explored. Therefore, there is a necessity to develop a non-toxic and efficient strategy for delivering siRNA into stem cells to control gene expression levels, such that we can maintain the biological functions of stem cells for extended periods of time and efficiently control their differentiation into specific cell types.

In an effort to address these limitations, herein we demonstrate a nanotopography-mediated reverse uptake (NanoRU) platform for delivering siRNA into neural stem cells (NSCs) in a non-toxic and highly effective manner. The importance of nanotopography in modulating cell behavior (including adhesion, morphology, proliferation and differentiation) has become increasingly evident in recent years [189,190]. Yet,

there are limited studies which report on the influence of nanotopography in facilitating cellular endocytosis, and in turn non-viral transfection [191,192]. In one such study, fibroblast and mesenchymal stem cells grown on nanotopographical patterned surfaces were shown to have enhanced endocytosis of gene plasmids, compared to unpatterned surfaces [192]. Nevertheless, while the cells were grown on the nanotopography, the gene vectors were still delivered through solution-mediated approaches (i.e. complexing with cationic polymers/lipids). Given that NSCs are known to be highly sensitive to nanotopographical and physical cues [111,193,194], we believe nanotopography can play a critical role in modulating siRNA uptake via substrate-mediated delivery. Our NanoRU platform was fabricated by assembling monodisperse nanoparticles on a glass substrate, which served to generate the desired nanotopographical features in the cellular microenvironment (Figure 3.1)

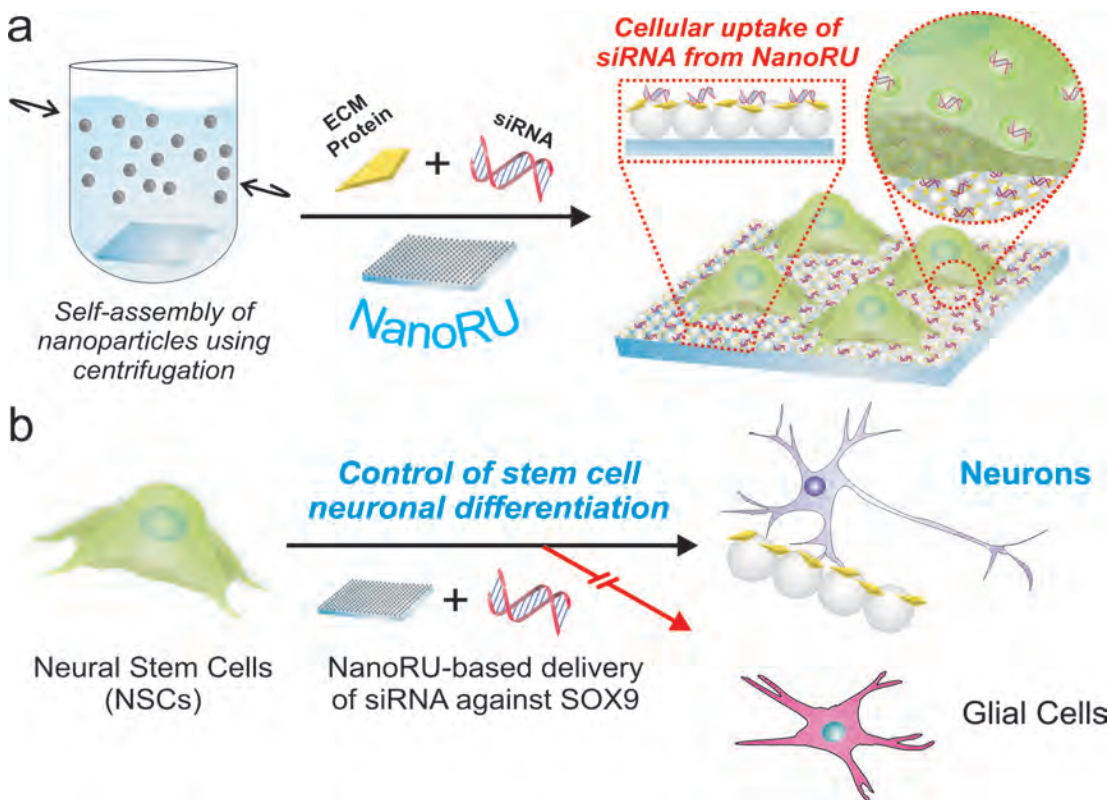


Figure 3.1: Schematic diagram depicting the application of NanoRU. (a) The cellular uptake of siRNA into NSCs from NanoRU coated with ECM protein and siRNA molecules. (b) The delivery of siRNA against the SOX9 transcription factor using NanoRU to promote neuronal differentiation of NSCs [145].

As a proof-of-concept, we studied the interaction of NSCs with different sizes of nanoparticles and identified an optimal nanoparticle size that facilitated the highest uptake of siRNA by the NSCs. To accomplish this, we assessed the efficiency of RNAi by examining the suppression of green fluorescent protein (GFP) in NSCs that were genetically modified to express GFP. Based on the GFP knockdown, we then utilized the optimized NanoRU to specifically knockdown the expression of a neural switch gene, SOX9, which resulted in significantly enhanced neuronal differentiation of NSCs. Thus, NanoRU relies upon the nanotopographical features of the extracellular microenvironment to deliver siRNA into NSCs, without using exogenous delivery vehicles. In particular, this novel siRNA delivery approach does not require the use of cationic transfection agents, which are generally cytotoxic to stem cells. In addition to stem cells, we further demonstrate that NanoRU can be successfully applied to deliver siRNA into various other cell lines. However, we utilize NSCs as a model cell line in order to establish NanoRU as a simple, biocompatible and efficient platform for stem cells, which are known to be much more sensitive and prone to cytotoxicity by the conventional non-viral systems used for the delivery of genetic material [147]. In turn, we used NanoRU not only to deliver siRNA into NSCs, but also to ensure the long-term survival and differentiation of the transfected NSCs.

As a proof-of-concept, we studied the interaction of NSCs with different sizes of nanoparticles and identified an optimal nanoparticle size that facilitated the highest uptake of siRNA by the NSCs. To accomplish this, we assessed the efficiency of RNAi by examining the suppression of green fluorescent protein (GFP) in NSCs that were genetically modified to express GFP. Based on the GFP knockdown, we then utilized the optimized NanoRU to specifically knockdown the expression of a neural switch gene, SOX9, which resulted in significantly enhanced neuronal differentiation of NSCs. Thus, NanoRU relies upon the nanotopographical features of the extracellular microenvironment to deliver siRNA into NSCs, without using exogenous delivery vehicles. In particular, this novel siRNA delivery approach does not require the use of cationic transfection agents, which are generally cytotoxic to stem cells. In addition to stem cells, we further demonstrate that NanoRU can be successfully applied to deliver siRNA into

various other cell lines. However, we utilize NSCs as a model cell line in order to establish NanoRU as a simple, biocompatible and efficient platform for stem cells, which are known to be much more sensitive and prone to cytotoxicity by the conventional non-viral systems used for the delivery of genetic material.[39] In turn, we used NanoRU not only to deliver siRNA into NSCs, but also to ensure the long-term survival and differentiation of the transfected NSCs.

### 3.1.2 Results and Discussion

#### **Nanotopographical features determine siRNA-based gene knockdown in NSCs**

To study the effect of nanotopographical features on the efficiency of siRNA transfection and gene knockdown in the GFP-labeled NSCs, NanoRUs were fabricated by assembling monolayers of silica nanoparticles (SiNPs) ranging from 100 nm to 700 nm in diameter on bare glass substrates. The nanoparticles were assembled on the surface by centrifuging the glass substrates in a solution of positively-charged SiNPs [85]. This size-dependent study is critical because the nanotopographical features of the extracellular microenvironment have been shown to affect the adhesion and growth of stem cells, which in turn can influence the substrate-mediated delivery of genetic materials into stem cells [190, 191, 195, 196]. For our initial studies, siRNA targeting GFP was selected to assess the efficiency of siRNA delivery and GFP knockdown in the NSCs. After nanoparticle assembly, the NanoRUs were coated with a solution of laminin (10  $\mu\text{g}/\text{mL}$ ) and siRNA molecules (1  $\mu\text{M}$ ) against GFP. Laminin is a well-established extracellular matrix (ECM) protein that binds to the integrin receptors on the surface of the NSCs, and is an essential ECM component for the adhesion, growth, and differentiation of NSCs [197, 198]. Negatively-charged siRNA molecules and laminin condensed together on the positively-charged SiNPs. After 4 h, the solution was removed and NSCs were then seeded on these NanoRUs (Figure 3.2a).

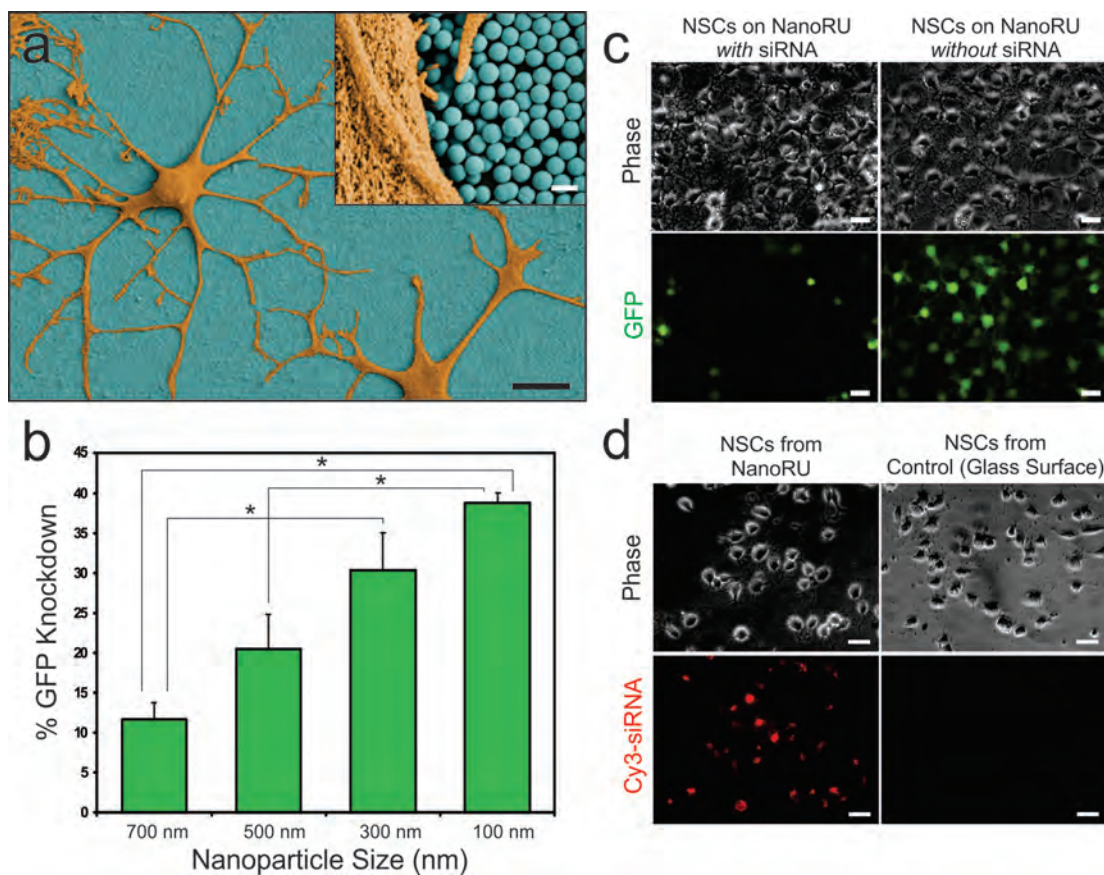


Figure 3.2: Characterizing cellular uptake of siRNA from NanoRU. (a) Scanning electron microscopy (SEM) image of NSCs on NanoRU. The NSCs (orange) and the NanoRU (blue) in the SEM image have been pseudocolored to enhance the contrast. Scale bar: 10  $\mu\text{m}$ . Inset: Magnified view. Scale bar: 500 nm. (b) Quantitative comparison of the percentage of GFP knockdown in NSCs on NanoRU containing nanoparticles ranging in size from 100-700 nm. Analysis of variance (ANOVA) was used for evaluating the statistical significance of GFP knockdown ( $* = P < 0.05$ ). (c) Phase and fluorescence images of NSCs on NanoRU with and without GFP siRNA. Scale bars: 20  $\mu\text{m}$  (d) Left column: Phase contrast and fluorescence image of NSCs grown on NanoRU coated with Silencer<sup>®</sup> Cy3-labeled control siRNA, and then reseeded in a 24-well plate. Right column: Phase image and fluorescence image of NSCs grown on a control substrate (bare glass surface without nanofeatures) coated with Silencer<sup>®</sup> Cy3-labeled control siRNA, and then re-seeded into a 24-well plate. Scale bars: 20  $\mu\text{m}$ . [145].

After 72 h, the NanoRUs were imaged using a fluorescence microscope and the knockdown of GFP in the NSCs was quantified. Interestingly, we observed a size-dependent knockdown of GFP in the NSCs, wherein the 100 nm SiNPs showed the highest knockdown and the 700 nm particles showed the lowest knockdown (Figure 3.2b). These results were normalized with the fluorescence from NSCs on control substrates

having no SiNPs (i.e. absence of nanotopography). The control substrates (without the SiNP monolayer) had a positively-charged surface, which was prepared by functionalizing glass substrates with self-assembled monolayers (SAMs) of 3-Aminopropyltrimethoxy silane (APTES) and subsequently coating them with the same concentrations of siRNA and laminin. To further substantiate that the siRNA uptake and gene knockdown was due to the differences in the nanotopographical features and not due to the differences in the amount of siRNA bound, we performed the Picogreen<sup>®</sup> assay to quantify the amount of siRNA bound to NanoRUs. From the Picogreen<sup>®</sup> assay, we confirmed that the amount of siRNA bound to all the NanoRUs (100-700 nm and control substrates) was around 30%, thus confirming that the siRNA uptake and gene knockdown was indeed due to the nanotopographical features on the NanoRUs. Given that the NanoRU fabricated using 100 nm SiNPs resulted in maximum GFP knockdown, all of the subsequent experiments were carried out using NanoRU with 100 nm SiNPs.

### **NanoRU delivers only siRNA into NSCs and not SiNPs**

Another important aspect that needed to be investigated was whether the SiNPs were being taken up along with the siRNA. To this end, we used SiNPs labeled with Alexa-Fluor<sup>®</sup>594 dye to generate nanotopographical features on glass substrates. We then deposited siRNA against GFP on the dye-labeled NanoRUs. After 36 h of incubation, the NSCs were detached gently from the NanoRU using the enzyme Accutase, and regrown in a 24-well plate. We did not observe any fluorescence (from the dye-labeled SiNPs) within the transfected NSCs. However, we observed a clear GFP knockdown due to the siRNA delivered into the NSCs (Figure 3.2c). We further used transmission electron microscopy (TEM) to confirm that the SiNPs are not taken up by the NSCs (Figure 3.3). We then confirmed the uptake and localization of siRNA from NanoRU using the Silencer<sup>®</sup> Cy3-labeled negative control siRNA (Ambion), which showed remarkably higher fluorescence compared to the control substrates (Figure 3.2d). This experimental data clearly indicates that the stem cells take up only siRNAs, and not SiNPs. We believe that this unique feature, where only the siRNA is taken up by the

NSCs, makes NanoRU particularly advantageous over conventional transfection methods for stem cell research.

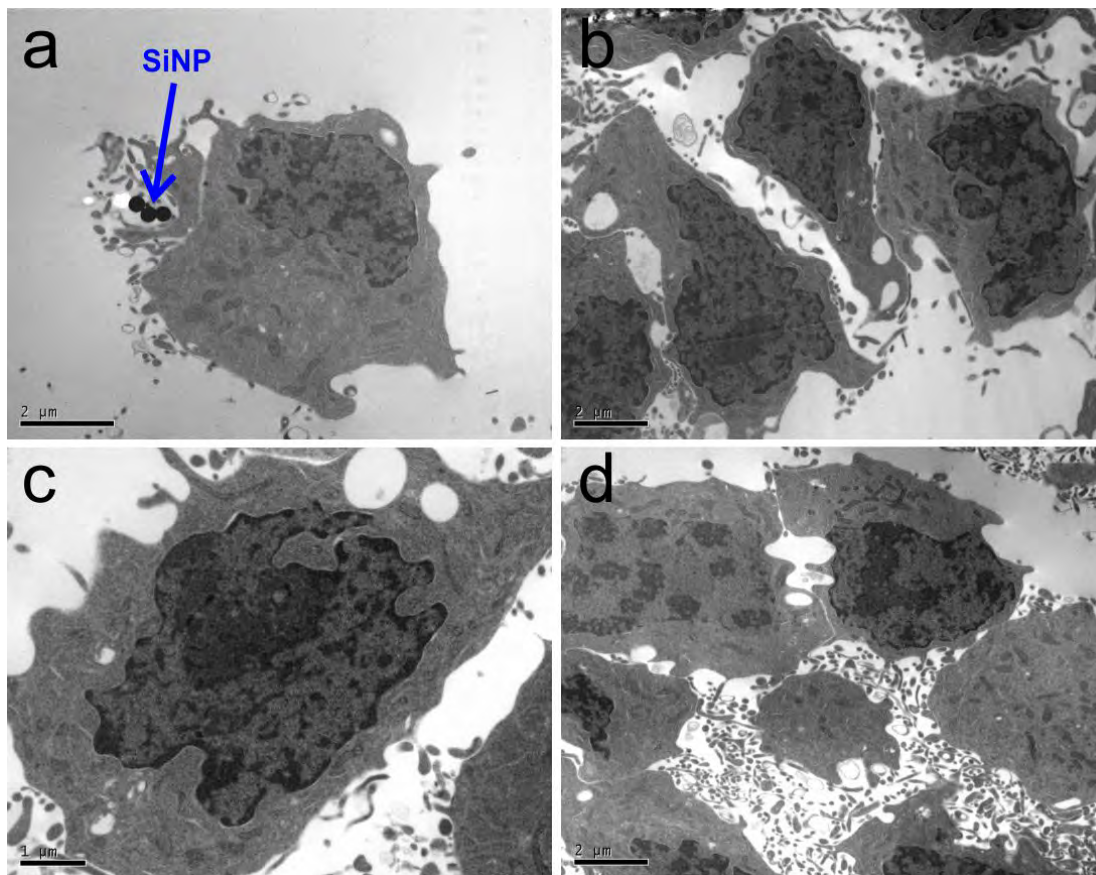


Figure 3.3: Transmission Electron Microscopy (TEM) to confirm SiNPs are not taken up by the NSCs. (a) and (b) TEM of NSCs seeded on NanoRU containing 300 nm SiNPs. The blue arrow shows the presence of SiNPs outside of the cell. (c) and (d) TEM of NSCs seeded on NanoRU containing 100 nm SiNPs [145].

We further sought to investigate the mechanism involved in the uptake of siRNA from NanoRU. ECM proteins such as laminin, fibronectin and collagen pre-adsorbed on surfaces have been previously implicated in enhancing gene delivery through endocytosis [195, 199, 200]. Gene delivery in such systems depended primarily upon caveolae- than clathrin-mediated endocytosis [199]. Caveolae-mediated endocytosis is known to be more efficient as it is able to circumvent the degradative lysosomal pathway [201]. To confirm if the dominant endocytic pathway involved in the uptake of siRNA by the NSCs cultured on NanoRU was indeed caveolae-mediated endocytosis, we treated the NSCs with 100 μM of indomethacin (10 min), a specific inhibitor of caveolae-mediated

endocytosis. We also treated the NSCs with a mixture of 10 mM sodium azide and 5 mM 2-Deoxy-D-glucose (10 min) as this mixture inhibits all endocytotic pathways within the NSCs. After 72 h, we observed a 13% knockdown of GFP in NSCs treated with Indomethacin and a 7% knockdown in NSCs treated with the mixture of sodium azide and 2-Deoxy-D-glucose, which was significantly lower than the 40% knockdown observed in untreated NSCs (Figure 3.4). Collectively, our results imply that the uptake of siRNA using NanoRU relies mainly on the caveolae-mediated endocytosis. However, there may be multiple pathways involved in the uptake of siRNA from NanoRU, which are currently under investigation in our lab.

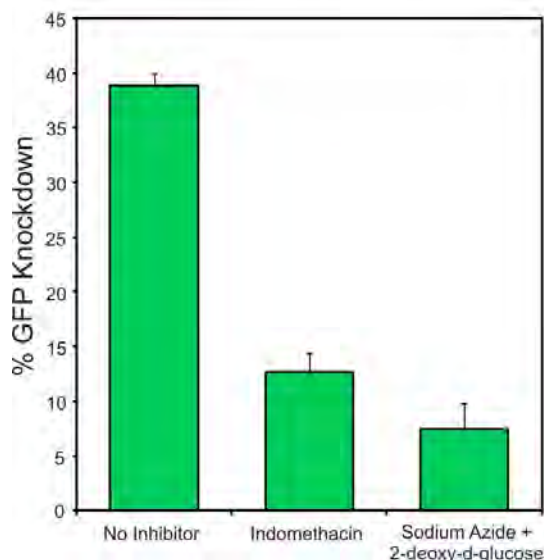


Figure 3.4: Effect of endocytosis inhibitors on GFP knockdown. Quantitative comparison of the percentage of GFP knockdown in the presence of endocytosis inhibitors, indomethacin and sodium azide plus 2-deoxy-d-glucose [145].

### Controlling neuronal differentiation of NSCs using NanoRU

Having demonstrated the efficiency of NanoRU by delivering siRNA against GFP, we focused on using NanoRU to enhance the neuronal differentiation of NSCs by suppressing the expression of a specific protein or gene. We used NanoRU to deliver siRNA against SOX9 (siSOX9), a well-established transcription factor which acts as a switch between neuronal and glial differentiation [158]. When the SOX9 gene is turned on, a higher percentage of NSCs differentiate into astrocytes (glial cells), and when turned off,

a higher percentage of NSCs differentiate into neurons [158, 159, 202]. To this end, we used NanoRU for the delivery of siRNA to turn off SOX9, wherein we coated NanoRU with laminin and siSOX9 following the experimental protocols we had established for knocking down GFP. The NSCs were then cultured on NanoRU. After 72 h, the knock-down of SOX9 was analyzed using RT-PCR and a significant decrease in the mRNA levels of SOX9 was observed (Figure 3.5a).

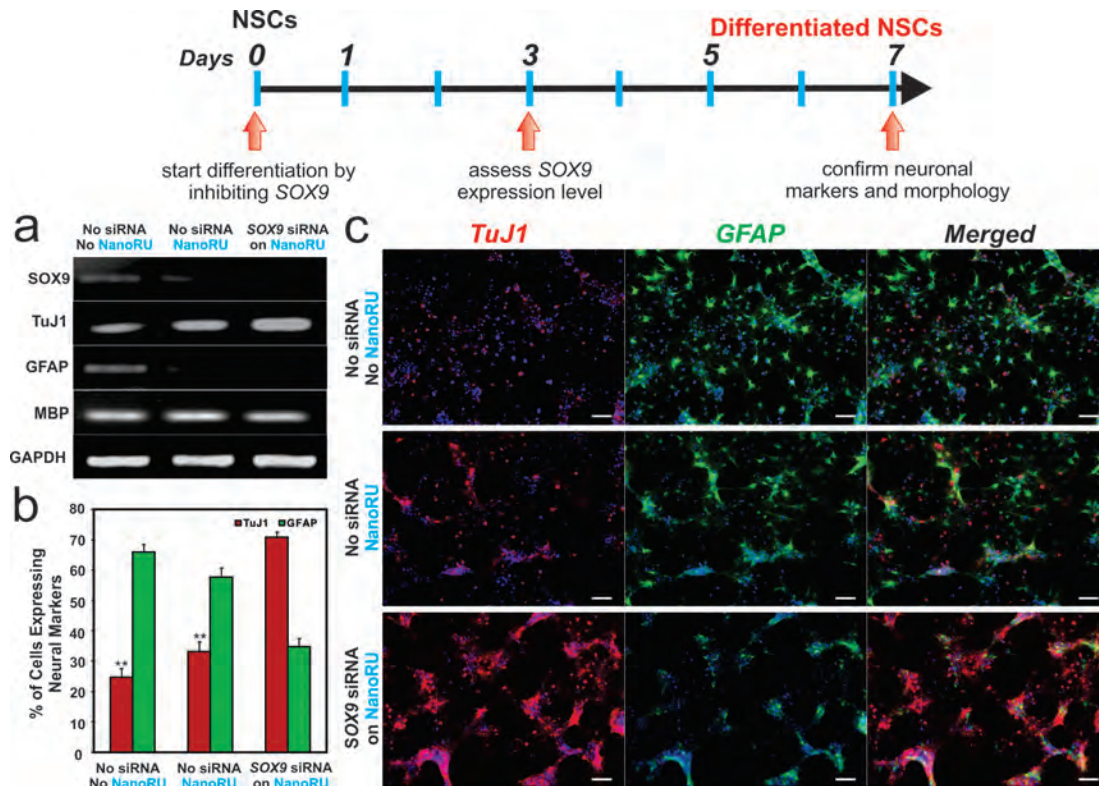


Figure 3.5: NSC differentiation on NanoRU coated with SOX9 siRNA (siSOX9). (a) RT-PCR analysis reveals differences in transcript levels for SOX9 and differentiation markers for neurons (TuJ1), astrocytes (GFAP) and oligodendrocytes (MBP) in the presence or absence of siSOX9 and/or NanoRU. (b) Quantitative comparison of the percentage of cells expressing TuJ1 and GFAP. Students unpaired t-test was used for evaluating the statistical significance for cells stained for TuJ1, compared to the siSOX9 on NanoRU condition (\*\* =  $P < 0.001$ ). (c) Fluorescence images of cells stained for the nucleus (blue), the neuronal marker TuJ1 (red, left column), the astrocyte marker GFAP (green, middle column) and merged (last column) show the extent of differentiation of NSCs grown on: no NanoRU nor siSOX9 coating (top row), NanoRU without siSOX9 coating (middle row), and NanoRU with siSOX9 coating (bottom row). Scale bars: 50  $\mu\text{m}$ . [145].

The NSCs were grown and differentiated on the NanoRU coated with the siSOX9 for

7 days. We then used RT-PCR to examine the expression levels of key neural markers (Figure 3.5a). A remarkable decrease in the expression of the glial marker, glial fibrillary acidic protein (GFAP), and an increase in the expression of the neuronal marker,  $\beta$ -III tubulin (TuJ1), was observed. No significant change was found in the expression of the oligodendrocyte marker, myelin-binding protein (MBP). We further confirmed and quantified our results by immunostaining for neuronal and astrocyte markers (Figure 3.5b and c). Compared to control substrates (substrates having no SiNPs), a remarkably higher percentage of NSCs differentiated into neurons on NanoRU coated with siSOX9 (Figure 3.5b). As expected, the number of astrocytes considerably decreased when SOX9 was knocked down. Neuronal differentiation was further confirmed by studying the co-localization of two different neuronal markers, TuJ1 and microtubule-associated protein 2 (MAP2) (Figure 3.6).

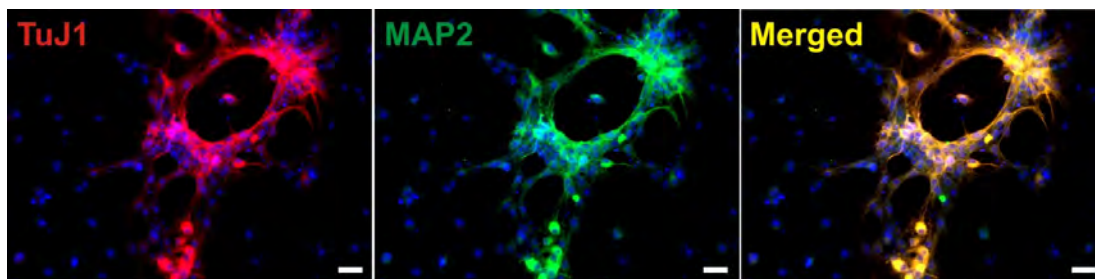


Figure 3.6: Colocalization of neuronal markers. Fluorescence images of NSCs grown on NanoRU coated with siSOX9, stained for the neuronal markers TuJ1 and MAP2. The merged image shows the co-localization of the two neuronal markers. Scale bars: 20  $\mu$ m. [145].

### NanoRU for delivering siRNA into other mammalian cells and miRNA into NSCs

After successfully demonstrating the proficiency of NanoRU for delivering siRNA into stem cells, we sought to explore the potential of using NanoRU as a platform for delivering siRNA into other mammalian cell lines. To this end, NanoRU was used to deliver Silencer<sup>®</sup> Cy3-labeled negative control siRNA into other mammalian cells such as astrocytes, brain cancer cells (U87-VIII), and breast cancer cells (SUM159). The cells were detached from NanoRU after 36 h, replated in 24 well plates, and then imaged

for siRNA uptake (Figure 3.7a and Figure 3.8). All of the cell lines showed the uptake of the dye-labeled siRNA from NanoRU, indicating that our technique is efficient and applicable to normal cells, cancer cells, as well as stem cells.

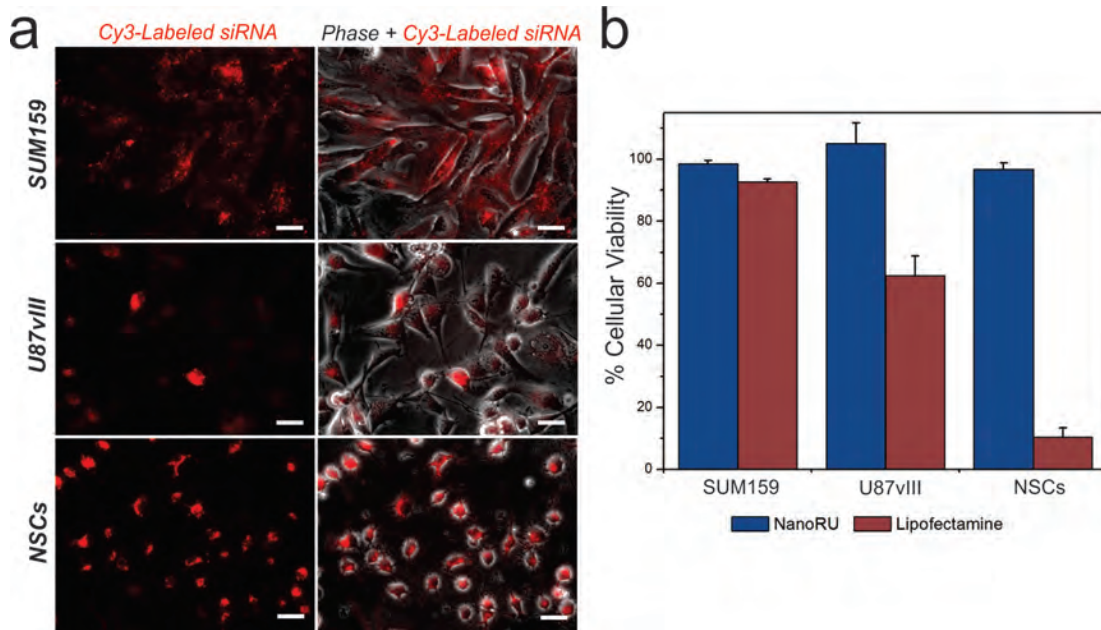


Figure 3.7: Cellular uptake of siRNA and cellular viability in different cell types. (a) Fluorescence (left column) and merged phase images (right column) of the Silencer<sup>®</sup> Cy3-labeled negative control siRNA from NanoRU in three cell lines: SUM159 (breast cancer cells), U87vIII (brain cancer cells) and rat NSCs (neural stem cells). Scale bars: 20  $\mu\text{m}$ . (b) MTS cellular viability of SUM159, U87vIII and NSCs grown on NanoRU [145].

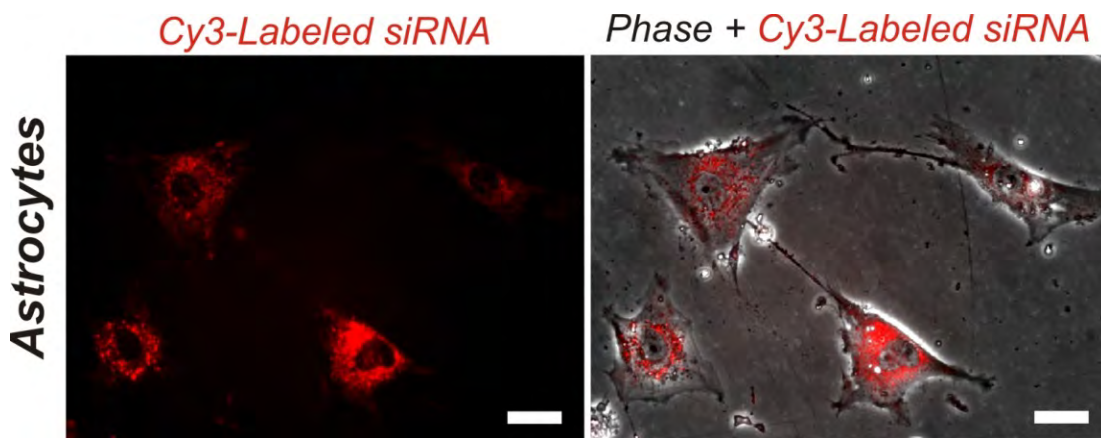


Figure 3.8: siRNA uptake within Astrocytes. Fluorescence and phase images depicting the cellular uptake of Silencer<sup>®</sup> negative control Cy3-labeled siRNA into human astrocytes. Scale bars: 20  $\mu\text{m}$ . [145].

Additionally, NanoRU can be easily extended to deliver miRNA, consisting of a larger number of nucleotide base pairs. We successfully delivered the Cy3-dye labeled Pre-miR<sup>®</sup> negative control (Ambion) using the same protocol that we used for delivering siRNA. The NSCs cultured on NanoRU coated with laminin and miRNA took up the miRNA in a highly efficient manner (Figure 3.9).

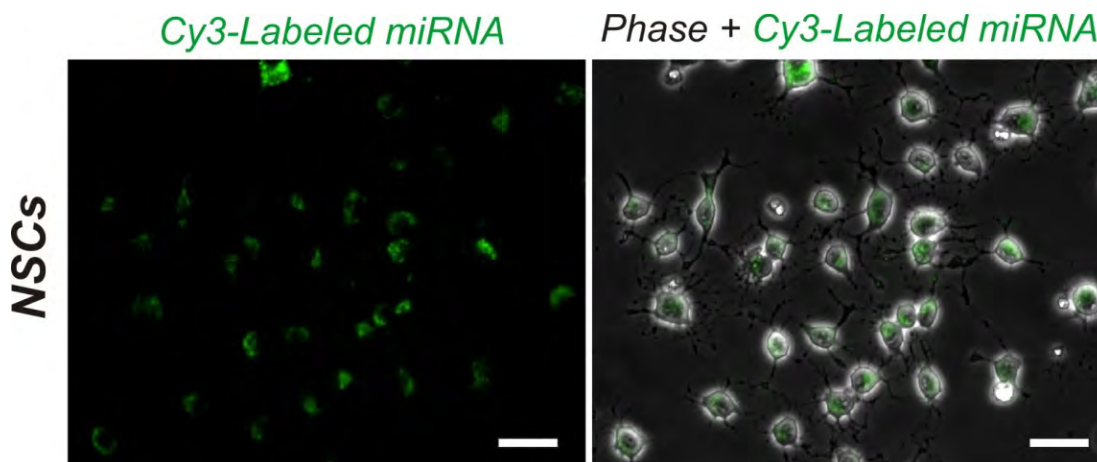


Figure 3.9: NanoRU for miRNA uptake. Fluorescence and phase images depicting the cellular uptake of Cy3-labeled miRNA (pseudocolored green) into rat neural stem cells. Scale bars: 20  $\mu\text{m}$ . [145].

### **NanoRU does not damage cell membranes and is non-toxic**

One of the biggest advantages of NanoRU is its biocompatibility and the fact that the transfection begins as soon as the cells are cultured on NanoRU, with the highest transfection observed at 36 h (Figure 3.10). On the other hand, most standard solution-mediated transfection protocols using cationic lipids and polymers require a wait period of at least 12-24 h before the cells can be transfected in order to minimize their toxicity. In addition, the serum proteins in the culture media are known to decrease the transfection efficiency due to the non-specific interaction of serum proteins with the delivery constructs [203].

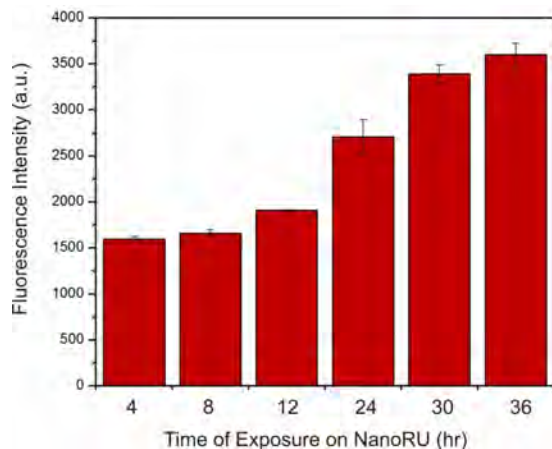


Figure 3.10: Time-dependent siRNA Uptake. Time-dependent uptake of Silencer negative control Cy3-labeled siRNA into rat neural stem cells [145].

We compared the cytotoxicity of NanoRU with a well-established lipid-based cationic transfection agent, Lipofectamine 2000<sup>®</sup> (Life Technologies) using the negative control siRNA in three different cell lines: SUM159, U87VIII and NSCs. The cytotoxic results were analyzed using a standard cell proliferation assay (MTS assay). Interestingly, we found that Lipofectamine2000<sup>®</sup>, while less toxic towards cancer cells, was extremely cytotoxic (using manufacturers recommended transfection condition) towards NSCs, which led to 95% cell death within 48 h of being transfected with the negative control siRNA (Figure 3.7b). NanoRU, on the other hand, was seen to be biocompatible with a minimal decrease in cell viability for all the cell lines tested. Moreover, we believe NanoRU does not cause any physical damage to the cell membranes as the NSCs showed high cellular viability and enhanced neuronal differentiation on NanoRU after an extensive period of 7 days. Hence, NanoRU can be especially useful for controlling NSC differentiation, a process which requires the NSCs to survive for more than seven days *in vitro*.

### 3.1.3 Conclusions

We have developed a novel nanotopography-mediated reverse uptake (NanoRU) platform, for the genetic manipulation of NSCs in a highly effective manner. This platform

was employed to control the neuronal differentiation of stem cells by using nanotopographical features to deliver siRNAs inside cells. We believe NanoRU and its application can significantly complement recent advances in research efforts to control stem cell differentiation based on physical cues such as patterns and bioactive scaffolds of ECM materials. Even though we have only explored proof-of-concept experiments involving genetic manipulation and differentiation of NSCs, we expect that NanoRU can be extended, with straightforward modifications of the aforementioned protocols, to a wide range of nanomaterials and biomolecules (e.g. miRNA, proteins, and small molecules). Finally, we believe NanoRU is a valuable platform which will complement conventional genetic manipulation tools in cell biology. For example, one of the key aspects behind stem cell-based therapies for many devastating diseases is to transplant stem cells or differentiated stem cells at the site of injury, after genetically manipulating them. The exogenous delivery vehicles used for siRNA delivery would be present within the stem cells and could trigger a strong immune response or tumor formation after stem cell transplantation. Therefore, our NanoRU-based siRNA delivery can potentially help overcome one of the critical barriers in stem cell-based tissue engineering.

### **3.1.4 Materials and Methods**

#### **NanoRU preparation**

Cover glass (Number 1, 22 mm x 22 mm; VWR) was cut equally into smaller pieces (18 mm x 6 mm) and sonicated in Nanopure water (18.2 mOhm) for 10 mins and then cleaned in piranha solution (a 3:1 mixture of sulphuric acid and hydrogen peroxide) for 10 min (Caution: Piranha solution is extremely corrosive). The glass coverslips were then washed again in Nanopure water (18.2 Mohm) and dried under a stream of pure nitrogen. To generate films of nanotopographical features, positively-charged (amine-terminated) silicon oxide nanoparticles (SiNPs, Corpuscular Inc) of different sizes were utilized. The washed cover slips were centrifuged at 2000 RPM for 2 min in a 2 mL eppendorf tube containing 25 mg/mL of the SiNP solution. The sizes used were 50 nm, 100 nm, 300 nm, 500 nm and 700 nm. The substrates were then washed with

Nanopure water and dried under a stream of pure nitrogen. For functionalization with (3-aminopropyl)triethoxysilane (APTES), the washed glass cover slips were left in a beaker containing 1% APTES solution in pure ethanol for 2 h. The cover slips were then rinsed thoroughly with ethanol and dried under nitrogen. They were then baked at 100 °C in an oven for 10 min.

### **Coating NanoRU with laminin and siRNA**

The NanoRUs were then coated with siRNA and laminin, both of which are negatively charged at in phosphate buffer saline (PBS, pH 7.4; Life Technologies). In a culture hood, NanoRUs were coated with a 10  $\mu\text{g}/\text{mL}$  solution of laminin containing 100 pmoles of the desired siRNA (against GFP or SOX9). The GFP siRNA sequence was: Antisense - 5-CCAACGACAUCAGCGACUAUU-3, Sense - 3-UUGGUUGCUGUAGUCGCUGA-U-5. The SOX9 siRNA sequence was Antisense - 5-AACGAGAGCGAGAAGAGACCC-3, Sense - 3-TTGCUCUCGCUCUUCUCUGGG-5. The solution was left on top of the NanoRUs for 3 h, and then simply removed by dipping the films once in sterile PBS. The negatively charged laminin and siRNA molecules simply condense on the positively charged NanoRU. The coated NanoRUs were then put into 12 well plates and 1 mL suspensions of NSCs were seeded with density of  $1.25 \times 10^5$  NSCs /ml of Millitrace media (Millipore) in the absence of growth factors such as basic fibroblast growth factor (bFGF). The NSCs were maintained in a humidified atmosphere at 37°C and 5% CO<sub>2</sub>. After 12 h, the films were transferred to new well plates to prevent non-specific attachment of the floating NSCs. The media was then changed every other day until Day 7. On Day 7, the cells were either fixed for immunocytochemistry or lysed for PCR analysis.

### **Rat neural stem cell (NSC) culture and differentiation**

Rat neural stem cell line (Millipore) were purchased and routinely expanded according to the manufactures protocol. The NSCs were maintained in laminin (Sigma, 20  $\mu\text{g}/\text{ml}$ ) coated culture dishes precoated with poly-L-lysine (10  $\mu\text{g}/\text{ml}$ ) in Millitrace media (Millipore) supplemented with the antibiotics, penicillin and streptomycin (Life

Technologies), in the presence of basic fibroblast growth factor (bFGF-2, 20 ng/ml, Millipore). All of the cells were maintained at 37°C in a humidified atmosphere of 5% CO<sub>2</sub>. For consistency, the experiments were carried out on cells between passages 2 and 5. Neural differentiation was initiated by changing the medium to basal medium (without bFGF-2) on the NanoRUs coated with laminin and siRNA. The cells were allowed to differentiate for 7 days with the basal medium in each being exchanged every other day.

### **Culturing U87-EGFRvIII, SUM159, and Astrocytes**

For each of the three non-stem cell lines, experiments were carried out on cells between passages 2 and 10. The NanoRU, coated with Silencer<sup>®</sup> Cy3-labeled negative control siRNA, were put into wells of a 12-well plate and each well containing the substrate was seeded with 80,000 cells. After 24 h, the substrates were moved into a new 12 well plate. The media components for U87-EGFRvIII cell line include DMEM (Dulbeccos modified Eagles medium) with high glucose (Invitrogen), 10% Fetal Bovine Serum (FBS), 1% streptomycin-penicillin, 1% glutamax (Invitrogen), and the selection marker, hygromycin B (30 µg/ml). The media components for SUM159 cell line include Hams F12 with insulin (5.0 µg/mL), hydrocortisone (1.0 µg/mL), 10 mM HEPES buffer, 5% Fetal Bovine Serum (FBS), 1% streptomycin-penicillin. The media components for the Astrocytes cell line DMEM with high glucose (Invitrogen), 10% Fetal Bovine Serum (FBS), 1% streptomycin-penicillin, 1% glutamax (Invitrogen).

### **Cell viability assays**

Cell viability of the above cell lines on NanoRU was compared with Lipofectamine 2000<sup>®</sup> (Life Technologies) for delivering Silencer<sup>®</sup> negative control siRNA (Ambion). The percentage of viable cells was determined by MTS assay following standard protocols described by the manufacturer. All experiments were conducted in triplicate and averaged. The quantification of cytotoxicity was done using MTS assay after incubating cells in the presence of the manufacturers recommended concentration of Lipofectamine 2000<sup>®</sup>. The data is represented as formazan absorbance at 490 nm, considering the

control (untreated) cells as 100% viable.

### **Immunocytochemistry**

To investigate the extent of neuronal differentiation, at Day 6, the basal medium was removed and the cells fixed for 15 minutes in Formalin solution (Sigma) followed by two PBS washes. Cells were permeabilized with 0.1% Triton X-100 in PBS for 10 minutes and non-specific binding was blocked with 5% normal goat serum (NGS, Life Technologies) in PBS for 1 hour at room temperature. To study the extent of neuronal differentiation the primary mouse antibody against TuJ1 (1:500, Covance) and primary rabbit antibody against MAP2 (1:100, Cell Signaling) was used and for glial differentiation the primary rabbit antibody against GFAP (1:300, Dako) was used. The fixed samples were incubated overnight at 4°C in solutions of primary antibodies in PBS containing 10% NGS. After washing three times with PBS, the samples were incubated for 1 h at room temperature in solution of anti-mouse secondary antibody labeled with Alexa-Fluor<sup>®</sup>647 and anti-rabbit secondary antibody labeled with Alexa-Fluor<sup>®</sup>546 (1:200, Life Technologies), Hoechst 33342(1:500, Life Technologies) in PBS containing 10% NGS to observe neuronal and glial differentiation. After washing the samples thrice with PBS, the substrates were mounted on glass slides using ProLong<sup>®</sup> Gold antifade (Life Technologies). The mounted samples were imaged using Nikon TE2000 Fluorescence Microscope. ImageJ (NIH) was used for comparative analysis and quantifying the cells expression TuJ1 and GFAP.

### **PCR analysis**

Total RNA was extracted using Trizol Reagent (Life Technologies) and the mRNA expression level of GFAP, MBP, SOX9 and TuJ1 were analyzed using Reverse Transcriptase PCR (RT-PCR) and quantitative PCR (qPCR). Specifically, cDNA was generated from 1 g of total RNA using the Superscript III First-Strand Synthesis System (Life Technologies). Analysis of mRNA was then accomplished using primers specific to each of the target mRNAs. RT-PCR reactions were performed in a Mastercycler Ep gradient S (Eppendorf) and images were captured using a Gel Logic 112 (Carestream) imaging

system. qPCR reactions were performed using SYBR Green PCR Master Mix (Applied Biosystems) in a StepOnePlus Real-Time PCR System (Applied Biosystems) and the resulting  $C_t$  values were normalized to GAPDH. Standard cycling conditions were used for all reactions with a melting temperature of 60°C. Primers are listed below in Table 3.1.

Table 3.1: Primers for PCR analysis

<b>Gene</b>	<b>F Primer</b>	<b>R Primer</b>	<b>Size (bp)</b>
<b>GAPDH</b>	5'-ATGACTCTACCCACGGCAAG-3'	5'-GGAAGATGGTGATGGGTTTC-3'	87
<b>GFAP</b>	5'-GAGAGAGATTCGCACTCAGTA-3'	5'-TGAGGTCTGCAAACCTGGAC-3'	89
<b>MBP</b>	5'-CACAAGAACTACCCACTACGG-3'	5'-GGGTGTACGAGGTGTCACAA-3'	103
<b>SOX9</b>	5'-AGGAAGCTGGCAGACCAGTACC-3'	5'-TCTCTTCTCGCTCTCGTTCA-3'	96
<b>TUJ1</b>	5'-ACTTTATCTTCGGTCAGAGTG-3'	5'-CTCACGACATCCAGGACTGA-3'	97

## 3.2 Controlling Differentiation of Neural Stem Cells Using Extracellular Matrix Protein Patterns

### 3.2.1 Introduction

The ability of stem cells to differentiate into specialized lineages within a specific microenvironment is vital for regenerative medicine. For harnessing the full potential of stem cells for regenerative therapies, it is important to investigate and understand the function of three types of microenvironmental cues - soluble signals, cell-cell interactions, and insoluble (physical) signals - that dynamically regulate stem cell differentiation [204–206]. Neural stem cells (NSCs) are multipotent and differentiate into neurons and glial cells [207,208], which can provide essential sources of engraftable neural cells for devastating diseases such as Alzheimers disease [209], Parkinsons disease [210–212] and spinal cord injury [213–215]. One of the major challenges involved in the differentiation of NSCs is to identify and optimize factors which result in an increased proportion of NSCs differentiating into neurons as opposed to glial cells. To this end, soluble cues such as brain-derived neurotrophic factor (BDNF) [216–218], sonic hedgehog (Shh) [219,220], retinoic acid (RA) [218], and neuropathiazol [221] have been shown to significantly increase neuronal differentiation of NSCs *in vitro*. However, the research toward studying the function of the other two microenvironmental cues (cell-cell interactions and insoluble cues) during the neuro-differentiation of NSCs is limited, mainly due to the lack of availability of methods for the investigation [193,222–224]. While various aspects such as cell-cell interactions [66], combinations of extracellular matrix (ECM) proteins [204,225], and physical properties of substrates have been shown to play a vital role in determining the fate of other adult stem cells such as mesenchymal stem cells (MSCs) [226–228], cardiac stem cells [229–231], and hematopoetic stem cells [232–234], little is known about the influence of such factors on the neuronal differentiation of NSCs. Therefore, there is a pressing need to develop methods for investigating the role of cell-cell interactions and insoluble signals in selectively inducing the differentiation of NSCs into specific neural cell lineages.

Herein, we demonstrate how ECM protein patterns can be used to investigate the effect of physical cues combined with cell-cell interactions on the differentiation of NSCs. Bio-surface chemistry combined with soft lithography was used to generate combinatorial patterns with varying geometries and dimensions of ECM proteins (e.g. laminin, fibronectin, and collagens) to study the influence of surface features and ECM compositions on the differentiation of NSCs. We hypothesized that the ECM protein patterns with variant geometries and dimensions would provide physical cues (e.g. mechanical or topographical cues), as well as guide cell-cell and cell-ECM interactions in a controlled manner, both of which would ultimately lead to a pattern geometry-dependent and pattern dimension-dependent neuronal and glial differentiation (Figure 3.11). Our data confirmed that the difference in the extent of neuronal and glial differentiation of NSCs on the ECM protein patterns was entirely due to the pattern geometry and dimension, as all the experiments were carried out in the absence of exogenous factors that promote neurogenesis; this suggests that NSCs can undergo differentiation by purely sensing the difference in ECM pattern geometries and dimensions.

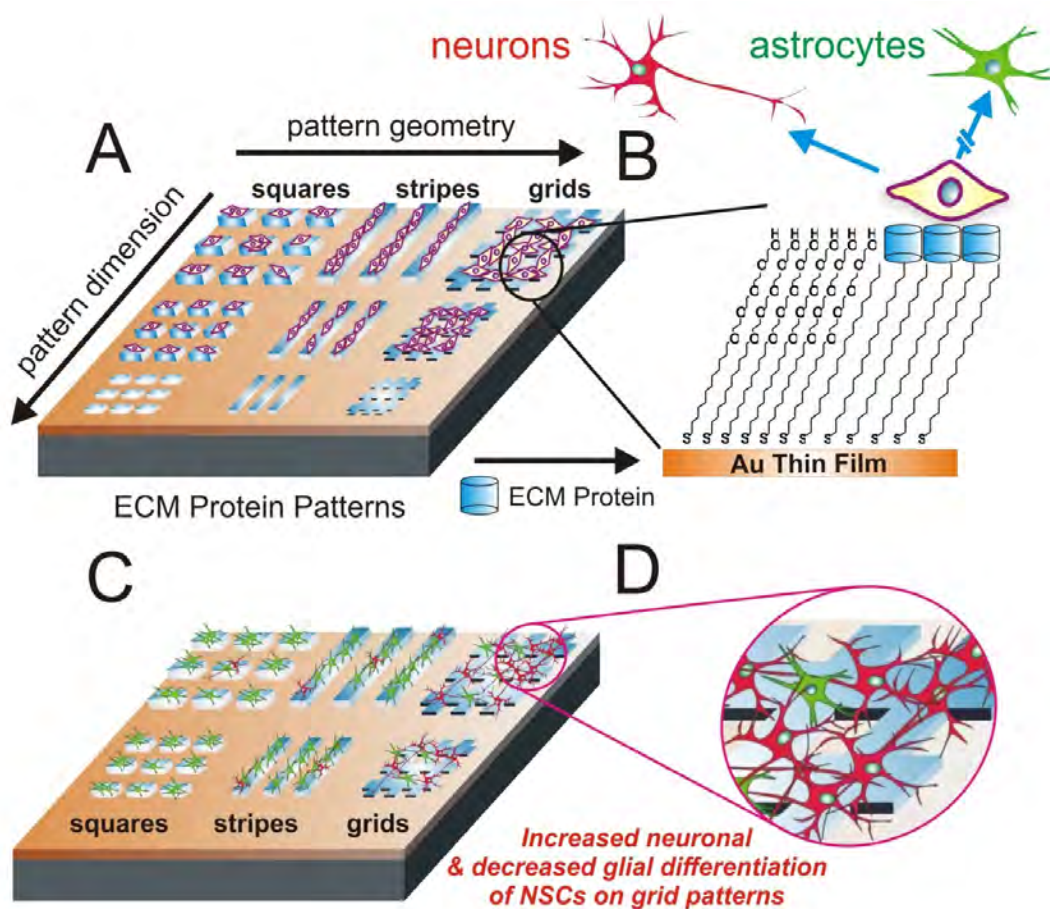


Figure 3.11: A schematic diagram of our approaches. (A) The fabrication of ECM protein patterns and their application for NSC differentiation. (B) The selective attachment of NSCs on the protein patterns and differentiation into two different kinds of neural cells. (C) The differentiation of NSCs into either neurons (red) or astrocytes (green) on the protein patterns. (D) Increased neuronal differentiation on the grid patterns, as compared to the stripes and squares [68].

### 3.2.2 Results and Discussion

Extracellular matrix protein patterns with variant geometries and dimensions were fabricated by initially patterning octadecanethiol (ODT, 5 mM in ethanol), a hydrophobic alkanethiol, which formed self-assembled monolayers (SAMs) of squares, stripes, and grids on glass substrates coated with a thin film (12 nm) of gold. In order to minimize the non-specific attachment of laminin, the background of the substrates was passivated by incubating in a solution (5 mM in ethanol) of tetraethylene glycol terminated alkanethiol [EG<sub>4</sub>-(CH<sub>2</sub>)<sub>11</sub>-SH, 12 h]. After passivating the background, a solution of

ECM protein [e.g. laminin (10  $\mu\text{g}/\text{ml}$ ) in phosphate buffered saline (PBS) buffer, pH 7.4] was added onto the substrates (3 h) and was preferentially adsorbed onto the hydrophobic regions (ODT patterns). The selective adsorption of laminin on hydrophobic regions was consistent with the results of other groups [235] and was also confirmed by immunostaining using anti-laminin IgG (Figure 3.12). Only the patterned regions, coated with ECM proteins, promoted cell adhesion and growth whereas the rest of the substrate remained inert (Figure 3.11). We similarly patterned several different ECM proteins including fibronectin and collagen, but found that laminin provided the optimum microenvironmental cues for NSC adhesion and growth. Hence, all our differentiation studies were carried out using laminin patterns.

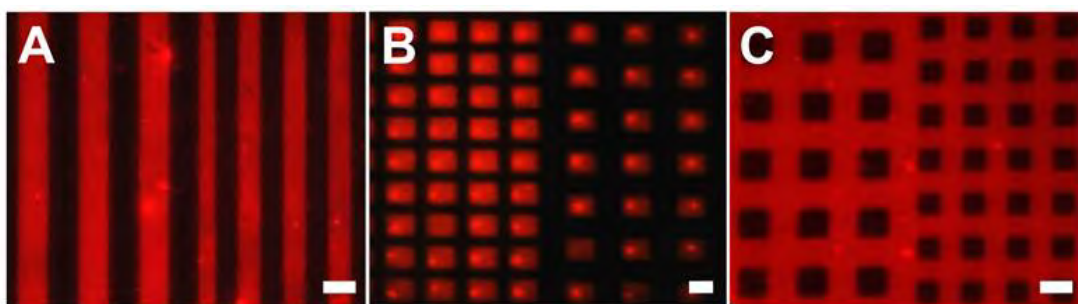


Figure 3.12: Immunostaining with anti-laminin IgG. The laminin patterns generated were confirmed using anti-laminin IgG (Sigma). Consistent results were obtained and reproduced for the three different geometries (A) Stripes, (B) Squares, and (C) Grids having varying dimensions. Scale bars: 20  $\mu\text{m}$  [68].

### Differentiating neural stem cells on ECM protein patterns

To examine the effect of the ECM protein patterns on stem cell differentiation, primary rat hippocampal neural stem cells (Millipore) were first expanded and maintained in an undifferentiated state in a homogeneous monolayer on a polyornithine and laminin-coated Petri dish in a defined serum-free growth medium [DMEM/F12 supplemented with B27 and basic fibroblast growth factor (bFGF, 20 ng/ml)]. For obtaining reproducible and consistent results, all experiments were carried out using NSCs from passages 2-5 at a constant cell density of 150,000 cells per substrate (1.5 cm x 1.5 cm), which was optimum for cell growth without clustering. Arresting the proliferation of NSCs and initiating their spontaneous differentiation was achieved by withdrawing

bFGF from the culture medium (resulting in basal medium), without the additional treatment with exogenous factors (proteins and small molecules). The basal medium (2 mL) containing the NSCs (75,000 cells/ml) was put in a single well of a 6-well plate containing a substrate with laminin patterns. After the NSCs attached onto the laminin patterns (1 hr), the substrates were rinsed with copious amounts of media in order to minimize non-specific interactions of NSCs with the passivated areas, and then incubated in fresh basal medium. The media was exchanged with fresh media every other day. During our screening approach to investigate the function of physical cues on neuronal differentiation of NSCs, we monitored the differentiation on ECM protein patterns by using two orthogonal assays, namely immunocytochemical and morphological assays. To assess the differentiation of NSCs, the down-regulation of the NSC marker (Nestin) and the geometry-dependent expression of the neuronal marker ( $\beta$ -III Tubulin, TuJ1) and glial marker (glial fibrillary acidic protein, GFAP) were monitored. In addition, the development of branches or spindle-like morphologies, and neurite outgrowths were observed by using an inverted phase contrast microscope (Zeiss Axiovert 200M equipped with AxioCam CCD).

### **Neuronal differentiation is dependent on the geometry of ECM micropatterns**

Patterns of ECM proteins with different geometries contributing to adhesion, proliferation, growth and migration of various cells (including stem cells) have been reported [236, 237]. For instance, striped patterns have been routinely used for generating patterns of neurons on a variety of surfaces. We initially hypothesized (taking into consideration the morphology and polarity of neurons) that striped laminin patterns could potentially result in the neuronal differentiation of a high number of NSCs [238]. However, we found that the NSCs on isolated stripes, having no interactions with the NSCs on adjacent stripes (Figure 3.13A1, differentiated into neurons to a lesser extent (36.0%, Figure 3.13A2 and Figure 3.14) as compared to the NSCs which crossed the passivation layer to interact with the NSCs on adjacent stripes. We thus concluded

that NSCs involved in a one-way interaction (with NSCs along the same stripe) differentiated into neurons to a lesser extent than the NSCs involved in interactions between adjacent stripes. These results were consistent with reports from the literature wherein cell-cell interactions have been shown to play a critical role in the differentiation of adult stem cells. For instance, it was recently shown that cell-cell interactions played an important role in the osteogenic (bone) differentiation of MSCs.[23]

To further confirm the influence of such interactions on the differentiation of NSCs, we used square patterns of laminin to isolate NSCs and restrict their growth within the square patterns (Figure 3.13B1). We hypothesized that the differentiation behaviour of NSCs can be considerably influenced by limiting cell-cell interactions. We observed that NSCs patterned on squares, having the same dimensions and spaces as the stripes, differentiated into neurons to a considerably lesser extent (28.1%, Figure 3.13B2 and Figure 3.14) as compared to the NSCs involved in one-way interactions on the striped laminin patterns.

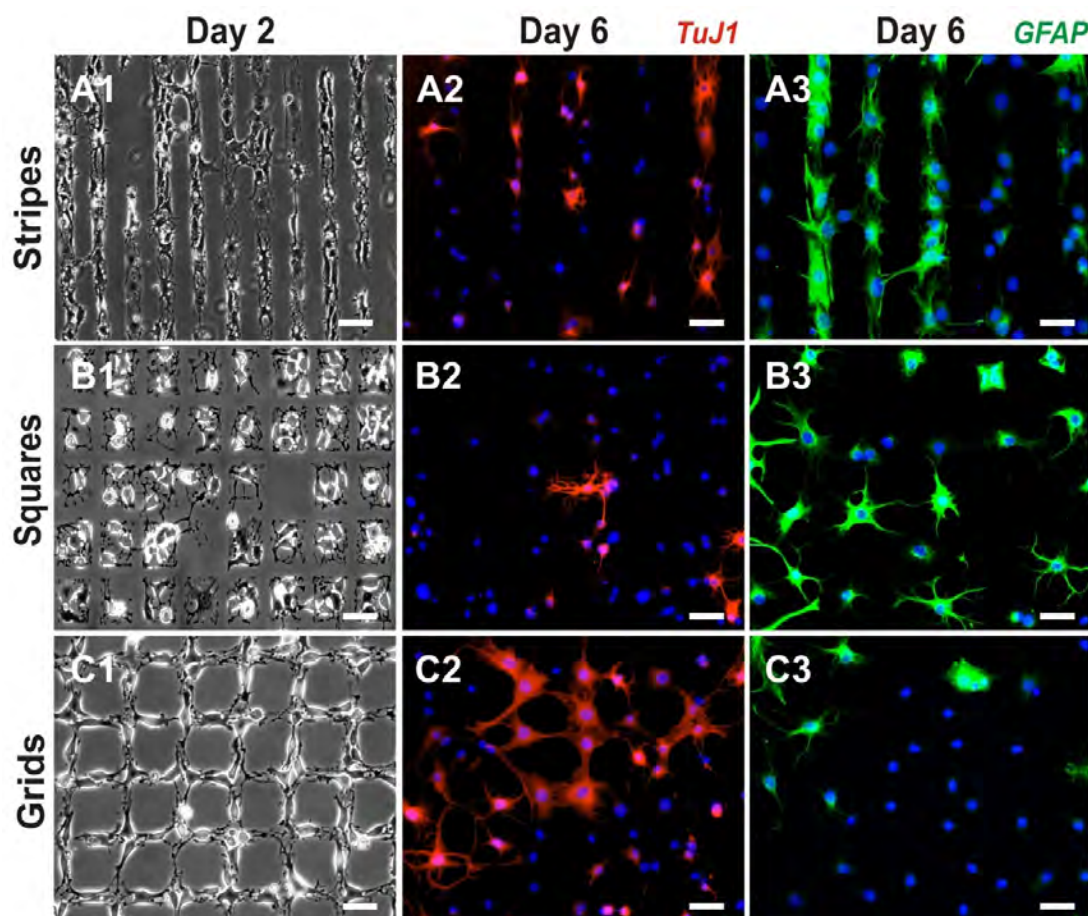


Figure 3.13: Growth and differentiation of NSCs on the laminin patterns. Phase contrast images show NSC attachment and growth on stripes (A1), squares (B1), and grids (C1) on Day 2 after seeding. Fluorescent images of cells stained for the neuronal marker TuJ1 (red) and nucleus (blue) show the extent of neuronal differentiation of NSCs on stripes (A2), squares (B2), and grids (C2) on Day 6 after seeding. Similarly, cells stained for astrocyte marker GFAP (green) and nucleus (blue) show the extent of glial differentiation on stripes (A3), squares (B3), and grids (C3) on Day 6 after seeding. Scale bars: 50  $\mu\text{m}$  [68].

At the same time, the number of NSCs that differentiated into astrocytes increased considerably on squares 76.9% on squares as compared to 64.3% on stripes (Figure 3.13B3 and Figure 3.14). Thus, the reduced cell-cell interactions with the NSCs on the surrounding patterns may have led to reduced neuronal differentiation and increased glial differentiation of the NSCs. Based on the observed differentiation of NSCs on stripes and squares, we further hypothesized that using specific pattern geometries promoting cell-cell interactions could lead to higher neuronal differentiation. For this

purpose, we used grid patterns of laminin, having the same dimensions as the stripe and square patterns, for NSC growth and differentiation. The grid patterns were specifically designed to increase cell-cell interactions in a controlled manner by promoting two-way interactions, (Figure 3.13C1). After six days in basal medium, as compared to the NSCs patterned on stripes and squares of laminin, we observed a remarkable increase in the number of NSCs that underwent neuronal differentiation (45.6%, Figure 3.13C2 and Figure 3.14) and a decrease in the number of cells that underwent glial differentiation on grid patterns of laminin (49.6%, Figure 3.13C3 and Figure 3.14). All the experiments were repeated several times under the same conditions. To maintain consistency and minimize the effects from other variables, we fabricated and used PDMS stamps to generate ECM protein patterns of all the three geometries (having the same dimensions and spacing) on the same substrate. Using this method, we could reproduce and confirm our results with relative ease. Neuronal and glial differentiation of NSCs was also monitored on control substrates which included substrates coated with laminin (unpatterned) and substrates without laminin. The NSCs on substrates without laminin did not attach and failed to survive, whereas 32.5% of the NSCs on the unpatterned substrates coated with laminin differentiated into neurons and 71.2% of the NSCs differentiated into astrocytes six days after seeding.

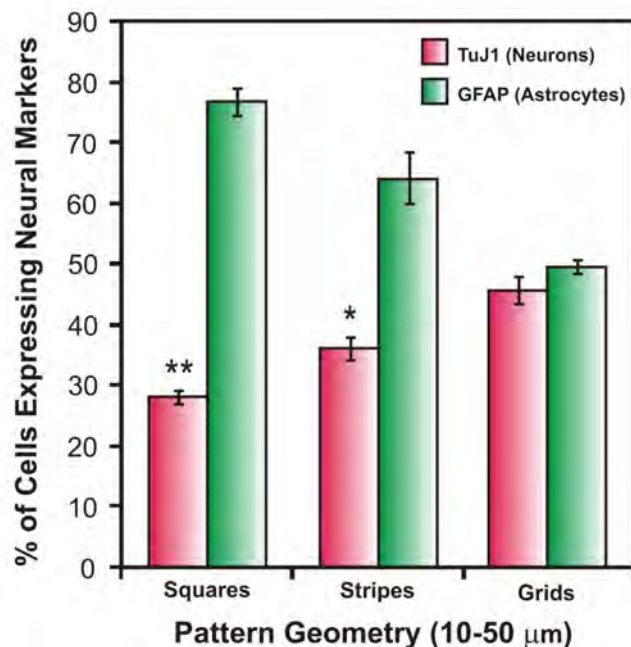


Figure 3.14: Quantitative comparison of the percentage of cells expressing the neuronal marker TuJ1 and astrocyte marker GFAP on laminin patterns of squares, stripes and grids. Six days after seeding, the differentiated cells were counted and plotted as a ratio of TuJ1-positive cells or GFAP-positive cells to the total number of cells ( $n=3$ ). Students unpaired t-test was used for evaluating the statistical significance for cells stained for TuJ1 on stripes and squares, compared to those on grids. (\* =  $P < 0.01$ , \*\* =  $P < 0.001$ ) [68].

### Neuronal differentiation is influenced by the size of ECM micropatterns

In addition to investigating the effect of pattern-geometry, we also studied the effect of dimensions on NSC differentiation. To this end, we generated ten different dimensions for each of the geometries, ranging from sizes as small as  $10 \mu\text{m}$  and as large as  $250 \mu\text{m}$  (Figure 3.15). Interestingly, for the three different geometries above  $50 \mu\text{m}$ , we observed little difference in the percentage of NSCs undergoing neuronal and glial differentiation. The result observed for pattern dimensions above  $50 \mu\text{m}$  was similar to that observed with unpatterned substrates. We believe the cells may not be able to sense the difference in pattern geometries above  $50 \mu\text{m}$  and thus show similar behaviour to the cells on unpatterned substrates. Since the NSCs showed remarkable difference in differentiation on patterns ranging from  $10\text{-}50 \mu\text{m}$ , all of our statistical analysis and investigation was done using pattern features within this range.

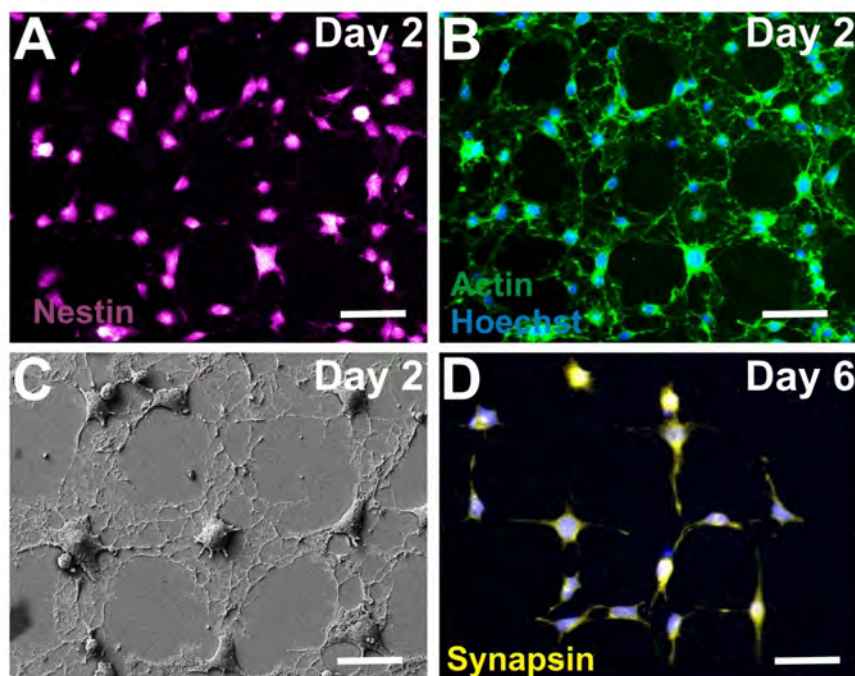


Figure 3.15: NSC alignment and differentiation on combinatorial ECM patterns. (A) NSCs on grids of laminin express the neural stem cell marker, nestin (purple) on Day 2 after seeding, thus confirming that the NSCs are undifferentiated. (B) NSCs stained for actin (green) show extensive spreading and cell-cell interactions on grid patterns of laminin on Day 2 after seeding, confirming that the NSCs, while still in the undifferentiated state, extensively interact with each other. (C) SEM image of NSCs on Day 2 after seeding, showing the early alignment and extension of processes on grid patterns of laminin. (D) NSCs previously shown to extend and grow on the grid patterns of laminin undergo neuronal differentiation and express the neuronal marker synapsin (pseudocolored yellow) on Day 6 after seeding. Scale bars: 20  $\mu\text{m}$  [68].

We observed that the laminin patterns of all three geometries enabled the NSCs to attach and grow within a day or two day after seeding. By staining for actin using phalloidin and using field emission scanning electron microscopy (FESEM, Zeiss Gemini), we further observed that the cytoskeleton of the NSCs aligned well within the laminin patterns, guiding cellular morphology and interactions (Figure 3.15B and C). To confirm that the laminin patterns influenced morphological changes before differentiation (as opposed to an early differentiation of NSCs which might have caused a change in alignment and morphology), the NSCs were immunostained for the neural stem cell marker nestin two days after seeding in basal medium. We observed that most of the NSCs that aligned along the patterns, stained positive for nestin (Figure

3.15A), confirming that cells are in an undifferentiated (multipotent) state when they align along the patterns (Figure 3.16).

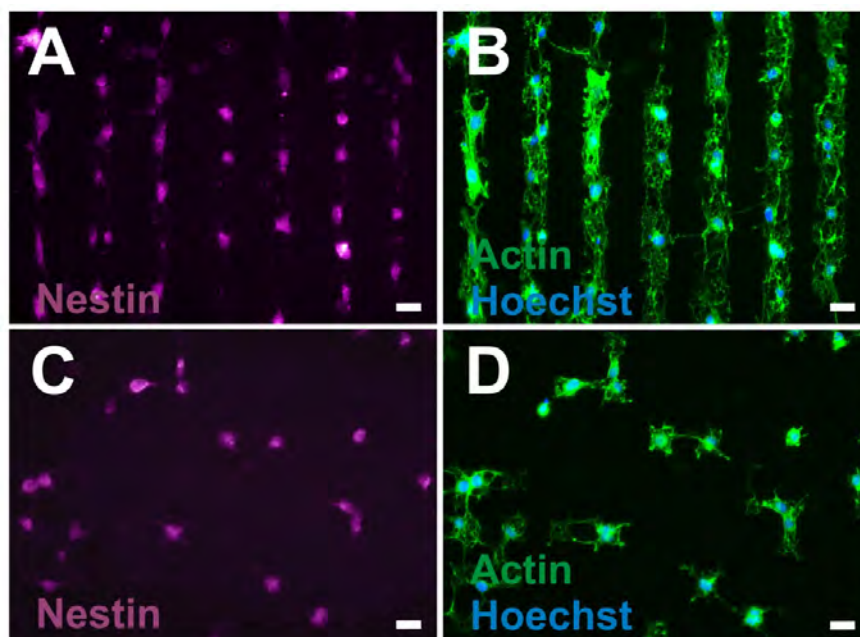


Figure 3.16: NSC alignment and differentiation on combinatorial ECM protein arrays. NSCs on stripes (A) and squares (C) of laminin express the neural stem cell marker, nestin (purple) on Day 2 after seeding, thus confirming that the NSCs are undifferentiated. NSCs stained for actin (green) on stripes (B) and squares (D) of laminin on Day 2 after seeding. Scale bars: 20  $\mu\text{m}$  [68].

We further confirmed neuronal differentiation of NSCs on the laminin patterns using synapsin as another neuronal marker in addition to TuJ1. After six days in basal medium, a remarkably high number of the NSCs growing along the grid patterns of laminin expressed synapsin (Figure 3.15D). In addition, colocalization of TuJ1 and synapsin was observed within the NSCs differentiated on the grid patterns, confirming that the neurons expressed both neuronal markers (Figure 3.17).

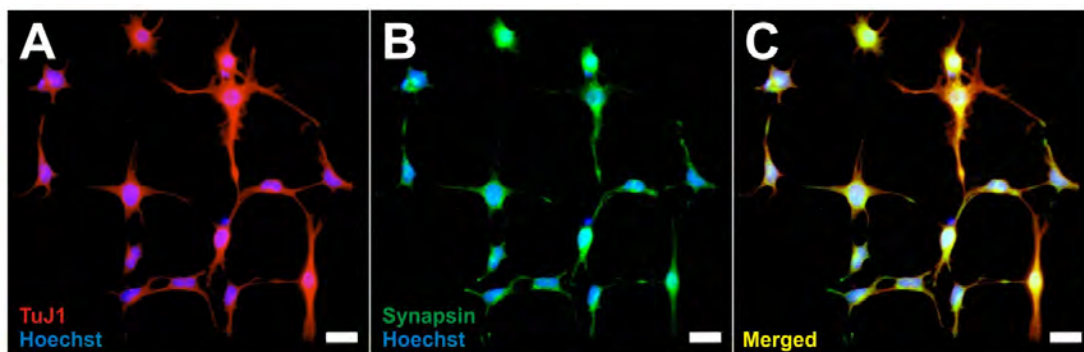


Figure 3.17: Colocalization of TuJ1 and synapsin within cells on grid patterns. (A) NSCs differentiated into neurons, on grid patterns, expressing the neuronal marker TuJ1 (red). (B) The differentiated NSCs also express another neuronal marker, synapsin (pseudocolored green). (C) Merged image showing the overlap of the two neuronal markers TuJ1 and synapsin. The overlapping regions within the neurons are yellow in color. Scale bars: 20  $\mu\text{m}$  [68].

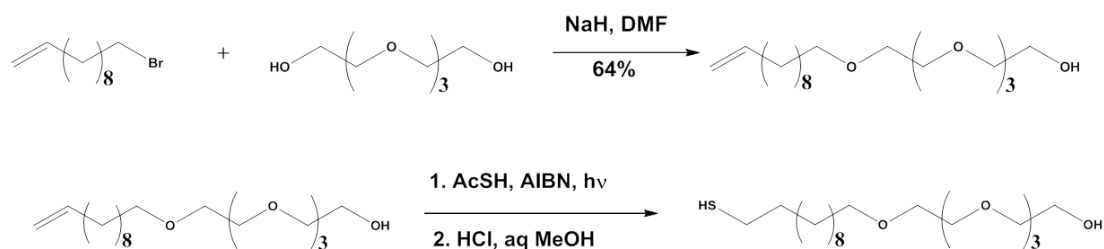
### 3.2.3 Conclusions

In summary, we fabricated and utilized patterns of ECM proteins for modulating the extent of neuronal and glial differentiation of NSCs in the absence of soluble cues such as small molecules and exogenous proteins. Potentially, our approach and methodology can be helpful for deconvoluting physical cues and cell-cell interactions from complex microenvironmental cues. More detailed mechanistic studies on how physical cues modulate the signaling cascades and the signaling pathways that are primarily involved in stem cell differentiation induced by such factors are currently under investigation. The implications of our results could also potentially be significant for tissue engineering for brain and spinal cord injuries, where NSCs or NSC-based differentiated cells can be transplanted into the damaged regions with scaffolds. For example, scaffolds having patterns promoting cell-cell interactions in a controlled manner could potentially lead to increased neuronal differentiation *in vivo*. Even though we have explored only proof-of-concept experiments focusing on differentiation of NSCs, a similar strategy could be extended to study and control the fate of other stem cells, such as MSCs and embryonic stem cells (work in progress). Our results substantiate the importance of pattern dimensions, pattern geometries, and cell-cell interactions in controlling stem cell fate.

### 3.2.4 Materials and Methods

#### Synthesis and Characterization of EG<sub>4</sub>-(CH<sub>2</sub>)<sub>11</sub>-SH

Tetraethyleneglycol (29.7 g, 153 mmoles) was dissolved in 75 ml of dry dimethylformamide under nitrogen. This solution was cooled to 0°C and NaH (1.22 g of 60% in mineral oil, 30.6 mmoles) was added in portions. After stirring at room temperature for one hour, 7.5 g of undecenyl bromide (30.6 mmoles of 95% purity) was added and the reaction was stirred at room temperature overnight. The reaction was then diluted with 75 ml of water and extracted with 4 x 50 ml of hexane. The combined extracts were then washed with 2 x 20 ml of water, 20 ml of saturated brine, dried over MgSO<sub>4</sub>, filtered and the solvent evaporated in vacuo. The crude product thus obtained was chromatographed on silica gel eluting with 2:1, 1:2 hexane/ethyl acetate and then with 100% ethyl acetate. The product was a light-yellow oil weighing 7.1 g (64%). The proton NMR was consistent with the desired product.



The alkene obtained previously (7.1 g, 20.5 mmoles) and thiolacetic acid (6.24 g, 82.0 mmoles) were dissolved in 75 ml of THF and this solution was deoxygenated with nitrogen. After the addition of 50 mg of AIBN, it was irradiated with 254 nm UV light overnight. The solvent was then removed in vacuo and the residue was evaporated with 3 x 50 ml of toluene to remove thiolacetic acid. The crude product so obtained was chromatographed on silica gel eluting with 2:1, 1:1, 1:2 hexane/ethyl acetate and finally with 100% ethyl acetate. The intermediate thioacetate product was a colorless liquid weighing 7.2 g. The proton NMR was consistent with the desired product.

The intermediate obtained above (3.0 g, 7.10 mmoles) was dissolved in a mixture

of 1.5 ml of conc. hydrochloric acid and 30 ml of 95% EtOH which had been deoxygenated with nitrogen and this solution was refluxed under nitrogen overnight. It was then cooled to room temperature and the solvent removed in vacuo. The residue was partitioned between 30 ml of saturated NaHCO<sub>3</sub> solution and 30 ml of ethyl acetate. The phases were separated and the aqueous phase was extracted with 2 x 30 ml of ethyl acetate. The combined extracts were dried over MgSO<sub>4</sub>, filtered and the solvent removed in vacuo. The product was a yellow liquid weighing 2.6 g (96%). The proton NMR was consistent with the desired product. MS: M<sup>+</sup>380.9

### **Generating ECM protein patterns**

Polycrystalline Au films were prepared by thermally depositing 5 nm thick Ti layer followed by 20nm Au deposition (1.5 cm x 1.5 cm) on cover glass substrates (Fisher No. 1) under a high vacuum condition (base pressure  $5 \times 10^{-6}$  torr). For micro contact printing, the molded PDMS stamps was prepared by conventional photolithography and 5mM 1-octadecanethiol (ODT) was used as ink molecule. The various patterns were designed using AutoCAD so as to incorporate more multiple geometries having varying dimensions on each stamp. Pattern dimensions and spacings for each of the geometries (stripes, squares, and grids) ranged from 10  $\mu\text{m}$  to 250 $\mu\text{m}$ . After patterning the ODT SAMs on the thin gold films, the background was passivated using EG<sub>4</sub>-(CH<sub>2</sub>)<sub>11</sub>-SH, a protein resistant thiol. The ECM proteins (from Sigma) such as laminin (10  $\mu\text{g}/\text{ml}$ ), collagen (50  $\mu\text{g}/\text{ml}$ ), and fibronectin (50  $\mu\text{g}/\text{ml}$ ) and their combinations were adsorbed on the ODT SAMs by incubating the protein solution of the SAMs for 3 h at room temperature. The protein micropatterns were then rinsed with sterile phosphate buffer saline pH 7.4 (PBS) multiple times and 2 ml suspensions of NSCs were seeded with density of  $7.5 \times 10^4$  /ml (in basal medium) in a 6-well plate. The samples were incubated for 30 min at 37°C and each culture well containing the samples was washed gently with the NSC basal medium to remove the NSCs weakly attached on the substrate. It was observed that laminin provided the most optimum microenvironment for the adhesion and growth of the NSCs, hence all the experiments were carried out with laminin as the ECM protein. The laminin micropatterns were confirmed using anti-laminin.

### **Rat neural stem cell (NSC) culture and differentiation**

Rat neural stem cell line (Millipore) were purchased and routinely expanded according to the manufactures protocol. The NSCs were maintained in laminin (Sigma, 20  $\mu\text{g}/\text{ml}$ ) coated culture dishes precoated with poly-L-lysine (10  $\mu\text{g}/\text{ml}$ ) in DMEM/F-12 media (Invitrogen) supplemented with B-27 (Gibco) and containing L-Glutamine (2 mM, Sigma), and antibiotics penicillin and streptomycin (Invitrogen) in the presence of basic fibroblast growth factor (bFGF-2, 20 ng/ml, Millipore). All the cells were maintained at 37°C in a humidified atmosphere of 5% CO<sup>2</sup>. For consistency, the experiments were carried out on the cells between passages 2 and 5. Neural differentiation was initiated by changing the medium to basal medium (without bFGF-2) on the laminin micropatterns. The cells were allowed to differentiate for 6 days, with the basal medium in each being exchanged every other day.

### **Immunocytochemistry**

To investigate the extent of neuronal differentiation, at Day 6, the basal medium was removed and the cells fixed for 15 minutes in Formalin solution (Sigma) followed by two PBS washes. Cells were permeabilized with 0.1% Triton X-100 in PBS for 10 minutes and non-specific binding was blocked with 5% normal goat serum (NGS, Invitrogen) in PBS for 1 hour at room temperature. To study the extent of neuronal differentiation the primary mouse antibody against TuJ1 (1:500, Covance) and primary mouse antibody against Synapsin (1:500, Santa Cruz Biotechnology) was used and for glial differentiation the primary rabbit antibody against GFAP (1:500, Dako) was used. The fixed samples were incubated overnight at 4°C in solutions of primary antibodies in PBS containing 10% NGS. After washing three times with PBS, the samples were incubated for 1 h at room temperature in solution of anti-mouse secondary antibody labelled with Cy3 and anti-rabbit secondary antibody labelled with Cy2 (1:400, Jackson ImmunoResearch), Hoechst (1:500, Invitrogen) in PBS containing 10% NGS to observe neuronal and glial differentiation. After washing the samples thrice with PBS the substrates were

mounted on glass slides using ProLong Gold antifade (Invitrogen) to minimize quenching by gold. To confirm that the NSCs on the micropatterns were undifferentiated at Day 2, the cells were similarly fixed and immunostained with primary and secondary antibodies. The primary rabbit polyclonal antibody against neural stem cell marker, nestin (1:400, Santa Cruz Biotechnology, Inc) was used. The secondary anti-rabbit antibody used was labelled with Cy5 (1:400, Jackson ImmunoResearch). Phalloidin (1:75, Invitrogen) labelled with Alexa-546 was added to the secondary antibody solution to observe the actin cytoskeleton and alignment of the NSCs along the patterns. The mounted samples were imaged using Zeiss. ImageJ (NIH) was used for comparative analysis of fluorescence signals of TuJ1 on the various pattern geometries of different dimensions, and on control samples (only laminin, no patterns).

### 3.3 Nanoparticle Arrays Decorated with Graphene Align Axons and Enhance Neuronal Differentiation of Human Neural Stem Cells

#### 3.3.1 Introduction

The ability to utilize substrate topography to control stem cell fate has great potential in regenerative medicine. Biomaterials for stem cell transplantation, using scaffolds and implantable devices, are now being designed in a manner that elicits specific cellular responses such as differentiation, migration and proliferation in response to the topographical cues. For spinal cord and peripheral nerve injuries, neuronal response to topography is critical as it is the specific guidance of axons that would lead to therapeutic solutions within the injured spinal cord [239]. If the nerve gaps created due to injuries are large, the distal and proximal sides of the damaged nerves will not be able to communicate efficiently, thus impeding the natural regeneration process [240]. As a result, a significant amount of emphasis is being placed upon the directional growth of axons within the injured spinal cord, thus making axonal alignment an important factor in designing biomaterials [240,241]. To this end, neural stem cells (NSCs), which differentiate into neurons and glial cells, have been transplanted within injured spinal cords as they hold great promise for hastening functional recovery [241–243]. We have previously shown that the growth, differentiation and polarization of NSCs is strongly influenced by the cell-cell interactions and cell-extracellular matrix (ECM) interactions [68, 71]. Furthermore, ECM proteins patterns and patterned nanotopographical features have been routinely employed to control the polarity, directional growth and influence the neuronal differentiation of NSCs [68, 145, 244, 245]. The challenge, however, is to provide an instructive microenvironment to the NSCs, through the use of novel materials, that can spontaneously lead to axonal alignment in the hopes of developing better treatments for spinal cord injuries. We believe the growth, differentiation and survival of well-aligned adult human neural stem cells (hNSCs) holds tremendous promise for regeneration of damaged neurons as they would help bridge the gaps between the proximal and distal ends of transected nerves thus aiding in restoring communication at the site of injury.

Graphene, a monolayer of carbon atoms arranged in a 2D honeycomb lattice [246], has been shown to be a very useful material in biomedical applications [73, 247, 248] due to its excellent flexibility, thermal properties, electrical conductivity, high strength, stiffness and biocompatibility [249]. Recently, the properties of graphene and its biocompatibility have inspired research groups to use graphene for tissue engineering [250]. For instance, graphene has been shown to support the proliferation and differentiation of adult and pluripotent stem cells [73, 251]. Due to its superior chemical stability that facilitates integration with neural tissues, we believe culturing and differentiating hNSCs on graphene would be an ideal model to clearly demonstrate its advantages [73, 252]. Furthermore, it was demonstrated that nanotopographical features using silica beads led to the acceleration of hippocampal neurons *in vitro* [253]. We thus hypothesized that substrates which consisted of nanotopographical features decorated with graphene would be an ideal platform to investigate the growth and differentiation of hNSCs. Towards this end, we have created nanotopographical features on a substrate using silica nanoparticles and decorated them with chemically derived graphene. We show that these substrates create an ideal microenvironment for the growth, alignment and enhanced neuronal differentiation of hNSCs. In particular, chemically derived graphene or graphene oxide (GO) is a chemically versatile compound that contains oxygen functional groups attached to the graphene basal plane. The oxygen functional groups allow the GO nanosheets to readily attach to molecules or surfaces - in our case they decorate the surface of 300 nm silica spheres. The control and test substrates used to grow and differentiate hNSCs in this study are shown in Figure 3.18a.

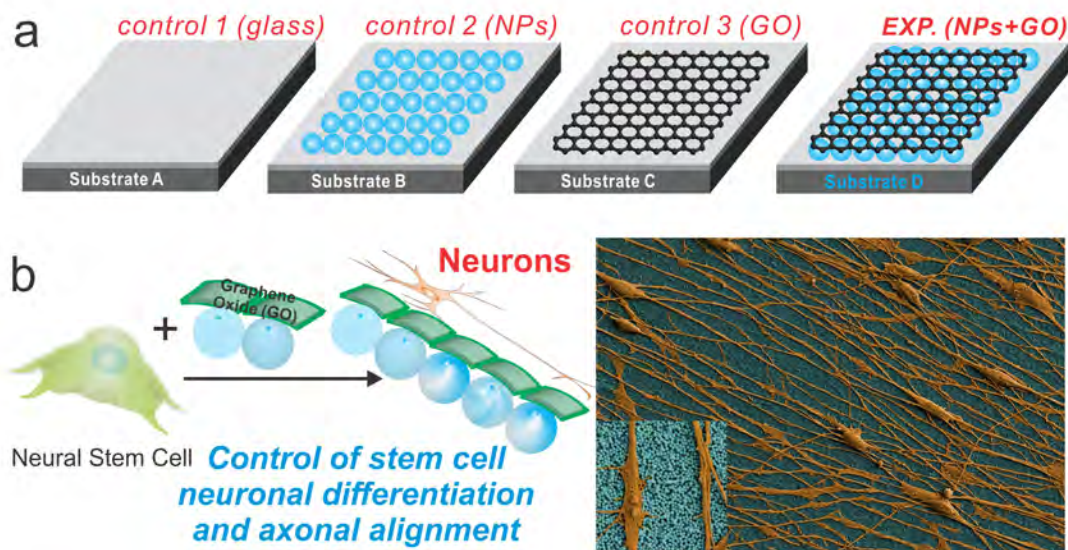


Figure 3.18: Schematic diagram depicting the influence of nanoparticle (NP) monolayers coated with graphene oxide (GO) on the alignment of the axons, extending from hNSCs, and the differentiation of hNSCs into neurons. (a) Different conditions for differentiating hNSCs into neurons. (b) hNSCs cultured and differentiated on Substrate D having a monolayers of NPs coated with GO show enhanced neuronal differentiation and axonal alignment. The differentiated hNSCs (orange) and the NPs-coated with GO (blue) in the SEM image have been pseudocolored to enhance the contrast. (Inset) Zoom-in image showing the axons aligned on a monolayer of NPs coated with GO.

### 3.3.2 Results and Discussion

#### Human NSCs align on GO and SiNP-GO substrates

Initially all of the substrates were treated with the ECM protein laminin ( $10 \mu\text{g}/\text{mL}$  for 4 h), which is essential for the adhesion, growth, and differentiation of hNSCs. It should be noted that the laminin was not patterned on the substrates nor was any patterning of the protein observed using atomic force, optical, or scanning electron microscopies after adsorption. Human NSCs were then seeded onto these substrates and proliferated in culture media containing basic fibroblast growth factor (bFGF,  $20 \text{ ng}/\text{mL}$ ) and epidermal growth factor (EGF,  $20 \text{ ng}/\text{mL}$ ). After 24 h, differentiation was initiated by withdrawing the culture medium and replacing it with basal medium lacking growth factors. Immunocytochemistry and quantitative polymerase chain reaction (qPCR) was performed on the differentiated hNSCs after 14 days to investigate the influence of SiNP, GO and SiNP-GO on neuronal differentiation. On Day 2, after removal of the

growth factors, the hNSCs on all substrates were observed to have attached well and were proliferating. The hNSCs continued to proliferate and extended in random directions until Day 5, after which they began aligning on the GO and SiNP-GO substrates. Finally, the differentiated hNSCs on the GO and SiNP-GO substrates on Day 14 were very well aligned and had well-extended axons (Figure 3.19a). On the other hand, the control hNSCs, which differentiated on the SiNP and glass substrates, also had extended axons, but showed no alignment. To quantify this, we calculated the variation in the angle of orientation of axons extending from hNSCs on substrates containing GO and compared it with the orientation of the axons from hNSCs differentiated on the control SiNP and glass substrates. Our calculations confirmed that the variation in the angle of orientation of axons from hNSCs on the GO and SiNP-GO was  $\pm 17.8^\circ$  and  $\pm 9.16^\circ$  respectively (Figure 3.19biii-iv), while the axons from the hNSCs on glass and SiNP extended randomly, having a much wider variation of  $\pm 42^\circ$  and  $\pm 46.11^\circ$ , respectively, in the angle of their orientation (Figure 3.19bi-ii).

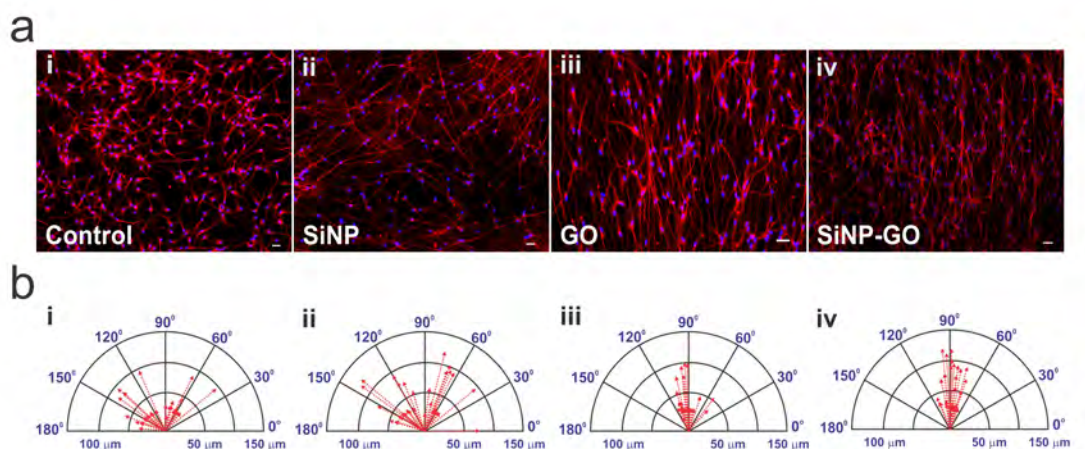


Figure 3.19: Aligned growth and extension of axons from differentiated hNSCs and compass plots showing the variation in the angle of orientation and the lengths of the axons. (a) Differentiated hNSCs are immunostained with TuJ1 (red). The axons show no alignment on glass and SiNPs, whereas the axons are significantly aligned on GO and SiNP-GO. (Scale bars:  $10 \mu\text{m}$ ) (b) The compass plots show a large variation in the angle of orientation of axons on glass ( $\pm 42^\circ$ ) and SiNPs ( $\pm 46.11^\circ$ ) and minimal variation on GO ( $\pm 17.8^\circ$ ) and SiNP-GO ( $\pm 9.16^\circ$ ). The compass plot also shows that axons extending on SiNP and SiNP-GO are longer than those extending on glass and GO.

The images clearly show that the axons extending from differentiated hNSCs aligned

exclusively on substrates having GO as a component of the ECM. Recently, self-assembled silica beads were shown to significantly accelerate the extension of axons from hippocampal neurons cultured on the beads [253]. We thus investigated the influence of nanotopographical features on the length of axons extending from hNSCs. We calculated the lengths of the extending axons from the hNSCs differentiated on the different substrates on Day 14. The average length of the axons extending from hNSCs cultured on SiNPs was 20.76% more than the average length of those cultured on glass, and 11.3% more than those cultured on GO (Figure 3.19b). We therefore hypothesize that the alignment of axons is exclusively due to the presence of GO within the ECM while the presence of the underlying SiNP monolayer leads to an increase in the average length of axons from hNSCs differentiated on SiNP-GO. This behavior of hNSCs was also confirmed using SEM (Figure 3.20a). It is important to note that we are currently investigating the underlying principles that govern the alignment of hNSCs in our lab. At this moment we are unable to control the direction of axonal alignment. However, a better understanding of the underlying mechanisms will enable us to control the direction of alignment in the future.

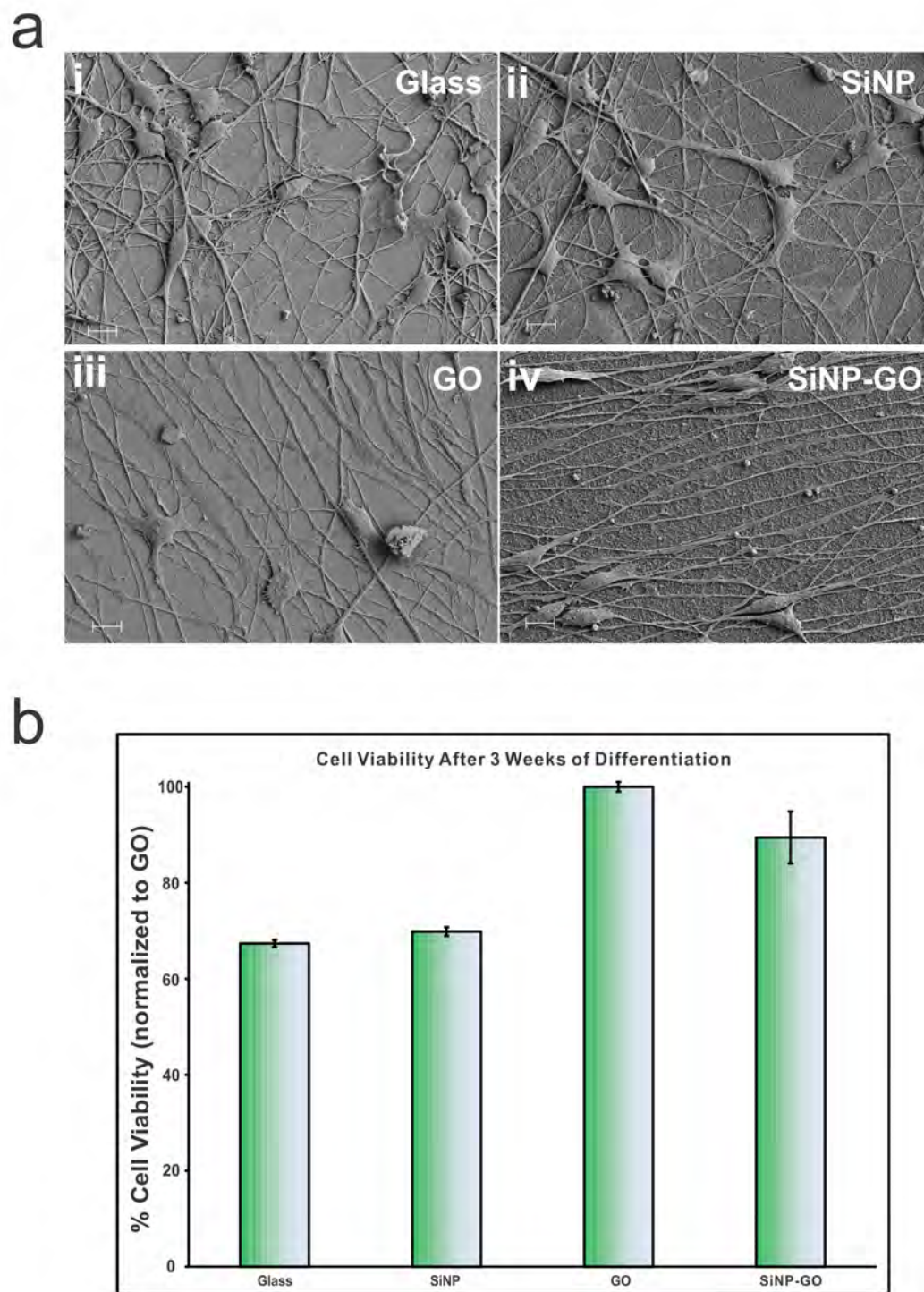


Figure 3.20: Scanning electron microscopy showing the behavior of hNSCs and MTS assay for biocompatibility and long term survival of differentiated hNSCs on GO and SiNP-GO. (a) SEM images confirm that the axons do not align on control and SiNPs and they align on GO and SiNP-GO. (Scale bars: 10  $\mu\text{m}$ ) (b) MTS assay results show that GO and SiNP-GO are biocompatible and aid in the long term survival of hNSCs as compared to glass and SiNPs. The results have been normalized to hNSC viability on GO.

We then went on to investigate whether the alignment of axons on GO and SiNP-GO was due to crowding of hNSCs and thus depended on the density of the seeded cells. It has been shown that differences in cell density can yield a noticeable difference in cell alignment [254]. To this end, we reduced the cell density by 50% and observed the behavior of the hNSCs over a period of two weeks. We observed that the cells behaved in the same manner, even at the lower cell density (Figure 3.21). This is a remarkable behavior, which we believe could be very useful, especially for developing scaffolds for restoring neuronal functioning within damaged regions of the central nervous system.

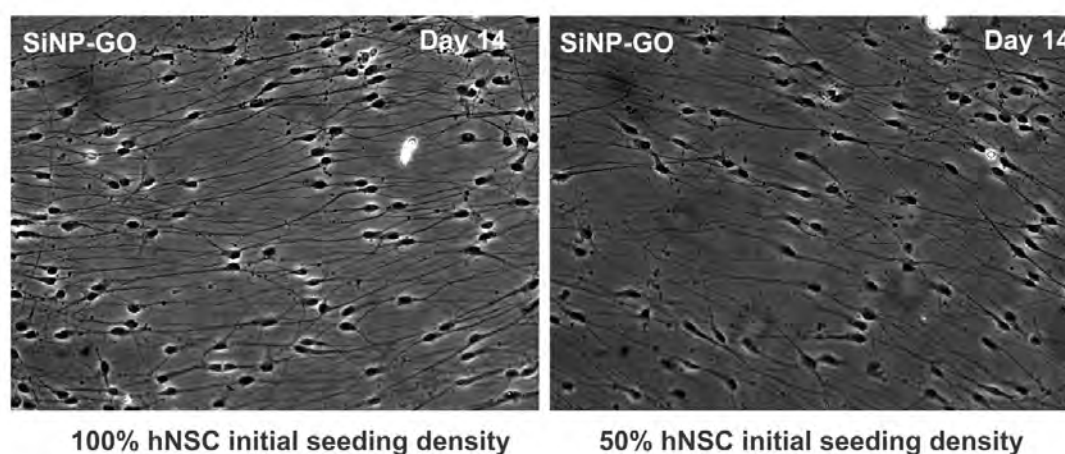


Figure 3.21: Axonal alignment and cell density. Phase contrast images showing axonal alignment of differentiated hNSCs cultured on SiNP-GO at different initial seeding densities. The axonal alignment was observed even when the initial seeding density was reduced by 50%.

### **GO and SiNP-GO substrates enhance cell survival**

The prerequisite for materials used to control cell behavior or develop scaffolds is that they should be biocompatible. In the case of regenerative medicine, the materials not only have to be biocompatible but must also support stem cell differentiation and survival for long periods of time. As a potentially advantageous material for tissue engineering, graphene has also been shown to support the long-term survival and induce neuronal differentiation of hNSCs [73]. As such, we used a standard cell viability assay (MTS assay) to confirm that the GO and SiNP-GO substrates significantly enhanced cells survival after 3 weeks of differentiation as compared to the control SiNP and glass

substrates (Figure 3.20b). This is particularly advantageous for stem cell biology and regenerative medicine as the differentiating stem cells are required to grow, differentiate and survive to have beneficial and lasting effects.

### **Neuronal differentiation of hNSCs**

We investigated the expression of immature and mature neuronal markers in the differentiated hNSCs after two weeks. Our immunostaining data showed that most of the aligned axons from differentiated hNSCs showed the expression of the neuronal marker TuJ1, and also the presence of mature neuronal markers such as MAP2 and synapsin (Figure 3.22a). We also confirmed the expression of axonal marker, GAP43. While the immunostaining data confirmed the presence of the neuronal markers, we could not use this data to quantify expression levels of the neuronal markers on the GO and SiNP-GO as compared to the SiNP and glass substrates. We thus performed qPCR analyses of the mRNA expression levels of the neuronal markers from the hNSCs differentiated on GO and SiNP-GO substrates and compared it to hNSCs differentiated on SiNP and glass substrates. While the expression levels of all neuronal and axonal markers were up-regulated on all substrates as compared to the control glass substrates, we found that the hNSCs differentiated on SiNP-GO substrates showed the highest expression levels of all neuronal markers such as TuJ1, MAP2 and synapsin (Figure 3.22b). Thus, we can conclude that the combined effect of having SiNP and GO on a single platform shows increased neuronal differentiation and remarkable alignment of differentiated hNSCs.

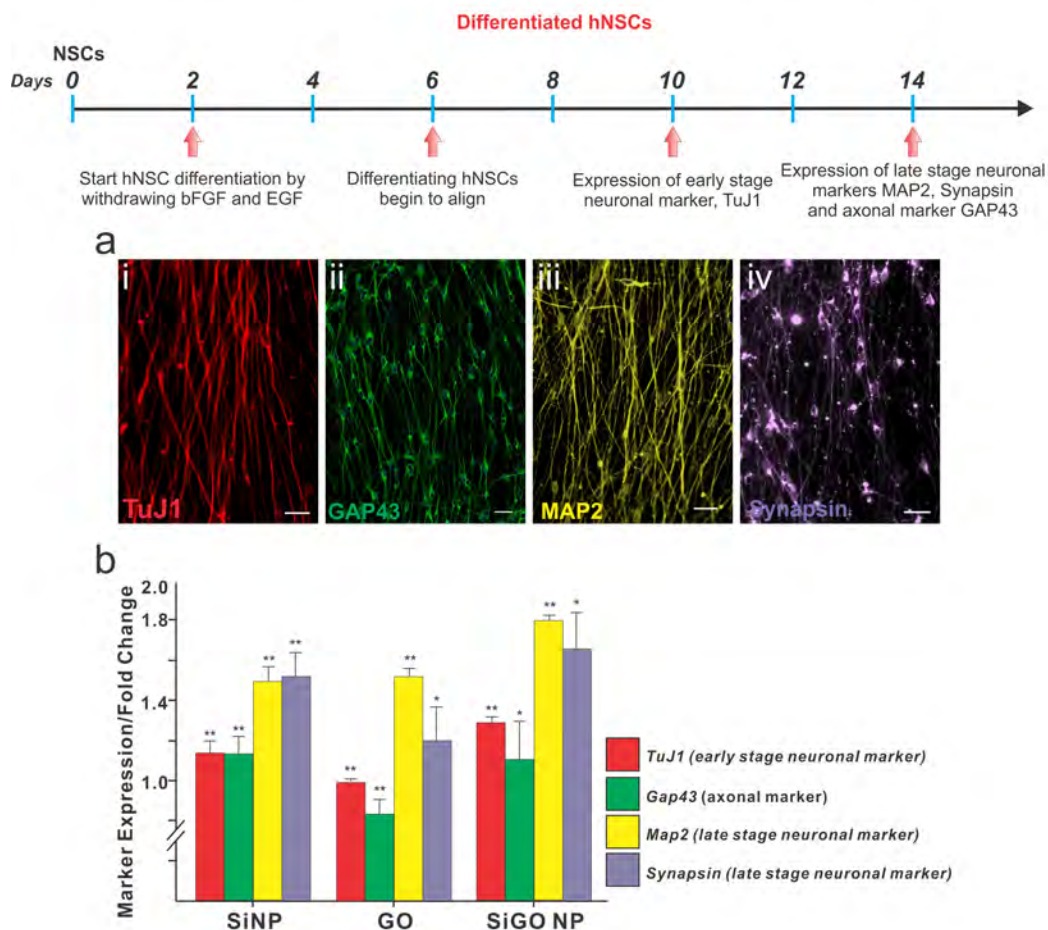


Figure 3.22: Enhanced neuronal differentiation of hNSCs on SiNP-GO. (a) hNSCs spontaneously differentiated on SiNP-GO show the presence of early stage neuronal marker TuJ1 (red) and late stage neuronal markers MAP2 (pseudocolored yellow) and synapsin (pseudocolored purple). They also highly express the axonal marker GAP43 (green). (Scale bar: 10  $\mu\text{m}$ ) (b) Quantitative RT-PCR (qPCR) results for early and late stage neuronal markers expressed by the hNSCs differentiated on the different substrates. The results are normalized to the expression levels of the neuronal markers in hNSCs differentiated on glass.  $N=4$  and  $*P < 0.05$ ,  $**P < 0.01$  compared to hNSCs differentiated on glass. The results clearly show that hNSCs differentiated on SiNP-GO show significantly enhanced expression of early and late stage neuronal markers. The expression of axonal marker GAP43 increases due to the presence of SiNP monolayers.

### Axonal alignment on pristine graphene

We also used pristine graphene deposited on glass, using chemical vapor deposition (CVD), to investigate if the differentiating hNSCs align on graphene as opposed to GO. Although this behavior has not been previously reported, we did observe alignment of

cells on pristine graphene, similar to the alignment observed on GO (Figure 3.23).

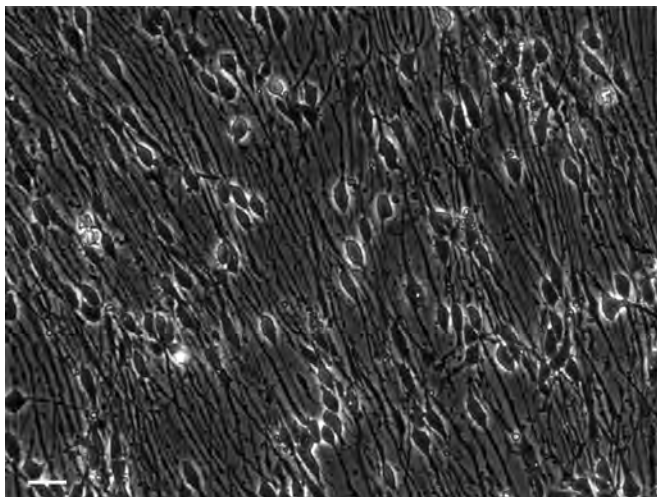


Figure 3.23: Axonal alignment on pristine graphene. Phase contrast image showing axonal alignment of differentiated hNSCs on pristine graphene. (Scale bar: 10  $\mu\text{m}$ )

However, the water solubility of GO and the presence of functional groups allows positively charged SiNP monolayers to be readily coated with GO, by simply dipping once into the solution of GO. Another factor that has to be considered is the interaction of the ECM protein, laminin, with graphene. Proteins have been shown to have higher and faster immobilization on GO, as compared to pristine graphene, due to the abundant surface oxygen-containing groups such as epoxide, hydroxyl and carboxyl groups present on GO [255]. The presence of these polar functional groups on GO makes the GO-coated substrates very hydrophilic as compared to the pristine graphene-coated substrates, which significantly affects the adsorption of proteins [251]. We thus believe that laminin, which is dissolved in water, readily assembles on GO as it is water soluble in contrast to pristine graphene, which is hydrophobic. Considering these factors, we believe GO is more advantageous for decorating SiNPs and align hNSCs as compared to graphene.

From our experiments, it was clear that the axonal alignment was due to the presence of graphene as component of the ECM. Therefore, we further investigated if the axonal alignment was due to the unique structure of graphene, which is composed of carbon atoms in a hexagonal lattice. For this purpose, we chose another novel material,

molybdenum disulfide ( $\text{MoS}_2$ ), which is from the family of two dimensional layered transition metal dichalcogenides and has a physical structure similar to that of graphene. Nanoflakes of  $\text{MoS}_2$  were deposited on glass substrates, onto which laminin was assembled. We then grew and differentiated hNSCs on  $\text{MoS}_2$ . We observed that the hNSCs grew well on  $\text{MoS}_2$  but showed no alignment, thus confirming that the unique structure of graphene causes the hNSCs to align (Figure 3.24).

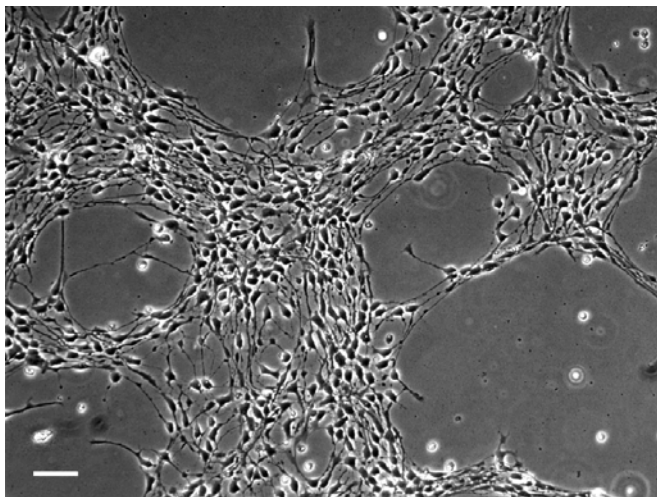


Figure 3.24: Human NSCs differentiated on molybdenum disulfide ( $\text{MoS}_2$ ). Phase contrast image showing hNSCs differentiated on molybdenum disulfide. (Scale bar:  $20 \mu\text{m}$ )

### Human NSC alignment on flexible polymeric substrates

For potential therapeutic applications in regenerative medicine, it is crucial to demonstrate the alignment and enhanced neuronal differentiation using flexible and biocompatible polymeric substrates which can be transplanted *in vivo*. We thus reproduced our results using flexible and biocompatible polymeric substrates made from polydimethylsiloxane (PDMS), a polymer which has been widely used for implantable neural devices such as flexible microelectrodes and three-dimensional scaffolds for tissue engineering [256, 257]. We prepared monolayers of SiNPs on thin, flexible PDMS substrates by stamping the PDMS substrates on monolayers of SiNPs generated on glass cover slips. The stamping led to clean and complete transfer of the SiNP monolayers on the PDMS surface (Figure 3.25a-b). We then dipped the PDMS substrates having

SiNPs into a solution of GO and dried the substrates using a stream of pure nitrogen gas. We achieved high-quality of SiNP monolayers coated with GO using PDMS. Control substrates were similarly prepared using PDMS polymer instead of glass. We then coated these substrates with laminin and differentiated the hNSCs as before. We observed that the differentiating hNSCs showed excellent alignment of axons on the PDMS substrates containing GO and SiNP-GO. SEM image analysis confirmed that the presence of SiNP-GO led to the alignment of axons as previously observed (Figure 3.25c). Immunostaining confirmed the presence of neuronal marker TuJ1 and axonal marker GAP43 (Figure 3.25d). We believe our results using flexible implantable polymeric substrates further demonstrates the potential of using SiNP-GO as a new hybrid material for enhancing neuronal differentiation and aligning axons, thus hastening the functional recovery of injured spinal cords.

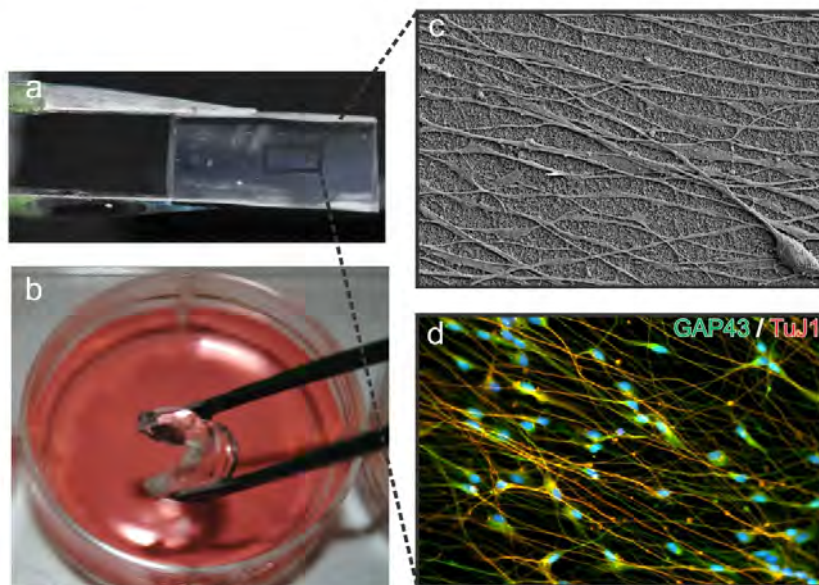


Figure 3.25: Axonal Alignment of differentiated hNSCs on SiNP-GO on flexible and biocompatible substrates made from polydimethylsiloxane (PDMS). (a) SiNP-GO monolayer on PDMS. (b) Flexible PDMS substrate with SiNP-GO in media for culturing hNSCs. (c) SEM image of SiNP-GO on PDMS substrate showing highly aligned axons from hNSCs on Day 14. (d) Immunocytochemistry results showing the expression of neuronal marker TuJ1 and axonal marker GAP43 in hNSCs.

### 3.3.3 Conclusions

In summary, we have demonstrated that the extracellular microenvironment consisting of nanotopographical features decorated with GO provides instructive physical cues that lead to enhanced neuronal differentiation of hNSCs along with significant axonal alignment. We also demonstrated the alignment of differentiating hNSCs on implantable, flexible polymeric substrates, which has tremendous potential use in regenerative medicine. However, we believe a better understanding of the underlying principles that govern the alignment of axons and the angle of their orientation would allow us to completely manipulate the direction of alignment of axons. We envision that the directional growth of axons using SiNP-GO can potentially be applied to developing GO-based materials for transplanting hNSCs into injured sites of the central nervous system in order to efficiently repair impaired communication. Overall, we believe our hybrid nanostructures comprised of a nanoparticle monolayers coated with GO have tremendous implications for the potential use of GO as a component for ECM especially in the field of neurobiology.

### 3.3.4 Materials and Methods

#### **Synthesis of chemically derived graphene, pristine graphene and MoS<sub>2</sub> nanoflakes**

Chemically derived graphene (CDG) or graphene oxide was obtained by the exfoliation of graphite oxide made through the modified Hummers method. Details of this method can be found elsewhere [258]. Thin films of graphene oxide can be formed from this suspension either by dip coating, spin coating, drop-casting or vacuum filtration methods.

Chemical vapor deposition (CVD) of graphene was done on copper by modifying the conditions mentioned in [259,260] to obtain large area graphene. Copper foil (Alfa Aesar, item No.13382) was annealed in Argon atmosphere for 30 mins at 1000°C and then methane was allowed into the furnace for two hours in the presence of argon at 1000°C. Graphene thus formed on copper was transferred onto glass substrates after spin coating PMMA (poly(methyl methacrylate)) and dissolving copper using 1M iron

chloride solution [260].

Bulk MoS<sub>2</sub> powder was purchased from Sigma-Aldrich (item number 69860) and exfoliated using lithium intercalation method to produce an aqueous suspension of exfoliated MoS<sub>2</sub> [261]. Thin films were made on glass substrates using vacuum filtration method and single layer was confirmed through optical microscopy and AFM images.

### **Preparation of different substrates**

The ECM protein in our experiments is laminin, which is essential for the adhesion, growth, and differentiation of hNSCs. Furthermore, ECM protein patterns and nanotopographical features have been shown to play a significant role in controlling the polarity of hNSCs and influence their neuronal differentiation [68, 71, 73]. We thus created nanotopographical features within the ECM using monolayers of positively charged silica nanoparticles (300 nm), as we have previously demonstrated [85, 145], and coated these monolayers with GO. Laminin was then adsorbed on these hybrid films to facilitate the attachment of hNSCs. We show that by using SiNP monolayers coated with GO, hNSCs not only align, but also show a remarkable increase in the expression of neuronal markers. We thus believe that incorporating GO along with nanotopographical features into the microenvironment of hNSCs provide significant advantages for the differentiation of hNSCs into neurons.

To prepare SiNP monolayers cover glass (Number 1, 22 mm x 22 mm; VWR) was cut equally into smaller pieces (18 mm x 6 mm) and sonicated in Nanopure water (18.2 mOhm) for 10 mins and then cleaned in piranha solution (a 3:1 mixture of sulphuric acid and hydrogen peroxide) for 10 min (Caution: Piranha solution is extremely corrosive). The glass coverslips were then washed again in Nanopure water (18.2 Mohm) and dried under a stream of pure nitrogen. To generate films of nanotopographical features, 300 nm silicon oxide nanoparticles (SiNPs, Corpuscular Inc) were utilized. The washed cover slips were centrifuged at 2000 RPM for 2 min in a 2 mL eppendorf tube containing 25 mg/mL of the positively charged (amine terminated) SiNP solution. The substrates were then washed with Nanopure water and dried under a stream of pure nitrogen. The cover slips were then rinsed thoroughly with ethanol and dried under nitrogen. They

were then baked at 100°C in an oven for 10 min.

Graphene Oxide (GO), which is negatively charged, was assembled on glass cover slips through electrostatic interactions. Specifically, these glass cover slips were first functionalized with self-assembled monolayers of positively charged APTES using a well-established protocol [145]. Each positively charged glass cover slip was then simply dipped once into a concentrated solution of nanometer sized GO (250 nm, 0.6 mg/mL) and dried using a stream of nitrogen. Furthermore, we generated substrates having nanotopographical features within the ECM using monolayers of positively charged silica nanoparticles (SiNP, 300 nm). The monolayers were fabricated using centrifugation as previously reported [145]. The substrates having the nanoparticles were then dipped into a concentrated solution of GO (0.6 mg/mL) as before and dried under a stream of nitrogen. As controls, we used bare glass and generated substrates having only SiNPs (without GO) as shown in Figure 3.18. The presence of GO on the substrates was confirmed using Raman spectroscopy and scanning electron microscopy (SEM) (Figure 3.26).

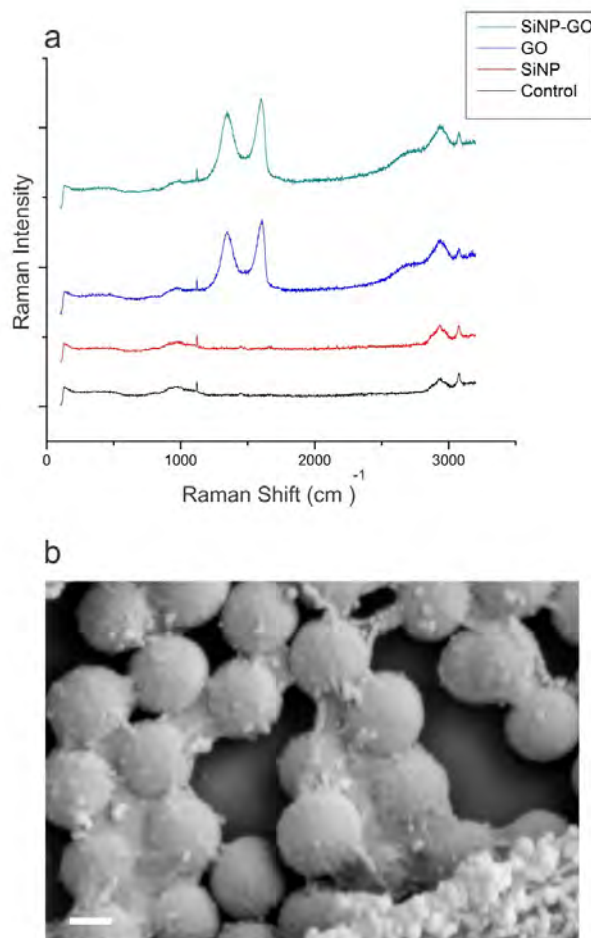


Figure 3.26: Raman Spectroscopy and SEM confirming the presence of graphene oxide. (a) raman Spectroscopy imaging shows the presence of the characteristic D and G bands on graphene oxide. The bare glass substrate and the substrate having on SiNP do not show the characteristic bands. (b) SEM image of SiNP-GO coated with laminin clearly shows the presence of GO on the SiNPs. (Scale bar: 200 nm)

### Human neural stem cell (hNSC) culture and differentiation

Human neural stem cell line (ReNCell VM, Millipore) was purchased and routinely expanded according to the manufactures protocol. The hNSCs were maintained in laminin (Sigma, 20  $\mu\text{g}/\text{ml}$ ) coated culture dishes precoated with poly-L-lysine (10  $\mu\text{g}/\text{ml}$ ) in ReNCell VM media (Millipore) supplemented with the antibiotics, gentamicin (Life Technologies), in the presence of basic fibroblast growth factor (bFGF-2, 20 ng/ml, Millipore) and epidermal growth factor (EGF, 20 mg/ml, Peprotech). All of the cells were

maintained at 37°C in a humidified atmosphere of 5% CO<sub>2</sub>. For consistency, the experiments were carried out on cells between passages 2 and 5. Neural differentiation was initiated by changing the medium to basal medium (without bFGF-2 and EGF) on the different substrates (SiNP, GO, SiNP-GO and control glass) coated with laminin. The cells were allowed to differentiate for 14 days with the basal medium in each being exchanged every other day.

### **Image analysis**

Image analysis on images taken from scanning electron microscopy was done to determine the axonal alignment and axonal length. Alignment is recorded by tracing axons through Adobe Photoshop software and measuring linear angle from connected cell bodies. Axonal length is done using a similar method by tracing axons and calculating the pixels spanned in Adobe Photoshop. Once the number of pixels has been obtained, it is converted to  $\mu\text{m}$  by referencing the amount of pixels the scale bar spanned. Since there needs to be a reference angle, SEM images are rotated so that the general directions of axons are similar among all conditions. The number of cells participated in image analysis is one hundred per condition. Data analysis was conducted after alignment angles were recorded for all four conditions. Due to the nature of sample loading of SEM, angles of axons are not a good statistical indicator of alignment. Instead, the angle of standard deviation is the better statistical representative of the effects of our platform.

### **Cell viability assay**

The percentage of viable cells on the different substrates was determined after 3 weeks of differentiation using the MTS cell viability assay following standard protocols described by the manufacturer. All experiments were conducted in triplicate and averaged. The data is represented as formazan absorbance at 490 nm, considering the differentiated hNSCs on SiNP-GO as 100% viable.

## **Immunocytochemistry**

To investigate the extent of neuronal differentiation, at Day 14, the basal medium was removed and the cells fixed for 15 minutes in Formalin solution (Sigma) followed by two PBS washes. Cells were permeabilized with 0.1% Triton X-100 in PBS for 10 minutes and non-specific binding was blocked with 5% normal goat serum (NGS, Life Technologies) in PBS for 1 hour at room temperature. To study neuronal differentiation, antibodies against neuronal markers were used. Mouse primary antibodies were used against TuJ1 (1:500, Covance), NeuN (1:100, Millipore) and rabbit primary antibodies were used against Synapsin (1:100, Santa Cruz Biotechnology) and MAP2 (1:100, Cell Signaling). The fixed samples were incubated overnight at 4°C in solutions of primary antibodies in PBS containing 10% NGS. After washing three times with PBS, the samples were incubated for 1 h at room temperature in solution of anti-mouse secondary antibody labeled with Alexa-Fluor<sup>®</sup>647 or Alexa-Fluor<sup>®</sup>546 and anti-rabbit secondary antibody labeled with Alexa-Fluor<sup>®</sup>546 or Alexa-Fluor<sup>®</sup>488 (1:200, Life Technologies), Hoechst 33342 (1:500, Life Technologies) in PBS containing 10% NGS to observe neuronal differentiation. After washing the samples thrice with PBS, the substrates were mounted on glass slides using ProLong<sup>®</sup> antifade (Life Technologies) to minimize photobleaching. The mounted samples were imaged using Nikon TE2000 Fluorescence Microscope.

## **PCR analysis**

Total RNA was extracted using Trizol Reagent (Life Technologies) and the mRNA expression level of TuJ1, MAP2, GAP43 and nestin were analyzed using Reverse Transcriptase PCR (RT-PCR) and quantitative PCR (qPCR). Specifically, cDNA was generated from 1  $\mu$ g of total RNA using the Superscript III First-Strand Synthesis System (Life Technologies). Analysis of mRNA was then accomplished using primers specific to each of the target mRNAs. RT-PCR reactions were performed in a Mastercycler Ep gradient S (Eppendorf) and images were captured using a Gel Logic 112 (Carestream) imaging system. qPCR reactions were performed using SYBR Green PCR

Master Mix (Applied Biosystems) in a StepOnePlus Real-Time PCR System (Applied Biosystems) and the resulting  $C_t$  values were normalized to Gapdh. Standard cycling conditions were used for all reactions with a melting temperature of 60°C. Primers are listed below in Table 3.2.

Table 3.2: Primers for PCR analysis

Gene	F Primer	R Primer	Size(bp)
FAK	5'-CAATGCCTCCAAATTGCCT-3'	5'-TCCATCCTCATCCGTTCTTC-3'	157
GAPDH	5'-ATGACTCTACCCACGGCAAG-3'	5'-GGAAGATGGTGATGGGTTTC-3'	87
Nestin	5'-GGAAGAGAACCTGGGAAAGG-3'	5'-CTTGGTCCTTCTCCACCGTA-3'	122
GAP43	5'-AACCTGAGGCTGACCAAGAA-3'	5'-GGGACTTCAGAGTGGAGCTG-3'	118
MAP2	5'-GAGAATGGGATCAACGGAGA-3'	5'-CTGCTACAGCCTCAGCAGTG-3'	100
TUJ1	5'-ACTTTATCTTCGGTCAGAGTG-3'	5'-CTCACGACATCCAGGACTGA-3'	97

## Chapter 4

### **Developing Biosensors for Highly Sensitive and Selective Detection of Biomarkers**

In an effort to develop biosensors capable of quantifying the expression of various stem cell markers, and the markers for differentiated cells, we began with optimizing the sensing abilities of our biosensors using already established markers such as cancer biomarkers. While the application of these biosensors for detecting markers for stem cell biology is currently under way, in this chapter will we see the fabrication and applications of biosensors based on hybrid nanostructures for detecting well-established biomarkers in a highly selective manner having high sensitivity.

## 4.1 Graphene-Encapsulated Nanoparticle-based Biosensor for the Selective Detection of Cancer Biomarkers

### 4.1.1 Introduction

Nanomaterials such as silicon nanowires (SiNWs) [262,263], carbon nanotubes (CNTs) [264–267], and graphene [84,268], have gained much attention for use in electrical biosensors due to their nanoscopic and electrical properties. For instance, SiNWs and CNTs can be integrated into field-effect transistors (FETs) to detect small amounts of target biomolecules with high sensitivity and selectivity by measuring electrical disturbances induced by the binding of these biomolecules to the surface of the nanostructure [87,269]. The detection of biomarker proteins with high sensitivity and selectivity is vital for the early diagnosis of many diseases such as cancer and HIV. For this purpose, carbon-based nanomaterials like CNTs and graphene have attracted significant attention for fabricating highly sensitive FET-based biosensors [83,84,267,269–273]. In particular, the use of graphene in FET-based biosensors is becoming more and more appealing not only due to its unique properties such as higher 2-D electrical conductivity, superb mechanical flexibility, large surface area, and high chemical and thermal stability, but also due to its ability to overcome the limitations of CNTs such as variations in electrical properties of CNT-based devices and the limited surface area of CNTs [81,246,260,274–279]. Nevertheless, there have been only a few reports on developing graphene FET-based biosensors [83,280], and their potential as biosensors has not been fully explored. It is therefore be critical develop nanoscopic graphene-based biosensors that are simple in device structure, small in size, allow label-free detection and real-time monitoring of biomarkers, all of which are essential criteria for biosensors. A key challenge in the above requirements is the achievement of both, well-organized two- or three-dimensional graphene structures, in microscopic-/nanoscopic biosensing devices and well-defined bioconjugation chemistry on graphene.

Herein, we demonstrate a novel strategy for the fabrication and application of a reduced graphene oxide (rGO) [258,281] encapsulated nanoparticle (NP)-based FET

biosensor for selective and sensitive detection of key biomarker proteins for breast cancer. It is important to note that in this manuscript we have used Human Epidermal growth factor Receptor 2 (HER2) and Epidermal Growth Factor Receptor (EGFR), which are known to be over-expressed in breast cancers [282–284], only as a proof-of-concept to demonstrate the high sensitivity and selectivity of our graphene-encapsulated NP biosensor. This biosensor could be used to detect any important cancer markers with relative ease.

#### 4.1.2 Results and Discussion

##### Fabrication of arrays of graphene-encapsulated nanoparticles

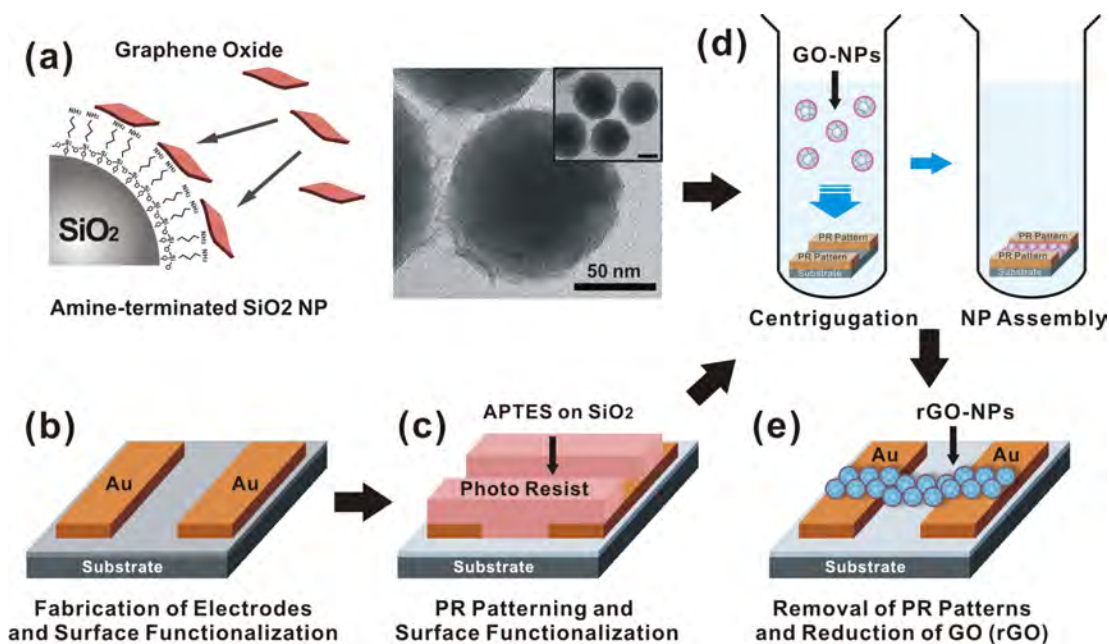


Figure 4.1: Fabrication process of biomolecular sensor based on graphene-coated NPs. (a) Schematic diagram of GO assembly on amine-functionalized NP and TEM image of NP coated with GO. (b) Fabrication of metal electrode on the oxide substrate and surface modification for the assembly of GO-NP. (c) Photoresist (PR) patterns on the metal electrodes. (d) GO-NP assembly in the centrifuge tube. (e) Removal of PR patterns and reduction of GO coated on the NP surface [85].

In our typical experiments for fabricating graphene encapsulated NPs-based biosensors, individual silicon oxide NPs (100 nm), functionalized with 3-aminopropyltriethoxysilane (APTES), were first coated with thin layers of graphene oxide (GO), which prevent

aggregation and maintain high electrical conductivity (Figure 4.1). This was mainly achieved via the electrostatic interaction between the negatively charged GO (Figure 4.2) and the positively charged silicon oxide NPs.

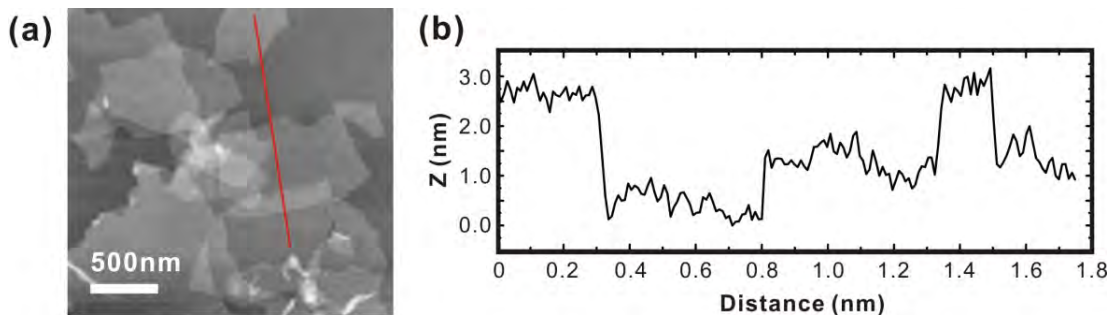


Figure 4.2: (a) AFM topography image of GO pieces assembled on SiO<sub>2</sub> substrate. (b) The height profile along the red line in the AFM image [85].

The GO solution (0.05mg/ml in deionized water) was simply injected into the NP solution (5 mg/ml), wherein the negatively charged GO assembled on the positively charged NP surface until equilibrium coverage was reached [285–287]. The transmission electron microscopy (TEM) image of the GO-coated NPs clearly shows the uniform assembly and saturation density of GO on the NP surface (Figure 4.1a). The GO thickness on the surface of the NPs was 5 nm, as measured from HR-TEM. As seen in the image, the NPs were connected through a film of GO which was used as an electrical carrier after its reduction to rGO. For efficient use of NP junctions as electrical channels, it was imperative to assemble the NPs with high density on the device. The scanning electron microscopy (SEM) images show well-defined, dense rGO-NP patterns uniformly covering a large area of the silicon oxide substrate (Figure 4.3a,b).

Furthermore, our modified self-assembly method (utilizing centrifugation) allowed us to assemble NPs with high density in a short span and by using minimal amount and concentration of the NP solution. Importantly, the high surface-to-volume ratio of the GO-encapsulated NPs can generate 3-D electrical surfaces that significantly enhance detection limits and enable label-free, highly reproducible detection of clinically important cancer markers.

One of the most attractive and advantageous aspects of our graphene-encapsulated NP biosensor is its ease of fabrication and measurement (Figure 4.3). The device was

fabricated using photolithography, followed by a lift-off process, both of which have been well established [287, 288]. We first generated gold electrodes on a silicon oxide substrate using photolithography and lift-off. To generate arrays of GO-NPs, we patterned the photoresist (AZ 5214) on the substrates with gold electrodes using photolithography. The exposed silicon oxide surface and gold surface were functionalized with self assembled monolayers (SAMs) of positively charged APTES and cysteamine, respectively. The SAM formation promoted the assembly of the negatively charged GO-NPs (through electrostatic interactions) [288, 289]. We then employed a relatively simple technique involving centrifugation for the uniform assembly of GO-NPs on the positively charged SAMs. In this technique, the substrate containing the patterned photoresist along with the SAMs was centrifuged in a solution of GO-NPs at 2000 RPM for 3 min in a centrifuge tube. Despite a low concentration of GO-NPs, we were able to achieve uniform films of NPs having a high density in a reproducible manner. This is in stark contrast to the standard methods used for assembling NPs on surfaces. Other methods generally rely on using larger volumes of solution containing higher concentrations of NPs, where contact of the NPs with the surface is mainly made through infrequent Brownian motion, which eventually causes the NP assembly. On the other hand, our centrifugation technique achieved uniform, highly dense layers of graphene-encapsulated NPs over a large area, in a short time span (Figure 4.3a,b). We then generated a uniform NP array by removing the patterned photoresist using acetone. The removal of photoresist did not disturb the assembly of GO-NPs. To render the insulating GO electrically conductive, we reduced the GO through an overnight exposure to hydrazine vapor. Our method of fabricating the device is very powerful as it can be integrated with conventional microfabrication processes, which makes our device cost effective and relatively easy to produce on a large scale.

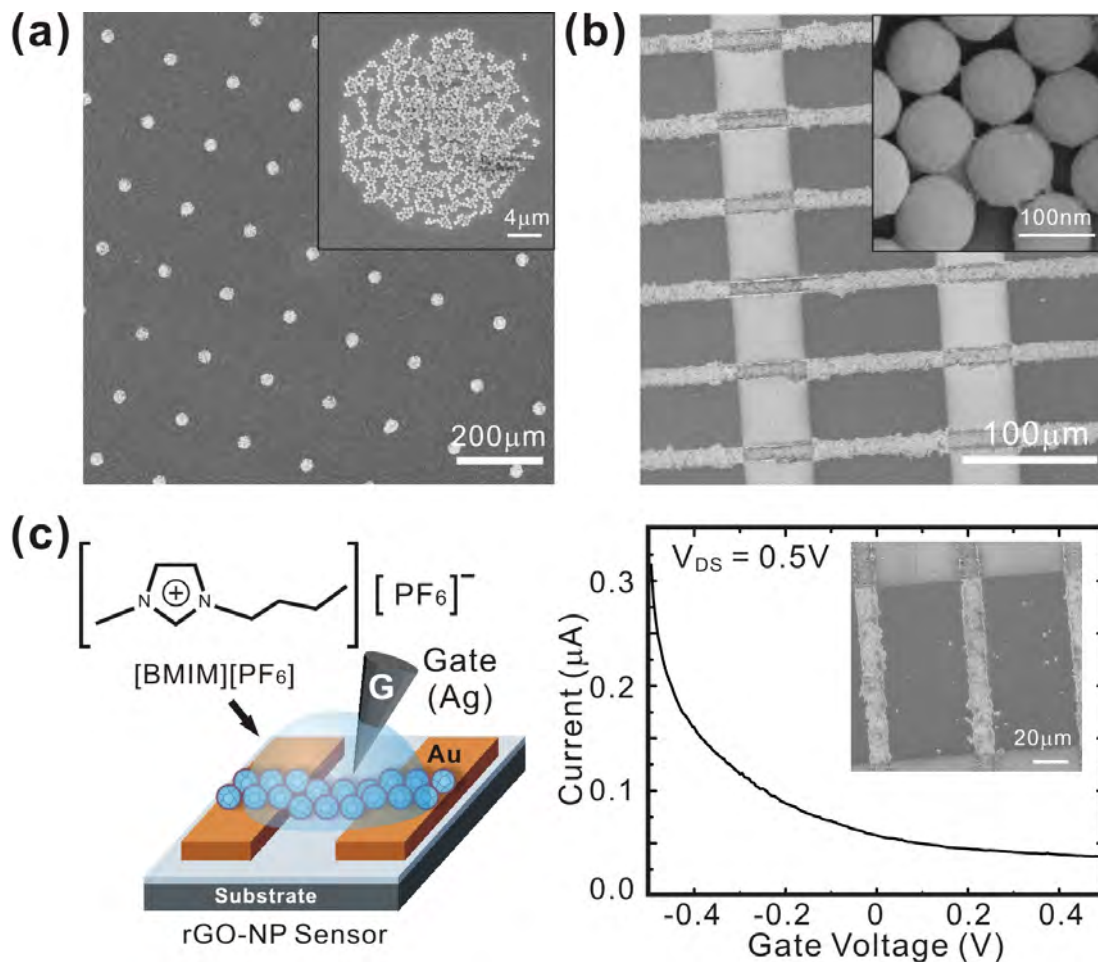


Figure 4.3: Reduced GO-NP patterns and the electrical property of the rGO-NP device. (a) SEM images of rGO-NPs assembled on a large area. (b) The SEM images of biosensors consisting of rGO-NP array with gold electrodes. (c) The schematic diagram of measuring process of gate effect utilizing ionic liquid (left diagram) and gate effect of ten rGO-NP junctions with 50mA channel length (right graph) [85].

### Gating effect of rGO-NP device

One of the key barriers of using graphene FET-based biosensors is to operate the device at physiological conditions (e.g. different pH and salt concentrations), in which different ionic environments affect the conductivity of graphene FET-based biosensors [290]. To study the working conditions of our graphene FET-based biosensors in aqueous solutions, we measured the gating effect of our rGO-NP-based biosensor using an ionic liquid gate (Figure 4.3c). A typical source-drain current vs. gate potential plot was obtained in an ionic liquid, 1-butyl-3-methylimidazolium tetrafluoroborate (BmimPF<sub>6</sub>).

In an ionic liquid, the high concentration of ions renders the thickness of the diffusion layer negligible, thus making it useful as a gate insulating layer. Silver (Ag) wire was used as the reference electrode for the measurements in the ionic liquid. The gating effect observed in our GO-NP devices was similar to that observed in rGO thin-film transistors that have ambipolar conduction and p-type behavior near zero gate voltage [287,291]. In our case, the top-gate bias was swept with 0.05V/sec sweep speed under the source-drain bias of 0.5V span (Figure 4.3c).

### **Sensitivity and selectivity of rGO-NP biosensor for detecting HER2**

The sensitivity of our rGO-NP devices, functionalized with HER2 mAbs, was determined by measuring the changes in conductance as the solution concentration of HER2 was varied from 10 fM to 1  $\mu$ M (Figure 4.4d). In all our experiments, only 1  $\mu$ L of each solution was added onto the device. Representative time-dependent data shows that on the addition of a 10 fM solution of HER2, no change in conductance was observed. However on increasing the concentration to 1 pM, a decrease in conductance of the p-type rGO-NP device was observed due to the binding of HER2 to the mAbs. As the concentrations of the solutions were subsequently increased, a concentration dependent decrease in the conductance of the rGO-NP device was observed. Thus, the detection limit of our biosensor was observed to be 1 pM in a solution containing only HER2 protein, which is a significant improvement over thin-film-transistor-type sensors based on the graphene [83,265,273]. The observed change in electrical conductivity can be attributed to the p-type characteristic of the rGO-NP FET-based sensors as the amine groups on the protein surface are positively charged. Binding of these positively charged target-biomolecules such as HER2 or EGFR to the rGO surface will induce positive potential gating effects that generate reduced hole density and electrical conductance.



Figure 4.4: Real-time detection of cancer marker, HER2. (a) The preparation of rGO-NP device. (b) Surface functionalization of rGO for immobilizing the antibody. (c) Measuring conductance of the devices when the target protein is introduced. (d) The sensitivity of the biosensor (relative conductance change, %) in response to the concentration of HER2 with  $V_{DS} = 1V$  and  $V_g = 0V$ . (e) The selectivity of the biosensor in response to PBS buffer, BSA with  $50\mu\text{g/ml}$  and HER2 (100 pM and 1  $\mu\text{M}$ ). (f) Sensor sensitivity (relative conductance change, %) as a function of the HER2 concentration with  $V_{DS} = 1V$  and  $V_g = 0V$ . Please note that all experiments were performed multiple times ( $n = 30$ ) to collect statistical data (with error bars) and confirm the reproducibility/robustness of our biosensing system [85].

To test the selectivity of our graphene FET-based biosensors, we further investigated the selective detection of our device in competitive binding studies with bovine serum albumin (BSA) (Figure 4.4e). Time-dependent conductance measurements recorded on our rGO-NP devices, functionalized with HER2 mAbs, showed no change in conductance on adding PBS, and  $50\mu\text{g/ml}$  BSA. However, on adding  $1\mu\text{L}$  of 100 pM solution of HER2 to the BSA solution on the device, a rapid and sharp change in conductance was observed, demonstrating the high selectivity of our device. On adding the  $1\mu\text{M}$  solution of HER2, the conductance further decreased rapidly and drastically. In spite of the presence of a solution having a very high concentration of BSA ( $50\mu\text{g/ml}$ ), the detection limit of the target protein, HER2, was 100 pM, which clearly demonstrates

the remarkable sensitivity and selectivity of our rGO-NP biosensor.

Figure 4.4f shows the sensitivity (relative conductance change) of our biosensor as a function of the HER2 concentration. The lowest HER2 concentration level that can be detected is 1 pM which shows a decrease in conductance (3.9 %). Similar to the non-linear behavior of CNT FET-based sensors [292–294], our sensor responses increase non-linearly with the increase in the HER2 concentration from 1 pM to 1  $\mu$ M, which clearly shows that the sensor response is due to the binding of HER2 to the HER2 mAbs.

### **Sensitivity and selectivity of rGO-NP biosensor for detecting EGFR**

In addition to HER2, we similarly investigated the sensitivity and selectivity of our device for detecting EGFR. We functionalized the device with EGFR mAbs and observed the change in conductance on the addition of EGFR solution. The trend in conductance change was similar to that observed with HER2, with the detection limit being 100 pM for EGFR, and 10 nM in the presence of BSA (50  $\mu$ g/ml) (Figure 4.5). We believe the slight decrease in sensitivity for detecting EGFR (relative to HER2) might be due to the difference in binding affinities of the two mAbs to their respective proteins. However, the result demonstrates the capacity of our biosensor to detect different biomarkers in a sensitive and selective manner.

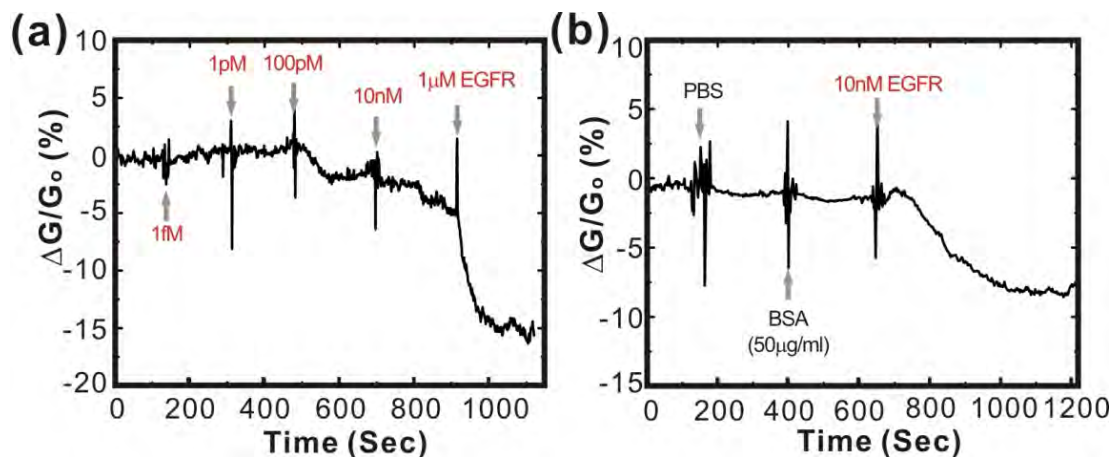


Figure 4.5: Real-time detection of cancer marker, EGFR. (a) Biosensor sensitivity (relative conductance change, %) in response to the concentration of EGFR with  $V_{DS} = 1V$  and  $V_g = 0V$ . (b) The biosensor selectivity in response to PBS buffer, BSA with  $50 \mu\text{g/ml}$  and  $10 \text{ nM}$  EGFR [85].

### 4.1.3 Conclusions

In conclusion, we have demonstrated the application of graphene encapsulated NP-based biosensor for highly selective and sensitive detection of cancer biomarkers by using surface chemistry principles combined with nanomaterials and micro-/nanofabrication techniques. The novel three-dimensional structure of graphene encapsulated NP significantly increases the surface-to-volume ratio in FET-type biosensors, thereby improving the detection limits ( $1 \text{ pM}$  of HER2 and  $100 \text{ pM}$  of EGFR) for our target cancer biomarkers. In addition, we also demonstrated the highly selective nature of our biosensor as we detected low concentrations of our target cancer biomarkers even in the presence of a highly concentrated BSA solution. The ease of fabrication and biocompatibility, along with excellent electrochemical and electrical properties of graphene nanocomposites, makes our graphene encapsulated NP-based biosensor an ideal candidate for future biosensing applications within a clinical setting.

#### 4.1.4 Materials and Methods

##### Preparation of reduced graphene oxide and SiO<sub>2</sub> NPs

GO was obtained from SP-1 graphite utilizing the modified Hummer method [258]. For the GO assembly on the surface of NPs, GO suspension was injected into the nanoparticle solution for 10min, and GO-NPs were separated from GO solution using a centrifuge. SiO<sub>2</sub> NP (100 nm) solution was purchased from Corpuscular Inc. For GO-NP assembly, the photo resist-patterned substrate was placed in the NP solution, and GO-NPs were assembled on the substrate by applying centrifugal force. After the deposition of GO-NPs on the substrate, the GO on the NP surface, having the low conductance, was reduced to graphene by exposure to hydrazine vapor overnight.

##### Synthesis of 4-(pyren-1-yl)butanal

10 mL of methylene chloride was added to 1.097 g (4 mmol) of 4-(pyren-1-yl) butyl alcohol and stirred vigorously at room temperature for 10 min hour. The reaction was followed by addition of 1.292 g (1.5 Equilibrium) of PCC (Pyridinium chlorochromate) in 10 mL methylene chloride and the reaction mixture was stirred for 2 h. The reaction mixture was then diluted with 5 volumes of anhydrous ether (100 mL) and washed with 1:1 brine: water, saturated aq. Na<sub>2</sub>SO<sub>3</sub> solution, and brine, respectively, dried over anhydrous Na<sub>2</sub>SO<sub>4</sub> and concentrated to give the aldehyde. The crude product was purified by silica gel flash chromatography (hexanes: ethyl acetate, 9:1, rf: 0.4) to yield 1.06 g (97%). Most of the crude products were very clean and could be used directly for further applications.

##### Surface molecular patterning

3-Aminopropyltriethoxysilane (APTES) and cysteamine molecules used in forming SAMs, and solvents were purchased from Sigma-Aldrich. For the patterning of APTES SAM on SiO<sub>2</sub>, the photoresist (AZ5214) was first patterned by photolithography using a short baking time (<10 min in 95°C). The patterned substrate was placed in the APTES solution (1:500 (v/v) in anhydrous hexane) for 7 min. For the patterning of APTES on

the on SiO<sub>2</sub> layer, the substrate with photoresist patterns was placed in an APTES solution (1:500 (v/v) in anhydrous hexane) for 10 min. The photoresist was then removed with acetone.

### **Metal deposition and measurement of graphene devices**

For the electrode fabrication, the photoresist was first patterned on the substrate. Ti/Au (10/30nm) was then deposited on the substrate and the remaining photoresist was then removed with acetone for the lift-off process. A Keithley-4200 semiconductor parameter analyzer was used for measurement and data collection.

### **Functionalization the rGO-NPs with monoclonal antibodies**

The bioconjugation chemistry is well established and involved three basic steps.[2,10] First, the reduced GO surface was functionalized with 4-(pyren-1-yl)butanal via  $\pi$ - $\pi$  interactions by incubating the device in a methanol solution (1:500) of 4-(pyren-1-yl)butanal for 30 min. Second, the aldehyde groups were coupled to the amine groups of the monoclonal HER2 or EGFR antibodies (1:50) through reductive amination in the presence of 4 mM sodium cyanoborohydride in PBS (pH 7.4) for two hours. Third, unreacted aldehyde groups were blocked using 100 mM ethanolamine in a similar manner to prevent non-specific interactions of proteins. Finally, we rinsed the device in a continuous flow of PBS (pH 7.4) for 10 min. We show that the surface chemistry used in our device plays a crucial role in achieving highly selective and sensitive detection of HER2 or EGFR protein. Furthermore, due to the large surface-to-volume ratio of the rGO-NPs, our biosensors were highly efficient as compared to the thin-film transistor-based biosensors.

## 4.2 Label-free Polypeptide-based Enzyme Detection Using a Graphene-nanoparticle Hybrid Sensor

### 4.2.1 Introduction

Over the last few decades, the carbon nanomaterial-based electrical detection of chemical and biological molecules has gained much attention with its extensive applications to genomic, proteomic and environmental analysis as well as for clinical diagnosis [81, 246, 260, 275–279, 295–298]. Typical carbon nanomaterial-based electrical detection systems are composed of two components: a biological recognition element and a signal transduction element. These devices are able to detect minute concentrations of target molecules by measuring the change in electrical conductance that results from the binding of target molecules to the surface of the carbon nanomaterial [83–85, 268, 273]. However, the sensitivity as well as selectivity of these devices depends heavily on the electrical properties of the nanomaterial used in the system and on the interfacial chemistry that exists between the nanomaterial and the receptor molecules. Carbon nanotube field-effect transistors (CNT-FETs) currently lead the field and are one of the most extensively developed systems [292–294, 299–301]. This is due to the excellent electrical properties and the relatively well-developed surface chemistry of CNTs. However, certain limitations do exist with CNT-based electrical detection devices. These include inconsistencies in the assembly of CNTs resulting in device unreliability, limits in its surface area, and a high-cost of fabrication.

An alternative nanomaterial, which has the potential to overcome the aforementioned limitations of CNTs, is graphene. Graphene consists of a single-atom-thick planar sheet of carbon atoms that are arranged in a perfect honeycomb lattice and has a zero-band gap. It forms ideal two-dimensional carbon crystals that show high electrical conductivity in the absence of any doping even at room temperature. Graphene also demonstrates superb mechanical flexibility and high chemical/thermal stability. Furthermore, due to its low noise level, graphene is extremely sensitive to perturbations in electrical conductance that are induced by biological reactions. These biological reactions can include, but are not limited to, the enzyme-mediated degradation of a target

substrate and the binding of proteins to other biomolecules. There have been a number of graphene-based protein sensors with detection limits on the  $\mu\text{M}$  scale [83, 268, 273]. However, there have been limited demonstrations utilizing graphene for the detection of enzymes, with most demonstrations relying on antibody-mediated recognition of their target proteins [273, 302, 303]. Enzyme detection is an especially clinically relevant issue as it has been reported that the enzyme levels found *in vivo* are strongly correlated with the diagnosis, prognosis, and treatment of many diseases such as HIV, cancer, and diabetes. Therefore, to improve our ability to detect enzyme levels and to enhance the clinical potential of graphene-based biosensors, it is possible to take advantage of graphenes sensitivity to changes in electrical conductance in order to detect the enzymatic cleavage of target peptides that are assembled on the sensor surface.

Herein, we report a novel approach for the detection of enzymes using a graphene-nanoparticle (NP) hybrid biosensor. This system can detect the activity of an enzyme and determine its concentration by measuring the change in electrical hysteresis that results from the interaction of the target enzyme with its corresponding substrate. In addition, we demonstrate its ability to achieve the sensitive and selective detection of the target enzyme. Similar electrical hysteretic behavior in carbon nanomaterial-based devices with gate have been observed previously and is presumably caused by charge transfer from neighboring adsorbates such as water molecules or from charge injection into the trap sites on the dielectric substrate [287]. However, this is the first report of NP-mediated electrical hysteresis in a graphene sensor. Moreover, the utilization of a hysteresis change for sensing is advantageous because the immobilization of specific enzymes on the graphene surface, which is required for field effect transistor-type sensors, is unnecessary in our system allowing us to preserve the superb electrical properties of graphene. The use of hysteresis as a detection method also allows graphene-based devices to overcome the low on-off ratio caused by the zero band gap of graphene. In the majority of previous studies [83–85, 268, 273], a Dirac shift or a conductance change at the fixed gate voltage that is associated with this Dirac shift when the specific target material was attached selectively on the graphene channel was utilized. When using only a Dirac shift for sensing, non-specific binding such as the physical attachment of

positively- or negatively-charged materials can also result in a Dirac voltage shift or conductance change. However, in our process, even though nonspecific binding on the channel occurred, the amount of electrical hysteresis of our devices did not change. Only when these devices were exposed to a specific condition, did the hysteresis phenomenon start to decrease. Specifically, our graphene-NP hybrid biosensor is composed of gold nanoparticles (AuNPs) that are assembled on a graphene surface using a functional polypeptide linker, which concomitantly functions as the substrate for the target enzyme. Proteolysis of the functional polypeptide linker by the target enzyme leads to disassembly of the NP layer and a measurable shift in electrical hysteresis that can be visualized in the gate sweep curve. This can then be used to quantify the enzyme concentration. AuNPs were chosen because they are able to store charge, resulting in hysteresis upon their release from the device surface [287]. In our case, as a proof-of-concept, we detected the activity of Carboxypeptidase B in order to demonstrate the high achievable sensitivity and selectivity of our graphene-NP hybrid biosensor [304]. This enzyme has been reported as a predictor of severe acute pancreatitis, which is an acute inflammatory condition of the pancreas. However, it is important to note that the reported biosensing method can be extended to detect any number of key enzymes, pH changes, and UV with the appropriate modification to the functional linker substrate.

#### 4.2.2 Results and Discussion

A schematic of our graphene-NP hybrid biosensor is depicted in Figure 4.6a. The device consists of gold source and drain electrodes that are connected by graphene channels [Figure 4.6b(i)]. The graphene channels are coated with a functional polypeptide linker that is specific for our target enzyme, Carboxypeptidase B, followed by a layer of AuNPs that have a negative charge on their surface, and a peripheral ionic liquid, which functions as the gate dielectric [Figure 4.6b(ii-iv)]. Introduction of Carboxypeptidase B would then initiate the hydrolysis of the specific enzyme substrate, which in this case is the functional polypeptide linkers. The degradation of the polypeptide linkers result in the release of AuNPs, which causes a hysteresis shift that can be measured using a silver gate electrode. The range of hysteresis shift has been found to be proportional to

the enzyme concentration and can therefore be used to determine the level of enzyme in the solution.

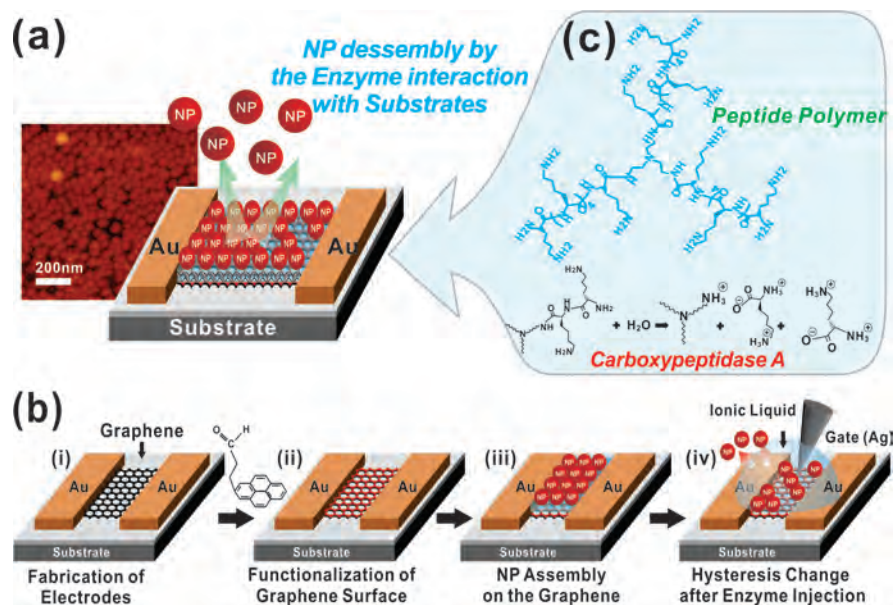


Figure 4.6: Schematic of the enzyme biosensor. (a) Graphene-nanoparticle hybrid devices for enzyme sensing. Fabrication process of the hybrid biosensor. (a) Fabrication of the graphene channel between the Au electrodes (i). Functionalization of the graphene surface with hydrophilic molecules (ii). Assembly of the functional peptide linker molecules and AuNPs on this polypeptide layer (iii). Sensing target biomolecules by measuring the change in electrical hysteresis (iv). (c) Chemical structure of the functional polypeptide linker molecule [305].

To fabricate the graphene-NP hybrid biosensor, the source and drain Au electrodes were first fabricated on a SiO<sub>2</sub> substrate via the lift-off process. Graphene was deposited and patterned as previously described[2] in order to form graphene channels between the Au electrodes [Figure 4.6b(i)]. Before assembling the AuNPs and the functional polypeptide linker molecules on the graphene surface, the surface was made hydrophilic through functionalization with 4-(pyren-1-yl)butanal, which occurs via  $\pi$ - $\pi$  interactions. Specifically, functionalization was achieved by incubating the device in a methanol solution (1:500) containing 4-(pyren-1-yl)butanal for 30 minutes [Figure 4.6b(ii)]. Next, the aldehyde groups of 4-(pyren-1-yl)butanal were coupled to the amine groups of the functional polypeptide linker through reductive amination for 6 hours. Once the graphene device, functionalized with polypeptide linker, was placed in the AuNP solution, the negatively charged AuNPs were able to self-assemble on the

positively charged functional polypeptide linker molecules via electrostatic interactions [Figure 4.6b(iii)]. Specifically, this is a result of the remaining positively charged amine groups on the functional polypeptide linkers. Finally, with the AuNPs assembled on the graphene surface, we were able to detect the electrical hysteresis and gate effect of our device utilizing an ionic liquid as the gate dielectric.

The fabrication method developed in our graphene-NP hybrid biosensor has several advantages over conventional graphene-based biosensors. First, we were able to fabricate high performance graphene-NP hybrid devices that have a large surface area available for biodetection and a high conductivity. This was accomplished at a high yield and uniformity by combining the properties of graphene with the nanoscopic features of the AuNPs [275]. Specifically, these properties allow for the development of biosensors that have high achievable current levels sufficient for the measurement of minute conductance changes regardless of the channel length between two electrodes in the devices (Figure 4.6 and Figure 4.7A1). As a result, our device provides a larger number of sites that can be conjugated with receptor molecules (e.g. antibody or functional polypeptide linker) in comparison with previous biosensors that used reduced graphene oxide. In addition, these reduced graphene oxide-based biosensors were limited by their low conductivity and limited achievable channel length (e.g. only a few micrometers) [276]. Second, the functionalization of the graphene surface with our functional polypeptide linker followed by assembly of AuNPs was accomplished using  $\pi$ - $\pi$  interactions (graphene-pyrene aldehyde) and electrostatic interactions (polypeptides-AuNPs). This method prevents the need to covalently bond the linker to the graphene surface, therefore preserving the superb electrical properties of graphene [306]. Finally, our fabrication method allows for the precise control of the number of graphene layers and can be used to deposit a large quantity of graphene on different substrates such as SiO<sub>2</sub>, metallic surfaces, or glass due to the flexible and stretchable properties of graphene. The devices can also be fabricated with conventional microfabrication techniques, and the entire process can be accomplished using only conventional microfabrication facilities. Therefore, our method allows us to fabricate graphene-based devices with present Si-based microelectronics, and would be readily accessible to the

present semiconductor industry. Collectively, our study presents a novel method that avoids the use of graphene oxide for the development of biosensors and provides a novel approach that combines the advantages provided by graphene and inorganic nanoparticles (e.g. metallic and semiconductive NPs) with the area of biosensing.

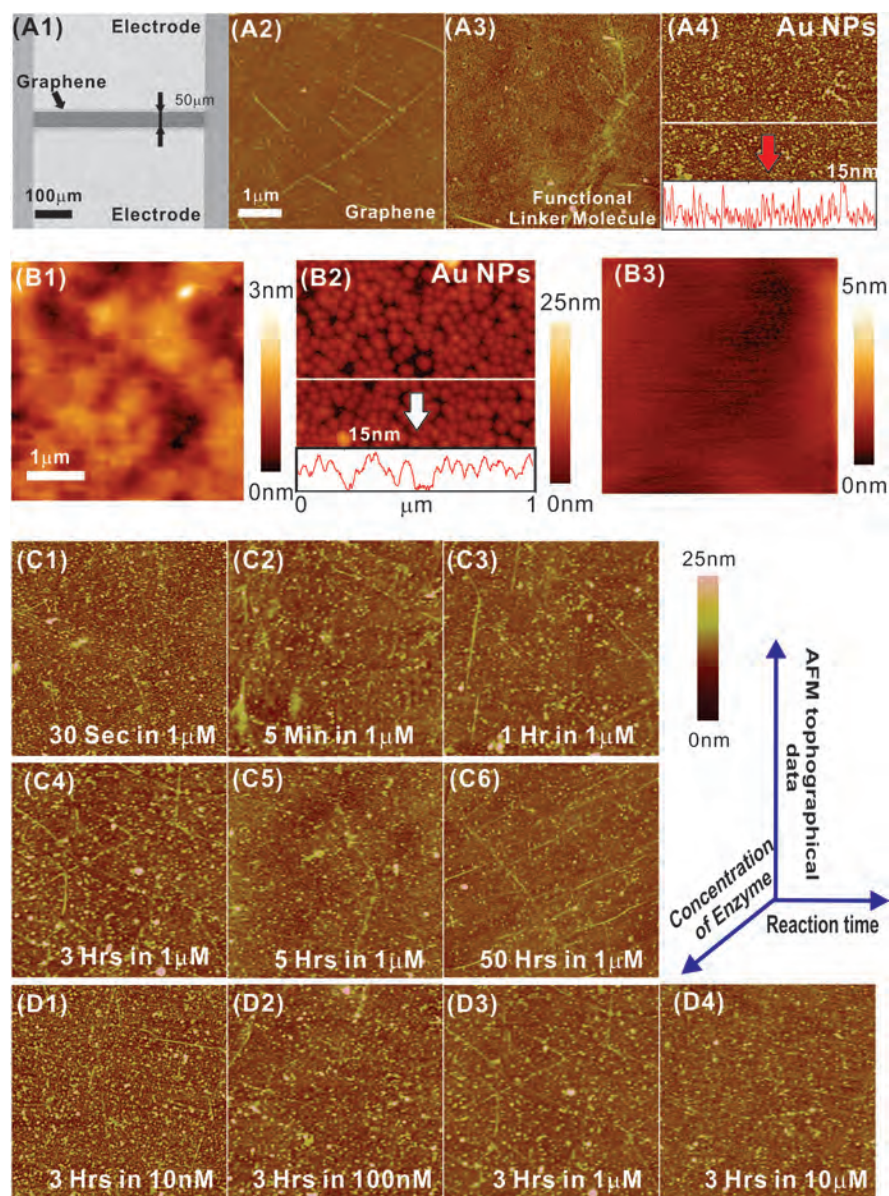


Figure 4.7: Characterization data of the biosensor using AFM and SEM. (A1) A SEM image of the junction between the Au electrodes, showing graphene channel (dark region) between two Au electrodes (bright area). AFM topography images of (A2) the graphene surface before the assembly of NPs and (A3) the graphene surface after the functionalization with linker molecules. (A4) An AFM image of AuNPs on the graphene surface. The height profile of the AFM image is shown below the image. (B1) An AFM topography image of the graphene surface before the assembly of NPs. (B2) An AFM image of AuNPs on the graphene surface. The height profile of the AFM image is shown below the image. (B3) An AFM topography image of graphene after exposure to a 10  $\mu\text{M}$  enzyme solution for 6 hours. (C1)-(C6) AFM topography images of graphene after exposure to a 1  $\mu\text{M}$  enzyme solution for from 30 sec to 50 hours, respectively. (D1)-(D4) AFM images after exposure to an enzyme solution with 10nM, 100nM, 1  $\mu\text{M}$  and 10  $\mu\text{M}$  for 3 hours, respectively [305].

Confirmation of graphene deposition followed by AuNP assembly in the junction between the Au electrodes was obtained using scanning electron microscopy (SEM) (Figure 4.7A1). The image shows that the two Au electrodes, separated by a  $50\ \mu\text{m}$  gap, are connected by a graphene channel that is  $420\ \mu\text{m}$  wide. In addition, after coating the graphene surface with the functional polypeptide linker, we confirmed that the negatively charged AuNPs (15 nm in diameter) successfully self-assembled as a monolayer on the graphene surface at a high density (Figure 4.7A4 and B2). This is mainly due to the large positive charge and the two-dimensional planar structure of the functional polypeptide linker. The negatively charged surface of the AuNPs also ensures that additional NPs are not assembled onto the underlying functional polypeptide linker. Therefore, the deposition of a single layer of AuNPs with high density was achieved on the graphene surface. It was also found that the complete disassembly of AuNPs was achieved after the device was exposed to a  $1\ \mu\text{M}$  Carboxypeptidase B enzyme solution for 50 hours (Figure 4.7C6) or a  $10\ \mu\text{M}$  solution for 3 hours (Figure 4.7D4).

The gating effect of our device was measured by employing an ionic liquid as the gate dielectric and a silver gate electrode. The use of an ionic liquid, which has a high ionic concentration, as the gate dielectric allowed the thickness of the diffusion layer to be considered negligible. It was found that the effect was similar to that observed in graphene transistors that have ambipolar conduction and no electrical hysteresis (Figure 4.8a upper graph) [291]. In our case, the top-gate bias was swept with a  $0.01\ \text{V}/\text{sec}$  sweep speed under a source-drain bias of  $0.1\ \text{V}$ . An ambipolar field effect was also observed with a Dirac point voltage ( $V_{\text{Dirac}}$ ) of  $0.25\ \text{V}$ , where charge carriers change polarity. After functionalization of the graphene surface with our functional polypeptide linker, it was observed that the gate curve shifted to a lower voltage level. This negative Dirac voltage shift is approximately  $0.05\ \text{V}$  and we hypothesize that this is due to the positively charged amine groups of the functional polypeptide linker. Furthermore, the graphene device with functional polypeptide linker is characterized by a gate curve that is similar to that seen previously with no observable electrical hysteresis [287]. However, when negatively charged AuNPs were assembled, a positive

Dirac voltage shift occurred resulting in a field effect due to the negative charge of the AuNPs. Interestingly, a large electrical hysteresis was achieved due to the memory effect during gate sweep. The difference in the Dirac voltage between the forward and backward gate voltage sweeps was defined as the hysteresis gap ( $\Delta V_{\text{Dirac}}$ ). In terms of the underlying mechanism, graphene has both holes and electrons as carriers, and the density of states in graphene near the Fermi level is low. Thus, it exhibited ambipolar behaviors of some gating effects depending on the gate bias voltages. Note that, in the case without AuNPs (pristine graphene FET or graphene FET with only linker molecules) [Figure 4.8a(i) - a(ii)], the graphene FETs exhibit only a small amount of hysteresis indicating that our devices do not have many charge trap defects. On the other hand, in the case of devices with AuNPs [Figure 4.8a(iii)], a large hysteresis is evident in the gate sweep curve due to the charge stored in the AuNPs.

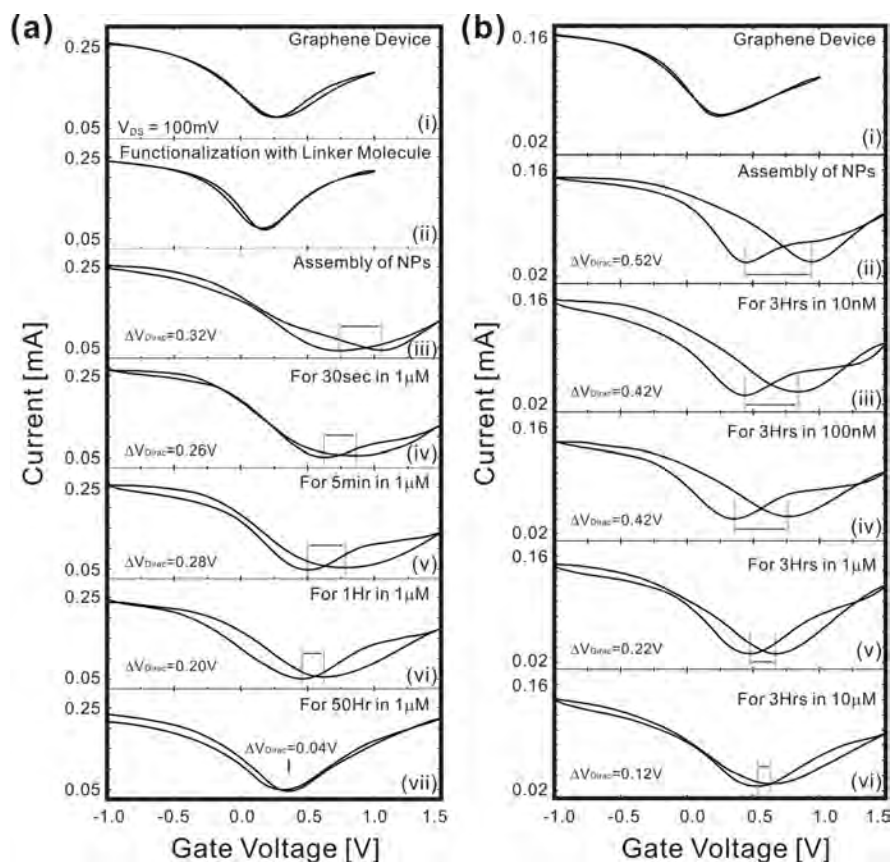


Figure 4.8: Measurement of the hysteresis change of the device after exposure to enzyme solutions. (a)  $\Delta V_{Dirac}$  change and gate effect of an initial graphene transistor (i), after the functionalization of graphene surface with functional polypeptide linker molecule (ii), after NP assembly on the graphene surface (iii), and after exposure to 1  $\mu M$  enzyme solution for 30 sec, 5 min, 1 hr and 50 hrs (iv - vii). (b) Changes in  $\Delta V_{Dirac}$  of graphene device (i) and after the exposure to Carboxypeptidase B in PBS solution with the concentration of 10 nM (ii), 100 nM (iii), 1  $\mu M$  (iv) and 10  $\mu M$  (v) for 3 hours [305].

As stated above, Carboxypeptidase B has been proposed as a predictor for severe acute pancreatitis [304]. This enzyme was used in our proof-of-concept due to the fact that our functional polypeptide linker contains a high number of lysines. Therefore, it acts as a substrate for this enzyme, which specifically cleaves basic amino acids such as lysine. When our graphene-NP hybrid device was exposed to the enzyme solution, the functional polypeptide linker degraded, resulting in the release of AuNPs into the surrounding media. To characterize the effect of the release of AuNPs from the graphene surface on the electrical hysteresis of this device, we measured the  $\Delta V_{Dirac}$  as a function of time using a 1  $\mu M$  enzyme solution (Figure 4.9b). We found that

increasing the exposure time of the enzyme resulted in an expected decrease in NP density [Figure 4.7(C1-C6)]. This decrease in NP density resulted in a decrease in the measured  $\Delta V_{Dirac}$ , which became saturated after 50 hours. Furthermore, due to the fact that the release of functional polypeptide linker caused the detachment of NPs from the graphene surface, the  $\Delta V_{Dirac}$  was very similar to the release profiles found for polypeptide films [307].

The sensitivity of our graphene-NP hybrid sensor with functional polypeptide and NPs was determined by measuring the  $\Delta V_{Dirac}$  as the concentration of Carboxypeptidase B in phosphate buffered saline (PBS) solution was varied from 10 nM to 10 M (Figure 4.8b). Representative sensing data shows that the difference between the  $\Delta V_{Dirac}$  for 10 nM and 100 nM solutions of Carboxypeptidase B after 3 hours of exposure was statistically similar. However, a statistically significant difference in  $\Delta V_{Dirac}$  was observed when the concentration of Carboxypeptidase B was increased to 1  $\mu$ M. Furthermore, as the concentration was subsequently increased, a concentration dependent decrease in the  $\Delta V_{Dirac}$  of our sensors was observed. Figure 4.9a illustrates the sensitivity ( $\Delta V_{Dirac}$ ) of our biosensors as a function of the enzyme concentration. For these experiments, we used ten graphene junctions for each step and repeated sensing experiments ten times demonstrating the repeatability of our results. From these results, we can conclude that the lowest concentration that can be detected using the current functional polypeptide linker is approximately 1  $\mu$ M and it was found that this concentration correlates with a decrease in the change ratio of  $\Delta V_{Dirac}$  (59.2 %).

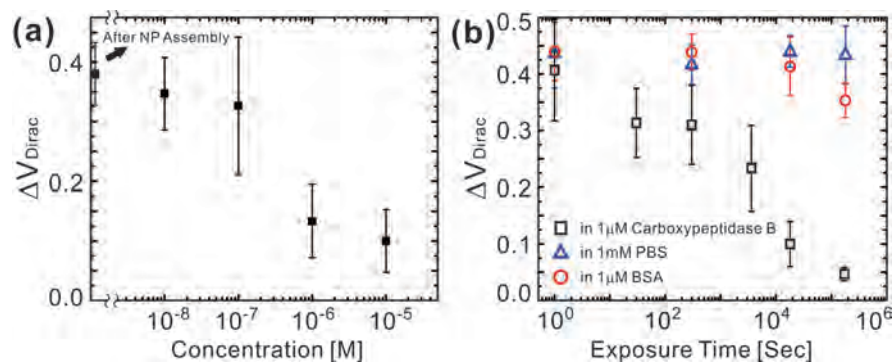


Figure 4.9: Enzyme detection using the graphene-nanoparticle hybrid sensor (a) Sensitivity ( $\Delta V_{Dirac}$ ) of graphene sensor as a function of enzyme concentration [n=10]. (b)  $\Delta V_{Dirac}$  change under various exposure periods to a 1  $\mu$ M Carboxypeptidase in PBS solution (black square), a 1 mM PBS solution (blue triangle) and 1 mM BSA in the PBS solution (red circles) [n=10] [305].

The results also confirm that there is a direct relationship between the  $\Delta V_{Dirac}$  and the concentration of enzyme. Specifically, similar to the non-linear behavior of other graphene-based sensors, the responses of our sensor increase non-linearly with an increase in the enzyme concentration from 10 nM to 10  $\mu$ M.[13,24-26] Finally, we tested the selectivity of this biosensor towards the target enzyme by using control samples such as PBS and different proteins such as bovine serum albumin (BSA). Results showed that PBS and BSA did not react with the functional polypeptide substrate (Figure 4.9b).

Our findings show that quantifying the change in electrical hysteresis of a graphene-NP hybrid biosensor is a viable method to measure enzyme activity sensitively and selectively. However, it is apparent that the critical factor that determines this sensitivity and selectivity is the functional polypeptide linker whose degradation results in the release of AuNPs and subsequent shift in hysteresis. Therefore, the performance of our sensor, in terms of its sensitivity and selectivity, can be further improved by modifying the functional polypeptide linker and changing the properties of the metallic nanoparticle system. In the current study, our novel graphene-based biosensor with functional polypeptide linker and NPs can confer a sensitivity of up to 1  $\mu$ M. However, to improve sensitivity and selectivity, we are synthesizing and screening a variety of functional polypeptide linker molecules that will be self-assembled with different

metallic NPs of varying compositions and sizes.

### 4.2.3 Conclusions

In summary, we have successfully developed a novel graphene-NP hybrid biosensor that uses an electrical hysteresis change to detect the enzymatic activity and concentration of a target enzyme (e.g. Carboxypeptidase B). Our results indicate that our novel graphene-NP hybrid biosensor has the ability to sense concentrations of Carboxypeptidase B down to the micron-scale, which is comparable to previously reported graphene-based biosensors [83, 268, 273]. More importantly, to the knowledge of the authors, this is the first demonstration of a graphene-based biosensor that utilizes a hysteresis change resulting from metallic NPs assembled on a graphene surface for enzyme detection. The current configuration developed in our graphene-NP hybrid biosensor holds a number of advantages over other graphene-based devices established to detect enzymes and other biomolecules. First, AuNP-mediated electrical hysteresis is a phenomenon that has not been studied in graphene-based electrical detection methods, even though it can overcome the limitations faced by current graphene-based sensing approaches. Second, the novel method of detection reported here provides an alternative to the low on-off ratio caused by the zero band gap of graphene. Third, in terms of the components used in our device, the functional polypeptide linker acts as the key-sensing component and can be modified to enhance sensitivity and selectivity for any target enzyme or to confer pH and UV sensitivity. In addition, by combining the properties of graphene with inorganic NPs, our device provides a larger number of sites that can be conjugated with receptor molecules and a high achievable current level. Fourth, the methods used to fabricate the device allow for the homogenous deposition of graphene, resulting in uniform electrical properties. Finally, the use of conventional microfabrication techniques allows for compatibility with facilities found in device industries and allows mass production of our device. Therefore, the results and developed methods presented here warrant the further study of graphene-NP hybrid biosensors for the sensitive and selective detection of enzymes and other biomolecules.

#### 4.2.4 Materials and Methods

##### Metal deposition and measurement of graphene devices

For the electrode fabrication, the photoresist was first patterned on the substrate. Ti/Au (10/30nm) was then deposited on the substrate and the remaining photoresist was then removed with acetone for the lift-off process. A Keithley-4200 semiconductor parameter analyzer was used for measurement and data collection.

##### Synthesis of 1-butyl-3-methylimidazolium hexafluorophosphate (BMIM-PF<sub>6</sub>)

The BMIM-PF<sub>6</sub> was prepared according to a modified procedure reported by Consorti et al. [308] 72.5 mL (64.2 g, 0.69 mol) of 1-chlorobutane and 50 mL of 1-methylimidazole (51.8 g, 0.63 mol) were added to a dry round-bottom flask fitted with a reflux condenser and a magnetic stirring bar. The reaction mixture was stirred at 80°C for 48 h. The unreacted 1-chlorobutane was evaporated at reduced pressure. 1-methylimidazole was washed three times by adding small amount of ethyl acetate to the mixture and decanted. 1-butyl-3-methylimidazolium chloride (BMIM-Cl) was obtained by evaporating the remaining ethyl acetate at reduced pressure and drying in a vacuum oven. 69.6 g (0.38 mol) of KPF<sub>6</sub> and 150 mL of H<sub>2</sub>O were added into a round-bottom flask, followed by the addition of 50mL (0.32 mol) of as-prepared BMIM-Cl. After vigorous stirring for 24 h at room temperature, undissolved KPF<sub>6</sub> disappeared and two phases were formed. The lower ionic liquid layer was separated and dissolved in 50 mL of dichloromethane. The dichloromethane solution was washed with water until no chloride (Cl<sup>-</sup>) anion in the water layer could be detected by AgNO<sub>3</sub> solution. Dichloromethane was evaporated and 1-butyl-3-methylimidazolium hexafluorophosphate (BMIM-PF<sub>6</sub>) was obtained as a colorless or slightly yellow viscous liquid after drying in a vacuum oven. 1-chlorobutane, 1-methylimidazole, ethyl acetate and dichloromethane were purchased from Sigma Aldrich Inc. The synthesized BMIM-PF<sub>6</sub> was analyzed with <sup>1</sup>H NMR. Spectra were recorded at 600 MHz. The following chemical shifts reported in ppm downfield to TMS ( $\delta=0$  ppm) were observed: <sup>1</sup>H NMR (600 MHz, DMSO-D<sub>6</sub>):  $\delta$  0.91(t, 3H),  $\delta$  1.27(m, 2H),  $\delta$  1.77(m, 2H),  $\delta$  3.85(s, 3H),  $\delta$  4.16(t, 2H),  $\delta$  7.67(s, 1H),  $\delta$  7.74(s, 1H),  $\delta$

9.08(s, 1H).

### **Synthesis of 4-(pyren-1-yl)butanal**

10 mL of methylene chloride was added to 1.097 g (4 mmol) of 4-(pyren-1-yl) butyl alcohol and stirred vigorously at room temperature for 10 min. The reaction was followed by the addition of 1.292 g (1.5 Equilibrium) of PCC (Pyridinium chlorochromate) in 10 mL methylene chloride and the reaction mixture was stirred for 2 h. The reaction mixture was then diluted with 5 volumes of anhydrous ether (100 mL) and washed with 1:1 brine: water, saturated aq.  $\text{Na}_2\text{SO}_3$  solution, and brine, respectively, dried over anhydrous  $\text{Na}_2\text{SO}_4$  and concentrated to give the aldehyde. The crude product was purified by silica gel flash chromatography (hexanes: ethyl acetate, 9:1, rf: 0.4) to yield 1.06 g (97%). Most of the crude products were very clean and could be used directly for further applications.

### **Synthesis of the amino acid N-carboxy anhydrides (2, NCAs)**

To synthesize the amino acid N-carboxy anhydrides, N-CBZ-l-lysine was converted to the corresponding N-carboxy anhydrides (NCAs). Specifically, N-CBZ-l-lysine was suspended in anhydrous THF (10 wt. %), and the reaction temperature was increased to 55°C. A calculated amount of triphosgene, dissolved in anhydrous THF, was added dropwise into the reaction mixture. Due to the addition of triphosgene, the suspended mixture became a clear solution as NCA was formed after a certain reaction time. To ensure ring formation, the reaction mixture was vigorously stirred for an additional 1 h. The reaction mixture was then condensed and poured into a 10-fold excess amount of anhydrous n-hexane to precipitate the amino acid NCAs. Finally, the amino acid NCAs were recovered by filtration and dried for 48 hours using a vacuum. Characterization of the amino acid NCAs was completed using  $^1\text{H}$  NMR.

### **Deposition and Patterning of Graphene**

In brief, graphene was grown on nickel layers using chemical vapor deposition. To transfer the graphene, an aqueous  $\text{FeCl}_3$  solution was used as an oxidizing etchant.

This solution slowly etched the nickel layers, separating the graphene film from the substrate. The resulting graphene film was then transferred to our device by simple contact with our SiO<sub>2</sub> substrate.

### **Synthesis of 3-armed polypeptides (5)**

The lysine-based polymer was synthesized by ring opening polymerization via the amino acid NCA using amino acids and triphosgene as shown in Figure 4.10. Calculated amounts of amino acid NCAs were placed in an 100 ml two-neck round bottom flask and dissolved in anhydrous DMF (10 wt.%) in a nitrogen atmosphere. Freshly distilled n-trisamine, previously diluted in anhydrous DMF, was added into the solution to initiate the ring-opening polymerization. The polymerization was continued for 72 h at room temperature to ensure consumption of all the NCA monomers. The resulting slightly viscous solution was then precipitated in 20-fold excess water. The precipitate was filtered and dried in vacuum overnight. Then, the protection groups of the polymer (CBZ groups in lysine side chains) were removed using HBr. Specifically, the polymer with protection groups was dissolved in 30% HBr/glacial acetic acid solution (20 ml/g). As the deprotection reaction progressed, carbon dioxide evolved out and the polymer rapidly precipitated from the solution. After 30 mins, a 10-fold excess amount of anhydrous diethyl ether was added to the reaction mixture. The precipitate was filtered and washed with diethyl ether. After drying, the deprotected polymer was dissolved again in deionized water, transferred to a pre-swollen dialysis membrane (MWCO=500) and dialyzed against deionized water for 2 days. Polylysine was obtained by freeze drying for 3 days. Polylysine was characterized by <sup>1</sup>H NMR.

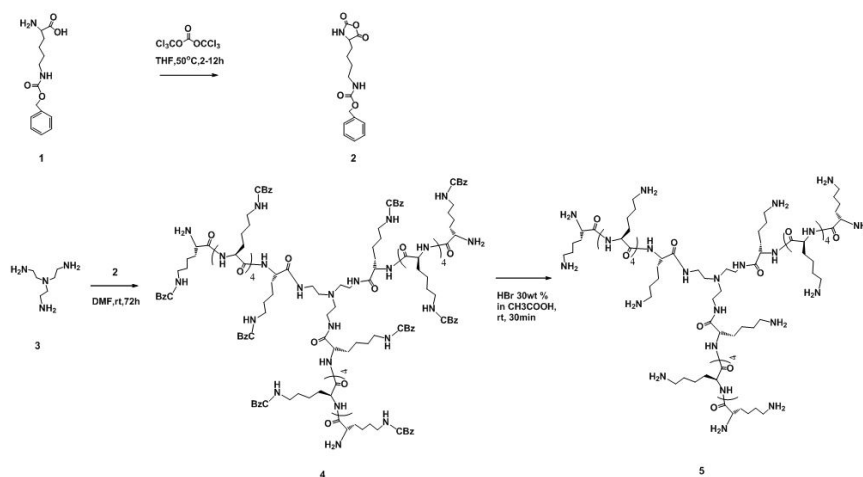


Figure 4.10: Synthetic Scheme of polypeptide linkers that is specific for our target enzyme, Carboxypeptidase B [305].

## 4.3 Zinc Oxide Thin Film Transistor Immunosensor with High Sensitivity and Selectivity

### 4.3.1 Introduction

The ion-selective field effect transistors (ISFET) have been used popularly as a sensitive pH sensor and various biochemical sensors [309,310]. Recently the ISFET structure has been integrated with Poly-Si thin film transistors (TFTs) and GaN/AlGa<sub>N</sub> high electron mobility transistors (HEMTs) for detection of DNA, penicillin, and cellular potentials [311,312]. However, the sensing procedure using the ISFET can be invasive as its entire gate serves as the sensing area which contains both the analyte solution and the reference electrode. Another class of FET-type biosensors is based on organic field-effect transistors (OFETs) [313–316]. The general structure of an OFET consists of a back-gate MOSFET with the conducting channel made of organic semiconductors. The OFET has the advantage of being easily controlled through biasing due to the back-gate configuration. However, OFETs require high bias voltages, and suffer from low channel mobility. Currently, nanowire-based FET sensors are demonstrated with high sensitivity reaching the order of fM [317,318]. However, these prototypes of sensors generally involve a complex fabrication process as they are constructed individually by manipulating and aligning a single strand of semiconducting nanowire such as TiO<sub>2</sub> or Si as the FET channel between the source and drain patterns. It is difficult to achieve repeatability and manufacturability in fabrication and integration of these devices for larger sensor arrays.

ZnO is emerging as a wide bandgap semiconductor oxide with multifunctional properties that makes it an attractive sensor material. ZnO and its nanostructures are compatible with intracellular material and ZnO-based sensors have been demonstrated for detection of biochemicals such as enzymes, antibodies, DNA immobilization and hybridization [319–321]. Herein, we report the highly sensitive and selective immunosensing ability of a ZnO based thin film transistor biosensor (ZnO-bioTFT). The EGFR is used as the example because the sensing of EGFR-antibodies reacting with EGFR proteins has its implications in cancer related studies and drug screening for cancer,

as EGFR is well-known to be over-expressed in solid tumors, especially breast cancers. The ZnO-TFT devices possess excellent and repeatable characteristics. It can be fabricated using the conventional microelectronic process and can be integrated into a large scale at low cost, which benefit for the further development of a platform not only for diagnosing cancers, but also for monitoring a patients response to therapy in real-time.

### 4.3.2 Results and Discussion

The bio-functionalization enables the exposed ZnO channel direct interaction with the biochemical species being detected. The mechanism of detection of antibody-antigen reaction is illustrated in Figure 4.14a-d. In the first step (Figure 4.14b) the unfunctionalized ZnO-bioTFT is positively biased at the drain and gate electrode. The positive voltage at the gate causes the majority carriers of the n-type ZnO channel to accumulate near the base of the ZnO layer to facilitate a conduction path for the current flow from drain to source. The positive voltage at the drain causes some of the carriers to also accumulate near the side of the drain electrode forming a wedge-shaped conduction path. The bias at the drain also acts as the electron pump to drive the current to flow. For the second step (Figure 4.14c), the exposed ZnO channel is functionalized with EGFR monoclonal antibodies (mAbs) having free lysine groups. The immobilized antibody molecules caused significant decrease in conductivity of the ZnO surface layer, thus, reducing the drain current. In the third step (Figure 4.14d), the EGFR protein captured by the EGFR mAbs forms a polarized molecule with a dominant partially-positive charged tip [322], which led to the accumulation of negative carriers within the ZnO channel to accumulate near the exposed surface where the antibody-protein pairs were present. This carrier accumulation was in addition to the conduction path created near the gate. The combined amount of accumulation layer caused an increase in the current flow. The top molecule layer (reacted protein) acted as a virtual top gate and the antibody layer acted as a virtual insulator layer, thus forming a pseudo-double gated field-effect conduction scheme for the ZnO-bioTFT. The actual measured drain currents that confirmed each step of the detection process are shown in Figure 4.14a. The drain voltage is fixed to 10V and the gate voltage is varied from -5V to +15V, and

the drain current is measured using an HP4156C semiconductor parameter analyzer and Cascade Microtech probe station.

### Sensitivity of the ZnO-bioTFT immunosensor

To demonstrate the high sensitivity of the ZnO-bioTFT, solutions of pure EGFR (in PBS) were prepared with four different Molar concentrations using serial dilutions, namely 10 nM, 100 pM, 1 pM, and finally 10 fM. Each EGFR solution (2  $\mu$ L) was introduced to a separate but similar ZnO-bioTFT fabricated on a single chip that were simultaneously functionalized with EGFR mAbs. The drain current was monitored as a function of gate voltage with a fixed drain voltage of 10V, for each concentration. Figure 4.11 shows the measured drain current versus gate voltage of the bioTFT. An increase in drain current was measured as the EGFR concentration was increased and the graph also shows that the device was able to detect as low as 10 fM of EGFR concentration. The trend in the current readings agrees with the hypothesis provided by the pseudo-double gating effect discussed above.

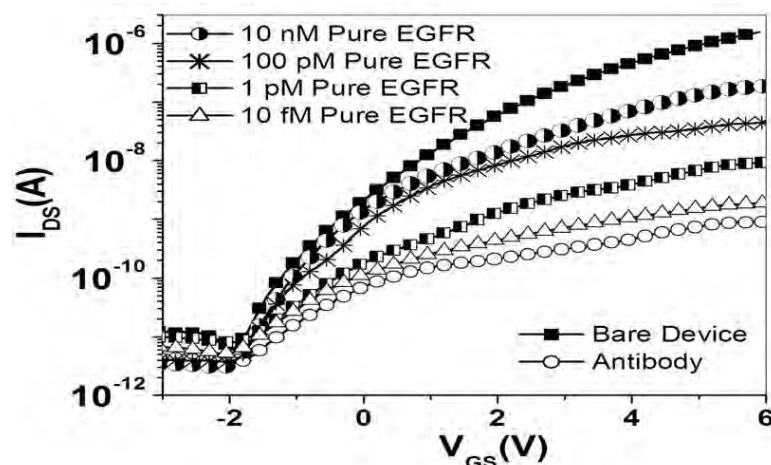


Figure 4.11: Drain current versus gate bias for various Molar concentrations of pure EGFR proteins detected by the ZnO-bioTFT to demonstrate sensitivity [323].

### Selectivity of the ZnO-bioTFT immunosensor

The highly selective sensing of EGFR using the ZnO-bioTFT was also demonstrated. In this experiment, a 5 mg/ml (in PBS, pH 7.4) goat serum solution was prepared, which

contains many different species of proteins. As mentioned above, different EGFR solutions were prepared, namely 100 pM, 1 pM, and 10 fM, using this serum solution as the solvent and not pure PBS. For all the concentrations, the total amount of serum present remained approximately the same. Each of the different solutions ( $2 \mu\text{L}$ ) was introduced onto a chip containing multiple similar bioTFT devices that were bio-functionalized with EGFR mAbs. The drain current of each device was measured as a function of gate voltage, with a fixed drain voltage of 10V. As a control, we first introduced serum solution without the EGFR proteins to the ZnO-bioTFT. Figure 4.12a shows no change in the drain current for the pure serum confirming that there were no EGFR molecules in the solution. The drain current increased as a function of EGFR concentration. The bio-TFT detected only the EGFR proteins out of the many different proteins present in the serum solution introduced onto the sensing area of the device. Moreover, the device was able to discern as low as 10 fM of EGFR protein concentration in the serum solution. The sensitivity plot of the device for both pure and in-serum detection is shown in Figure 4.12b which exhibits linearity in the x-y logarithmic scale.

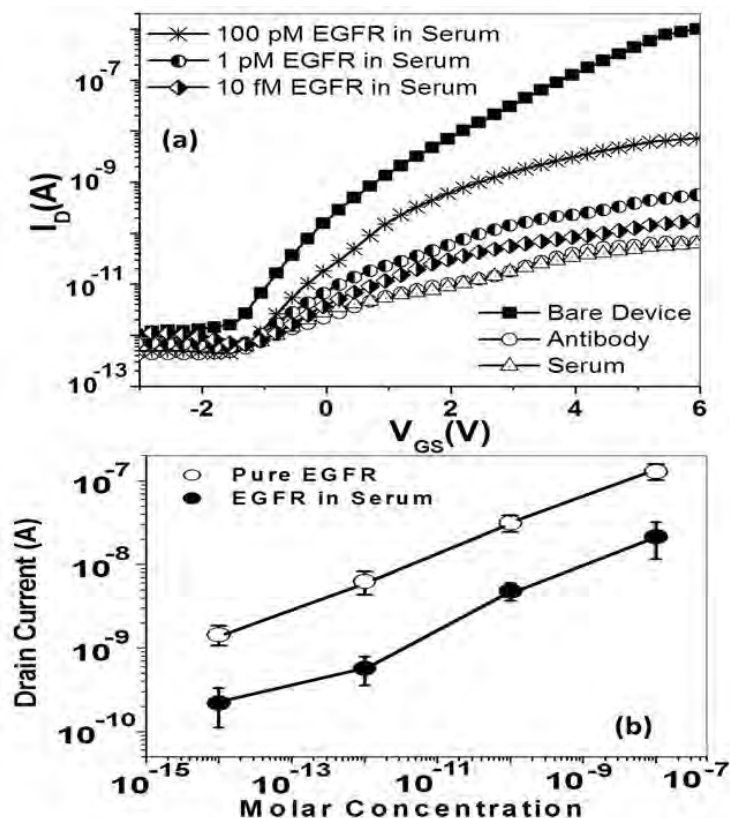


Figure 4.12: (a) Drain current versus gate bias for various Molar concentrations of EGFR-proteins in a serum solution containing many different proteins. (b) Sensitivity plot of the device for pure protein and protein in serum detection [323].

### 4.3.3 Conclusions

In summary, we have demonstrated a ZnO bioTFT that has the ability to perform immunosensing with high sensitivity and selectivity. The channel of the bioTFT is functionalized with amine-terminated EGFR monoclonal antibodies. EGFR proteins with the lowest concentration of 10 fM were detected by the device in both pure state and selectively in a concentration serum solution containing various other protein species. The ZnO-bioTFT enables bias-controlled operation through its bottom gate configuration. The high sensitivity of the device is attributed to its high on-off ratio, and the output current trend is explained by the pseudo-double gating electric field effect. The realization of the ZnO-bioTFT functionalized with EGFR mAbs reacting with EGFR proteins has potential applications in cancer diagnosis and treatment.

### 4.3.4 Materials and Methods

#### Device fabrication

The device schematic is shown as the inset of Figure 4.13. It follows a back-gate inverted-staggered configuration. A Si substrate was covered with 1  $\mu\text{m}$  layer of  $\text{SiO}_2$  through wet oxidation followed by e-beam deposition of a layer of Au (50 nm)/Cr (100 nm) that serves as the gate electrode. A 70 nm layer of  $\text{SiO}_2$  serving as the gate oxide was then deposited through plasma enhanced chemical vapor deposition (PECVD) with substrate temperature of  $250^\circ\text{C}$  and using  $\text{SiH}_4$  and  $\text{N}_2\text{O}$  as the source gases. A 50 nm ZnO thin film was grown using metalorganic chemical vapor deposition (MOCVD) on the top of the  $\text{SiO}_2$  to serve as the n-type conduction channel, with substrate temperature at  $350^\circ\text{C}$  and using diethyl zinc (DEZn) as the metal precursor and ultra-high purity  $\text{O}_2$  as oxidizer. Au (50 nm)/Ti (100 nm) was deposited through e-beam evaporation for the source and drain Ohmic contacts. The exposed ZnO channel acts as the sensing area and has a dimension of  $200\ \mu\text{m} \times 400\ \mu\text{m}$ , giving a W/L ratio of 2.

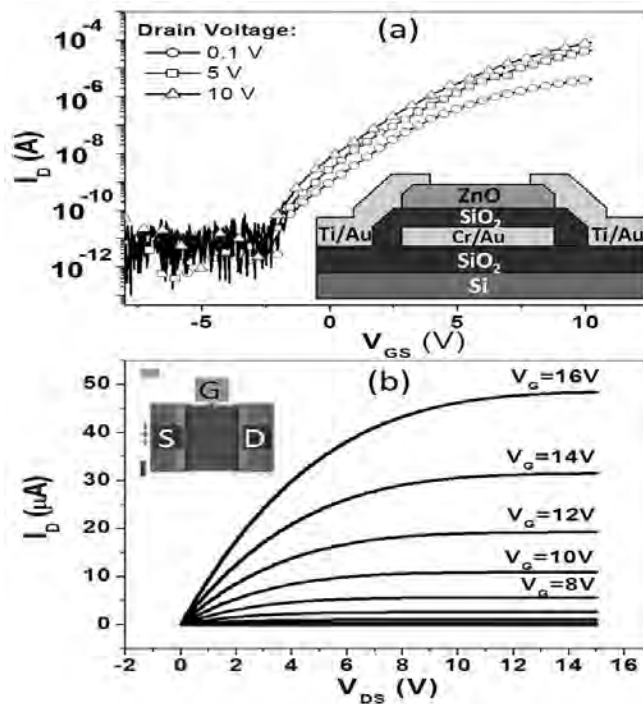


Figure 4.13: (a) Transconductance curve of the ZnO-bioTFT and its vertical structure schematic (inset); (b) transistor characteristic curves for various gate bias, and the top view of the device (inset) [323].

Shown in the inset of Figure 4.13b is the top view of the TFT device. The electrical characteristics of the ZnO-bioTFT are shown in Figure 4.13a and b. The transconductance curve (drain current ( $I_D$ ) vs gate voltage ( $V_{GS}$ )) in Figure 4.14a shows that the bioTFT is a normally-OFF enhancement mode transistor with a threshold voltage of 4.25 V and an ON-OFF ratio of  $10^2$ .

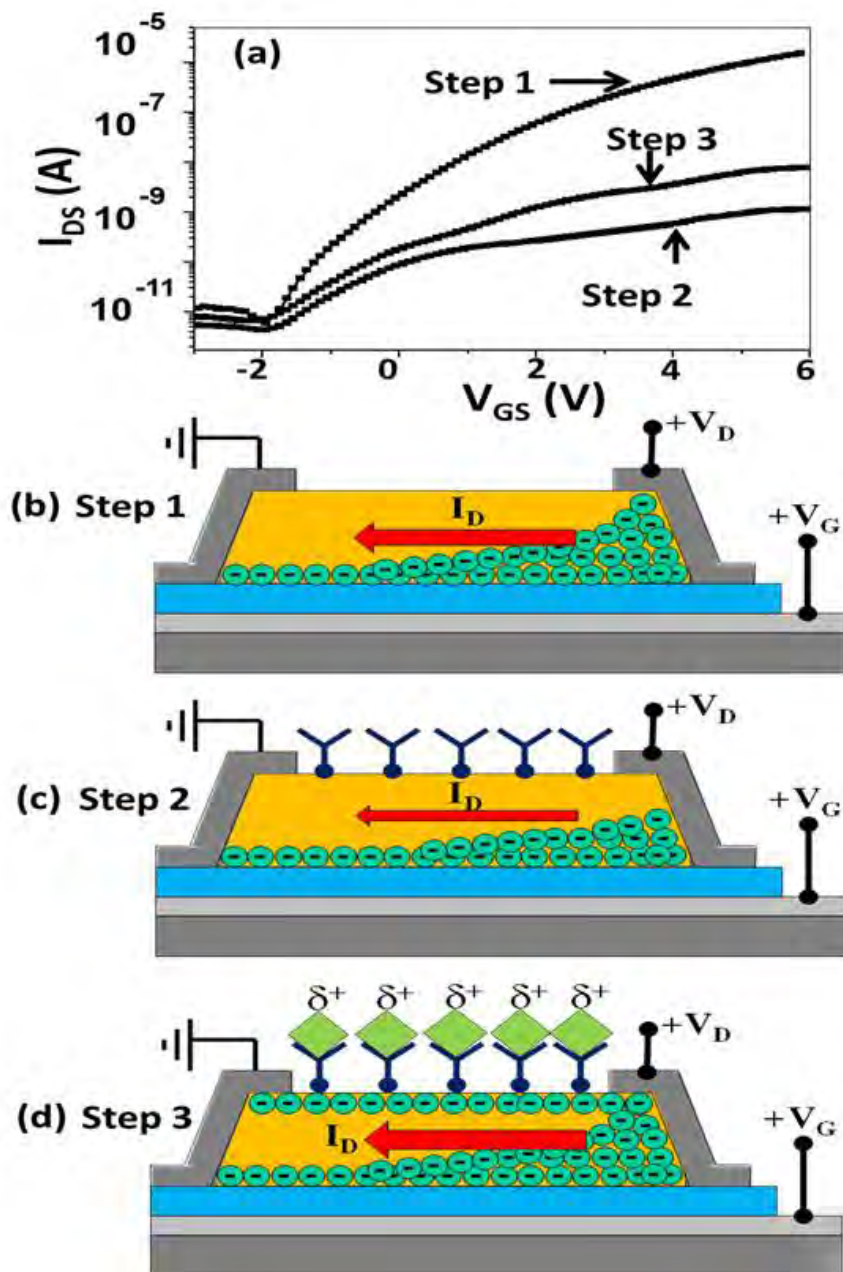


Figure 4.14: (a) Drain current versus gate bias for fixed drain bias of 10V. Step 1: bare device, Step 2: EGFR-antibody immobilization, and Step 3: EGFR protein detection; (b-d) schematic of the carrier modulation mechanism for steps 1 to 3 respectively [323].

The high ON-OFF ratio of the device provides the high sensitivity of the device to the charge modulation within the ZnO channel. Figure 4.14b shows the transistor characteristic curves with drain current versus drain voltage for various gate-biasing of the device.

### **Bio-functionalization of device with antibodies**

To realize the immunosensing ability of the ZnO-bioTFT, the exposed ZnO channel was functionalized using linkage chemistry, which involves three basic steps. First, the ZnO channel was functionalized with trimethoxysilane aldehyde (having a reactive aldehyde end group) by incubating the device in 1% v/v solution of the silane-aldehyde in 95% ethanol for 30 min. The device was then cured at 120°C for 15 min. Second, the aldehyde groups were coupled to the amine groups of the monoclonal EGFR antibodies (1:50) through reductive amination in the presence of 4 mM sodium cyanoborohydride in PBS (pH 7.4) for two hours. Third, unreacted aldehyde groups were blocked using 100 mM ethanolamine in a similar manner to prevent non-specific interactions of proteins. Finally, the device was rinsed in a continuous flow of PBS, pH 7.4 for 10 min.

## Chapter 5

### Conclusions and Perspectives

We are just beginning to see the impact of nanotechnology in the field of regenerative medicine. The platforms developed in the past decade have set very high expectations for solving key questions in medical sciences. With the emergence of induced pluripotent stem cells (iPSCs), the field is now open wider than ever before as all the ethical concerns regarding embryonic stem cells have been bypassed. However, strict monitoring will be required to use these technologies for controlling the behavior of stem cells. While a lot of attention has been given to the reprogramming for somatic cells to iPSCs in the last decade, it is equally important to develop approaches that can control the differentiation of stem cells into functional cells of interest, *in vitro* and *in vivo*. This thesis provided a few examples of methods, based on nanotechnology, to control and enhance the neuronal differentiation of NSCs. Most of the methods can also be used for other adult stem cell lines to control their differentiation.

In chapter 2, the delivery of siRNA into brain tumor cells using quantum dots (QDs) was demonstrated. The delivery platform not only helped to deliver the therapeutic siRNA, which inhibited the growth of the brain tumor cells, but also helped to track the delivery of siRNA due to the highly fluorescent property for the QDs. This part of research helped in optimization of siRNA delivery methods into cells. The following section presented the synthesis and application of DexAM, a cyclodextrin-polyamine construct that was used to deliver hydrophobic small molecules and siRNA into NSCs. DexAM is particularly advantageous as its cyclodextrin component can encapsulate hydrophobic small molecules, thus precluding the use of toxic solvents such as DMSO, which have been shown to affect stem cell behaviors. Additionally, the highly concentrated positive charge on the surface of DexAM is useful for forming polyplexes with

the negatively charged siRNA molecules. The cyclodextrin component also helped in reducing the cytotoxicity from the highly positive charge on the surface, thus making the delivery system biocompatible. DexAM was used to simultaneously deliver siRNA against SOX9 and the hydrophobic small molecule retinoic acid (RA), a well-known small molecule for enhancing neuronal differentiation. SOX9, when inhibited, leads to enhanced neuronal differentiation. Thus their simultaneous delivery using a single platform led to a significantly enhanced neuronal differentiation of NSCs, as compared to the differentiation achieved when they were used alone.

Chapter 3 focused on surface chemistry and modifications for controlling the growth and differentiation of NSCs. In Chapter 2, as discussed above, conventional delivery systems by way of solution-based (forward) transfection were used, wherein the delivery vehicle also entered the NSCs along with siRNA. In Chapter 3, however, the approaches presented, led to enhanced neuronal differentiation of NSCs by way of interacting with the ECM, which is a vital part of the cellular microenvironment. NanoRU, was presented as being a platform for the delivery of siRNA (against SOX9) into NSCs by way of nanotopography-mediated reverse uptake, wherein only the siRNA molecules were taken up the NSCs. This is a very novel approach and completely depends on the nanotopographical features presented to the cells. In addition to NSCs, NanoRU was shown to be applicable for siRNA delivery into cancer cells and normal healthy cells. Furthermore, miRNA was also shown to be taken up by the NSCs using NanoRU, thus pointing to the potential of this platform for culturing stem cells. In Chapter 3, the impact of surface chemistry by way of patterning ECM proteins was also presented. Micropatterns of an ECM protein (laminin) were generated in a high-throughput fashion using microcontact printing. NSC differentiation was completely controlled by using micropatterns of a specific geometry in a given size-range. It was observed that the highest neuronal differentiation of NSCs (in the absence of exogenous proteins and small molecules) took place on grid patterns (promoted cell-cell interactions), while the least was observed on square patterns (cell-cell interactions were highly restricted). Lastly, in Chapter 3, the impact of novel nanomaterials, such as graphene, on stem cell differentiation was demonstrated. It was seen that the mere presence of graphene oxide

(GO) as part of the ECM led to the alignment of axons from differentiating human NSCs. It was also shown that the use of GO-SiNP hybrid structures not only led to the alignment of axons but also resulted in enhanced neuronal differentiation. However, the direction of the alignment could not be controlled as the reason for alignment is yet unknown and is currently under investigation. Once the mechanism leading to the alignment of hNSCs on GO is elucidated, it would be easier to control the direction of the aligning axons.

In Chapter 4, the applications of nanotechnology in the emerging field of diagnostics were discussed. The initial idea for developing biosensors stemmed from the notion that the different biomarkers for differentiating stem cells should be quantified to give a better idea about the process of stem cell differentiation. However, the initial optimization for developing the biosensors, using nanostructures, began with detecting cancer biomarkers. Graphene-encapsulated nanoparticle arrays were used to develop a biosensor capable of detecting breast cancer biomarkers such as HER2 and EGFR. In addition to being a sensitive and selective biosensor, its fabrication process was relatively straightforward, making it highly amenable to industrial manufacturing. Another graphene-nanoparticle hybrid sensor was developed for sensing the presence of a specific enzyme. The enzyme lysed a specific linker which attached the gold nanoparticles (AuNPs) to graphene. Thus, when the linker was lysed the AuNPs got detached from the surface of graphene, which led to a change in hysteresis, and thus the detection of the amount of enzyme causing the hysteresis. The enzyme was carboxypeptidaseB, which is a marker for acute pancreatitis. The last part of Chapter 4 discussed the development and application of a zinc oxide (ZnO)-based device for detecting the cancer biomarker EGFR. This project showed application and usefulness of a new material, ZnO as a component of a biosensor. The sensor demonstrated exceptional sensitivity and selectivity towards the targeted biomarker. The use of ZnO-based nanostructures as part of a new biosensor is currently under way.

The work from this thesis has been remarkably novel, with the ideas being quite fresh. It is hoped that this work will be used for developing many more approaches for controlling the behaviors of stem cells, which will eventually transpire to something

relevant in the clinic. It is also hoped that the work with biosensors will help in developing a new generation of biosensors, which are not only sensitive and selective, but also quick and cheap.

## References

- [1] A. Solanki, J. D. Kim, and K. B. Lee, "Nanotechnology for regenerative medicine: nanomaterials for stem cell imaging," *Nanomedicine*, vol. 3, no. 4, pp. 567–578, 2008.
- [2] K. Bogunia-Kubik and M. Sugisaka, "From molecular biology to nanotechnology and nanomedicine," *Biosystems*, vol. 65, no. 2-3, pp. 123–138, 2002.
- [3] L. Ferreira, J. M. Karp, L. Nobre, and R. Langer, "New opportunities: the use of nanotechnologies to manipulate and track stem cells," *Cell Stem Cell*, vol. 3, no. 2, pp. 136–46, 2008.
- [4] S. Wang, N. Mamedova, N. Kotov, W. Chen, and J. Studer, "Antigen/antibody immunocomplex from cdte nanoparticle bioconjugates," *Nano Letters*, vol. 2, no. 8, pp. 817–822, 2002.
- [5] M. Lewin, N. Carlesso, C. H. Tung, X. W. Tang, D. Cory, D. T. Scadden, and R. Weissleder, "Tat peptide-derivatized magnetic nanoparticles allow in vivo tracking and recovery of progenitor cells," *Nature Biotechnology*, vol. 18, no. 4, pp. 410–414, 2000.
- [6] J. W. M. Bulte, T. Douglas, B. Witwer, S. C. Zhang, E. Strable, B. K. Lewis, H. Zywicke, B. Miller, P. van Gelderen, B. M. Moskowitz, I. D. Duncan, and J. A. Frank, "Magnetodendrimers allow endosomal magnetic labeling and in vivo tracking of stem cells," *Nature Biotechnology*, vol. 19, no. 12, pp. 1141–1147, 2001.
- [7] E. R. Chemaly, R. Yoneyama, J. V. Frangioni, and R. J. Hajjar, "Tracking stem cells in the cardiovascular system," *Trends in Cardiovascular Medicine*, vol. 15, no. 8, pp. 297–302, 2005.
- [8] E. Sykova and P. Jendelova, *In vivo tracking of stem cells in brain and spinal cord injury*, vol. 161 of *Progress in Brain Research*, pp. 367–383. 2007.
- [9] D. L. J. Thorek, A. Chen, J. Czupryna, and A. Tsourkas, "Superparamagnetic iron oxide nanoparticle probes for molecular imaging," *Annals of Biomedical Engineering*, vol. 34, no. 1, pp. 23–38, 2006.
- [10] P. Jianhong Zhu, M.D., M. Liangfu Zhou, P. Jianhong Zhu, M.D., and M. Liangfu Zhou, "Tracking neural stem cells in patients with brain trauma," *The new england journal of medicine*, vol. 355, no. 22, pp. 2376–2378, 2006.
- [11] C. R. Thomas, D. P. Ferris, J. H. Lee, E. Choi, M. H. Cho, E. S. Kim, J. F. Stoddart, J. S. Shin, J. Cheon, and J. I. Zink, "Noninvasive remote-controlled release of drug molecules in vitro using magnetic actuation of mechanized nanoparticles," *J Am Chem Soc*, vol. 132, no. 31, pp. 10623–5, 2010.

- [12] J. W. M. Bulte and D. L. Kraitchman, "Monitoring cell therapy using iron oxide mr contrast agents," *Current Pharmaceutical Biotechnology*, vol. 5, no. 6, pp. 567–584, 2004.
- [13] . Jeff W. M. Bulte<sup>1</sup> and D. L. Kraitchman<sup>1</sup>, "Iron oxide mr contrast agents for molecular and cellular imaging," *NMR in Biomedicine*, vol. 17, pp. 484–499, 2004.
- [14] S. Dutz, W. Andra, R. Hergt, R. Muller, C. Oestreich, C. Schmidt, J. Topfer, M. Zeisberger, and M. E. Bellemann, "Influence of dextran coating on the magnetic behaviour of iron oxide nanoparticles," *Journal of Magnetism and Magnetic Materials*, vol. 311, no. 1, pp. 51–54, 2007.
- [15] R. Lawaczeck, M. Menzel, and H. Pietsch, "Superparamagnetic iron oxide particles: contrast media for magnetic resonance imaging," *Applied Organometallic Chemistry*, vol. 18, no. 10, pp. 506–513, 2004.
- [16] A. K. Gupta and A. S. G. Curtis, "Lactoferrin and ceruloplasmin derivatized superparamagnetic iron oxide nanoparticles for targeting cell surface receptors," *Biomaterials*, vol. 25, no. 15, pp. 3029–3040, 2004.
- [17] W. J. Rogers, C. H. Meyer, and C. M. Kramer, "Technology insight: in vivo cell tracking by use of mri," *Nature Clinical Practice Cardiovascular Medicine*, vol. 3, no. 10, pp. 554–562, 2006.
- [18] C. W. Lu, Y. Hung, J. K. Hsiao, M. Yao, T. H. Chung, Y. S. Lin, S. H. Wu, S. C. Hsu, H. M. Liu, C. Y. Mou, C. S. Yang, D. M. Huang, and Y. C. Chen, "Bifunctional magnetic silica nanoparticles for highly efficient human stem cell labeling," *Nano Letters*, vol. 7, no. 1, pp. 149–154, 2007.
- [19] J. Emerit, C. Beaumont, and F. Trivin, "Iron metabolism, free radicals, and oxidative injury," *Biomedicine and Pharmacotherapy*, vol. 55, no. 6, pp. 333–339, 2001.
- [20] F. H. Wang, I. H. Lee, N. Holmstrom, T. Yoshitake, D. K. Kim, M. Muhammed, J. Frisen, L. Olson, C. Spenger, and J. Kehr, "Magnetic resonance tracking of nanoparticle labelled neural stem cells in a rat's spinal cord," *Nanotechnology*, vol. 17, no. 8, pp. 1911–1915, 2006.
- [21] C. M. Niemeyer and B. Ceyhan, "Dna-directed functionalization of colloidal gold with proteins," *Angewandte Chemie-International Edition*, vol. 40, pp. 3685–3688, 2001.
- [22] J. W. M. Bulte, S.-C. Zhang, P. v. Gelderen, V. Heryneki, E. K. Jordan, I. D. Duncan, and J. A. Frank, "Neurotransplantation of magnetically labeled oligodendrocyte progenitors: Magnetic resonance tracking of cell migration and myelination," *Proceedings of the National Academy of Sciences*, vol. 96, no. 26, p. 1525615261, 1999.
- [23] I. D. Duncan and E. A. Milward, "Glial-cell transplants - experimental therapies of myelin diseases," *Brain Pathology*, vol. 5, no. 3, pp. 301–310, 1995.

- [24] D. L. Kraitchman, A. W. Heldman, E. Atalar, L. C. Amado, B. J. Martin, M. F. Pittenger, J. M. Hare, and J. W. Bulte, "In vivo magnetic resonance imaging of mesenchymal stem cells in myocardial infarction," *Circulation*, vol. 107, pp. 2290–2293, 2003.
- [25] M. R. Pickard, P. Barraud, and D. M. Chari, "The transfection of multipotent neural precursor/stem cell transplant populations with magnetic nanoparticles," *Biomaterials*, vol. 32, no. 9, pp. 2274–84, 2011.
- [26] S. I. Jenkins, M. R. Pickard, N. Granger, and D. M. Chari, "Magnetic nanoparticle-mediated gene transfer to oligodendrocyte precursor cell transplant populations is enhanced by magnetofection strategies," *ACS Nano*, vol. 5, no. 8, pp. 6527–38, 2011.
- [27] S. Lin, X. Y. Xie, M. R. Patel, Y. H. Yang, Z. J. Li, F. Cao, O. Gheysens, Y. Zhang, S. S. Gambhir, J. H. Rao, and J. C. Wu, "Quantum dot imaging for embryonic stem cells," *Bmc Biotechnology*, vol. 7, 2007.
- [28] W. W. Wu and A. D. Li, "Optically switchable nanoparticles for biological imaging," *Nanomedicine*, vol. 2, no. 4, pp. 523–531, 2007.
- [29] X. H. Gao, L. L. Yang, J. A. Petros, F. F. Marshal, J. W. Simons, and S. M. Nie, "In vivo molecular and cellular imaging with quantum dots," *Current Opinion in Biotechnology*, vol. 16, no. 1, pp. 63–72, 2005.
- [30] X. Michalet, F. F. Pinaud, L. A. Bentolila, J. M. Tsay, S. Doose, J. J. Li, G. Sundaresan, A. M. Wu, S. S. Gambhir, and S. Weiss, "Quantum dots for live cells, in vivo imaging, and diagnostics," *Science*, vol. 307, no. 5709, pp. 538–544, 2005.
- [31] M. N. Rhyner, A. M. Smith, X. H. Gao, H. Mao, L. L. Yang, and S. M. Nie, "Quantum dots and multifunctional nanoparticles: new contrast agents for tumor imaging," *Nanomedicine*, vol. 1, no. 2, pp. 209–217, 2006.
- [32] S. M. Nie, Y. Xing, G. J. Kim, and J. W. Simons, "Nanotechnology applications in cancer," *Annual Review of Biomedical Engineering*, vol. 9, pp. 257–288, 2007.
- [33] X. H. Gao, W. C. W. Chan, and S. M. Nie, "Quantum-dot nanocrystals for ultrasensitive biological labeling and multicolor optical encoding," *Journal of Biomedical Optics*, vol. 7, no. 4, pp. 532–537, 2002.
- [34] S. M. Nie, "Luminescent quantum dots for multiplexed optical tagging of genes, proteins, and cells," *Cytometry*, pp. 25–25, 2002.
- [35] X. H. Gao and S. M. Nie, "Molecular profiling of single cells and tissue specimens with quantum dots," *Trends in Biotechnology*, vol. 21, no. 9, pp. 371–373, 2003.
- [36] B. X. Cui, C. B. Wu, L. Chen, A. Ramirez, E. L. Bearer, W. P. Li, W. C. Mobley, and S. Chu, "One at a time, live tracking of ngf axonal transport using quantum dots," *Proceedings of the National Academy of Sciences of the United States of America*, vol. 104, no. 34, pp. 13666–13671, 2007.

- [37] D. Maysinger, M. Behrendt, M. Lalancette-Herbert, and J. Kriz, "Real-time imaging of astrocyte response to quantum dots: In vivo screening model system for biocompatibility of nanoparticles," *Nano Letters*, vol. 7, no. 8, pp. 2513–2520, 2007.
- [38] P. Subramaniam, S. J. Lee, S. Shah, S. Patel, V. Starovoytov, and K. B. Lee, "Generation of a library of non-toxic quantum dots for cellular imaging and sirna delivery," *Adv Mater*, vol. 24, no. 29, pp. 4014–9, 2012.
- [39] A. S. Arbab, V. Frenkel, S. D. Pandit, S. A. Anderson, G. T. Yocum, M. Bur, H. M. Khuu, E. J. Read, and J. A. Frank, "Magnetic resonance imaging and confocal microscopy studies of magnetically labeled endothelial progenitor cells trafficking to sites of tumor angiogenesis," *Stem Cells*, vol. 24, no. 3, pp. 671–678, 2006.
- [40] A. B. Rosen, D. J. Kelly, A. J. T. Schuldt, J. Lu, I. A. Potapova, S. V. Doronin, K. J. Robichaud, R. B. Robinson, M. R. Rosen, P. R. Brink, G. R. Gaudette, and I. S. Cohen, "Finding fluorescent needles in the cardiac haystack: Tracking human mesenchymal stem cells labeled with quantum dots for quantitative in vivo three-dimensional fluorescence analysis," *Stem Cells*, vol. 25, no. 8, pp. 2128–2138, 2007.
- [41] J. R. Slotkin, L. Chakrabarti, H. N. Dai, R. S. E. Carney, T. Hirata, B. S. Bregman, G. I. Gallicano, J. G. Corbin, and T. F. Haydar, "In vivo quantum dot labeling of mammalian stem and progenitor cells," *Developmental Dynamics*, vol. 236, pp. 3393–3401, 2007.
- [42] J. C. Wu, "Comparison of imaging techniques for tracking cardiac stem cell therapy," *Journal of Nuclear Medicine*, vol. 48, pp. 1916–1919, 2007.
- [43] H. Chen, I. Titushkin, M. Stroschio, and M. Cho, "Altered membrane dynamics of quantum dot-conjugated integrins during osteogenic differentiation of human bone marrow derived progenitor cells," *Biophysical Journal*, vol. 92, no. 1399–1408, p. 1399, 2007.
- [44] B. J. Muller-Borer, M. C. Collins, P. R. Gunst, W. E. Cascio, Kypson, and A. P., "Quantum dot labeling of mesenchymal stem cells," *Journal of Nanobiotechnology*, vol. 5, no. 9, 2007.
- [45] L. S. Shah, P. A. Clark, E. K. Moioli, M. A. Stroschio, and J. J. Mao, "Labeling of mesenchymal stem cells by bioconjugated quantum dots," *Nano Letters*, vol. 7, pp. 3071–3079, 2007.
- [46] A. Rak-Raszewska, M. Marcello, S. Kenny, D. Edgar, V. See, and P. Murray, "Quantum dots do not affect the behaviour of mouse embryonic stem cells and kidney stem cells and are suitable for short-term tracking," *PLoS One*, vol. 7, no. 3, p. e32650, 2012.
- [47] T. Jamieson, R. Bakhshi, D. Petrova, R. Pocock, M. Imani, and A. M. Seifalian, "Biological applications of quantum dots," *Biomaterials*, vol. 28, pp. 4717–4732, 2007.

- [48] B. I. Ipe, M. Lehnig, and C. M. Niemeyer, "On the generation of free radical species from quantum dots," *Small*, vol. 1, no. 7, pp. 706–709, 2005.
- [49] C. Kirchner, T. Liedl, S. Kudera, T. Pellegrino, A. M. Javier, H. E. Gaub, S. Stolze, N. Fertig, and W. J. Parak, "Cytotoxicity of colloidal cdse and cdse/zns nanoparticles," *Nano Letters*, vol. 5, no. 2, pp. 331–338, 2005.
- [50] I. L. Medintz, H. T. Uyeda, E. R. Goldman, and H. Mattoussi, "Quantum dot bioconjugates for imaging labelling and sensing," *Nature Materials*, vol. 4, pp. 435–446, 2005.
- [51] A. P. Alivisatos, W. W. Gu, and C. Larabell, "Quantum dots as cellular probes," *Annual Review of Biomedical Engineering*, vol. 7, pp. 55–76, 2005.
- [52] P. Ghosh, G. Han, M. De, C. K. Kim, and V. M. Rotello, "Gold nanoparticles in delivery applications," *Adv Drug Deliv Rev*, vol. 60, no. 11, pp. 1307–15, 2008.
- [53] A. Verma and F. Stellacci, "Effect of surface properties on nanoparticle-cell interactions," *Small*, vol. 6, no. 1, pp. 12–21, 2010.
- [54] C. Yi, D. Liu, C. C. Fong, J. Zhang, and M. Yang, "Gold nanoparticles promote osteogenic differentiation of mesenchymal stem cells through p38 mapk pathway," *ACS Nano*, vol. 4, no. 11, pp. 6439–48, 2010.
- [55] J. L. Santos, D. Pandita, J. Rodrigues, A. P. Pego, P. L. Granja, G. Balian, and H. Tomas, "Receptor-mediated gene delivery using pamam dendrimers conjugated with peptides recognized by mesenchymal stem cells," *Mol Pharm*, vol. 7, no. 3, pp. 763–74, 2010.
- [56] M. Goldberg, R. Langer, and X. Jia, "Nanostructured materials for applications in drug delivery and tissue engineering," *J Biomater Sci Polym Ed*, vol. 18, no. 3, pp. 241–68, 2007.
- [57] C. L. Gebhart and A. V. Kabanov, "Evaluation of polyplexes as gene transfer agents," *J Control Release*, vol. 73, no. 2-3, pp. 401–16, 2001.
- [58] D. Pandita, J. L. Santos, J. Rodrigues, A. P. Pego, P. L. Granja, and H. Tomas, "Gene delivery into mesenchymal stem cells: a biomimetic approach using rgd nanoclusters based on poly(amidoamine) dendrimers," *Biomacromolecules*, vol. 12, no. 2, pp. 472–81, 2011.
- [59] D. T. Scadden, "The stem-cell niche as an entity of action," *Nature*, vol. 441, no. 7097, pp. 1075–9, 2006.
- [60] N. J. Sniadecki, R. A. Desai, S. A. Ruiz, and C. S. Chen, "Nanotechnology for cell-substrate interactions," *Ann Biomed Eng*, vol. 34, no. 1, pp. 59–74, 2006.
- [61] P. G. Gillespie and R. G. Walker, "Molecular basis of mechanosensory transduction," *Nature*, vol. 413, no. 6852, pp. 194–202, 2001.
- [62] R. J. Jackman, J. L. Wilbur, and G. M. Whitesides, "Fabrication of submicrometer features on curved substrates by microcontact printing," *Science*, vol. 269, no. 5224, pp. 664–6, 1995.

- [63] M. Mrksich and G. M. Whitesides, "Using self-assembled monolayers to understand the interactions of man-made surfaces with proteins and cells," *Annu Rev Biophys Biomol Struct*, vol. 25, pp. 55–78, 1996.
- [64] B. A. Langowski and K. E. Uhrich, "Microscale plasma-initiated patterning (mupip)," *Langmuir*, vol. 21, no. 23, pp. 10509–14, 2005.
- [65] R. Delgado-Rivera, J. Griffin, C. L. Ricupero, M. Grumet, S. Meiners, and K. E. Uhrich, "Microscale plasma-initiated patterning of electrospun polymer scaffolds," *Colloids Surf B Biointerfaces*, vol. 84, no. 2, pp. 591–6, 2011.
- [66] J. Tang, R. Peng, and J. Ding, "The regulation of stem cell differentiation by cell-cell contact on micropatterned material surfaces," *Biomaterials*, vol. 31, no. 9, pp. 2470–2476, 2010.
- [67] K. A. Kilian, B. Bugarija, B. T. Lahn, and M. Mrksich, "Geometric cues for directing the differentiation of mesenchymal stem cells," *Proc Natl Acad Sci U S A*, vol. 107, no. 11, pp. 4872–7, 2010.
- [68] A. Solanki, S. Shah, K. A. Memoli, S. Y. Park, S. Hong, and K. B. Lee, "Controlling differentiation of neural stem cells using extracellular matrix protein patterns," *Small*, vol. 6, no. 22, pp. 2509–13, 2010.
- [69] L. Gao, R. McBeath, and C. S. Chen, "Stem cell shape regulates a chondrogenic versus myogenic fate through *rac1* and *n-cadherin*," *Stem Cells*, vol. 28, no. 3, pp. 564–72, 2010.
- [70] K. Y. Baik, S. Y. Park, K. Heo, K. B. Lee, and S. Hong, "Carbon nanotube monolayer cues for osteogenesis of mesenchymal stem cells," *Small*, vol. 7, no. 6, pp. 741–5, 2011.
- [71] S. Y. Park, D. S. Choi, H. J. Jin, J. Park, K. E. Byun, K. B. Lee, and S. Hong, "Polarization-controlled differentiation of human neural stem cells using synergistic cues from the patterns of carbon nanotube monolayer coating," *ACS Nano*, vol. 5, no. 6, pp. 4704–11, 2011.
- [72] T. R. Nayak, H. Andersen, V. S. Makam, C. Khaw, S. Bae, X. Xu, P. L. Ee, J. H. Ahn, B. H. Hong, G. Pastorin, and B. Ozyilmaz, "Graphene for controlled and accelerated osteogenic differentiation of human mesenchymal stem cells," *ACS Nano*, vol. 5, no. 6, pp. 4670–8, 2011.
- [73] S. Y. Park, J. Park, S. H. Sim, M. G. Sung, K. S. Kim, B. H. Hong, and S. Hong, "Enhanced differentiation of human neural stem cells into neurons on graphene," *Advanced Materials*, vol. 23, no. 36, pp. H263–+, 2011. Park, Sung Young Park, Jaesung Sim, Sung Hyun Sung, Moon Gyu Kim, Kwang S. Hong, Byung Hee Hong, Seunghun.
- [74] Y. R. Shih, C. N. Chen, S. W. Tsai, Y. J. Wang, and O. K. Lee, "Growth of mesenchymal stem cells on electrospun type I collagen nanofibers," *Stem Cells*, vol. 24, no. 11, pp. 2391–7, 2006.

- [75] G. T. Christopherson, H. Song, and H. Q. Mao, "The influence of fiber diameter of electrospun substrates on neural stem cell differentiation and proliferation," *Biomaterials*, vol. 30, no. 4, pp. 556–64, 2009.
- [76] S. H. Lim, X. Y. Liu, H. Song, K. J. Yarema, and H. Q. Mao, "The effect of nanofiber-guided cell alignment on the preferential differentiation of neural stem cells," *Biomaterials*, vol. 31, no. 34, pp. 9031–9, 2010.
- [77] S. H. Lee, J. H. Sung, and T. H. Park, "Nanomaterial-based biosensor as an emerging tool for biomedical applications," *Ann Biomed Eng*, vol. 40, no. 6, pp. 1384–97, 2012.
- [78] X. Zhang, Q. Guo, and D. Cui, "Recent advances in nanotechnology applied to biosensors," *Sensors (Basel)*, vol. 9, no. 2, pp. 1033–53, 2009.
- [79] M. Pacios, I. Martin-Fernandez, X. Borrise, M. del Valle, J. Bartroli, E. Lora-Tamayo, P. Godignon, F. Perez-Murano, and M. J. Esplandiu, "Real time protein recognition in a liquid-gated carbon nanotube field-effect transistor modified with aptamers," *Nanoscale*, vol. 4, no. 19, pp. 5917–23, 2012.
- [80] M. B. Lerner, J. D'Souza, T. Pazina, J. Dailey, B. R. Goldsmith, M. K. Robinson, and A. T. Johnson, "Hybrids of a genetically engineered antibody and a carbon nanotube transistor for detection of prostate cancer biomarkers," *ACS Nano*, vol. 6, no. 6, pp. 5143–9, 2012.
- [81] K. S. Novoselov, A. K. Geim, S. V. Morozov, D. Jiang, Y. Zhang, S. V. Dubonos, I. V. Grigorieva, and A. A. Firsov, "Electric field effect in atomically thin carbon films," *Science*, vol. 306, no. 5696, pp. 666–669, 2004.
- [82] Y. Liu, X. Dong, and P. Chen, "Biological and chemical sensors based on graphene materials," *Chem Soc Rev*, vol. 41, no. 6, pp. 2283–307, 2012.
- [83] Y. Ohno, K. Maehashi, Y. Yamashiro, and K. Matsumoto, "Electrolyte-gated graphene field-effect transistors for detecting ph protein adsorption," *Nano Letters*, vol. 9, no. 9, pp. 3318–3322, 2009.
- [84] S. Mao, G. Lu, K. Yu, Z. Bo, and J. Chen, "Specific protein detection using thermally reduced graphene oxide sheet decorated with gold nanoparticle-antibody conjugates," *Advanced Materials*, vol. 22, no. 32, pp. 3521–+, 2010.
- [85] S. Myung, A. Solanki, C. Kim, J. Park, K. S. Kim, and K. B. Lee, "Graphene-encapsulated nanoparticle-based biosensor for the selective detection of cancer biomarkers," *Adv Mater*, vol. 23, no. 19, pp. 2221–5, 2011.
- [86] A. Gao, N. Lu, Y. Wang, P. Dai, T. Li, X. Gao, and C. Fan, "Enhanced sensing of nucleic acids with silicon nanowire field effect transistor biosensors," *Nano Lett*, vol. 12, no. 10, pp. 5262–8, 2012.
- [87] G. F. Zheng, F. Patolsky, Y. Cui, W. U. Wang, and C. M. Lieber, "Multiplexed electrical detection of cancer markers with nanowire sensor arrays," *Nature Biotechnology*, vol. 23, no. 10, pp. 1294–1301, 2005.

- [88] R. J. Chen, S. Bangsaruntip, K. A. Drouvalakis, N. W. S. Kam, M. Shim, Y. M. Li, W. Kim, P. J. Utz, and H. J. Dai, "Noncovalent functionalization of carbon nanotubes for highly specific electronic biosensors," *Proceedings of the National Academy of Sciences of the United States of America*, vol. 100, no. 9, pp. 4984–4989, 2003.
- [89] Z. Medarova, W. Pham, C. Farrar, V. Petkova, and A. Moore, "In vivo imaging of sirna delivery and silencing in tumors," *Nature Medicine*, vol. 13, no. 3, pp. 372–377, 2007.
- [90] D. M. Dykxhoorn, D. Palliser, and J. Lieberman, "The silent treatment: sirnas as small molecule drugs," *Gene Therapy*, vol. 13, no. 6, pp. 541–552, 2006.
- [91] L. Wasungu and D. Hoekstra, "Cationic lipids, lipoplexes and intracellular delivery of genes," *Journal of Controlled Release*, vol. 116, no. 2, pp. 255–264, 2006. 9th European Symposium on Controlled Drug Delivery Apr 05-07, 2006 Noordwijk, NETHERLANDS Alza; FIP Int Pharmaceut Federat; Janssen Pharmaceut; Johnson and Johnson Pharmaceuticals ; NV Organon; Traskbritt; Twente Reg; DSM Res; Medtronic; OctoPlus; Elsevier; Innocore; Purac; Inst BioMed Technol.
- [92] J. H. Jeong, H. Mok, Y.-K. Oh, and T. G. Park, "sirna conjugate delivery systems," *Bioconjugate Chemistry*, vol. 20, no. 1, pp. 5–14, 2009.
- [93] M. L. Patil, M. Zhang, S. Betigeri, O. Taratula, H. He, and T. Minko, "Surface-modified and internally cationic polyamidoamine dendrimers for efficient sirna delivery," *Bioconjugate Chemistry*, vol. 19, no. 7, pp. 1396–1403, 2008.
- [94] A. Zintchenko, A. Philipp, A. Dehshahri, and E. Wagner, "Simple modifications of branched pei lead to highly efficient sirna carriers with low toxicity," *Bioconjugate Chemistry*, vol. 19, no. 7, pp. 1448–1455, 2008.
- [95] J.-H. Lee, K. Lee, S. H. Moon, Y. Lee, T. G. Park, and J. Cheon, "All-in-one target-cell-specific magnetic nanoparticles for simultaneous molecular imaging and sirna delivery," *Angewandte Chemie-International Edition*, vol. 48, no. 23, pp. 4174–4179, 2009.
- [96] A. M. Derfus, A. A. Chen, D.-H. Min, E. Ruoslahti, and S. N. Bhatia, "Targeted quantum dot conjugates for sirna delivery," *Bioconjugate Chemistry*, vol. 18, no. 5, pp. 1391–1396, 2007.
- [97] L. Qi and X. Gao, "Quantum dot-amphipol nanocomplex for intracellular delivery and real-time imaging of sirna," *Acs Nano*, vol. 2, no. 7, pp. 1403–1410, 2008.
- [98] J.-S. Lee, J. J. Green, K. T. Love, J. Sunshine, R. Langer, and D. G. Anderson, "Gold, poly(beta-amino ester) nanoparticles for small interfering rna delivery," *Nano Letters*, vol. 9, no. 6, pp. 2402–2406, 2009.
- [99] M. V. Yezhelyev, L. Qi, R. M. O'Regan, S. Nie, and X. Gao, "Proton-sponge coated quantum dots for sirna delivery and intracellular imaging," *Journal of the American Chemical Society*, vol. 130, no. 28, pp. 9006–9012, 2008.

- [100] D. A. Giljohann, D. S. Seferos, A. E. Prigodich, P. C. Patel, and C. A. Mirkin, "Gene regulation with polyvalent sirna-nanoparticle conjugates," *Journal of the American Chemical Society*, vol. 131, no. 6, pp. 2072–+, 2009.
- [101] R. Kikkeri, B. Lepenies, A. Adibekian, P. Laurino, and P. H. Seeberger, "In vitro imaging and in vivo liver targeting with carbohydrate capped quantum dots," *Journal of the American Chemical Society*, vol. 131, no. 6, pp. 2110–+, 2009.
- [102] A. A. Bhirde, V. Patel, J. Gavard, G. Zhang, A. A. Sousa, A. Masedunskas, R. D. Leapman, R. Weigert, J. S. Gutkind, and J. F. Rusling, "Targeted killing of cancer cells in vivo and in vitro with egf-directed carbon nanotube-based drug delivery," *Acs Nano*, vol. 3, no. 2, pp. 307–316, 2009.
- [103] Q. W. Fan and W. A. Weiss, "Rna interference against a glioma-derived allele of egfr induces blockade at g(2)m," *Oncogene*, vol. 24, no. 5, pp. 829–837, 2005.
- [104] E. Arwert, S. Hingtgen, J.-L. Figueiredo, H. Bergquist, U. Mahmood, R. Weissleder, and K. Shah, "Visualizing the dynamics of egfr activity and antiglioma therapies in vivo," *Cancer Research*, vol. 67, no. 15, pp. 7335–7342, 2007.
- [105] A. Veeravagu, Z. Liu, G. Niu, K. Chen, B. Jia, W. Cai, C. Jin, A. R. Hsu, A. J. Connolly, V. Tse, F. Wang, and X. Chen, "Integrin alpha(v)beta(3)-targeted radioimmunotherapy of glioblastoma multiforme," *Clinical Cancer Research*, vol. 14, no. 22, pp. 7330–7339, 2008.
- [106] M. S. Lesniak and H. Brem, "Targeted therapy for brain tumours," *Nature Reviews Drug Discovery*, vol. 3, no. 6, pp. 499–508, 2004.
- [107] A. J. Ekstrand, N. Sugawa, C. D. James, and V. P. Collins, "Amplified and rearranged epidermal growth-factor receptor genes in human glioblastomas reveal deletions of sequences encoding portions of the n-terminal and or c-terminal tails," *Proceedings of the National Academy of Sciences of the United States of America*, vol. 89, no. 10, pp. 4309–4313, 1992.
- [108] P. A. Humphrey, A. J. Wong, B. Vogelstein, M. R. Zalutsky, G. N. Fuller, G. E. Archer, H. S. Friedman, M. M. Kwatra, S. H. Bigner, and D. D. Bigner, "Antisynthetic peptide antibody reacting at the fusion junction of deletion mutant epidermal growth-factor receptors in human glioblastoma," *Proceedings of the National Academy of Sciences of the United States of America*, vol. 87, no. 11, pp. 4207–4211, 1990.
- [109] I. Vivanco and C. L. Sawyers, "The phosphatidylinositol 3-kinase-akt pathway in human cancer," *Nature Reviews Cancer*, vol. 2, no. 7, pp. 489–501, 2002.
- [110] F. Yamoutpour, V. Bodernpudi, S. E. Park, W. Pan, M. J. Mauzy, R. A. Kratzke, A. Dudek, D. A. Potter, R. A. Woo, D. M. O'Rourke, D. J. Tindall, and F. Farasati, "Gene silencing for epidermal growth factor receptor variant iii induces cell-specific cytotoxicity," *Molecular Cancer Therapeutics*, vol. 7, no. 11, pp. 3586–3597, 2008.

- [111] J. Jung, A. Solanki, K. A. Memoli, K.-i. Kamei, H. Kim, M. A. Drahl, L. J. Williams, H.-R. Tseng, and K. Lee, "Selective inhibition of human brain tumor cells through multifunctional quantum-dot-based sirna delivery," *Angewandte Chemie-International Edition*, vol. 49, no. 1, pp. 103–107, 2010. Times Cited: 36.
- [112] J. J. Li, Y. A. Wang, W. Z. Guo, J. C. Keay, T. D. Mishima, M. B. Johnson, and X. G. Peng, "Large-scale synthesis of nearly monodisperse cdse/cds core/shell nanocrystals using air-stable reagents via successive ion layer adsorption and reaction," *Journal of the American Chemical Society*, vol. 125, no. 41, pp. 12567–12575, 2003.
- [113] R. G. Xie, U. Kolb, J. X. Li, T. Basche, and A. Mews, "Synthesis and characterization of highly luminescent cdse-core cds/zno.5cd0.5s/zns multishell nanocrystals," *Journal of the American Chemical Society*, vol. 127, no. 20, pp. 7480–7488, 2005.
- [114] W. Liu, M. Howarth, A. B. Greytak, Y. Zheng, D. G. Nocera, A. Y. Ting, and M. G. Bawendi, "Compact biocompatible quantum dots functionalized for cellular imaging," *Journal of the American Chemical Society*, vol. 130, no. 4, pp. 1274–1284, 2008.
- [115] K. Susumu, H. T. Uyeda, I. L. Medintz, T. Pons, J. B. Delehanty, and H. Mattoussi, "Enhancing the stability and biological functionalities of quantum dots via compact multifunctional ligands," *Journal of the American Chemical Society*, vol. 129, no. 45, pp. 13987–13996, 2007.
- [116] S. Kida, M. Maeda, K. Hojo, Y. Eto, S. Nakagawa, and K. Kawasaki, "Studies on heterobifunctional cross-linking reagents, 6-maleimidohexanoic acid active esters," *Chemical & Pharmaceutical Bulletin*, vol. 55, no. 4, pp. 685–687, 2007.
- [117] A. S. M. Kamruzzahan, A. Ebner, L. Wildling, F. Kienberger, C. K. Riemer, C. D. Hahn, P. D. Pollheimer, P. Winklehner, M. Hoelzl, B. Lackner, D. M. Schoerkl, P. Hinterdorfer, and H. J. Gruber, "Antibody linking to atomic force microscope tips via disulfide bond formation," *Bioconjugate Chemistry*, vol. 17, no. 6, pp. 1473–1481, 2006.
- [118] S. Bauhuber, C. Hozsa, M. Breunig, and A. Goepferich, "Delivery of nucleic acids via disulfide-based carrier systems," *Advanced Materials*, vol. 21, no. 32-33, pp. 3286–3306, 2009.
- [119] Y. L. Chiu, A. Ali, C. Y. Chu, H. Cao, and T. M. Rana, "Visualizing a correlation between sirna localization, cellular uptake, and rna interference in living cells," *Chemistry & Biology*, vol. 11, no. 8, pp. 1165–1175, 2004.
- [120] J. Xie, K. Chen, H.-Y. Lee, C. Xu, A. R. Hsu, S. Peng, X. Chen, and S. Sun, "Ultras-small c(rgdyk)-coated fe(3)o(4) nanoparticles and their specific targeting to integrin alpha(v)beta(3)-rich tumor cells," *Journal of the American Chemical Society*, vol. 130, no. 24, pp. 7542–+, 2008.

- [121] W. B. Cai, D. W. Shin, K. Chen, O. Gheysens, Q. Z. Cao, S. X. Wang, S. S. Gambhir, and X. Y. Chen, "Peptide-labeled near-infrared quantum dots for imaging tumor vasculature in living subjects," *Nano Letters*, vol. 6, no. 4, pp. 669–676, 2006.
- [122] C. C. Berry, "Intracellular delivery of nanopartides via the hiv-1 tat pepticle," *Nanomedicine*, vol. 3, no. 3, pp. 357–365, 2008.
- [123] G. Ruan, A. Agrawal, A. I. Marcus, and S. Nie, "Imaging and tracking of tat peptide-conjugated quantum dots in living cells: new insights into nanoparticle uptake, intracellular transport, and vesicle shedding," *Journal of the American Chemical Society*, vol. 129, no. 47, pp. 14759–14766, 2007.
- [124] A. M. Derfus, W. C. W. Chan, and S. N. Bhatia, "Probing the cytotoxicity of semiconductor quantum dots," *Nano Letters*, vol. 4, no. 1, pp. 11–18, 2004.
- [125] A. Meyer, C. M. van Golen, B. Kim, K. L. van Golen, and E. L. Feldman, "Integrin expression regulates neuroblastoma attachment and migration," *Neoplasia*, vol. 6, no. 4, pp. 332–342, 2004.
- [126] L. Martiniova, E. W. Lai, A. G. Elkahloun, M. Abu-Asab, A. Wickremasinghe, D. C. Solis, S. M. Perera, T.-T. Huynh, I. A. Lubensky, A. S. Tischler, R. Kvetnansky, S. Alesci, J. C. Morris, and K. Pacak, "Characterization of an animal model of aggressive metastatic pheochromocytoma linked to a specific gene signature," *Clinical & Experimental Metastasis*, vol. 26, no. 3, pp. 239–250, 2009.
- [127] Z.-b. Li, W. Cai, Q. Cao, K. Chen, Z. Wu, L. He, and X. Chen, "64cu-labeled tetrameric and octameric rgd peptides for small-animal pet of tumor alpha(v)beta(3) integrin expression," *Journal of Nuclear Medicine*, vol. 48, no. 7, pp. 1162–1171, 2007.
- [128] M. Y. Wang, K. V. Lu, S. Zhu, E. Q. Dia, I. Vivanco, G. M. Shackelford, W. K. Cavenee, I. K. Mellinghoff, T. F. Cloughesy, C. L. Sawyers, and P. S. Mischel, "Mammalian target of rapamycin inhibition promotes response to epidermal growth factor receptor kinase inhibitors in pten-deficient and pten-intact glioblastoma cells," *Cancer Research*, vol. 66, no. 16, pp. 7864–7869, 2006.
- [129] R. C. Schugar, P. D. Robbins, and B. M. Deasy, "Small molecules in stem cell self-renewal and differentiation," *Gene Ther*, vol. 15, no. 2, pp. 126–35, 2008.
- [130] Y. Xu, Y. Shi, and S. Ding, "A chemical approach to stem-cell biology and regenerative medicine," *Nature*, vol. 453, no. 7193, pp. 338–344, 2008.
- [131] T. Lin, R. Ambasudhan, X. Yuan, W. Li, S. Hilcove, R. Abujarour, X. Lin, H. S. Hahm, E. Hao, A. Hayek, and S. Ding, "A chemical platform for improved induction of human ipscs," *Nat Meth*, vol. 6, no. 11, pp. 805–808, 2009.
- [132] C. A. Lyssiotis, L. L. Lairson, A. E. Boitano, H. Wurdak, S. Zhu, and P. G. Schultz, "Chemical control of stem cell fate and developmental potential," *Angew Chem Int Ed Engl*, vol. 50, no. 1, pp. 200–42, 2011.
- [133] W. L. Jorgensen and E. M. Duffy, "Prediction of drug solubility from structure," *Adv Drug Deliv Rev*, vol. 54, no. 3, pp. 355–66, 2002.

- [134] K. V. Balakin, N. P. Savchuk, and I. V. Tetko, "In silico approaches to prediction of aqueous and dmsolubility of drug-like compounds: trends, problems and solutions," *Curr Med Chem*, vol. 13, no. 2, pp. 223–41, 2006.
- [135] R. Pal, M. K. Mamidi, A. K. Das, and R. Bhonde, "Diverse effects of dimethyl sulfoxide (dmsol) on the differentiation potential of human embryonic stem cells," *Arch Toxicol*, vol. 86, no. 4, pp. 651–61, 2012.
- [136] D. Bumcrot, M. Manoharan, V. Koteliensky, and D. W. Y. Sah, "Rnai therapeutics: a potential new class of pharmaceutical drugs," *Nature Chemical Biology*, vol. 2, no. 12, pp. 711–719, 2006.
- [137] D. H. Kim and J. J. Rossi, "Strategies for silencing human disease using rna interference," *Nature Reviews Genetics*, vol. 8, no. 3, pp. 173–184, 2007.
- [138] H. Zaehres, M. W. Lensch, L. Daheron, S. A. Stewart, J. Itskovitz-Eldor, and G. Q. Daley, "High-efficiency rna interference in human embryonic stem cells," *Stem Cells*, vol. 23, no. 3, pp. 299–305, 2005.
- [139] L. Ding and F. Buchholz, "Rnai in embryonic stem cells," *Stem Cell Rev.*, vol. 2, no. 1, pp. 11–18, 2006.
- [140] W. W. Y. Yau, P. O. Rujitanaroj, L. Lam, and S. Y. Chew, "Directing stem cell fate by controlled rna interference," *Biomaterials*, vol. 33, no. 9, pp. 2608–2628, 2012.
- [141] M. L. Hribal, J. Nakae, T. Kitamura, J. R. Shutter, and D. Accili, "Regulation of insulin-like growth factor-dependent myoblast differentiation by foxo forkhead transcription factors," *J Cell Biol*, vol. 162, no. 4, pp. 535–41, 2003.
- [142] Z. He, J. Li, C. Zhen, L. Feng, and X. Ding, "Knockdown of p53 by rna in es cells facilitates ra-induced differentiation into muscle cells," *Biochem Biophys Res Commun*, vol. 335, no. 3, pp. 676–83, 2005.
- [143] M. Dominska and D. M. Dykxhoorn, "Breaking down the barriers: sirna delivery and endosome escape," *J Cell Sci*, vol. 123, no. Pt 8, pp. 1183–9, 2010.
- [144] J. Wang, Z. Lu, M. G. Wientjes, and J. L. Au, "Delivery of sirna therapeutics: barriers and carriers," *AAPS J*, vol. 12, no. 4, pp. 492–503, 2010.
- [145] A. Solanki, S. Shah, P. T. Yin, and K. B. Lee, "Nanotopography-mediated reverse uptake for sirna delivery into neural stem cells to enhance neuronal differentiation," *Sci Rep*, vol. 3, p. 1553, 2013. Solanki, Aniruddh Shah, Shreyas Yin, Perry T Lee, Ki-Bum England Scientific reports *Sci Rep*. 2013 Mar 27;3:1553. doi: 10.1038/srep01553.
- [146] T. Merdan, J. Kopecek, and T. Kissel, "Prospects for cationic polymers in gene and oligonucleotide therapy against cancer," *Advanced Drug Delivery Reviews*, vol. 54, no. 5, pp. 715–758, 2002.
- [147] S. K. Dhara, A. Majumder, M. C. Dodla, and S. L. Stice, "Nonviral gene delivery in neural progenitors derived from human pluripotent stem cells," *Methods Mol Biol*, vol. 767, pp. 343–54, 2011.

- [148] F. Zhao, Y. Zhao, Y. Liu, X. L. Chang, C. Y. Chen, and Y. L. Zhao, "Cellular uptake, intracellular trafficking, and cytotoxicity of nanomaterials," *Small*, vol. 7, no. 10, pp. 1322–1337, 2011.
- [149] M. E. Davis and M. E. Brewster, "Cyclodextrin-based pharmaceuticals: Past, present and future," *Nature Reviews Drug Discovery*, vol. 3, no. 12, pp. 1023–1035, 2004.
- [150] M. E. Brewster and T. Loftsson, "Cyclodextrins as pharmaceutical solubilizers," *Advanced Drug Delivery Reviews*, vol. 59, no. 7, pp. 645–666, 2007.
- [151] K. Uekama, F. Hirayama, and T. Irie, "Cyclodextrin drug carrier systems," *Chemical Reviews*, vol. 98, no. 5, pp. 2045–2076, 1998.
- [152] S. Yang and S. May, "Release of cationic polymer-dna complexes from the endosome: A theoretical investigation of the proton sponge hypothesis," *J Chem Phys*, vol. 129, no. 18, p. 185105, 2008.
- [153] S. H. Pun, N. C. Bellocq, A. J. Liu, G. Jensen, T. Machemer, E. Quijano, T. Schluep, S. F. Wen, H. Engler, J. Heidel, and M. E. Davis, "Cyclodextrin-modified polyethylenimine polymers for gene delivery," *Bioconjugate Chemistry*, vol. 15, no. 4, pp. 831–840, 2004.
- [154] C. Kim, B. P. Shah, P. Subramaniam, and K.-B. Lee, "Synergistic induction of apoptosis in brain cancer cells by targeted codelivery of sirna and anticancer drugs," *Molecular Pharmaceutics*, vol. 8, no. 5, pp. 1955–1961, 2011.
- [155] M. E. Davis and N. C. Bellocq, "Cyclodextrin-containing polymers for gene delivery," *Journal of Inclusion Phenomena and Macrocyclic Chemistry*, vol. 44, no. 1-4, pp. 17–22, 2002.
- [156] J. D. Heidel, S. Hu, X. F. Liu, T. J. Triche, and M. E. Davis, "Lack of interferon response in animals to naked sirnas," *Nat Biotechnol*, vol. 22, no. 12, pp. 1579–82, 2004.
- [157] J. D. Heidel, S. W. Hu, X. F. Liu, T. Triche, and M. E. Davis, "Cyclodextrin-containing polycations (cdps) for in vivo delivery of sirna," *Abstracts of Papers of the American Chemical Society*, vol. 227, pp. 208–BIOT, 2004.
- [158] C. C. Stolt, P. Lommes, E. Sock, M. C. Chaboissier, A. Schedl, and M. Wegner, "The sox9 transcription factor determines glial fate choice in the developing spinal cord," *Gene. Dev.*, vol. 17, no. 13, pp. 1677–1689, 2003.
- [159] L. C. Cheng, E. Pastrana, M. Tavazoie, and F. Doetsch, "mir-124 regulates adult neurogenesis in the subventricular zone stem cell niche," *Nature Neurosci.*, vol. 12, no. 4, pp. 399–408, 2009.
- [160] S. Jacobs, D. C. Lie, K. L. DeCicco, Y. Shi, L. M. DeLuca, F. H. Gage, and R. M. Evans, "Retinoic acid is required early during adult neurogenesis in the dentate gyrus," *Proceedings of the National Academy of Sciences of the United States of America*, vol. 103, no. 10, pp. 3902–3907, 2006.

- [161] J. Marill, N. Idres, C. C. Capron, E. Nguyen, and G. G. Chabot, "Retinoic acid metabolism and mechanism of action: a review," *Curr Drug Metab*, vol. 4, no. 1, pp. 1–10, 2003.
- [162] F. Leyboldt, J. Lewerenz, and A. Methner, "Identification of genes up-regulated by retinoic-acid-induced differentiation of the human neuronal precursor cell line ntera-2 cl.d1," *J Neurochem*, vol. 76, no. 3, pp. 806–14, 2001.
- [163] Y. K. Jang, J. J. Park, M. C. Lee, B. H. Yoon, Y. S. Yang, S. E. Yang, and S. U. Kim, "Retinoic acid-mediated induction of neurons and glial cells from human umbilical cord-derived hematopoietic stem cells," *J Neurosci Res*, vol. 75, no. 4, pp. 573–84, 2004.
- [164] C. E. Scott, S. L. Wynn, A. Sesay, C. Cruz, M. Cheung, M. V. Gomez Gaviro, S. Booth, B. Gao, K. S. Cheah, R. Lovell-Badge, and J. Briscoe, "Sox9 induces and maintains neural stem cells," *Nat Neurosci*, vol. 13, no. 10, pp. 1181–9, 2010.
- [165] S. Kumar, D. Chanda, and S. Ponnazhagan, "Therapeutic potential of genetically modified mesenchymal stem cells," *Gene Ther.*, vol. 15, no. 10, pp. 711–715, 2008.
- [166] J. J. Green, B. Y. Zhou, M. M. Mitalipova, C. Beard, R. Langer, R. Jaenisch, and D. G. Anderson, "Nanoparticles for gene transfer to human embryonic stem cell colonies," *Nano Letters*, vol. 8, no. 10, pp. 3126–3130, 2008.
- [167] F. Yang, S. W. Cho, S. M. Son, S. R. Bogatyrev, D. Singh, J. J. Green, Y. Mei, S. Park, S. H. Bhang, B. S. Kim, R. Langer, and D. G. Anderson, "Genetic engineering of human stem cells for enhanced angiogenesis using biodegradable polymeric nanoparticles," *Proc. Natl. Acad. Sci. USA*, vol. 107, no. 8, pp. 3317–3322, 2010.
- [168] J. Zoldan, A. K. R. Lytton-Jean, E. D. Karagiannis, K. Deiorio-Haggar, L. M. Bellan, R. Langer, and D. G. Anderson, "Directing human embryonic stem cell differentiation by non-viral delivery of sirna in 3d culture," *Biomaterials*, vol. 32, no. 31, pp. 7793–7800, 2011.
- [169] A. Heidrsbach, A. Gaspar-Maia, M. T. McManus, and M. Ramalho-Santos, "Rna interference in embryonic stem cells and the prospects for future therapies," *Gene Ther.*, vol. 13, no. 6, pp. 478–486, 2006.
- [170] T. Geng, Y. H. Zhan, J. Wang, and C. Lu, "Transfection of cells using flow-through electroporation based on constant voltage," *Nature Protoc.*, vol. 6, no. 8, pp. 1192–1208, 2011.
- [171] J. E. Kim, J. Y. Shin, and M. H. Cho, "Magnetic nanoparticles: an update of application for drug delivery and possible toxic effects," *Arch. Toxicol.*, vol. 86, no. 5, pp. 685–700, 2012.
- [172] E. V. B. van Gaal, R. van Eijk, R. S. Oosting, R. J. Kok, W. E. Hennink, D. J. A. Crommelin, and E. Mastrobattista, "How to screen non-viral gene delivery systems in vitro?," *J. Control. Release*, vol. 154, no. 3, pp. 218–232, 2011.

- [173] M. Rosner, N. Siegel, C. Fuchs, N. Slabina, H. Dolznig, and M. Hengstschlager, "Efficient sirna-mediated prolonged gene silencing in human amniotic fluid stem cells," *Nature Protoc.*, vol. 5, no. 6, pp. 1081–1095, 2010.
- [174] K. M. McMahon, R. K. Mutharasan, S. Tripathy, D. Veliceasa, M. Bobeica, D. K. Shumaker, A. J. Luthi, B. T. Helfand, H. Ardehali, C. A. Mirkin, O. Volpert, and C. S. Thaxton, "Biomimetic high density lipoprotein nanoparticles for nucleic acid delivery," *Nano Lett.*, vol. 11, no. 3, pp. 1208–1214, 2011.
- [175] S. J. Tseng and S. C. Tang, "Development of poly(amino ester glycol urethane)/sirna polyplexes for gene silencing," *Bioconjugate Chem.*, vol. 18, no. 5, pp. 1383–1390, 2007.
- [176] Y. Omid, J. Barar, and S. Akhtar, "Toxicogenomics of cationic lipid-based vectors for gene therapy: impact of microarray technology," *Curr Drug Deliv*, vol. 2, no. 4, pp. 429–41, 2005.
- [177] S. Akhtar and I. Benter, "Toxicogenomics of non-viral drug delivery systems for rna: potential impact on sirna-mediated gene silencing activity and specificity," *Adv Drug Deliv Rev*, vol. 59, no. 2-3, pp. 164–82, 2007.
- [178] L. Braydich-Stolle, S. Hussain, J. J. Schlager, and M. C. Hofmann, "In vitro cytotoxicity of nanoparticles in mammalian germline stem cells," *Toxicol. Sci.*, vol. 88, no. 2, pp. 412–419, 2005.
- [179] S. J. H. Soenen and M. De Cuyper, "Assessing iron oxide nanoparticle toxicity in vitro: current status and future prospects," *Nanomedicine*, vol. 5, no. 8, pp. 1261–1275, 2010.
- [180] J. W. Yoo, D. J. Irvine, D. E. Discher, and S. Mitragotri, "Bio-inspired, bioengineered and biomimetic drug delivery carriers," *Nature Rev. Drug Discov.*, vol. 10, no. 7, pp. 521–535, 2011.
- [181] T. Segura, M. J. Volk, and L. D. Shea, "Substrate-mediated dna delivery: role of the cationic polymer structure and extent of modification," *J Control Release*, vol. 93, no. 1, pp. 69–84, 2003.
- [182] Z. Bengali, A. K. Pannier, T. Segura, B. C. Anderson, J. H. Jang, T. A. Mustoe, and L. D. Shea, "Gene delivery through cell culture substrate adsorbed dna complexes," *Biotechnol Bioeng*, vol. 90, no. 3, pp. 290–302, 2005.
- [183] S. Mehrotra, I. Lee, and C. Chan, "Multilayer mediated forward and patterned sirna transfection using linear-pei at extended n/p ratios," *Acta Biomater*, vol. 5, no. 5, pp. 1474–88, 2009.
- [184] A. Oyane, H. Tsurushima, and A. Ito, "Highly efficient gene transfer system using a laminin-dna-apatite composite layer," *J Gene Med*, vol. 12, no. 2, pp. 194–206, 2010.
- [185] K. R. Kam, L. A. Walsh, S. M. Bock, M. Koval, K. E. Fischer, R. F. Ross, and T. A. Desai, "Nanostructure-mediated transport of biologics across epithelial tissue: Enhancing permeability via nanotopography," *Nano Lett*, vol. 13, no. 1, pp. 164–71, 2013.

- [186] S. Park, Y. S. Kim, W. B. Kim, and S. Jon, "Carbon nanosyringe array as a platform for intracellular delivery," *Nano Lett*, vol. 9, no. 4, pp. 1325–9, 2009.
- [187] A. K. Shalek, J. T. Gaublotme, L. Wang, N. Yosef, N. Chevrier, M. S. Andersen, J. T. Robinson, N. Pochet, D. Neuberg, R. S. Gertner, I. Amit, J. R. Brown, N. Hacohen, A. Regev, C. J. Wu, and H. Park, "Nanowire-mediated delivery enables functional interrogation of primary immune cells: Application to the analysis of chronic lymphocytic leukemia," *Nano Letters*, vol. 12, no. 12, pp. 6498–6504, 2012.
- [188] A. K. Shalek, J. T. Robinson, E. S. Karp, J. S. Lee, D. R. Ahn, M. H. Yoon, A. Sutton, M. Jorgolli, R. S. Gertner, T. S. Gujral, G. MacBeath, E. G. Yang, and H. Park, "Vertical silicon nanowires as a universal platform for delivering biomolecules into living cells," *Proc Natl Acad Sci U S A*, vol. 107, no. 5, pp. 1870–5, 2010.
- [189] C. J. Bettinger, R. Langer, and J. T. Borenstein, "Engineering substrate topography at the micro- and nanoscale to control cell function," *Angew Chem Int Ed Engl*, vol. 48, no. 30, pp. 5406–15, 2009.
- [190] E. K. Yim, E. M. Darling, K. Kulangara, F. Guilak, and K. W. Leong, "Nanotopography-induced changes in focal adhesions, cytoskeletal organization, and mechanical properties of human mesenchymal stem cells," *Biomaterials*, vol. 31, no. 6, pp. 1299–306, 2010.
- [191] A. F. Adler and K. W. Leong, "Emerging links between surface nanotechnology and endocytosis: impact on nonviral gene delivery," *Nano Today*, vol. 5, no. 6, pp. 553–569, 2010.
- [192] B. K. Teo, S. H. Goh, T. S. Kustandi, W. W. Loh, H. Y. Low, and E. K. Yim, "The effect of micro and nanotopography on endocytosis in drug and gene delivery systems," *Biomaterials*, vol. 32, no. 36, pp. 9866–75, 2011.
- [193] K. Saha, A. J. Keung, E. F. Irwin, Y. Li, L. Little, D. V. Schaffer, and K. E. Healy, "Substrate modulus directs neural stem cell behavior," *Biophysical Journal*, vol. 95, no. 9, pp. 4426–4438, 2008.
- [194] A. A. Moe, M. Suryana, G. Marcy, S. K. Lim, S. Ankam, J. Z. Goh, J. Jin, B. K. Teo, J. B. Law, H. Y. Low, E. L. Goh, M. P. Sheetz, and E. K. Yim, "Microarray with micro- and nano-topographies enables identification of the optimal topography for directing the differentiation of primary murine neural progenitor cells," *Small*, vol. 8, no. 19, pp. 3050–61, 2012.
- [195] A. Dhaliwal, J. Lam, M. Maldonado, C. Lin, and T. Segura, "Extracellular matrix modulates non-viral gene transfer to mouse mesenchymal stem cells," *Soft Matter*, vol. 8, no. 5, pp. 1451–1459, 2012.
- [196] S. Khormae, O. A. Ali, J. Chodosh, and D. J. Mooney, "Optimizing sirna efficacy through alteration in the target cell-adhesion substrate interaction," *J Biomed Mater Res A*, vol. 100, no. 10, pp. 2637–43, 2012.

- [197] A. H. Reddi, "Role of morphogenetic proteins in skeletal tissue engineering and regeneration," *Nature Biotech.*, vol. 16, no. 3, pp. 247–252, 1998.
- [198] R. Kalluri, "Basement membranes: Structure, assembly and role in tumour angiogenesis," *Nature Rev. Cancer*, vol. 3, no. 6, pp. 422–433, 2003.
- [199] Z. Bengali, J. C. Rea, and L. D. Shea, "Gene expression and internalization following vector adsorption to immobilized proteins: dependence on protein identity and density," *J Gene Med*, vol. 9, no. 8, pp. 668–78, 2007.
- [200] H. J. Kong, S. Hsiong, and D. J. Mooney, "Nanoscale cell adhesion ligand presentation regulates nonviral gene delivery and expression," *Nano Lett*, vol. 7, no. 1, pp. 161–6, 2007.
- [201] L. Pelkmans, T. Burli, M. Zerial, and A. Helenius, "Caveolin-stabilized membrane domains as multifunctional transport and sorting devices in endocytic membrane traffic," *Cell*, vol. 118, no. 6, pp. 767–780, 2004.
- [202] E. V. Makeyev, J. W. Zhang, M. A. Carrasco, and T. Maniatis, "The microRNA mir-124 promotes neuronal differentiation by triggering brain-specific alternative pre-mrna splicing," *Mol. Cell*, vol. 27, no. 3, pp. 435–448, 2007.
- [203] T. Sato, T. Ishii, and Y. Okahata, "In vitro gene delivery mediated by chitosan. effect of ph, serum, and molecular mass of chitosan on the transfection efficiency," *Biomaterials*, vol. 22, no. 15, pp. 2075–2080, 2001.
- [204] F. Guilak, D. M. Cohen, B. T. Estes, J. M. Gimble, W. Liedtke, and C. S. Chen, "Control of stem cell fate by physical interactions with the extracellular matrix," *Cell Stem Cell*, vol. 5, no. 1, pp. 17–26, 2009.
- [205] C. J. Flaim, S. Chien, and S. N. Bhatia, "An extracellular matrix microarray for probing cellular differentiation," *Nature Methods*, vol. 2, no. 2, pp. 119–125, 2005.
- [206] C. J. Flaim, D. Teng, S. Chien, and S. N. Bhatia, "Combinatorial signaling microenvironments for studying stem cell fate," *Stem Cells and Development*, vol. 17, no. 1, pp. 29–39, 2008.
- [207] F. H. Gage, J. Ray, and L. J. Fisher, "Isolation, characterization, and use of stem-cells from the cns," *Annual Review of Neuroscience*, vol. 18, pp. 159–192, 1995.
- [208] F. H. Gage, "Mammalian neural stem cells," *Science*, vol. 287, no. 5457, pp. 1433–1438, 2000.
- [209] E. D. Roberson and L. Mucke, "100 years and counting: Prospects for defeating alzheimer's disease," *Science*, vol. 314, no. 5800, pp. 781–784, 2006.
- [210] A. Bjorklund and O. Lindvall, "Cell replacement therapies for central nervous system disorders," *Nature Neuroscience*, vol. 3, no. 6, pp. 537–544, 2000.
- [211] J. H. Kim, J. M. Auerbach, J. A. Rodriguez-Gomez, I. Velasco, D. Gavin, N. Lumelsky, S. H. Lee, J. Nguyen, R. Sanchez-Pernaute, K. Bankiewicz, and R. McKay, "Dopamine neurons derived from embryonic stem cells function in an animal model of parkinson's disease," *Nature*, vol. 418, no. 6893, pp. 50–56, 2002.

- [212] O. Lindvall and Z. Kokaia, "Stem cells for the treatment of neurological disorders," *Nature*, vol. 441, no. 7097, pp. 1094–1096, 2006.
- [213] C. B. Johansson, S. Momma, D. L. Clarke, M. Risling, U. Lendahl, and J. Frisen, "Identification of a neural stem cell in the adult mammalian central nervous system," *Cell*, vol. 96, no. 1, pp. 25–34, 1999.
- [214] G. Martino and S. Pluchino, "The therapeutic potential of neural stem cells," *Nature Reviews Neuroscience*, vol. 7, no. 5, pp. 395–406, 2006.
- [215] F. Barnabe-Heider and J. Frisen, "Stem cells for spinal cord repair," *Cell Stem Cell*, vol. 3, no. 1, pp. 16–24, 2008.
- [216] K. G. Bath and F. S. Lee, "Neurotrophic factor control of adult svz neurogenesis," *Developmental Neurobiology*, vol. 70, no. 5, pp. 339–349, 2010. Si.
- [217] N. Matsuda, H. Lu, Y. Fukata, J. Noritake, H. Gao, S. Mukherjee, T. Nemoto, M. Fukata, and M.-m. Poo, "Differential activity-dependent secretion of brain-derived neurotrophic factor from axon and dendrite," *Journal of Neuroscience*, vol. 29, no. 45, pp. 14185–14198, 2009.
- [218] H. J. Song, C. F. Stevens, and F. H. Gage, "Neural stem cells from adult hippocampus develop essential properties of functional cns neurons," *Nature Neuroscience*, vol. 5, no. 5, pp. 438–445, 2002.
- [219] X.-J. Li, X. Zhang, M. A. Johnson, Z.-B. Wang, T. LaVaute, and S.-C. Zhang, "Coordination of sonic hedgehog and wnt signaling determines ventral and dorsal telencephalic neuron types from human embryonic stem cells," *Development*, vol. 136, no. 23, pp. 4055–4063, 2009.
- [220] N.-E. Szabo, T. Zhao, X. Zhou, and G. Alvarez-Bolado, "The role of sonic hedgehog of neural origin in thalamic differentiation in the mouse," *Journal of Neuroscience*, vol. 29, no. 8, pp. 2453–2466, 2009.
- [221] M. Warashina, K. H. Min, T. Kuwabara, A. Huynh, F. H. Gage, P. G. Schultz, and S. Ding, "A synthetic small molecule that induces neuronal differentiation of adult hippocampal neural progenitor cells," *Angewandte Chemie-International Edition*, vol. 45, no. 4, pp. 591–593, 2006.
- [222] A. Banerjee, M. Arha, S. Choudhary, R. S. Ashton, S. R. Bhatia, D. V. Schaffer, and R. S. Kane, "The influence of hydrogel modulus on the proliferation and differentiation of encapsulated neural stem cells," *Biomaterials*, vol. 30, no. 27, pp. 4695–4699, 2009.
- [223] N. D. Leipzig and M. S. Shoichet, "The effect of substrate stiffness on adult neural stem cell behavior," *Biomaterials*, vol. 30, no. 36, pp. 6867–6878, 2009.
- [224] A. K. Magnusson, P. Linderholm, C. Vieider, M. Ulfendahl, and A. Erlandsson, "Surface protein patterns govern morphology, proliferation, and expression of cellular markers but have no effect on physiological properties of cortical precursor cells," *Journal of Neuroscience Research*, vol. 86, no. 11, pp. 2363–2375, 2008.

- [225] M. M. Harper, E.-A. Ye, C. C. Blong, M. L. Jacobson, and D. S. Sakaguchi, “Integrins contribute to initial morphological development and process outgrowth in rat adult hippocampal progenitor cells,” *Journal of Molecular Neuroscience*, vol. 40, no. 3, pp. 269–283, 2010.
- [226] S. Y. Park, S. Y. Park, S. Namgung, B. Kim, J. Im, Y. Kim, K. Sun, K. B. Lee, J.-M. Nam, Y. Park, and S. Hong, “Carbon nanotube monolayer patterns for directed growth of mesenchymal stem cells,” *Advanced Materials*, vol. 19, no. 18, pp. 2530–+, 2007.
- [227] C. M. Nelson, R. P. Jean, J. L. Tan, W. F. Liu, N. J. Sniadecki, A. A. Spector, and C. S. Chen, “Emergent patterns of growth controlled by multicellular form and mechanics,” *Proceedings of the National Academy of Sciences of the United States of America*, vol. 102, no. 33, pp. 11594–11599, 2005.
- [228] S. A. Ruiz and C. S. Chen, “Emergence of patterned stem cell differentiation within multicellular structures,” *Stem Cells*, vol. 26, no. 11, pp. 2921–2927, 2008.
- [229] G. Forte, F. Carotenuro, F. Pagliari, S. Pagliari, P. Cossa, R. Fiaccavento, A. Ahiwalia, G. Vozzi, B. Vinci, A. Serafino, A. Rinaldi, E. Traversa, L. Carosella, M. Minieri, and P. Di Nardo, “Criticality of the biological and physical stimuli array inducing resident cardiac stem cell determination,” *Stem Cells*, vol. 26, no. 8, pp. 2093–2103, 2008.
- [230] T. P. Kraehenbuehl, P. Zammaretti, A. J. Van der Vlies, R. G. Schoenmakers, M. P. Lutolf, M. E. Jaconi, and J. A. Hubbell, “Three-dimensional extracellular matrix-directed cardioprogenitor differentiation: Systematic modulation of a synthetic cell-responsive peg-hydrogel,” *Biomaterials*, vol. 29, no. 18, pp. 2757–2766, 2008.
- [231] T. P. Kraehenbuehl, L. S. Ferreira, P. Zammaretti, J. A. Hubbell, and R. Langer, “Cell-responsive hydrogel for encapsulation of vascular cells,” *Biomaterials*, vol. 30, no. 26, pp. 4318–4324, 2009.
- [232] R. S. Taichman, “Blood and bone: two tissues whose fates are intertwined to create the hematopoietic stem-cell niche,” *Blood*, vol. 105, no. 7, pp. 2631–2639, 2005.
- [233] M. J. Kiel and S. J. Morrison, “Uncertainty in the niches that maintain haematopoietic stem cells,” *Nature Reviews Immunology*, vol. 8, no. 4, pp. 290–301, 2008.
- [234] G. B. Adams and D. T. Scadden, “The hematopoietic stem cell in its place,” *Nature Immunology*, vol. 7, no. 4, pp. 333–337, 2006.
- [235] H. Agheli, J. Malmstrom, E. M. Larsson, M. Textor, and D. S. Sutherland, “Large area protein nanopatterning for biological applications,” *Nano Letters*, vol. 6, no. 6, pp. 1165–1171, 2006.
- [236] M. Nakajima, T. Ishimuro, K. Kato, I.-K. Ko, I. Hirata, Y. Arima, and H. Iwata, “Combinatorial protein display for the cell-based screening of biomaterials that direct neural stem cell differentiation,” *Biomaterials*, vol. 28, no. 6, pp. 1048–1060, 2007.

- [237] A. Ruiz, L. Buzanska, D. Gilliland, H. Rauscher, L. Sirghi, T. Sobanski, M. Zychowicz, L. Ceriotti, F. Bretagnol, S. Coecke, P. Colpo, and F. Ross, "Microstamped surfaces for the patterned growth of neural stem cells," *Biomaterials*, vol. 29, no. 36, pp. 4766–4774, 2008.
- [238] B. Knoell, C. Weigl, A. Nordheim, and F. Bonhoeffer, "Stripe assay to examine axonal guidance and cell migration," *Nature Protocols*, vol. 2, no. 5, pp. 1216–1224, 2007.
- [239] H. M. Geller and J. W. Fawcett, "Building a bridge: Engineering spinal cord repair," *Experimental Neurology*, vol. 174, no. 2, pp. 125–136, 2002. Times Cited: 129.
- [240] C. Miller, S. Jęftinija, and S. Mallapragada, "Synergistic effects of physical and chemical guidance cues on neurite alignment and outgrowth on biodegradable polymer substrates," *Tissue Engineering*, vol. 8, no. 3, pp. 367–378, 2002. Times Cited: 58.
- [241] Y. D. Teng, E. B. Lavik, X. L. Qu, K. I. Park, J. Ourednik, D. Zurakowski, R. Langer, and E. Y. Snyder, "Functional recovery following traumatic spinal cord injury mediated by a unique polymer scaffold seeded with neural stem cells," *Proceedings of the National Academy of Sciences of the United States of America*, vol. 99, no. 5, pp. 3024–3029, 2002. Times Cited: 442.
- [242] M. Abematsu, K. Tsujimura, M. Yamano, M. Saito, K. Kohno, J. Kohyama, M. Namihira, S. Komiya, and K. Nakashima, "Neurons derived from transplanted neural stem cells restore disrupted neuronal circuitry in a mouse model of spinal cord injury," *Journal of Clinical Investigation*, vol. 120, no. 9, pp. 3255–3266, 2010. Times Cited: 35.
- [243] B. Sandner, P. Prang, F. J. Rivera, L. Aigner, A. Blesch, and N. Weidner, "Neural stem cells for spinal cord repair," *Cell and Tissue Research*, vol. 349, no. 1, pp. 349–362, 2012. Times Cited: 1.
- [244] G. Kumar, C. K. Tison, K. Chatterjee, P. S. Pine, J. H. McDaniel, M. L. Salit, M. F. Young, and J. Simon, Carl G., "The determination of stem cell fate by 3d scaffold structures through the control of cell shape," *Biomaterials*, vol. 32, no. 35, pp. 9188–9196, 2011. Times Cited: 9.
- [245] D.-H. Kim, P. P. Provenzano, C. L. Smith, and A. Levchenko, "Matrix nanotopography as a regulator of cell function," *Journal of Cell Biology*, vol. 197, no. 3, pp. 351–360, 2012. Times Cited: 6.
- [246] A. K. Geim and K. S. Novoselov, "The rise of graphene," *Nature Materials*, vol. 6, no. 3, pp. 183–191, 2007. Times Cited: 6772.
- [247] K. Yang, S. Zhang, G. Zhang, X. Sun, S.-T. Lee, and Z. Liu, "Graphene in mice: Ultrahigh in vivo tumor uptake and efficient photothermal therapy," *Nano Letters*, vol. 10, no. 9, pp. 3318–3323, 2010. Times Cited: 180.
- [248] J.-L. Li, H.-C. Bao, X.-L. Hou, L. Sun, X.-G. Wang, and M. Gu, "Graphene oxide nanoparticles as a nonbleaching optical probe for two-photon luminescence

- imaging and cell therapy,” *Angewandte Chemie-International Edition*, vol. 51, no. 8, pp. 1830–1834, 2012. Times Cited: 10.
- [249] Y. Zhu, S. Murali, W. Cai, X. Li, J. W. Suk, J. R. Potts, and R. S. Ruoff, “Graphene and graphene oxide: Synthesis, properties, and applications,” *Advanced Materials*, vol. 22, no. 35, pp. 3906–3924, 2010. Times Cited: 526.
- [250] S. Some, S.-M. Ho, P. Dua, E. Hwang, Y. H. Shin, H. Yoo, J.-S. Kang, D.-K. Lee, and H. Lee, “Dual functions of highly potent graphene derivative-poly-l-lysine composites to inhibit bacteria and support human cells,” *Acs Nano*, vol. 6, no. 8, pp. 7151–7161, 2012. Times Cited: 1.
- [251] G. Y. Chen, D. W. P. Pang, S. M. Hwang, H. Y. Tuan, and Y. C. Hu, “A graphene-based platform for induced pluripotent stem cells culture and differentiation,” *Biomaterials*, vol. 33, no. 2, pp. 418–427, 2012. Times Cited: 16.
- [252] N. A. Kotov, J. O. Winter, I. P. Clements, E. Jan, B. P. Timko, S. Campidelli, S. Pathak, A. Mazzatenta, C. M. Lieber, M. Prato, R. V. Bellamkonda, G. A. Silva, N. W. S. Kam, F. Patolsky, and L. Ballerini, “Nanomaterials for neural interfaces,” *Advanced Materials*, vol. 21, no. 40, pp. 3970–4004, 2009. Times Cited: 91.
- [253] K. Kang, S.-E. Choi, H. S. Jang, W. K. Cho, Y. Nam, I. S. Choi, and J. S. Lee, “In vitro developmental acceleration of hippocampal neurons on nanostructures of self-assembled silica beads in filopodium-size ranges,” *Angewandte Chemie-International Edition*, vol. 51, no. 12, pp. 2855–2858, 2012. Times Cited: 0.
- [254] M. T. Lam, S. Sim, X. Zhu, and S. Takayama, “The effect of continuous wavy micropatterns on silicone substrates on the alignment of skeletal muscle myoblasts and myotubes,” *Biomaterials*, vol. 27, no. 24, pp. 4340–4347, 2006. Times Cited: 53.
- [255] J. Zhang, F. Zhang, H. Yang, X. Huang, H. Liu, J. Zhang, and S. Guo, “Graphene oxide as a matrix for enzyme immobilization,” *Langmuir*, vol. 26, no. 9, pp. 6083–6085, 2010. Times Cited: 57.
- [256] D. F. Cooke, A. B. Goldring, I. Yamayoshi, P. Tsourkas, G. H. Recanzone, A. Tiriach, T. Pan, S. I. Simon, and L. Krubitzer, “Fabrication of an inexpensive, implantable cooling device for reversible brain deactivation in animals ranging from rodents to primates,” *Journal of Neurophysiology*, vol. 107, no. 12, pp. 3543–3558, 2012. Times Cited: 0.
- [257] N. Hallfors, A. Khan, M. D. Dickey, and A. M. Taylor, “Integration of pre-aligned liquid metal electrodes for neural stimulation within a user-friendly microfluidic platform,” *Lab on a Chip*, vol. 13, no. 4, pp. 522–526, 2013. Times Cited: 0.
- [258] G. Eda, G. Fanchini, and M. Chhowalla, “Large-area ultrathin films of reduced graphene oxide as a transparent and flexible electronic material,” *Nature Nanotechnology*, vol. 3, no. 5, pp. 270–274, 2008. Times Cited: 960.
- [259] A. Reina, X. Jia, J. Ho, D. Nezich, H. Son, V. Bulovic, M. S. Dresselhaus, and J. Kong, “Large area, few-layer graphene films on arbitrary substrates by chemical vapor deposition,” *Nano Letters*, vol. 9, no. 1, pp. 30–35, 2009. Times Cited: 1180.

- [260] X. Li, W. Cai, J. An, S. Kim, J. Nah, D. Yang, R. Piner, A. Velamakanni, I. Jung, E. Tutuc, S. K. Banerjee, L. Colombo, and R. S. Ruoff, "Large-area synthesis of high-quality and uniform graphene films on copper foils," *Science*, vol. 324, no. 5932, pp. 1312–1314, 2009. Times Cited: 1613.
- [261] G. Eda, H. Yamaguchi, D. Voiry, T. Fujita, M. Chen, and M. Chhowalla, "Photoluminescence from chemically exfoliated mos<sub>2</sub>," *Nano Letters*, vol. 11, no. 12, pp. 5111–5116, 2011. Times Cited: 48.
- [262] Y. Cui, Q. Q. Wei, H. K. Park, and C. M. Lieber, "Nanowire nanosensors for highly sensitive and selective detection of biological and chemical species," *Science*, vol. 293, no. 5533, pp. 1289–1292, 2001.
- [263] F. Patolsky, G. Zheng, and C. M. Lieber, "Fabrication of silicon nanowire devices for ultrasensitive, label-free, real-time detection of biological and chemical species," *Nature Protocols*, vol. 1, no. 4, pp. 1711–1724, 2006.
- [264] K. Bradley, M. Briman, A. Star, and G. Gruner, "Charge transfer from adsorbed proteins," *Nano Letters*, vol. 4, no. 2, pp. 253–256, 2004.
- [265] R. J. Chen, H. C. Choi, S. Bangsaruntip, E. Yenilmez, X. W. Tang, Q. Wang, Y. L. Chang, and H. J. Dai, "An investigation of the mechanisms of electronic sensing of protein adsorption on carbon nanotube devices," *Journal of the American Chemical Society*, vol. 126, no. 5, pp. 1563–1568, 2004.
- [266] A. Star, Y. Lu, K. Bradley, and G. Gruner, "Nanotube optoelectronic memory devices," *Nano Letters*, vol. 4, no. 9, pp. 1587–1591, 2004.
- [267] X. Tang, S. Bansaruntip, N. Nakayama, E. Yenilmez, Y.-L. Chang, and Q. Wang, "Carbon nanotube dna sensor and sensing mechanism," *Nano Letters*, vol. 6, no. 8, pp. 1632–1636, 2006.
- [268] J. Lu, I. Do, L. T. Drzal, R. M. Worden, and I. Lee, "Nanometal-decorated exfoliated graphite nanoplatelet based glucose biosensors with high sensitivity and fast response," *Acs Nano*, vol. 2, no. 9, pp. 1825–1832, 2008.
- [269] A. T. Woolley, C. Guillemette, C. L. Cheung, D. E. Housman, and C. M. Lieber, "Direct haplotyping of kilobase-size dna using carbon nanotube probes," *Nature Biotechnology*, vol. 18, no. 7, pp. 760–763, 2000.
- [270] D. Du, Z. Zou, Y. Shin, J. Wang, H. Wu, M. H. Engelhard, J. Liu, I. A. Aksay, and Y. Lin, "Sensitive immunosensor for cancer biomarker based on dual signal amplification strategy of graphene sheets and multienzyme functionalized carbon nanospheres," *Analytical Chemistry*, vol. 82, no. 7, pp. 2989–2995, 2010.
- [271] J. H. Jung, D. S. Cheon, F. Liu, K. B. Lee, and T. S. Seo, "A graphene oxide based immuno-biosensor for pathogen detection," *Angewandte Chemie-International Edition*, vol. 49, no. 33, pp. 5708–5711, 2010.
- [272] C.-H. Lu, H.-H. Yang, C.-L. Zhu, X. Chen, and G.-N. Chen, "A graphene platform for sensing biomolecules," *Angewandte Chemie-International Edition*, vol. 48, no. 26, pp. 4785–4787, 2009.

- [273] C. Shan, H. Yang, J. Song, D. Han, A. Ivaska, and L. Niu, "Direct electrochemistry of glucose oxidase and biosensing for glucose based on graphene," *Analytical Chemistry*, vol. 81, no. 6, pp. 2378–2382, 2009.
- [274] P. Avouris, "Graphene: Electronic and photonic properties and devices," *Nano Letters*, vol. 10, no. 11, pp. 4285–4294, 2010.
- [275] K. S. Kim, Y. Zhao, H. Jang, S. Y. Lee, J. M. Kim, K. S. Kim, J.-H. Ahn, P. Kim, J.-Y. Choi, and B. H. Hong, "Large-scale pattern growth of graphene films for stretchable transparent electrodes," *Nature*, vol. 457, no. 7230, pp. 706–710, 2009.
- [276] K. S. Novoselov, A. K. Geim, S. V. Morozov, D. Jiang, M. I. Katsnelson, I. V. Grigorieva, S. V. Dubonos, and A. A. Firsov, "Two-dimensional gas of massless dirac fermions in graphene," *Nature*, vol. 438, no. 7065, pp. 197–200, 2005.
- [277] Y. B. Zhang, Y. W. Tan, H. L. Stormer, and P. Kim, "Experimental observation of the quantum hall effect and berry's phase in graphene," *Nature*, vol. 438, no. 7065, pp. 201–204, 2005.
- [278] L. Jiao, L. Zhang, X. Wang, G. Diankov, and H. Dai, "Narrow graphene nanoribbons from carbon nanotubes," *Nature*, vol. 458, no. 7240, pp. 877–880, 2009.
- [279] X. Du, I. Skachko, A. Barker, and E. Y. Andrei, "Approaching ballistic transport in suspended graphene," *Nature Nanotechnology*, vol. 3, no. 8, pp. 491–495, 2008.
- [280] X. Dong, Y. Shi, W. Huang, P. Chen, and L.-J. Li, "Electrical detection of dna hybridization with single-base specificity using transistors based on cvd-grown graphene sheets," *Advanced Materials*, vol. 22, no. 14, pp. 1649–+, 2010.
- [281] D. A. Dikin, S. Stankovich, E. J. Zimney, R. D. Piner, G. H. B. Dommett, G. Evmenenko, S. T. Nguyen, and R. S. Ruoff, "Preparation and characterization of graphene oxide paper," *Nature*, vol. 448, no. 7152, pp. 457–460, 2007.
- [282] A. Citri and Y. Yarden, "Egf-erbB signalling: towards the systems level," *Nature Reviews Molecular Cell Biology*, vol. 7, no. 7, pp. 505–516, 2006.
- [283] N. E. Hynes and H. A. Lane, "ErbB receptors and cancer: The complexity of targeted inhibitors," *Nature Reviews Cancer*, vol. 5, no. 5, pp. 341–354, 2005.
- [284] Y. Yarden and M. X. Sliwkowski, "Untangling the erbB signalling network," *Nature Reviews Molecular Cell Biology*, vol. 2, no. 2, pp. 127–137, 2001.
- [285] I. Jung, D. A. Dikin, R. D. Piner, and R. S. Ruoff, "Tunable electrical conductivity of individual graphene oxide sheets reduced at "low" temperatures," *Nano Letters*, vol. 8, no. 12, pp. 4283–4287, 2008.
- [286] T. Kobayashi, N. Kimura, J. Chi, S. Hirata, and D. Hobar, "Channel-length-dependent field-effect mobility and carrier concentration of reduced graphene oxide thin-film transistors," *Small*, vol. 6, no. 11, pp. 1210–1215, 2010.
- [287] S. Myung, J. Park, H. Lee, K. S. Kim, and S. Hong, "Ambipolar memory devices based on reduced graphene oxide and nanoparticles," *Advanced Materials*, vol. 22, no. 18, pp. 2045–+, 2010.

- [288] S. Myung, M. Lee, G. T. Kim, J. S. Ha, and S. Hong, "Large-scale "surface-programmed assembly" of pristine vanadium oxide nanowire-based devices," *Advanced Materials*, vol. 17, no. 19, pp. 2361–+, 2005.
- [289] M. Lee, J. Im, B. Y. Lee, S. Myung, J. Kang, L. Huang, Y. K. Kwon, and S. Hong, "Linker-free directed assembly of high-performance integrated devices based on nanotubes and nanowires," *Nature Nanotechnology*, vol. 1, no. 1, pp. 66–71, 2006.
- [290] W. Yang, K. R. Ratinac, S. P. Ringer, P. Thordarson, J. J. Gooding, and F. Braet, "Carbon nanomaterials in biosensors: Should you use nanotubes or graphene?," *Angewandte Chemie-International Edition*, vol. 49, no. 12, pp. 2114–2138, 2010.
- [291] F. Chen, Q. Qing, J. Xia, J. Li, and N. Tao, "Electrochemical gate-controlled charge transport in graphene in ionic liquid and aqueous solution," *Journal of the American Chemical Society*, vol. 131, no. 29, pp. 9908–+, 2009.
- [292] A. Star, J. C. P. Gabriel, K. Bradley, and G. Gruner, "Electronic detection of specific protein binding using nanotube fet devices," *Nano Letters*, vol. 3, no. 4, pp. 459–463, 2003.
- [293] M. Abe, K. Murata, A. Kojima, Y. Ifuku, M. Shimizu, T. Ataka, and K. Matsumoto, "Quantitative detection of protein using a top-gate carbon nanotube field effect transistor," *Journal of Physical Chemistry C*, vol. 111, no. 24, pp. 8667–8670, 2007.
- [294] B. L. Allen, P. D. Kichambare, and A. Star, "Carbon nanotube field-effect-transistor-based biosensors," *Advanced Materials*, vol. 19, no. 11, pp. 1439–1451, 2007.
- [295] M. Y. Han, B. Oezylmaz, Y. Zhang, and P. Kim, "Energy band-gap engineering of graphene nanoribbons," *Physical Review Letters*, vol. 98, no. 20, 2007.
- [296] J. B. Oostinga, H. B. Heersche, X. Liu, A. F. Morpurgo, and L. M. K. Vandersypen, "Gate-induced insulating state in bilayer graphene devices," *Nature Materials*, vol. 7, no. 2, pp. 151–157, 2008. Times Cited: 518.
- [297] K. I. Bolotin, K. J. Sikes, Z. Jiang, M. Klima, G. Fudenberg, J. Hone, P. Kim, and H. L. Stormer, "Ultrahigh electron mobility in suspended graphene," *Solid State Communications*, vol. 146, no. 9-10, pp. 351–355, 2008.
- [298] Y.-M. Lin and P. Avouris, "Strong suppression of electrical noise in bilayer graphene nanodevices," *Nano Letters*, vol. 8, no. 8, pp. 2119–2125, 2008.
- [299] M. Ganzhorn, A. Vijayaraghavan, S. Dehm, F. Hennrich, A. A. Green, M. Fichtner, A. Voigt, M. Rapp, H. von Loehneysen, M. C. Hersam, M. M. Kappes, and R. Krupke, "Hydrogen sensing with diameter- and chirality-sorted carbon nanotubes," *Acs Nano*, vol. 5, no. 3, pp. 1670–1676, 2011.
- [300] M. R. Diehl, D. W. Steuerman, H. R. Tseng, S. A. Vignon, A. Star, P. C. Celestre, J. F. Stoddart, and J. R. Heath, "Single-walled carbon nanotube based molecular switch tunnel junctions," *Chemphyschem*, vol. 4, no. 12, pp. 1335–1339, 2003.

- [301] B. Li, X. Cao, H. G. Ong, J. W. Cheah, X. Zhou, Z. Yin, H. Li, J. Wang, F. Boey, W. Huang, and H. Zhang, "All-carbon electronic devices fabricated by directly grown single-walled carbon nanotubes on reduced graphene oxide electrodes," *Advanced Materials*, vol. 22, no. 28, pp. 3058–3061, 2010.
- [302] X. Kang, J. Wang, H. Wu, I. A. Aksay, J. Liu, and Y. Lin, "Glucose oxidase-graphene-chitosan modified electrode for direct electrochemistry and glucose sensing," *Biosensors & Bioelectronics*, vol. 25, no. 4, pp. 901–905, 2009.
- [303] S. Alwarappan, C. Liu, A. Kumar, and C.-Z. Li, "Enzyme-doped graphene nanosheets for enhanced glucose biosensing," *Journal of Physical Chemistry C*, vol. 114, no. 30, pp. 12920–12924, 2010.
- [304] C. Hjalmarsson, J. Stenflo, and A. Borgstrom, "Activated protein c-protein c inhibitor complex, activation peptide of carboxypeptidase b and c-reactive protein as predictors of severe acute pancreatitis," *Pancreatology*, vol. 9, no. 5, pp. 700–707, 2009.
- [305] S. Myung, P. T. Yin, C. Kim, J. Park, A. Solanki, P. I. Reyes, Y. Lu, K. S. Kim, and K.-B. Lee, "Label-free polypeptide-based enzyme detection using a graphene-nanoparticle hybrid sensor," *Advanced Materials*, vol. 24, no. 45, pp. 6081–+, 2012. Times Cited: 1.
- [306] D. B. Farmer, R. Golizadeh-Mojarad, V. Perebeinos, Y.-M. Lin, G. S. Tulevski, J. C. Tsang, and P. Avouris, "Chemical doping and electron-hole conduction asymmetry in graphene devices," *Nano Letters*, vol. 9, no. 1, pp. 388–392, 2009.
- [307] L. Bajzar, J. Morser, and M. Nesheim, "Tafi, or plasma procarboxypeptidase b, couples the coagulation and fibrinolytic cascades through the thrombin-thrombomodulin complex," *Journal of Biological Chemistry*, vol. 271, no. 28, pp. 16603–16608, 1996.
- [308] C. S. Consorti, A. P. Umpierre, R. F. de Souza, J. Dupont, and P. A. Z. Suarez, "Selective hydrogenation of 1,3-butadiene by transition metal compounds immobilized in 1-butyl-3-methyl imidazolium room temperature ionic liquids," *Journal of the Brazilian Chemical Society*, vol. 14, no. 3, pp. 401–405, 2003. Times Cited: 15.
- [309] P. Bergveld, "Thirty years of isfetology - what happened in the past 30 years and what may happen in the next 30 years," *Sensors and Actuators B-Chemical*, vol. 88, no. 1, pp. 1–20, 2003. 9th IMCS Meeting 2002 Boston, massachusetts Imcs.
- [310] P. Gimmel, K. D. Schierbaum, W. Gopel, H. H. Vandenvlekkert, and N. F. Derooij, "Microstructured solid-state ion-sensitive membranes by thermal-oxidation of ta," *Sensors and Actuators B-Chemical*, vol. 1, no. 1-6, pp. 345–349, 1990. 5th international conf on solid-state sensors and actuators and eurosensors 3 ( transducers 89 ) Jun 25-30, 1989 Montreux, switzerland.
- [311] P. Estrela, A. G. Stewart, F. Yan, and P. Migliorato, "Field effect detection of biomolecular interactions," *Electrochimica Acta*, vol. 50, no. 25-26, pp. 4995–5000,

2005. 55th Annual Meeting of the International-Society-of-Electrochemistry Sep, 2004 Thessaloniki, GREECE Int Soc Electrochem.
- [312] J. Yu, S. K. Jha, L. Xiao, Q. Liu, P. Wang, C. Surya, and M. Yang, "Algan/gan heterostructures for non-invasive cell electrophysiological measurements," *Biosensors & Bioelectronics*, vol. 23, no. 4, pp. 513–519, 2007.
- [313] J. T. Mabeck and G. G. Malliaras, "Chemical and biological sensors based on organic thin-film transistors," *Analytical and Bioanalytical Chemistry*, vol. 384, no. 2, pp. 343–353, 2006.
- [314] L. Torsi, A. Dodabalapur, L. Sabbatini, and P. G. Zambonin, "Multi-parameter gas sensors based on organic thin-film-transistors," *Sensors and Actuators B-Chemical*, vol. 67, no. 3, pp. 312–316, 2000.
- [315] J. Liu, M. Agarwal, and K. Varahramyan, "Glucose sensor based on organic thin film transistor using glucose oxidase and conducting polymer," *Sensors and Actuators B-Chemical*, vol. 135, no. 1, pp. 195–199, 2008.
- [316] Q. Zhang and V. Subramanian, "Dna hybridization detection with organic thin film transistors: Toward fast and disposable dna microarray chips," *Biosensors & Bioelectronics*, vol. 22, no. 12, pp. 3182–3187, 2007.
- [317] K. S. Chang, C. C. Chen, J. T. Sheu, and Y.-K. Li, "Detection of an uncharged steroid with a silicon nanowire field-effect transistor," *Sensors and Actuators B-Chemical*, vol. 138, no. 1, pp. 148–153, 2009.
- [318] Y.-M. Chu, C.-C. Lin, H.-C. Chang, C. Li, and C. Guo, "Tio(2) nanowire fet device: Encapsulation of biomolecules by electro polymerized pyrrole propylic acid," *Biosensors & Bioelectronics*, vol. 26, no. 5, pp. 2334–2340, 2011.
- [319] S. M. Al-Hilli, R. T. Al-Mofarji, and M. Willander, "Zinc oxide nanorod for intracellular ph sensing," *Applied Physics Letters*, vol. 89, no. 17, 2006.
- [320] A. Wei, X. W. Sun, J. X. Wang, Y. Lei, X. P. Cai, C. M. Li, Z. L. Dong, and W. Huang, "Enzymatic glucose biosensor based on zno nanorod array grown by hydrothermal decomposition," *Applied Physics Letters*, vol. 89, no. 12, 2006.
- [321] P. I. Reyes, Z. Zhang, H. Chen, Z. Duan, J. Zhong, G. Saraf, Y. Lu, O. Taratula, E. Galoppini, and N. N. Boustany, "A zno nanostructure-based quartz crystal microbalance device for biochemical sensing," *Ieee Sensors Journal*, vol. 9, no. 10, pp. 1302–1307, 2009.
- [322] R. Murali, P. J. Brennan, T. KieberEmmons, and M. I. Greene, "Structural analysis of p185(c-neu) and epidermal growth factor receptor tyrosine kinases: Oligomerization of kinase domains," *Proceedings of the National Academy of Sciences of the United States of America*, vol. 93, no. 13, pp. 6252–6257, 1996.
- [323] P. I. Reyes, C.-J. Ku, Z. Duan, Y. Lu, A. Solanki, and K.-B. Lee, "Zno thin film transistor immunosensor with high sensitivity and selectivity," *Applied Physics Letters*, vol. 98, no. 17, 2011. Times Cited: 5.